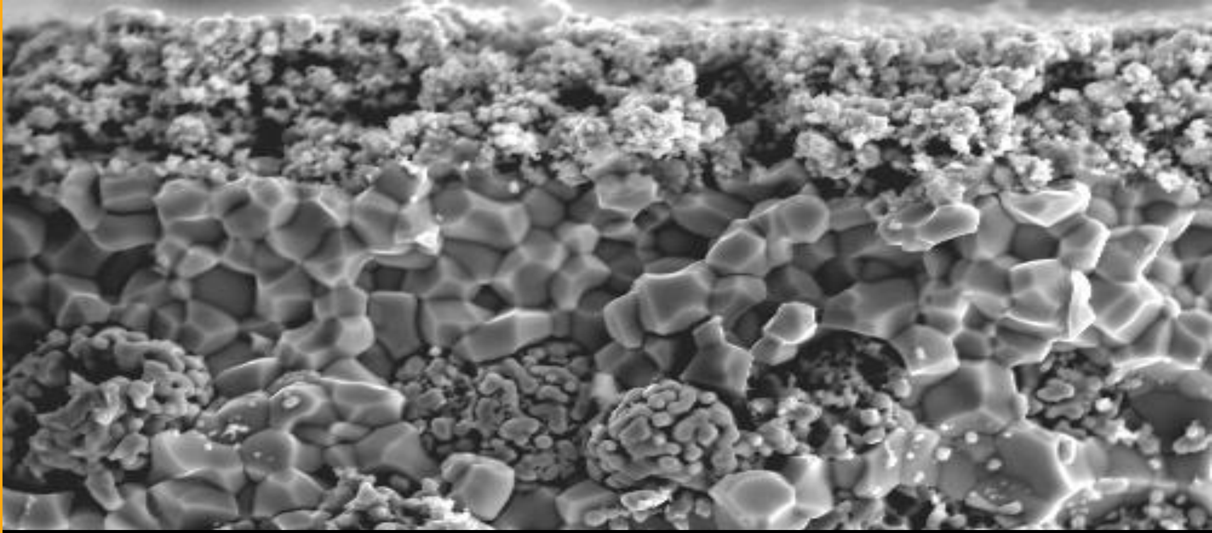

Development of electrocatalytic layers and thermo-fluid dynamic evaluation for high temperature membrane reactors

Thesis submitted by

David Catalán Martínez

To apply for the Degree of Doctor

Supervisor:

Prof. José Manuel Serra Alfaro

Valencia, October 2019

UNIVERSITAT
POLITÈCNICA
DE VALÈNCIA

INSTITUTO DE
TECNOLOGÍA
QUÍMICA

CSIC
CONSEJO SUPERIOR DE INVESTIGACIONES CIENTÍFICAS

Table of contents

1. SCOPE OF THE THESIS & OBJECTIVES 9

1.1 References 15

2. RESUMEN/SUMMARY/RESUM 17

2.1. Resumen 19

2.2. Summary 22

2.3. Resum 24

3. INTRODUCTION 27

3.1. Introduction to the membrane reactors 29

3.2. Membrane assemblies based on ionic ceramic conductors 34

3.2.1. Pure oxygen ion conductors 42

3.2.2. Pure proton conductors 45

3.2.3. Mixed ion – electronic conductors 49

3.3. Membrane reactor using high temperature ceramic materials 54

3.3.1. Hydrogen production 54

3.3.2. Syngas production 56

3.3.3. Higher hydrocarbons production 57

3.3.4. Methane production 60

3.3.5. Ammonia production 61

3.4. Electrodes for protonic conducting ceramics 62

3.5. Finite elements for high temperature membrane reactors .. 63

3.6. References 66

4. EXPERIMENTAL METHODOLOGY 77

4.1. Materials synthesis 79

4.1.1. Sol-gel method 79

4.1.2. Solid state reaction 81

4.1.3. Co-precipitation method 82

4.2. Deposition techniques 83

4.2.1. Tubular support tested 83

4.2.2. Dip-coating 84

4.2.3. Sputtering 85

4.2.4. Screen-printing 87

4.3. Structural characterization 88

4.3.1. X-ray powder diffraction 88

4.3.2. Scanning electron microscope 91

4.3.3. Field emission scanning electron microscope 93

4.4. Chemical characterization 94

4.4.1. Inductively Coupled Plasma Optical Emission Spectroscopy (ICP-OES) 94

4.5. Electrochemical characterization 94

4.5.1. Electrochemical Impedance Spectroscopy (EIS) 94

4.6. References 101

5. DIP-COATING METHOD TO DEVELOP COPPER BASED ANODES FOR HIGH TEMPERATURE MEMBRANE REACTORS 103

5.1. Introduction 105

5.2. Results 107

5.2.1. Characterization of synthesized materials 107

5.2.2. Optimization of the dip-coating methodology 110

5.2.3. Effect of the sintering process in the cermet microstructure 116

5.2.4. Effect of the dipping conditions 120

5.2.5. Electrochemical characterization 122

5.2.6. Stability of the cermet electrode 127

5.2.7. Dip-coating on asymmetric initially reduced tubes .. 128

5.3. Summary 131

5.4. References 132

6. COPPER SPUTTERED ANODES FOR MEMBRANE REACTORS AT HIGH TEMPERATURE 135

6.1. Introduction 137

6.2. Results 138

6.2.1. Sputtering at room temperature 139

6.2.2. Sputtering at high temperature 141

6.3. Future works 147

6.4. Summary 147

6.5. References 148

7. CHARACTERIZATION OF OXYGEN TRANSPORT ON BSCF MEMBRANES ASSISTED BY FLUID DYNAMIC SIMULATIONS 151

7.1. Introduction 153

7.2. Methods 156

7.3.1. Experimental procedure 156

7.3.2. Modelling 158

7.3.3. Fitting procedure 165

7.3.4. Description of the simulation studies 167

7.3. Results 171

7.3.5. Fitting results 171

7.3.6. Results of the CFD simulations of the 3D permeation setup 173

7.4. Summary 191

7.5. References 195

8. ENERGETIC EVALUATION OF SOLID OXIDE ELECTROLYSER USING PROTONIC CONDUCTORS 205

8.1. Introduction 208

8.2. Methods 210

8.2.1. Methodology to evaluate the thermofluid dynamic of the electrolysis process by finite elements 210

8.2.2.Methodology to evaluate the efficiency of the electrolysis process 221

8.3.Results 227

8.3.1.Evaluation of the thermofluid dynamic of electrolysis based on protonic conducting materials at high temperature 227

8.3.2.Evaluation of the efficiency of electrolysis process based on protonic conducting materials at high temperature 244

8.4.Summary 254

8.5.References 257

9. THERMOFLUID DYNAMIC EVALUATION OF THE HYDROGEN EXTRACTION IN A PROTONIC MEMBRANE REFORMER 261

9.1.Introduction 264

9.2.Objectives 266

9.3.Methods 267

9.3.1. Description of the process 267

9.3.2. Experimental procedure 268

9.3.3. Geometry 268

9.3.4. Physics equations 270

9.3.5. Studies performed and conditions 281

9.3.6. Effect of the radiation in the heat transference 288

9.3.7. Meshing and solver 289

9.4.Results 290

9.4.1. Brief description of the experimental results 290

9.4.2. Validation of the finite element model........................... 294

9.4.3. Analysis of the PMR in adiabatic conditions 307

9.5. Summary 323

9.6. References.. 327

10. FLUID DYNAMIC EVALUATION OF THE HYDROGEN EXTRACTION IN METHANE DEHYDROAROMATIZATION REACTOR 333

10.1. Introduction 335

10.2. Methods.. 338

10.2.1. Experimental setup and reference conditions........... 338

10.2.2. Model implementation 339

10.2.3. Fitting of the kinetic model to experimental data..... 346

10.2.4. Studies performed 346

10.3. Results... 348

10.3.1. Fitting the kinetics to the experimental data 349

10.3.2. Spatial distribution of the reaction rates................... 350

10.3.3. Hydrogen extraction analysis 353

10.3.4. Influence of gas inlet velocity 356

10.3.5. Influence of reactor geometry 359

10.3.6. Influence of catalyst bed porosity 363

10.3.7. Influence of the ethylene formation kinetics............ 364

10.4. Summary 366

10.5. References 369

11. GENERAL REMARKS AND CONCLUSION 373

11. General conclusions 375

12. Acronyms 379

13. Figure list 381

14. Table list 399

15. Scientific contribution 401

1. SCOPE OF THE THESIS & OBJECTIVES

The development of the society has caused the continuous rise in energy and chemicals demand across the years. Today, the energetic demands are mainly covered with fossil fuels (oil, coal and natural gas) (Figure 1.1). While renewable energy sources are a clean alternative to produce energy chemicals demands (like plastics and other polymers or pharmaceutical chemicals) are produced mainly from oil. Indeed, more than 90% of the worldwide hydrogen production comes from fossil resources (coal, oil or natural gas) or the complete benzene production comes from upgrading of the oil in refineries.

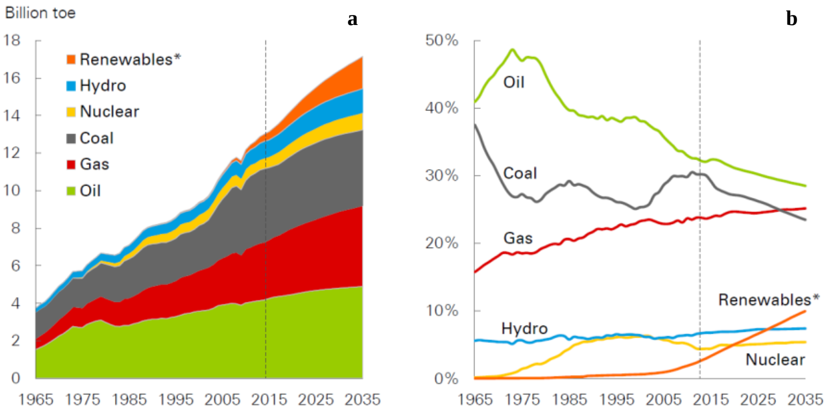

*Figure 1.1: Worldwide energy outlook and perspectives. (a) primary energy consumption by fuel (toe: tonne of oil equivalent); (b) shares for equivalent energy. * Renewables includes wind, solar, geothermal, biomass and biofuels [1].*

The current perspectives indicate that oil and natural gas sources will be depleted during this century and coal reserves until next century with the current consumptions. During the next two decades, oil and natural gas will reach a peak of production and, in the posterior decades, production will be decreasing gradually and, consequently, their prices will increase [2].

The occidental countries (USA, European Union, Japan, Australian, Canada) are gradually increasing their efforts in the research of clean and viable alternatives for energy and chemicals. In the next decades, the energy and chemical demands will continue increasing according the current perspectives. This is mainly due to the rise of emergent countries, especially China and India which have around the 30% of the world population. Therefore, as oilfields are depleting, the necessity to find viable and clean alternatives to fossil fuels – not only to obtain energy – increases.

Although the development of the renewable energy sources has achieved to take almost the 20% of the primary energy (hydro and renewable in the Figure 1.1), for the next decades the dependency to the non-renewable energy sources will be higher. Therefore, the development, improvement and optimization of the processes which uses this kind of primary energy is (and will be) necessary.

Hydrogen can be a clean energy source due to it does not cause direct CO_2 emissions but, as previously was mention, more than the 90% of the hydrogen production comes from fossil fuels while reforming processes. Therefore, this hydrogen presents carbon footprint (8.62 kg CO_2 equivalent per each kg of H_2 [3]). The clean alternative to obtain hydrogen is the electrolysis. However, currently this process is not competitive with the reforming process because its high electrical demands. Integrating renewable energy sources with electrolysis could be the key to improve the efficiency this energy sources because their intermittent nature. Among the electrochemical storage systems, the protonic ceramic materials show the best performance allowing the production of hydrogen dry and pressurized in one step. Although these materials are in the lab scale, they are proved to be mature to scale up. Naturally, further developments and researches are necessary to consolidate this electrochemical technology.

Membrane reactors are chemical-conversion units which use selective membranes in order to shift chemical equilibrium reactions to improve the yield of the process and rise energy efficiency. The range of operation temperatures of ionic ceramic materials (protonic and oxygen ionic) allows the integration of this kind of cells on a huge range of industrial reactive processes allowing their intensification: (i) shifting the equilibrium controlled reaction improving the yield; (ii) simplifying the process (reducing the size of the plant integrating several units in one); (iii) coupling exo- and endothermical process improving the thermal balance. Using the same strategy that in electrolysis, renewable energy coupled with this kind of membrane reactors, or/and electrochemical membrane reactors, could make the difference to lead this technology to be competitive, especially against the conventional technology. Integrating all these concepts, it leads until a clean, high efficiency, compact and modular and, therefore, is an attractive approach. Electrification of industrial processes based on renewable energy is a crucial pathway to reach carbon neutrality within the coming decades and electrochemical separators and reactors are suitable approaches to achieve this in a flexible and efficient manner.

This thesis presents two main work lines: (i) experimental work focuses on the development of nickel-free electrodes for protonic cells at high temperature and (ii) modelling work focused on the study of different processes using ionic ceramic conductors at high temperature. Therefore, the main objectives of this thesis can be divided in two:

O1. Development of highly selective electrodes for tubular electrochemical reactors based on proton conductors. These electrodes have to allow the hydrogen dissociation and does not promote coking under non-oxidative conditions.

O2. Study with finite elements methodology for the fitting, analysis and optimization of the membrane reactors based on ion conducting materials at high temperature.

To reach the objective **O1**, it was necessary to differentiate between the different techniques used to deposit the electrode on the tubular cell. Depending on the deposition technique, different materials were used as electrode:

- Deposition of electrodes based on copper cermets by dip-coating technique.
- Deposition of copper by sputtering technique.

In the modelling work (objective **O2**) different models were developed:

- Model of oxygen permeation across mixed ionic and electronic conducting membranes.
- Model of water electrolysis using proton conducting cells at high temperature.
- Model of the integration of a proton conducting cell in a steam methane reformer to extract the hydrogen at high pressure.

- Model of the intensification of a methane dehydroaromatization using catalytic membrane reactor based on a co-ionic electrolyte.

References

1. BP, *BP Energy outlook*. 2017.
2. Sorrell, S., et al., Energy Policy, 2010. **38**(9): p. 4990-5003.
3. Spath, P.L. and M.K. Mann., *Life Cycle Assessment of Hydrogen Production via Natural Gas Steam Reforming*. 2001, National Renewable Energy Laboratory: Golden, CO.

2. RESUMEN/SUMMARY/RESUM

2.1.Resumen

En la presente tesis se han desarrollados estudios sobre reactores de membrana de alta temperatura. Entre estos se puede diferenciar entre un trabajo experimental y un trabajo de simulación.

En el bloque experimental se han desarrollado electrodos basados en cobre para reactores de membrana electroquímicos tubulares de alta temperatura basados en electrolitos protónicos. Para depositar estos electrodos sobre los tubos se han desarrollado diferentes técnicas. Se ha optimizado el método dip-coating para depositar un cermet basado en cobre utilizando la misma cerámica que el electrolito de los soportes tubulares. Las condiciones con las que se llevó a cabo el proceso de dip-coating provocan disminuciones de varios ordenes de magnitud en la resistencia de polarización del electrodo final. Se trata de un método que es muy sensible a posibles defectos en electrolito, como pequeñas grietas o poros, ya que el cobre del electrodo depositado se introduce por estos defectos reaccionando con el níquel del electrodo interno. Asimismo, se ha empleado el método de sputtering para depositar cobre metálico sobre soportes tubulares electroquímicos. Aumentar la temperatura de deposición genera mejores fijaciones electrodo-electrolito. Las celdas con el cobre depositado a alta temperatura mostraron resistencias de polarización inferiores a 0.1 $\Omega\cdot\mathrm{cm}^2$.

En el bloque de simulaciones mediante métodos de elementos finitos se han desarrollado diferentes modelos para la caracterización de los fenómenos que tienen lugar en reactores de membrana de alta temperatura. Se ha estudiado: (i) la permeación de oxígeno a través de una membrana de conducción iónica-electrónica mixta; (ii) la electrólisis del agua utilizando celdas basadas en conductores protónicos de alta temperatura; (iii) la integración de una celda protónica para la extracción de hidrógeno en un reformador de metano; (iv) la integración de una celda de conductividad co-iónica en la deshidroaromatización de metano en un reactor de lecho catalítico.

El modelo de permeación de oxígeno a través de una membrana de conductividad mixta se ajustó a datos experimentales. El modelo ajustado ha permitido caracterizar la importancia del efecto dilutivo y de arrastre sobre el transporte de oxígeno a través de la membrana. Se ha observado que, aunque el efecto de arrastre tenga menor importancia que el dilutivo, su efecto es importante ya que previene la formación de concentraciones de polarización.

El estudio de electrolizadores que utilizan conductores protónicos sólidos de alta temperatura ha permitido estudiar el efecto del escalado en este proceso y evaluar la eficiencia en el almacenamiento de energía.

El modelo de un reactor de membrana electroquímico basado en conductores protónicos integrado en un reformador de metano ha permitido comprobar que la demanda térmica del proceso se cubre por el efecto Joule y la electrocompresión del hidrógeno. Se ha comprobado como el coarsening observado en las partículas de níquel no limita la extracción de hidrógeno para la celda estudiada.

Un último modelo fue construido para estudiar un reactor de membrana para el proceso de deshidrogenación de metano utilizando una celda co-iónica. El modelo fue validado utilizando datos experimentales. Se utilizó el modelo validado para realizar estudios para analizar posibles limitaciones del proceso. Finalmente, se ha comprobado que el desplazamiento del equilibrio de reacción mediante la extracción de hidrógeno se frena debido a limitaciones cinéticas.

2.2.Summary

In this thesis several studies were developed about membranes reactor at high temperature. Two differentiated blocks could be identified: (i) experimental works; (ii) modelling works.

In the experimental block, electrodes based on copper was developed for tubular protonic based cells. The deposition of the copper layer on the tubes was developed by different techniques. Dip-coating method was optimized to a copper-based cermet on the tube. Conditions of the dip-coating procedure has a critical impact in the final performance of the electrochemical cell whose supposes several orders of magnitude in the polarization resistance. It is a sensitive process with the defect of the tube as shows the copper spread over these defects. Additionally, sputtering technique was used to deposit copper layer on the tube. High temperature is required to achieve suitable attachments copper-tube. This high temperature deposited layer present polarization resistances lower than 0.1 $\Omega \cdot cm^2$.

In the modelling block, finite element methodology was used to build different models to study different phenomena concerning membrane reactors at high temperature. It was studied: (i) the oxygen permeation across a mixed ionic and electronic conducting membrane; (ii) water electrolysis based on high temperature protonic cells; (iii) hydrogen extraction from a steam methane reforming using a protonic cell; (iv) the intensification of the methane dehydromatization reactor using co-ionic membrane.

Oxygen permeation model was built to evaluate the effect of the dilutive and the sweep contribution over the permeation process. The fitted

model allowed the importance of the dilutive and sweep effect over the oxygen permeation. Although the sweep effect present lower influence in the oxygen transport across the membrane, its effect prevents concentration polarization limitations.

Modelling the protonic cell based electrolysis allowed to study the effect of the scale up in this process and to evaluate the efficiency in the energy storing in form of hydrogen.

Modelling protonic membrane reformer allowed checking the thermal microintegration of all the heats which take place in the setup. The electrocompression of hydrogen is an isothermal phenomenon which releases the demanded energy as heat. The model allowed to check the coarsening of the Ni particles does not limit the hydrogen extraction for the studied cell.

A final model was built to study a catalytic membrane reactor for the methane dehydroaromatization using co-ionic conducting cells. The model was validated using experimental data. Additionally, different studies were performed to analyze possible limitation in the process. Results show that there are no hydrogen diffusion limitations in this process. Additionally, the shift of the equilibrium by extracting hydrogen has to be stopped because kinetic limitations.

2.3. Resum

Esta tesi presenta resultats sobre reactors de membrana a alta temperatura. Dos blocs diferenciades poden ser identificats: (i) treball experimental; (ii) treball de modelat.

En el bloc experimental, elèctrodes basats en coure han siguts optimitzats per a tubular cells de conductor protòniques. La deposició de la capa basada en coure es va fer amb diferents tècniques. La tècnica de dip-coating ha sigut usada per a depositar una capa de cermet basada en coure. Aquesta tècnica es molt sensible a les condicions amb les que es desenvolupa la deposició perquè causa canvis de varis ordres de magnitud en la resistència de polarització del elèctrode. A més, la tècnica de sputtering ha sigut triada per a depositar coure. Per a depositar correctament la capa de coure, altes temperatures durant la deposició foren requerides. El elèctrode optimitzat presenta resistències de polarització inferiors a 0.1 $\Omega\cdot cm^2$.

En el treball de modelat, la metodologia de elements finits va ser utilitzada per a modelar diferents fenòmens concernits a reactors de membrana de elevada temperatura.

La permeació de oxigen per membranes de conducció mixta ha sigut modelada per a avaluar la importància de la dilució i del arrossegament. Els resultats mostren que, encara que el efecte dilutiu es predominant, el efecte del arrossegament no pot ser depreciat. Un adequat arrossegament del oxigen permeat es necessari per evitar polaritzacions en la concentració del oxigen els quals limitarien la permeació. El efecte del arrossegament es major quan el gas portador es mes pesat.

El model per estudiar un procés de electròlisis basat en conductors protòniques a elevada temperatura ha permès estudiar l'efecte de l'escalat de aquest procés i avaluar l'eficiència en l'emmagatzemament d'energia.

Modelant un reformador de membrana protònica ha permès comprovar la microintegració tèrmica de tots el fenòmens que tenen lloc en aquest procés. Aquest procés compren les reaccions de reformat, extracció electroquímica de hidrogen i electrocompressió del hidrogen generat. La electrocompressió del hidrogen és un procés isoterma que allibera la energia demanda en forma de calor. El model ha permès comprovar que l'engrossiment de les partícules de níquel no limita l'extracció de hidrogen.

Un últim model va ser construït per estudiar l'extracció de hidrogen en un reactor de membrana per al procés de dehidroaromatizatió de metà. El reactor de membrana utilitza materials co-iòniques per l'extracció de hidrogen de la càmera de reacció. Aquest model va ser validat amb resultats experimentals. El model va mostrar que no hi ha limitacions amb la difusió del hidrogen. A més, el desplaçament del equilibri mediant l'extracció de hidrogen està limitat per la baixa activitat cinètica del procés.

3. INTRODUCTION

3.1.Introduction to the membrane reactors

The development of membrane reactors has produced important advances for a large number of reactions that have allowed the improvement of current processes and the opening of the development of new processes which could lead to important advantages regarding the respective conventional processes. That is reflected in the increase of the publications in this topic during the last years (Figure 3.1).

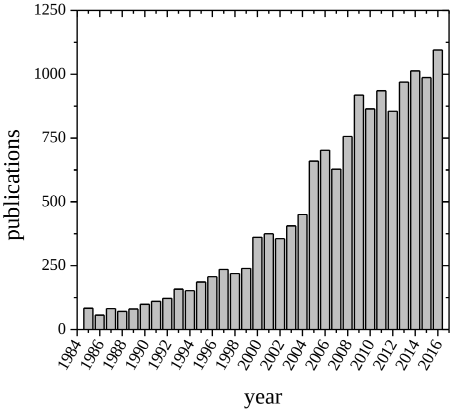

Figure 3.1. Publications about membrane reactors [1].

A membrane reactor is a unit where a chemical reaction (or reactions) takes place and, simultaneously, one (or more) of the active species (as reactive or products) is selectively separated (or injected) from the reaction chamber using a selective membrane. Membrane reactor processes typically improve chemical reaction systems where the chemical equilibrium limits significantly the productivity of the system. Considering the Le Chatelier's principle, a selective membrane may improve an equilibrium-limited process removing product compound (Figure 3.2.a) or injecting reactive compounds (Figure 3.2.b).

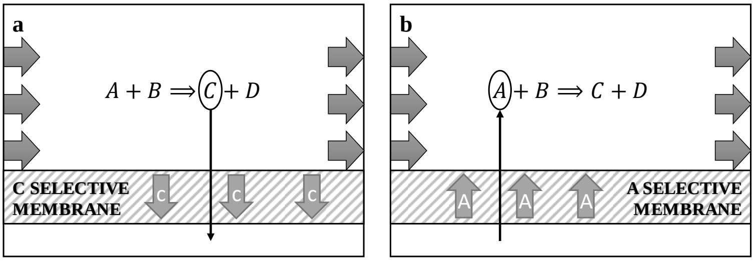

Figure 3.2: membrane reactor principle. (a) Shifting the chemical equilibrium removing products of the reaction chamber; (b) Shifting the chemical equilibrium injecting reactive of the reaction chamber.

Membrane reactor processes are conventionally classified considering the membrane material. Table 3.1 shows a brief analysis of this kind of classification. Here, inorganic membranes are more expensive than the organic membranes, especially compared with the polymeric ones (10 – 50 times cheaper). However, inorganic materials offer important advantages considering mechanical and chemical stability and resistance even at high temperatures or well-defined porous structure between others.

The study of polymeric membranes is mostly focused on the biotechnology field where the temperature range does not put in risk the integrity of the material [2-6]. Regarding the catalytic membrane reactors (no biotechnological field), polymers are far from commercial applications mainly due to slow kinetics caused for low temperatures. Higher efforts will be necessary to make competitive this type of processes, where special polymers are being synthesized and developed overcoming the typical limitations of the polymeric membranes, specially temperature limitations [7-10].

Table 3.1: Classification of membrane reactor considering the membrane material [11]

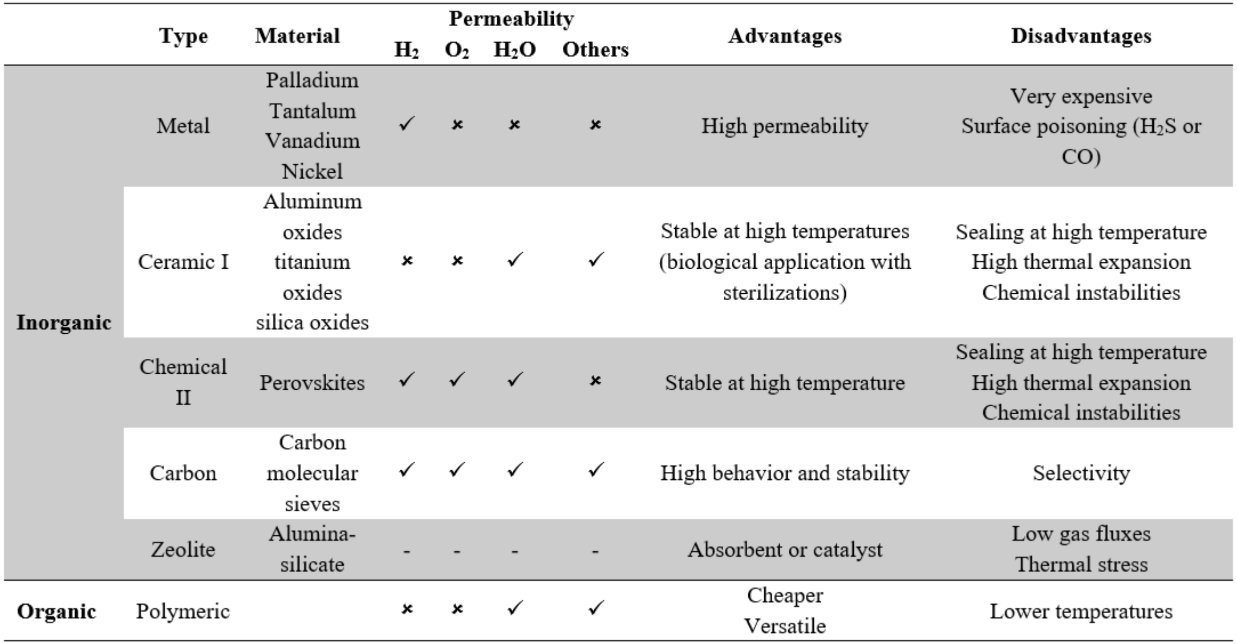

	Type	Material	Permeability				Advantages	Disadvantages
			H_2	O_2	H_2O	Others		
Inorganic	Metal	Palladium Tantalum Vanadium Nickel	✓	×	×	×	High permeability	Very expensive Surface poisoning (H_2S or CO)
	Ceramic I	Aluminum oxides titanium oxides silica oxides	×	×	✓	✓	Stable at high temperatures (biological application with sterilizations)	Sealing at high temperature High thermal expansion Chemical instabilities
	Chemical II	Perovskites	✓	✓	✓	×	Stable at high temperature	Sealing at high temperature High thermal expansion Chemical instabilities
	Carbon	Carbon molecular sieves	✓	✓	✓	✓	High behavior and stability	Selectivity
	Zeolite	Alumina-silicate	-	-	-	-	Absorbent or catalyst	Low gas fluxes Thermal stress
Organic	Polymeric		×	×	✓	✓	Cheaper Versatile	Lower temperatures

Considering metal membranes, most of these materials are based on palladium. Pd-based membranes present very high hydrogen permeance and selectivities but is a very expensive material and is poisoned by typical gas compounds found in hydrocarbon processing. Therefore, there are several studies to find how to overcome these limitations. Among the proposed solutions it can distinguish two groups [12-16]: (i) to alloy the Pd with other metal which can improve its resistance against poisoning by CO or H_2S and to enhance its hydrogen permeability (like Ag or Cu); (ii) to support the dense Pd-based membrane to reduce the price of the assembly (like stainless steel, alumina and Vycor glass).

Carbon molecular sieves are porous solids with high separation properties and stability, based on containing constricted pores that approach the molecular dimensions of diffusing gas molecules [17-20]. Molecules with only slight dimension differences can be effectively separated through this molecular sieving. However, the carbon membranes must reach very high performances to compensate for their high cost and improve the problems due to its brittleness [21]. In addition, the presence of steam could have adverse effects in the membrane performance.

Zeolites are microporous alumina-silicates used as catalysts or adsorbents in form of micron or submicron-sized crystallites embedded on millimeter-sized granules. However, membranes based on zeolites present low gas fluxes compared with other inorganic membranes, limiting the reaction process and several problems during the fabrication [22]. Furthermore, the thermal effect of zeolites could mean important thermal stress problems [14, 23-25].

Molecular sieving silica membranes are amorphous microporous ceramic membranes which separates gas species based on their adsorption behaviour and kinetic diameters [26]. These materials present excellent thermal, mechanical and chemical stability those depends on the synthesis conditions and the overall membrane morphology [27]. The major drawback is their chemical and structural instability against steam atmospheres [28-30]. Hydrophobic membranes can be obtained in hybrid organic-inorganic membranes to overcome this limitation; however, their selectivity decreases significantly [31, 32]. Metal and metal oxides additions have allowed important improvements on the silica membrane performances [33-37].

Other ceramic membranes are made with complex oxides, typically perovskites and fluorites structures [24, 38-40]. These materials present defects in their crystal lattice usually in form of ion vacancies created by doping agents introduced into these structures. These defects are the rails for charge carriers when a potential difference is applied conferring ionic conductivity to the material. Advance analysis of the ionic conductivity mechanism is described far ahead. Depending on the material and conditions, hydrogen or oxygen can be obtained with very high selectivities (up to 100%). However, there is a large pathway in order to decrease manufacturing costs and develop suitable sealings which can operate at the temperatures which these materials require. Figure 3.3 shows different membrane reactor process using oxygen and hydrogen permeable membranes.

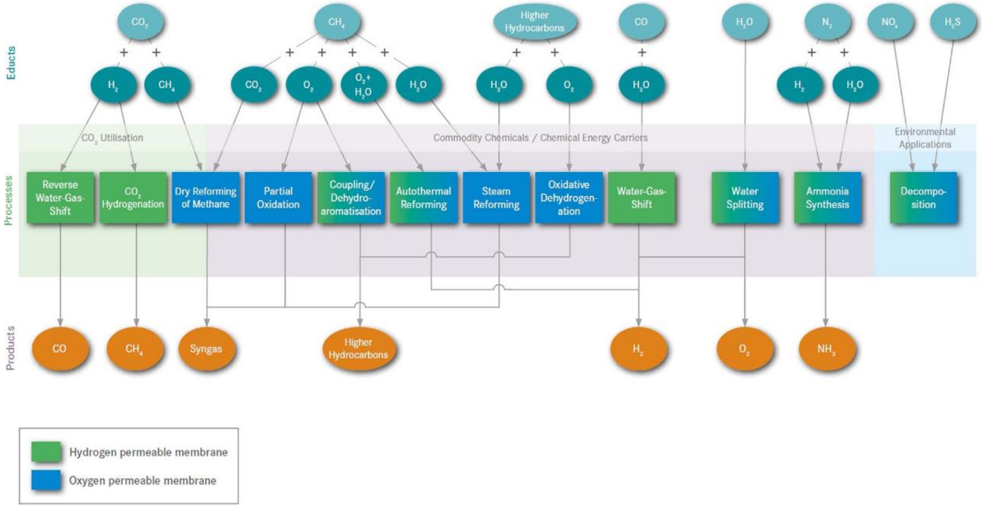
Educts
Processes
Products
CO_2
CH_4
Higher Hydrocarbons
CO
H_2O
N_2
NO_x
H_2S
H_2
CH_4
CO_2
O_2
O_2+ H_2O
H_2O
H_2O
O_2
H_2O
H_2
H_2O
CO_2 Utilisation
Commodity Chemicals / Chemical Energy Carriers
Environmental Applications
Reverse Water-Gas-Shift
CO_2 Hydrogenation
Dry Reforming of Methane
Partial Oxidation
Coupling/ Dehydro-aromatisation
Autothermal Reforming
Steam Reforming
Oxidative Dehydrogen-ation
Water-Gas-Shift
Water Splitting
Ammonia Synthesis
Decompo-sition
CO
CH_4
Syngas
Higher Hydrocarbons
H_2
O_2
NH_3
🟩 Hydrogen permeable membrane
🟦 Oxygen permeable membrane

Figure 3.3. Summary of processes where oxygen- and hydrogen-permeable membranes for membrane reactors at high temperatures. Figure from [41].

3.2.Membrane assemblies based on ionic ceramic conductors

Ceramic conducting materials (alkaline-based material no considered) can divided into pure ionic conducting and mixed ionic conducting materials. Typically, the mixed ionic conducting materials have electronic and ionic conductivity, but there are materials that present oxygen ion and proton conducting behavior simultaneously. Considering this distinction, different applications are possible: pure ionic conducting materials only can be used in electrochemical applications (fuel cell mode, electrolysis mode or ionic pump mode) while the mixed electronic ionic conducting materials can work only driven by partial pressure difference.

Electrochemical cells allow the conversion of electrical energy and chemicals. The electrochemical assemblies can work in three different ways:

i. **electrolysis mode: (electricity → chemicals)** where the electric energy is applied to produce chemicals (most common for hydrogen production)
ii. **fuel cell mode**: **(chemicals → electricity)** where electrical energy is obtained from chemicals
iii. **ionic pump mode: (chemicals + electricity → chemicals)** although it works as fuel cell mode, the charge transport resistance causes additional energy is required to complete the process.

Figure 3.4 shows an illustration of the typical electrochemical discharge curve and showing all electrochemical modes depending on the electrical current.

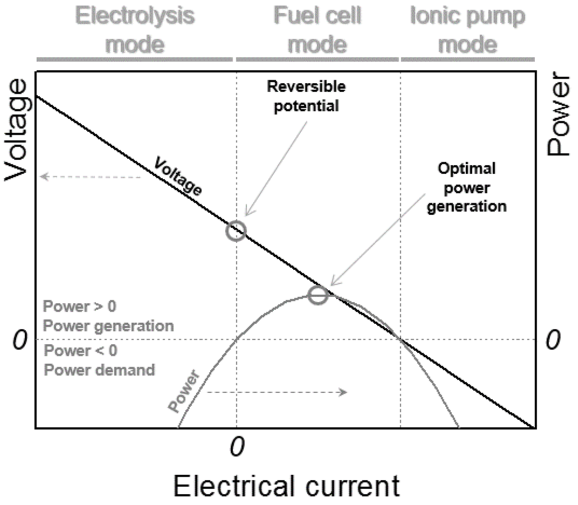
Electrolysis mode
Fuel cell mode
Ionic pump mode
Voltage
Power
Reversible potential
Voltage
Optimal power generation
Power > 0
Power generation
Power < 0
Power demand
Power
0
0
0
Electrical current

Figure 3.4. Electrochemical cells: generical discharge electrochemical curve.

Electrochemical cells are built of anode electrode, electrolyte and cathode electrode (Figure 3.5). The anode electrode is defined as the electrode where the oxidation reaction occurs. The cathode is the reaction where the reduction takes place. Considering anionic electrolyte, the active specie is reduced in the cathode and the ions flow through the solid electrolyte and react in the anode. This reaction generates electrons that are transported in the external circuit to the cathode for the reduction. Considering cationic electrolyte, the active specie is oxidized in the anode and the ions flow through the solid electrolyte and react in the cathode. Therefore, the reactions of oxidation and reduction take place in the interface electrode and electrolyte, where electrons, gases and ions are in contact. This point is also called Triple Phase Boundary (TPB).

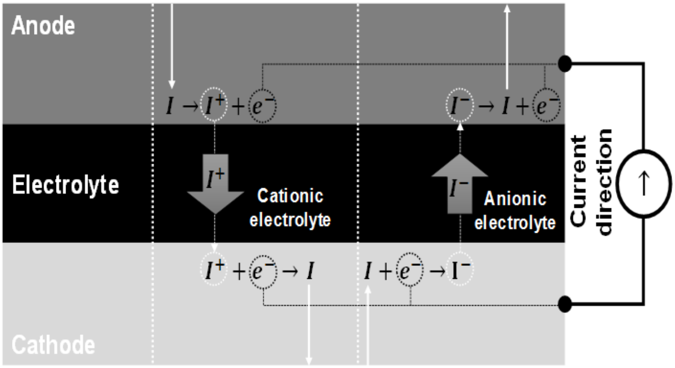
Anode
$I \rightarrow I^+ + e^-$
$I^- \rightarrow I + e^-$
Electrolyte
I^+
Cationic electrolyte
I^-
Anionic electrolyte
Current direction
↑
$I^+ + e^- \rightarrow I$
$I + e^- \rightarrow I^-$
Cathode

Figure 3.5. Electrochemical cells: view of general assembly considering cationic conducting based cell or anionic conducting based cell.

The electrochemical cells are typically classified according to the electrolyte material (Table 3.2). At lower temperatures, the available technologies are Polymer Electrolyte Membrane Fuel Cell (PEMFC), Alkaline Fuel Cell (AFC), Direct Methanol Fuel Cell (DMFC) and

Phosphoric Acid Fuel Cell (PAFC) and at high temperatures the technologies Molten Carbonate Fuel Cell (MCFC) and Solid Oxide Fuel Cell (SOFC). In this last group it can be differentiated SOFC based on the oxygen conducting electrolytes and SOFC based on protonic conducting electrolytes.

In the present thesis, fuel cells with high temperature conducting solid-state ceramics have been selected as membrane electrochemical reactors. These types of cells present some advantages, being the most important the component management, since there are solid electrolytes. The reaction processes considered have to work inside the temperatures range where these cells work (400 – 1000ºC).

The charge conductivity in solid materials is typically based on the properties of the crystal lattice. The charge can be transported by means of electrons, ions or valence-band electrons (also called holes) giving materials with a unique type of charge conductivity (e.g. metals with electronic conductivity), or materials which present various charge conductivity simultaneously (e.g. perovskites can hold electronic, oxygen ion conductivity and proton conductivity).

The materials for this thesis present electronic and ionic conductivities. The total conductivity (σ) of the material comes from the combination of ionic and electronic contribution. The ionic contributions come from anions (σ_{a^-}) or cations (σ_{c^+}) movement. The electronic conductivity come from electron movement (σ_n) or electron holes (σ_p).

$$\sigma = \sigma_{a^-} + \sigma_{c^+} + \sigma_n + \sigma_p \qquad (3.1)$$

Table 3.2. Summary of the fuel cell technologies [42-44]. [a]: oxygen ion conducting ceramics; [b]: proton ion conducting ceramics.

	PEMFC	AFC	PAFC	DMFC	MCFC	OC-SOFC[a]	PC-SOFC[b]
Primary fuel	H_2	H_2	H_2	CH_3OH	H_2, CO, CH_4, …	H_2, CO, CH_4, …	H_2, CO, CH_4, …
Temperature range	20 – 100 ºC	65 – 90 – 220 ºC	200 ºC	80 ºC	650 ºC	600 – 1000 ºC	600 – 1000 ºC
Charge carrier	H_3O^+/H^+	OH^-	H^+	H_3O^+/H^+	CO_3^{2-}	O^{2-}	H^+
Ext. Reforming	Yes	Yes	Yes	No	No	No	No
Anode	Pt/C	Ni raney	Pt/C	Pt/Ru/C	Ni	Ni-ZrO_2	Ni-based
Electrolyte	Polymers	KOH	H_3PO_4	Polymers	Li_2CO_3, K_2CO_3	Ceramics[a]	Ceramics[b]
Cathode	Pt/C	Ag	Pt/C	Pt/$Mo_2Ru_5S_5$	NiO	$LaMnO_3$/Sr	
Power density	4.1 – 7.1 kW/m^3	4.3 – 8.2 kW/m^3	0.8 – 1.9 kW/m^3	0.6 kW/m^3	1.5 – 2.6 kW/m^3	0.1-1.5 kW/m^3	-
Efficiency	35 – 45 %	35 – 55 %	40 %	30 – 40 %	> 50 %	> 50 %	> 50 %
Applications	Portable, back-up, stationary transport	Military, aerospace, stationary	Combined heat and power production	Portable	Combined heat and power production, stationary	Combined heat and power production, stationary, portable	Combined heat and power production, stationary, portable
Status	Commercial	Commercial	Commercial	Commercial	Research	Research	Research
Advantages	Low temperatures, high pressures, quick startup, solid electrolyte	Low component cost, scalability, quick startup, lifetime	Low temperatures, high tolerance of pollutants	High energy density of CH3OH, low temperatures	High efficiency, fuel flexibility, variety of catalyst	Fuel flexibility, high electrical efficiency, high tolerance, fuel impurities, solid components, waste heat recovery	Fuel flexibility, high electrical efficiency, high tolerance, fuel impurities, solid components
Drawbacks	Expensive catalyst, poisoning CO, H_2S, H_2 ultrapure is required	Sensitivity to fuel impurities: CO, H_2S, H_2, CH_4; difficult in the KOH management	Expensive catalysts, slow startup and corrosive electrolyte	Lower power density	Slow startup, corrosion of cell components and intolerant sulfur	High cost, sensitivity to S, slow startup, stability	High cost, limited power, sensitivity to S

- **Ionic conductivity**

The ionic conductivity is based on defects in their crystal lattice. These defects can be given in form of [45]:

- Vacant lattice sites or vacancies
- Ions placed at normally unoccupied sites, called interstitials
- Foreign ions present as impurity or dopant
- Ions with charges different from those expected from the overall stoichiometry.

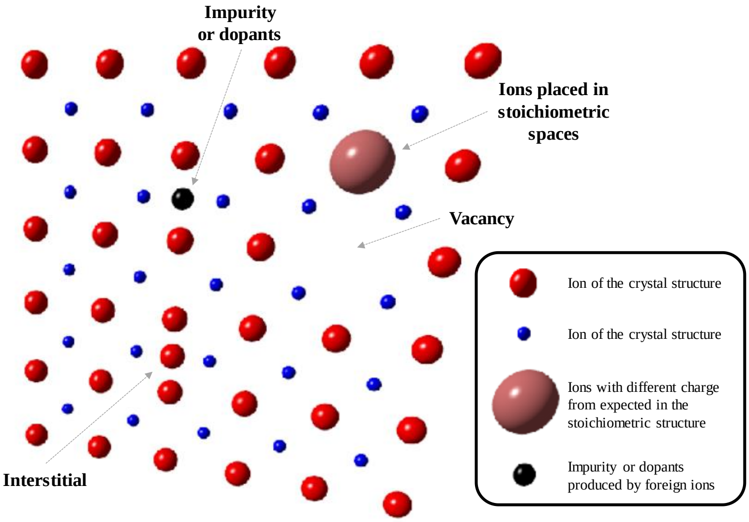
Impurity or dopants
Ions placed in stoichiometric spaces
Vacancy
Interstitial
Ion of the crystal structure
Ion of the crystal structure
Ions with different charge from expected in the stoichiometric structure
Impurity or dopants produced by foreign ions

Figure 3.6. Ilustration of the different defects in a plane of the crystal structure.

In absence of external electric fields or chemical gradients, the electroneutrality must be kept. Therefore, this kind of defects cannot present individually, thus combinations of these defects are needed to compensate the charges in the crystal structure, which in many cases are not necessarily close together. Some of these combinations are:

i. **Schottky disorder**, where vacancies of different charged appears in the crystal structure,
ii. **Frenkel disorder**, where a particle (usually cation) leaves its place in the lattice, creating a vacancy, and becomes an interstitial by lodging in a nearby location,
iii. **Anti-site disorder**, where the particles exchange these positions in some places of the crystal structure;

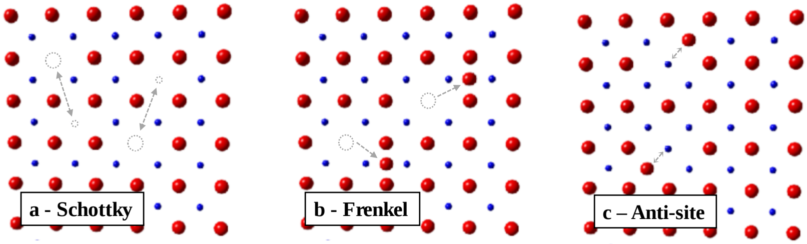

Figure 3.7. Examples of combination of defects to keep the electroneutrality. (a) Schottky disorder; (b) Frenkel disorder; (c) Anti-site disorder.

- **Electronic conductivity**

According the quantum theory, one atom displays discontinuous energy levels. The energy band appears from the aggregation of large number of atoms formed by the electrons belonging to similar energy levels (Figure 3.8). The relevant bands and band gaps for electronics (and for optoelectronics) are those with energies near the Fermi level. The Fermi level (E_F) is the chemical potential for electrons and represents the thermodynamic work to add an electron to the body. The bands and band gaps near the Fermi level are given special names, depending on the material. The highest occupied band for the electrons of the material (in energy terms) is named valence band. The conduction band, normally empty, is defined as the lowest unfilled energy band. In the conduction band, electrons can move freely and are generally called conduction electrons.

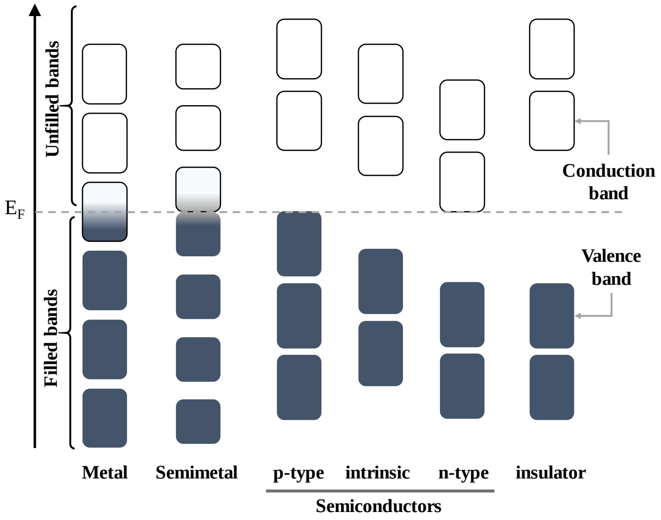
Unfilled bands
Filled bands
E_F
Conduction band
Valence band
Metal
Semimetal
p-type
intrinsic
n-type
insulator
Semiconductors

Figure 3.8. Electric conductivity for different materials according their energy bands

Conventional charge conductors are based on electronic conductivity (extra electron holes in the valence band (p-type conductivity) and extra electrons in the conduction band (n-type conductivity)). Electronic conducting oxides are characterized by n-type conductivity, transport of electrons, or p-type conductivity, when the electron holes transport prevails. However, other materials are predominantly ionic conductors or mixed electronic and ionic conductors. Furthermore, some materials can transport protons in hydrogen or water vapor atmospheres.

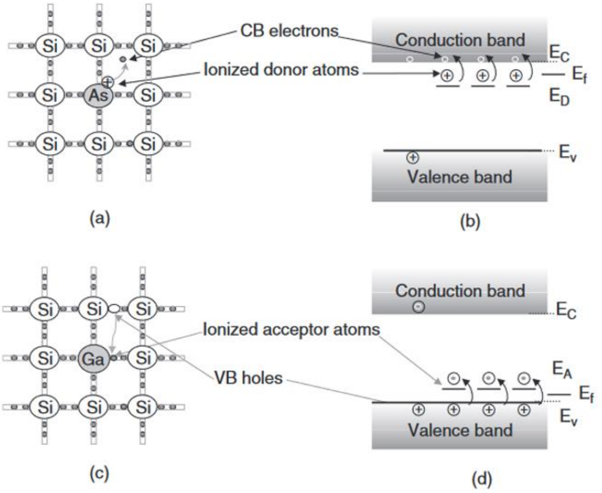
Si
As
CB electrons
Ionized donor atoms
Conduction band
E_C
E_f
E_D
E_v
Valence band
(a)
(b)
Ga
Ionized acceptor atoms
VB holes
Conduction band
E_C
E_A
E_f
E_v
Valence band
(c)
(d)

Figure 3.9. Semiconductors type n (a-b) and type p (c-d). (a) Two-dimensional representation and (b) corresponding energy bands for n-doped Si with As. (c) Two-dimensional representation and (d) corresponding energy bands for p-doped Si with Ga. CB: conduction band; E_C: lower energy level of the conduction band; E_D: energy level of the donor atoms; E_V: upper energy level of the valence band; E_A: energy level of the acceptor atoms. Image extracted from [46].

3.2.1. Pure oxygen ion conductors

These materials conduce oxygen ions (O^{2-}) when an electric field is applied. The transport of the ions across the material depends on the crystal lattice. Based on the crystal lattice, the most common oxygen ion conducting materials are fluorite-based materials and perovskite-based materials.

Fluorite-based ion conducting materials (Figure 3.10) present cubic crystal lattices, AB_2, where the tetravalent cations (A) occupy face-centered positions in a cubic unit cell with anions (B) in the eight tetrahedral sites between them [40]. The most common fluorite oxygen ion conducting material is doped ZrO_2. Pure ZrO_2 is not a good conductor and only present fluorite structure at temperatures higher than 2300ºC. Doping this material allows stabilizing it and to increase oxygen vacancies concentration. Typical subvalent dopants are Ca^{2+} and Y^{3+}, producing calcia-stabilized zirconia (CSZ) and yttria-stabilized zirconia (YSZ), respectively, the latter exhibiting good oxide-ion conductivity above about 700ºC. Another well-known fluorite structure is the CeO_2 that does not need phase stabilization to increase the vacancy concentration. This material is doped with Gd_2O_3 or Sm_2O_3 producing gadolinia-doped ceria (CGO) and samaria-doped cera (CSO), respectively; which present better ionic conductivities than YSZ. However, this material is not stable in reducing conditions where the Ce^{+4} is reduced to Ce^{+3} form providing electronic conductivity to the material (n-type). It is important to know this mixed conductivity because for pure ionic applications the appearance of the electronic conductivity drops the efficiency of the system [47].

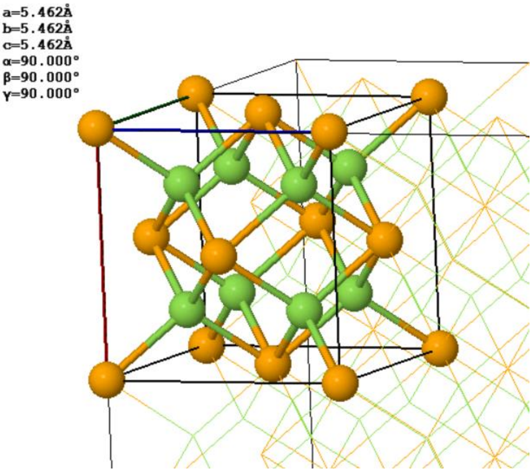

Figure 3.10. Fluorite crystal structure, AB_2, where the orange balls are tetravalent cations while green balls are the anions (in this case, O^{2-}). Image extracted from [48].

Perovskite-based materials also have been reported as ionic conducting materials. Perovskites present cubic lattice based on ABO_3 (Figure 3.10). The large A cation is coordinated to twelve anions, with the B cation occupying a six-coordinate site, forming a network of corner-sharing BO_6 octahedra. Tilting of these octahedra leads to deviations from the ideal cubic symmetry. (Sr,Mg)-doped LaGaO3 perovskites present higher conductivities than YSZ, but these materials present poor long term stabilities [49].

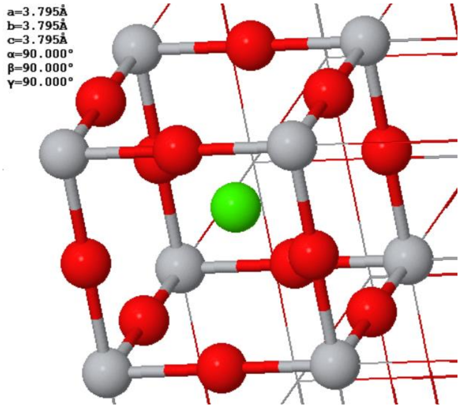

Figure 3.11. Perovskite crystal structure, ABO_3. Green ball is the A large cation centered in the crystal cell; grey balls represent the B cations and the red balls are the O^{2-}. Image extracted from [48].

Finally, Figure 3.11 shows a comparison of the ionic conductivity of the typical oxygen ion conductor materials. In addition, there are three additional materials which are not based on fluorite or perovskites. That are LAMOX, based on $La_2Mo_2O_9$, and Si-apatite and Ge-apatite, based on $M_{10}(XO_4)_6O_{2\pm y}$, where M is rare-earth or alkaline-earth cation and X is a p-block element such P, Si or Ge. The last materials are in research step and are still far for practical applications.

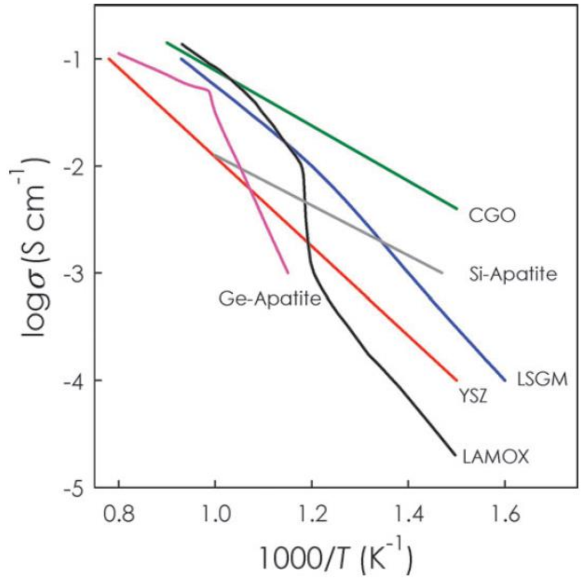

Figure 3.12. Oxygen ion conductivity as function of the reciprocal temperature. LAMOX: $La_2Mo_2O_9$. [40].

3.2.2. Pure proton conductors

There are several types of materials that present proton conductivity. Considering this thesis is focused on membrane reactors of high temperatures (> 500 °C), the materials considered is based on proton conducting ceramics. Comparing the proton conducting materials with oxygen ion conducting materials for solid oxide fuel cell applications, the proton conducting materials present higher efficiency and fuel utilization and it is possible working at lower temperatures because energy activation of proton transport is lower [50-55].

Results more relevant for proton conducting materials using solid oxides use perovskites (Figure 3.10). Acceptor-doped perovskites based on $BaCeO_3$, $BaZrO_3$, $SrCeO_3$, $SrZrO_3$, $CaZrO_3$ among others. In high temperature proton conductors based on complex oxides, the transport of protons roughly corresponds to the so-called Grotthuss mechanism [55, 56]. Bare H^+ ions do not exist in solids under equilibrium condition; they strongly interact with the electron density of electronegative oxygen ions. However, the formed O-H bond is weaker than that in the hydroxyl ion OH^- [57]. The proton migration is a result of the thermally activated hopping process requiring the breaking of the O-H bond [58, 59]. The hopping mechanism of protons (Figure 3.12) consists of the following two steps: (i) fast rotation of the proton which is localized on the oxygen ion and (ii) proton transfer by hopping toward a neighboring oxygen ion.

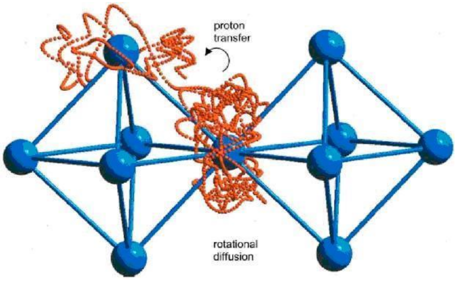

Figure 3.13. Grotthus type proton mechanism. Traces of the oxygen atoms of two octahedra where the protonic motion generates the ring -like object around the oxygen atom in the center and it diffuses to another oxygen position. Image obtained from [60] and mechanism discussed in [61].

The presence of oxygen vacancies in the oxide material is the main condition for the accomplishment of the proton transport (reaction 3.1). The oxygen vacancies in proton conducting materials can be created by acceptor doping or can be a structural element of oxides. Upon hydration, the oxygen vacancies are filled by oxygen from water according the dissociative mechanism of water dissolution. The interaction of the most proton conducting materials with water vapor produces new structure elements. Here, it can be observed how the surface processes is described using the Kröger-Vink notation

$$H_2O + V_O^{\cdot\cdot} + O_O^x \rightleftarrows 2\ OH_O^{\cdot} \qquad \text{(r 3.1)}$$

where O_O^x is the oxygen ion in the oxygen ion lattice site, $OH_O^{\cdot}$ is the proton localized on the oxygen ion (proton defect), and $V_O^{\cdot\cdot}$ is the oxygen vacancy created in the crystal lattice during acceptor substitution.

Table 3.3 shows a summary of the types of high temperature protonic conducting materials. Acceptor-doped Barium Zirconates ($BaZrO_3$) or Cerates ($BaCeO_3$) are typical examples of a ceramic class that allows for protonic conduction, rather than the more familiar oxygen ion conduction seen in ceramics such as YSZ, SDC, and LSGM. It has been recognized that these ceramics are also steam permeable under certain conditions, an additional benefit that may be exploited in new fuel cell systems or stand-alone applications [55]. These materials exhibit p-type conductivity in absence of hydrogen or water vapor. However, in steam or hydrogen conditions (at high temperatures), the p-type conductivity decreases, and the protonic conductivity prevails. Doping the pure material improves the protonic conductivity because it causes an increase of oxygen vacancies in the lattice [62]. Furthermore, it has been reported that the steam incorporation into the lattice is an exothermic process [60, 63, 64] thus, the proton uptake in perovskite oxides increases with decreasing temperature. Finally, the Figure 3.13 shows the protonic conductivity of different materials.

Table 3.3: Comparison of target properties of the proton-conducting electrolytes. [55]

System	Advantages	Disadvantages
$BaCeO_3$	• High oxygen and protonic conductivity • Enough densification	○Low chemical stability ○Phase transitions ○Non-monotonic thermal expansion
$BaZrO_3$	• High chemical stability • High bulk conductivity	○Poor sinterability ○High sintering temperatures ○Low grain-boundary conductivity ○Low TEC value ○High contribution of p-type conductivity
$BaCeO_3$ – $BaZrO_3$	• Acceptable stability • Thermal and transport properties	○Low information of chemical compatibility with other components
$A(Ce,Zr)O_3$, A=Ca, Sr	• Acceptable protonic conductivity	○High contribution of p-type electronic conductivity ○no information concerning chemical compatibility with other materials

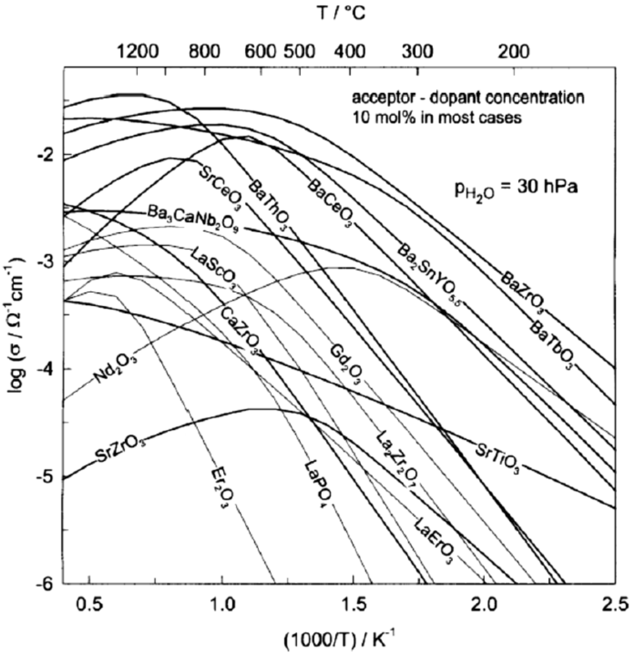

Figure 3.14. Summary of the protonic conductivity of different materials [60].

3.2.3. Mixed ion – electronic conductors

At the end, all these materials present mixed conductivity between oxygen, protonic and electronic conductivity where depending on the material and the conditions the type of conductivity which prevails is different. That multi-type conductivity decreases the efficiency of the setup, especially the electronic conductivity which the material may present for current assisted membrane reactors. Even so, the co-ionic conductivity could also improve the overall process. An example was reported for Morejudo et.al [65] where a protonic conducting material was introduced in a catalytic reactor system to extract the hydrogen and to shift an equilibrium-limited reaction to the products. In this work, the conditions and the properties of the electrolyte ($BaZrO_3$ based material) caused a co-ionic transport for the current extracting hydrogen (for the protonic conductivity) from the catalytic chamber and injecting oxygen (for the oxygen conductivity) in the catalytic bed. That oxygen injection causes the suppression of coke depositions which is the main cause of deactivation of the catalyst for this process.

However, the most important way to take profit of mixed conducting materials until is using electronic conductivity and ionic conductivity simultaneously to separate oxygen (or hydrogen) when a partial pressure difference appears between both sides of the membrane. Here, the oxygen or hydrogen separated is transported across the membrane without external electric current achieving the oxygen or hydrogen permeates across membrane. The solid-state permeation of oxygen through these materials is possible due to the presence of oxygen vacancies in the crystalline lattice. At high temperatures (> 500 °C), oxygen ion is transported through the ceramic crystalline material hopping from vacancy to vacancy and, in parallel to ionic diffusion, the counter-diffusion of electronic carriers keeping the electroneutrality in all the material. Therefore, mixed ionic and electronic conductivity (MIEC) enables the oxygen transport.

The driving force for oxygen permeation is the chemical potential gradient applied through the membrane. Therefore, high differences between the oxygen concentration at feed and permeate sides will result in high oxygen permeation rates. Since MIEC membranes are dense, O_2 transport across membrane is not done in the molecular form but in the ionic form O^{-2}. Oxygen permeates through MIEC membranes via three main steps, i.e., oxygen exchange at the gas–solid interface of retention side, oxygen–electron (or hole) ambipolar diffusion through the membrane bulk, and oxygen exchange at the gas–solid interface of permeation side, as shown in Figure 3.14. The reactions related to oxygen exchange at the gas–solid interfaces are also called surface exchange reactions. The surface exchange reactions are complicated, because there are four electrons related to the reactions.

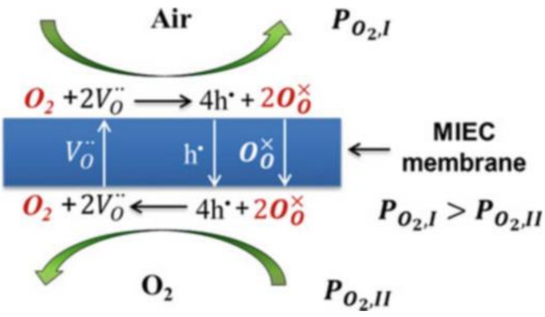
Air
$P_{O_2,I}$
$O_2 + 2V_O^{\cdot\cdot} \longrightarrow 4h^{\cdot} + 2O_O^{\times}$
$V_O^{\cdot\cdot}$
$h^{\cdot}$
$O_O^{\times}$
MIEC membrane
$O_2 + 2V_O^{\cdot\cdot} \longleftarrow 4h^{\cdot} + 2O_O^{\times}$
$P_{O_2,I} > P_{O_2,II}$
O_2
$P_{O_2,II}$

Figure 3.15. Mechanism of oxygen permeation through an MIEC membrane [66]

Surface exchange reactions can be written as follows:

Feed side $1/2\ O_2 + V_O^{\cdot\cdot} \rightleftarrows O_O^X + 2\ h^{\cdot}$ (r 3.2)

Permeation side $O_O^X + 2\ h^{\cdot} \rightleftarrows 1/2\ O_2 + V_O^{\cdot\cdot}$ (r 3.3)

where $h^{\cdot}$, denote the holes.

There are two diffusion paths for oxygen ions through the membrane bulk: one is via the oxygen vacancies and the other is via the oxygen interstitial sites. For most ABO_3 perovskites and fluorites, the transport of oxygen ions follows the vacancy diffusion mechanism, while for the K_2NiF_4-type oxides, the transport of oxygen ions follows the interstitial diffusion mechanism or a mixed interstitial and vacancy diffusion mechanism. In the oxygen permeation process, oxygen ions transport from the retention side to the permeation side, while the electrons or holes (depending on the type of conductivity) diffuses in an inverse direction to keep the electric neutrality throughout the MIEC membranes. Unlike an oxygen pump, which is based on pure oxygen ionic conductors, such as yttria-stabilized zirconia (YSZ), and needs an outside electric circle, the MIEC membranes can transfer electrons internally, and thus, the complexity of the setup is significantly reduced and facile to the large-scale applications. Besides these materials, other compounds exhibiting interesting oxygen transport properties are pyrochlore ($A_2B_2O_7$), brownmillerite ($A_2B_2O_5$), Ruddlesden-Popper series ($A_{n+1}B_nO_{3n+1}$), and $SrFe_{6-x}Co_xO_{13}$ [67-70]. However, these last materials and the K_2NiF_4-type present lower performance in comparison with fluorites and perovskites.

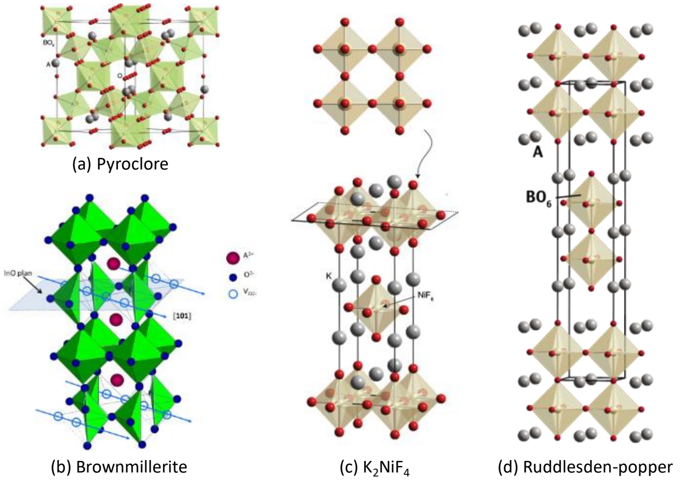

(a) Pyroclore

(b) Brownmillerite

(c) K_2NiF_4

(d) Ruddlesden-popper

Figure 3.16. Crystal structure of the oxygen permeation materials based on mixed ion and electronic materials. (a) pyrochlore ($A_2B_2O_7$)) (obtained from [48]); (b) brownmillerite ($A_2B_2O_5$) (obtained from [71]); (c) K_2NiF_4 (obtained from [48]); (d) Ruddlesden-popper (obtained from [48]).

Fluorites exhibit high chemical stabilities under typical harsh environments of industrial applications, nevertheless the low electronic conductivity that also present leads to very low oxygen permeation. On the contrary, perovskites exhibit outstanding permeation fluxes, but at the same time low stability behaviors that restrict industrial applications.

Therefore, dual-phase composite materials comprising two different materials (one providing electronic conductivity and the other ionic conductivity) are a very promising option for obtaining stable materials with enough mixed-conduction for fulfilling oxygen permeation requirements (Figure 3.17). Some examples of composites materials for oxygen applications are:

- Ceramic – metal composites [72-74]
- Ceramic – ceramic composites: fluorite/spinel [75-78], perovskite/spinel [79], fluorite/perovskite [80-82]

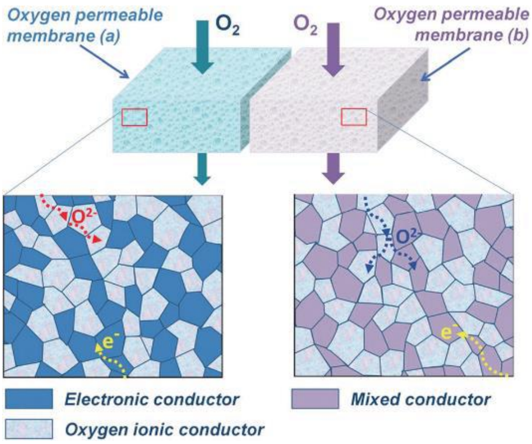
Oxygen permeable membrane (a)
O_2
O_2
Oxygen permeable membrane (b)
O^{2-}
e^-
O^{2-}
e^-
Electronic conductor
Oxygen ionic conductor
Mixed conductor

Figure 3.17. Schematic picture of dual-phase membranes. Image extracted from [83]

3.3. Membrane reactor using high temperature ceramic materials

Ion conducting ceramic membranes reactors offer an opportunity to integrate separation membranes enhancing chemical process. Considering the different ceramic materials already described, now the uses of these materials for membrane reactor is analyzed considering the product desired.

3.3.1. Hydrogen production

Nowadays, hydrogen is mainly produced by steam reforming. These processes combine the central steam reforming units (where the hydrocarbon becomes in CO – reaction 3.4), water gas shift units (where CO turns into CO_2 – reaction 3.5) and the hydrogen separation unit (normally a PSA unit). Therefore, steam reforming processes requires large plants.

$$CH_4 + H_2O \rightleftarrows CO + 3\,H_2 \qquad \text{(r 3.4)}$$

$$CO + H_2O \rightleftarrows CO_2 + H_2 \qquad \text{(r 3.5)}$$

$$CH_4 + 2\,H_2O \rightleftarrows CO_2 + 4\,H_2 \qquad \text{(r 3.6)}$$

Considering previous reactions, hydrogen selective membranes could overcome the equilibrium limitations integrating all the steps of the conventional process poses in a single reactor [84, 85].

Several strategies to produce and separate the hydrogen have been studied using high temperature ionic ceramics. Considering electrochemical membrane reactors, electrolysis is an interesting alternative to storage the surplus of the energy from renewable sources. This kind of processes are known as Power-to-hydrogen (P2h) [42, 86-92]. Eventually, MIEC materials can be used to produce hydrogen from three different processes: water splitting, water-gas shift reaction and autothermal reaction.

Water splitting consists of the dissociation of water. However, as the equilibrium constant of the dissociation of water to generate hydrogen is very low and, consequently, it needs extreme conditions (partial pressures) to obtain significant amounts of hydrogen. Further, it is a very endothermic reaction leading to a high energy consumption of the reaction.

Water splitting using oxygen permeable membranes has been proved using different materials: CGO-based [93, 94], $La_{0.3}Sr_{0.7}FeO_{3-\delta}$ [95], $0.5SrTi_{0.5}Fe_{0.5}O_{3-\delta}$–$0.5Ce_{0.8}(Sm_{0.8}Sr_{0.2})_{0.2}O_{2-\delta}$ [96]. The process is substantially improved using the permeated oxygen to oxidize a fuel gas as it allows low oxygen partial pressures in this chamber improving the driving force. That concept has been successful tested using different MIEC materials: $La_{0.9}Ca_{0.1}FeO_{3-\delta}$ [97], a composite of $Ce_{0.85}Sm_{0.15}O_{1.925}$ $Sm_{0.6}Sr_{0.4}Al_{0.3}Fe_{0.7}O_{3-\delta}$ [98], $La_{0.6}Sr_{0.4}Co_{0.2}Fe_{0.8}O_{3-\delta}$ [99], $La_{0.7}Sr_{0.3}Cu_{0.2}Fe_{0.8}O_{3-\delta}$ (LSCF) and $BaFe_{0.9}Zr_{0.1}O_{3-\delta}$ (BFZ) [100].

Water-gas shift reaction (reaction 3.5) is thermodynamically favored at lower temperatures and kinetically favored at high temperatures [41]. Conventionally, this process takes place in two sequential units at 550ºC and 200 – 250ºC. Considering, a hydrogen selective membrane reactor is theoretically possible full conversion in a unique step. The concept was proved using $SrCe_{0.7}Zr_{0.2}Eu_{0.1}O_{3-\delta}$ perovskite membrane achieving 90% of CO conversion at 900ºC (thermodynamics at this temperature lends to CO) [101].

3.3.2. Syngas production

Syngas is a valuable gas mixture of CO and H_2 as intermediate reaction product, for example in the ammonia production (Haber Bosch process) or gas-to-liquids applications (Fisher Tropps processes) [41]. This gas mixture can be obtained by partial oxidation, steam reforming, reverse water gas shift reaction and dry reforming of methane. Syngas also can be obtained from thermochemical treatment (gasification and pyrolysis) of biomass and coal [102, 103].

Partial oxidation of methane is an exothermic reaction so with a suitable heat management of this heat, the process would not need heat supply (reaction 3.7).

$$CH_4 + \frac{1}{2}\,O_2 \rightarrow CO + 2\,H_2 \quad \Delta H^o = -36\,\frac{kJ}{mol} \qquad \text{(r 3.7)}$$

The oxidations, in this case partial oxidations, are not reactions limited by thermodynamic equilibrium. However, using oxygen permeable MIEC membranes it possible to measure out the oxygen supply. In addition, as previously it was explained, perovskites have low stabilities under CO_2 atmospheres. Eventually, the oxygen needs to be introduced suitability to avoid undesired coke and CO_2 formations.

Perovskites with high oxygen ion and electronic conductivities are the most suitable materials for this process [41]. Using this kind of materials in a Ni-based catalyst bed 85 – 96 % of CO yields have been found [104-108]. Composite using cer-cer [109-112] or Ag/CGO [113] have also studied for this process but with lower CO yields than single phase perovskite until now.

Reforming reactions can be used to obtain syngas. Here, ceramic ionic conducting membranes can be used to improve these processes. Oxygen permeable membranes uses a fraction of the reformer were the oxygen injection allows control the thermal balance [114, 115]. With hydrogen permeable membranes, the separated hydrogen is oxidized to balance the process.

The dry reforming process allows to obtain syngas using CO_2 in spite of steam (reaction 3.8). It is about a process favored at high temperatures, where the main limitation comes because these conditions, which favor carbon depositions and, thus, the process deactivation. However, coke deposition could be avoided increasing the ratio CO_2/CH_4 [116]. As it happens for conventional steam reforming, it is a process highly endothermic, which involves high thermal energy demands to keep the temperature of the process. Here, using a hydrogen selective membrane it is possible decrease the temperature of the process and shift the equilibrium until full conversion. The concept has been proved in previous works [117, 118].

$$CH_4 + CO_2 \rightleftarrows 2\ CO + 2\ H_2 \quad \Delta H^o = 247\,\frac{kJ}{mol} \tag{r 3.8}$$

3.3.3. Higher hydrocarbons production

Hydrocarbons are conventionally obtained fractionating the petroleum. Therefore, although using a membrane reactor to obtain higher hydrocarbons since methane, CO_2 or biomass is not currently competitive, as the fossil fuels sources is going depleting, alternative processes will be necessary.

Higher hydrocarbons can be obtained via conducting ceramic membranes with coupling of methane, hydrogenation, dehydrogenation and dehydroaromatization.

Methane coupling reaction allows to obtain ethane (reaction 3.9 and 3.11) and ethylene (reaction 3.10 and 3.12) with oxidative and non-oxidative reactions. The oxidative via uses oxygen-conducting membranes (injecting the oxygen in the reaction chamber) and the non-oxidative via uses hydrogen-conducting membranes (removing the hydrogen from the reaction chamber).

$$2\ CH_4 + \frac{1}{2}\ O_2 \rightleftarrows C_2H_6 + H_2O \qquad \text{(r 3.9)}$$

$$2\ CH_4 + O_2 \rightleftarrows C_2H_4 + 2\ H_2O \qquad \text{(r 3.10)}$$

$$2\ CH_4 \rightleftarrows C_2H_6 + H_2 \qquad \text{(r 3.11)}$$

$$2\ CH_4 \rightleftarrows C_2H_4 + 2\ H_2 \qquad \text{(r 3.12)}$$

Considering the oxidative pathway, it is more beneficial because the reaction is exothermic and the process is easier to be auto-sustainable [41]. However, the injection of oxygen needs to be carefully implemented because the reaction products are more reactive than methane and, therefore, this oxygen could degrade them [119]. The best results show C_2 yield until 38 % [120].

Using non-oxidative pathway, using an electrochemical membrane reactor with a protonic conducting membrane very high C_2 selectivities can be achieved for low current densities [121, 122]. However, these materials present co-ionic conductivities at hydrogen and oxygen so, as the current density and consequently the hydrogen extraction increases, the oxygen injection increases too. Therefore, it may cause a degradation of the catalyst and the hydrocarbons. Finally, using this approach the best results reported are 58% of methane conversion with 13.4% of C_2 yield [123].

Alkane dehydrogenation to obtain olefins are interesting processes to integrate this kind of membranes. Most researched process to integrate a membrane in the process is the ethylene formation from ethane using oxygen permeable membranes (oxidative dehydrogenation of ethane to ethylene). Perovskites are the most preferred membranes where ethylene yield up to 75% can be achieved at temperatures below 800ºC and until 83% at 850ºC [124, 125]. Non-oxidative dehydrogenation of ethane using hydrogen extraction membranes are limited for the equilibrium of the reaction and it is because it is not so interesting than oxidative pathway [41]. Propane dehydrogenation is also very attractive process under research using membrane reactors [125].

$$C_2H_6 + \frac{1}{2}\,O_2 \rightarrow C_2H_4 + H_2O \qquad \text{(r 3.13)}$$

Methane dehydroaromatization allows obtaining aromatics from methane in one step. However, it is a process limited by the equilibrium (12% of methane conversion at 700°C) and the coke formation. As previous processes, it can be developed with a non-oxidative process (reaction 3.14) and oxidative process (reaction 3.15) and, consequently, these processes can be enhanced using hydrogen permeable and oxygen permeable membranes, respectively. Considering the non-oxidative pathway, in the last years very stable and aromatic selective process has been developed using a current assisted process with a proton conductor membrane [65]. Non-oxidative pathway has been investigated achieving aromatics yield until 6% with oxygen permeable membranes [126].

$$6\,CH_4 \rightleftarrows C_6H_6 + 9\,H_2 \qquad \text{(r 14)}$$

$$6\,CH_4 + \frac{9}{2}O_2 \rightleftarrows C_6H_6 + 9\,H_2O \qquad \text{(r 15)}$$

Morejudo et. al. [65] proved the injection of controlled amounts of oxygen while the hydrogen is removed with a co-ionic (protonic and oxygen ion) conducting membrane allows to enhance the stability because the suppression of coke depositions. Several works about methane dehydroaromatization cofeeding with steam shows an improvement of the catalytic stability due to coke suppression but higher steam content of 2.6% causes a fall in the catalytic activity after several hours due to the steam reacts with the catalyst, in particular, with the C of the MoC sites according previous works [127-129].

3.3.4. Methane production

Nowadays, methane demands are covered because natural gas is mainly methane (around 90%). However, methane can be a way to storage surplus energy from renewable sources. In fact, nowadays, there is an increasing of the effort to make viable and competitive to becomes CO_2 and surplus of energy from renewable sources (solar and wind) in CH_4

[130-132] where the CO_2 can be obtained from biomass by mean of thermochemical processes [131].

Methanation process allows becoming CO_2 into methane reverting the methane steam reforming reaction (reaction 3.16). That pathway is favored at lower temperatures and high pressures [133, 134]. Alternative current assisted process has been developed to overcome the equilibrium limitations where the CO_2 is reduced to CH_4 by an electrochemical pathway [135-138], (reactions 3.17 and 3.18 shows the electrochemical reduction of CO2 until CH4 by means of proton conducting and oxygen ion conducting assemblies, respectively). The protonic pathway (reaction 3.17) causes mixtures of methane and steam, therefore, low temperatures are required to keep the methane and avoid reforming reactions.

$$CO_2 + 4\,H_2 \rightarrow CH_4 + 2\,H_2O \qquad \text{(r 3.16)}$$

$$CO_2 + 8\,H^+ + 8\,e^- \rightarrow CH_4 + 2\,H_2O \qquad \text{(r 3.17)}$$

$$CO_2 + 2\,H_2 + 4\,e^- \rightarrow CH_4 + 2\,O^{2-} \qquad \text{(r 3.18)}$$

3.3.5. Ammonia production

Ammonia synthesis using ionic conducting ceramics is possible by means of electrochemical cells. However, the electrochemical synthesis of ammonia is still far from conventional Haber-Bosch process and it requires more efforts to find optimal assemblies which are competitive and viable [41].

Electrochemical cells to obtain ammonia would allow to reduce the dramatically conditions of Haber-Bosch process (200-300 bar & 500 °C). Suitable ionic conducting ceramics as membrane materials are perovskites as barium cerates and fluorites as cerium oxides. Using protonic conducting membranes reduces the power demand due to oxygen conducting requires water dissociation and, therefore the reversible work is considerable higher (Table 3.4). Relevant studies using proton conducting perovskites have been developed to obtain ammonia [139-141]. Reaction rates and faradaic efficiencies as high as a $3.3\cdot10^{-8}$ mol s^{-1} cm^{-2} [142] and 90.4 % [143], respectively, have been reported.

Table 3.4. Reactions for electrochemical synthesis of ammonia using oxygen ion conducting and protonic conducting materials.

Overall reaction	**Anode**	**Cathode**
Oxygen conducting		
$N_2 + 3\,H_2O \rightarrow 2\,NH_3 + \frac{3}{2}O_2$	$2\,O^{2-} \rightarrow O_2 + 4\,e^-$	$N_2 + 3\,H_2O + 6e^- \rightarrow 2\,NH_3 + 3\,O^{2-}$
Protonic conducting		
$N_2 + 3\,H_2 \rightarrow 2\,NH_3$	$H_2 \rightarrow 2\,H^+ + 2\,e^-$	$N_2 + 6\,H^+ + 6\,e^- \rightarrow 2\,NH_3$

3.4.Electrodes for protonic conducting ceramics

The selection of the materials for electrodes depends on the final applications. However, the electrode material must reach several properties and conditions:

i. Stability: chemical, morphological and dimensional in the working conditions.
ii. Conductivity: electronic conductivity must be as higher as possible. In addition, considering that the surface exchange reaction take place in the triple phase boundary (TPB), the electrode must present ionic conductivity.
iii. Porosity: allowing the gas transport to the TPB points.

iv. Thermal expansion coefficient: it must be similar to the electrolyte.

v. Compatibility with the rest of the materials of the cell: electrolyte, supports, etc.

vi. Catalytic activity: must have enough catalytic activity for the different reactions to avoid polarization problems.

The typical H_2 electrode for SOFC applications (both protonic and oxygen ion conductor membranes) is based on nickel [144, 145]. It usually uses nickel cermet with the electrolyte material to maximize the TPB points. However, the electrode material must be stable at the working conditions and nickel presents several drawbacks like coarsening and coke depositions under hydrocarbons atmospheres and reoxidation in O2 or steam atmospheres. Therefore, alternatives to nickel are needed to overcome these problems. Considering other metals as Pd, Fe, Cu, Ru and Pt have been checked finding Fe and Ag-Pd good alternatives to nickel [146-148]. The copper- based anodes in combination with ceria catalysts, which may be of interest for hydrocarbon-fueled SOFCs due to low catalytic activity of Cu toward the C–C bond formation, exhibit a poor electrochemical performance and undergo fast degradation [144]. Considering the ionic conductor material, these materials were described before (see section 3.2).

3.5. Finite elements for high temperature membrane reactors

The finite element method or computational fluid dynamics (CFD) is used to solve physical problems in engineering analysis and design [149]. Finite elements approach allows forward and complete analysis of a setup (for dynamic or steady states) considering the phenomena which take place and the properties of the materials. The methodology is based on a discretization of the geometry in interconnected nodes. As more complex is the geometry and/or the process, this method could require high computational resources to carry on. The analysis of an engineering system usually requires the idealization of the system into a form that can be solved, the formulation of the mathematical model, the solution of this model, and the interpretation of the results.

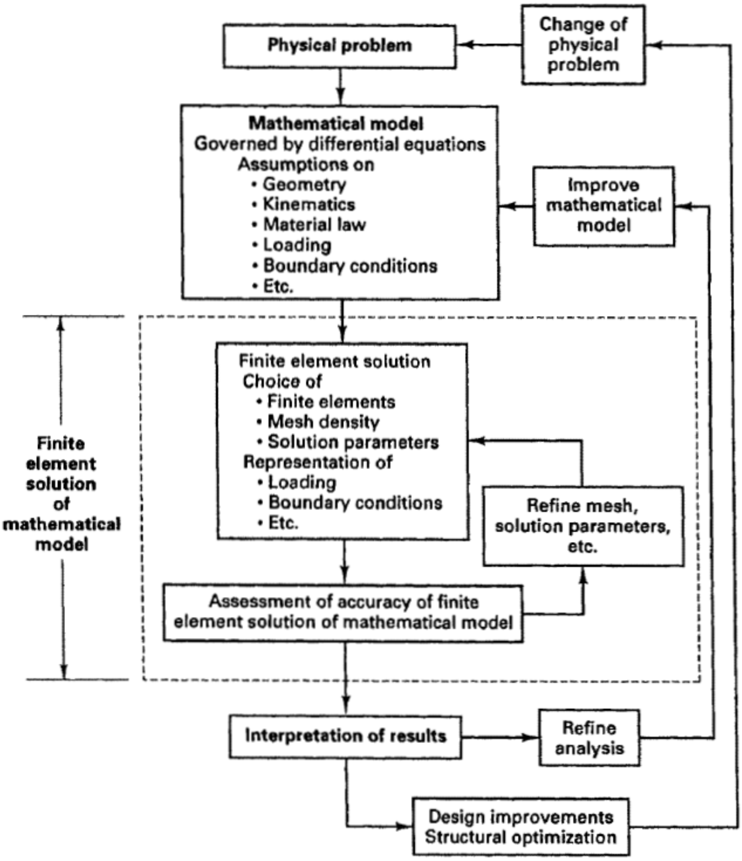
Physical problem
Change of physical problem
Mathematical model
Governed by differential equations
Assumptions on
• Geometry
• Kinematics
• Material law
• Loading
• Boundary conditions
• Etc.
Improve mathematical model
Finite element solution of mathematical model
Finite element solution
Choice of
• Finite elements
• Mesh density
• Solution parameters
Representation of
• Loading
• Boundary conditions
• Etc.
Refine mesh, solution parameters, etc.
Assessment of accuracy of finite element solution of mathematical model
Interpretation of results
Refine analysis
Design improvements
Structural optimization

Figure 3.18. Methodology to use finite elements. Image extracted from [149].

The utilization of finite elements requires a validation step which allows to demonstrate the model offers suitable predictions comparing with the experimental results. Several works are focused in the validation steps because is not always an easy step due to the high number of variables to model the process phenomena [150-152]. CFD models are usually used to find the optimal conditions of that processes [153-156] and to evaluate the scale up and designing the final commercial setup [157].

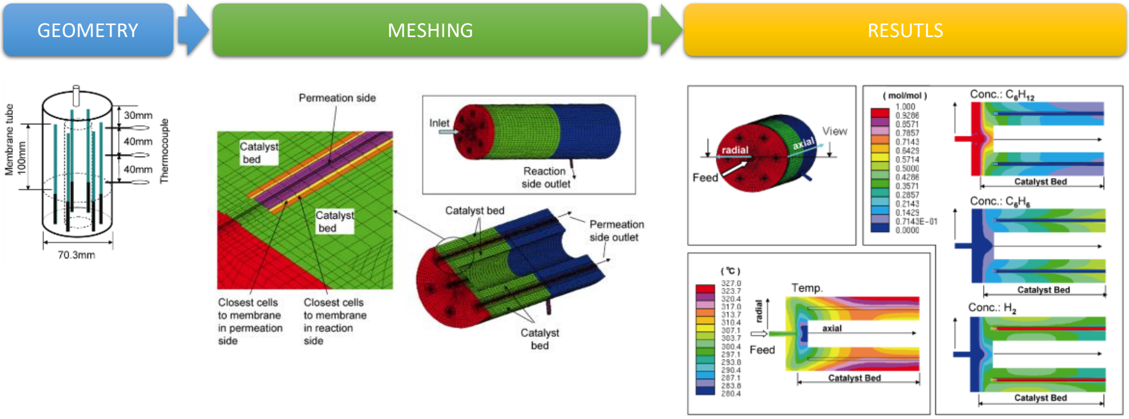
GEOMETRY
MESHING
RESUTLS
Membrane tube
100mm
30mm
40mm
40mm
Thermocouple
70.3mm
Permeation side
Catalyst bed
Catalyst bed
Closest cells to membrane in permeation side
Closest cells to membrane in reaction side
Inlet
Reaction side outlet
Catalyst bed
Permeation side outlet
Catalyst bed
View
radial
axial
Feed
(mol/mol)
1.000
0.9286
0.8571
0.7857
0.7143
0.6429
0.5714
0.5000
0.4286
0.3571
0.2857
0.2143
0.1429
0.7143E-01
0.0000
Conc.: C_6H_{12}
Catalyst Bed
Conc.: C_6H_6
Catalyst Bed
Conc.: H_2
Catalyst Bed
(℃)
327.0
323.7
320.4
317.0
313.7
310.4
307.1
303.7
300.4
297.1
293.8
290.4
287.1
283.8
280.4
Temp.
radial
axial
Feed
Catalyst Bed

Figure 3.19: Main results of CFD model of cyclohexane dehydrogenation in a hydrogen membrane reactor. [151].

Finite elements have been used to characterize ionic conductor ceramics for fuel cell mode [158-163] and electrolysis [164, 165] with different geometries and adapting works which use different materials as electrolyte. Between a large number of works, it could find as several works have improved the understanding of permeation processes [166-169], adsorption [170, 171] or fluid dynamics at high temperatures [172-174]. All these works allow doing estimations about membrane reactor using these kinds of processes.

Eventually, CFD buildings have proved the enhancement of integrating membrane reactors for water gas shift process [152, 175-177], steam reforming process [153, 156, 178, 179] and others [150, 180]. These works have allowed to improve the knowledge of these reactions and evaluating the effect of the different operation conditions and parameters in yields and efficiencies of the overall process.

3.6.References

1. www.scope.com. 2017.
2. Giorno, L. and E. Drioli, Trends in Biotechnology, 2000. **18**(8): p. 339-49.
3. Ozdemir, S.S., et al., Applied Catalysis A: General, 2006. **307**(2): p. 167-83.
4. Lütz, S., et al., Chem. Eng. Technol., 2006. **29**(12): p. 1404-15.
5. Charcosset, C., Biotechnology Advances, 2006. **24**(5): p. 482-92.
6. Coutte, F., et al., *10 - Recent Trends in Membrane Bioreactors A2 - Larroche, Christian*, in *Current Developments in Biotechnology and Bioengineering*, M.Á. Sanromán, et al., Editors. 2017, Elsevier. p. 279-311.
7. Vankelecom, I.F.J., Chemical Reviews, 2002. **102**(10): p. 3779-810.
8. Sousa, J.M., et al., *Polymeric Membrane Reactors*, in *Simulation of Membrane Reactors*, A.B.a.F. Gallucci, Editor. 2006.
9. Koros, W.J. and D.G. Woods, Journal of Membrane Science, 2001. **181**(2): p. 157-66.
10. Ghasemzadeh, K., et al., *Polymeric Membrane Reactors*, in *Membrane Reactor Engineering*. 2016, John Wiley & Sons, Ltd. p. 104-37.
11. Gallucci, F., Basile, A. & Hai, F. Ibney, *Introduction - A review of membrane reactors*, in *Membranes for membrane reactors: preparation, optimization and selection*, J.W. sons, Editor. 2011, University of Wollongong: Australia. p. 1-61.
12. Rahimpour, M.R., et al., Chemical Engineering and Processing: Process Intensification, 2017.
13. Al-Mufachi, N.A., et al., Renewable and Sustainable Energy Reviews, 2015. **47**: p. 540-51.

14. Gallucci, F., et al., Chemical Engineering Science, 2013. **92**: p. 40-66.
15. Yun, S. and S. Ted Oyama, Journal of Membrane Science, 2011. **375**(1): p. 28-45.
16. Hatlevik, Ø., et al., Separation and Purification Technology, 2010. **73**(1): p. 59-64.
17. Ismail, A.F. and L.I.B. David, Journal of Membrane Science, 2001. **193**(1): p. 1-18.
18. Hosseini, S.S. and T.S. Chung, Journal of Membrane Science, 2009. **328**(1): p. 174-85.
19. Campo, M.C., et al., Journal of Membrane Science, 2010. **350**(1): p. 180-8.
20. Tseng, H.-H., et al., Journal of Membrane Science, 2016. **510**(Supplement C): p. 391-404.
21. Tao, Z., et al., Progress in Materials Science, 2015. **74**: p. 1-50.
22. Algieri, C., et al., *6 - Zeolite membrane reactors A2 - Basile, Angelo*, in *Handbook of Membrane Reactors*. 2013, Woodhead Publishing. p. 245-70.
23. Briceño, K., et al., *10 - Carbon-based membranes for membrane reactors*, in *Handbook of Membrane Reactors*. 2013, Woodhead Publishing. p. 370-400.
24. Ghasemzadeh, K. and A. Basile, *Ceramic Membrane Reactors*, in *Membrane Reactor Engineering*. 2016, John Wiley & Sons, Ltd. p. 138-62.
25. Caro, J. and M. Noack, Microporous and Mesoporous Materials, 2008. **115**(3): p. 215-33.
26. de Lange, R.S.A., et al., Journal of Membrane Science, 1995. **104**(1): p. 81-100.
27. Smart, S., et al., *9 - Microporous silica membranes: fundamentals and applications in membrane reactors for hydrogen separation A2 - Basile, Angelo*, in *Handbook of Membrane Reactors*. 2013, Woodhead Publishing. p. 337-69.
28. Leboda, R. and E. Mendyk, Materials Chemistry and Physics, 1991. **27**(2): p. 189-212.
29. Fotou, G.P., et al., Journal of Materials Science, 1995. **30**(11): p. 2803-8.
30. Leboda, R., et al., Colloids and Surfaces A: Physicochemical and Engineering Aspects, 1995. **105**(2): p. 191-7.
31. de Vos, R.M., et al., Journal of Membrane Science, 1999. **158**(1): p. 277-88.

32. Duke, M.C., et al., Journal of Membrane Science, 2004. **241**(2): p. 325-33.
33. Kanezashi, M., et al., Separation Science and Technology, 2005. **40**(1-3): p. 225-38.
34. Ikuhara, Y.H., et al., Journal of the American Ceramic Society, 2007. **90**(2): p. 546-52.
35. Battersby, S., et al., Separation and Purification Technology, 2009. **66**(2): p. 299-305.
36. Uhlmann, D., et al., Journal of Membrane Science, 2011. **380**(1): p. 48-54.
37. Gu, Y. and S.T. Oyama, Journal of Membrane Science, 2009. **345**(1): p. 267-75.
38. Caro, J. and Y. Wei, *Ceramic Membranes with Mixed Ionic and Electronic Conductivity*, in *Membrane Reactor Engineering*. 2016, John Wiley & Sons, Ltd. p. 75-103.
39. Sunarso, J., et al., Journal of Membrane Science, 2008. **320**(1): p. 13-41.
40. Malavasi, L., et al., Chemical Society Reviews, 2010. **39**(11): p. 4370-87.
41. Deibert, W., et al., Journal of Membrane Science, 2017. **543**(Supplement C): p. 79-97.
42. Götz, M., et al., Renewable Energy, 2016. **85**: p. 1371-90.
43. EG&G Technical Services, I., 2005.
44. Świerczek, K. and W. Skubida, E3S Web Conf., 2017. **14**: p. 01044.
45. Gellings, P.J. and H.J.M. Bouwmeester, *The CRC handbook of solid state electrochemistry*. 1997: CRC Press.
46. Haram, S.K., *9 - Semiconductor Electrodes A2 - Zoski, Cynthia G*, in *Handbook of Electrochemistry*. 2007, Elsevier: Amsterdam. p. 329-89.
47. Gaudillere, C., et al., International Journal of Hydrogen Energy, 2014. **39**(7): p. 3047-54.
48. Liverpool, U.o. *http://www.chemtube3d.com/solidstate/_table.htm*. 2017 November 2017].
49. Weber, A. and E. Ivers-Tiffée, Journal of Power Sources, 2004. **127**(1): p. 273-83.
50. Serra, J.M. and W.A. Meulenberg, Journal of the American Ceramic Society, 2007. **90**(7): p. 2082-9.
51. Bonano, N., et al., Solid State Ionics, 1991. **44**(3): p. 305-11.

52. Sundmacher, K., et al., Catalysis Today, 2005. **104**(2–4): p. 185-99.

53. Demin, A. and P. Tsiakaras, International Journal of Hydrogen Energy, 2001. **26**(10): p. 1103-8.

54. Jamsak, W., et al., Chemical Engineering Journal, 2006. **119**(1): p. 11-8.

55. Medvedev, D., et al., *Proton-Conducting Electrolytes for Solid Oxide Fuel Cell Applications*, in *Advances in Medium and High Temperature Solid Oxide Fuel Cell Technology*, M. Boaro and A.A. Salvatore, Editors. 2017, Springer International Publishing: Cham. p. 77-118.

56. J T de Grotthuss, C., *Memoir on the decomposition of water and of the bodies that it holds in solution by means of galvanic electricity*. Vol. 1757. 2006. 871-5.

57. Hibino, T., et al., Solid State Ionics, 1992. **58**(1): p. 85-8.

58. Kreuer, K.D., et al., Solid State Ionics, 1995. **77**(Supplement C): p. 157-62.

59. Kreuer, K.D., Solid State Ionics, 1999. **125**(1): p. 285-302.

60. Kreuer, K.D., Annual Review of Materials Research, 2003. **33**(1): p. 333-59.

61. Münch, W., et al., Solid State Ionics, 1996. **86-88**(Part 1): p. 647-52.

62. Escolastico, S., et al., RSC Advances, 2012. **2**(11): p. 4932-43.

63. Saiful Islam, M. and P.R. Slater, MRS Bulletin, 2009. **34**(12): p. 935-41.

64. Norby, T. and Y. Larring, Current Opinion in Solid State and Materials Science, 1997. **2**(5): p. 593-9.

65. Morejudo, S.H., et al., Science, 2016. **353**(6299): p. 563-6.

66. Zhe;, X. and W. Yang, *Mixed Conducting Ceramic Membranes. Fundamentals, Materials and Applications*. 2017, Germany: Springer Nature.

67. Kharton, V.V., et al., Journal of Solid State Electrochemistry, 2003. **7**(8): p. 468-76.

68. Shaula, A., et al., 2012.

69. Xue, J., et al., Journal of Materials Chemistry A, 2015. **3**(37): p. 19107-14.

70. Bochkov, D.M., et al., Solid State Ionics, 1999. **120**(1): p. 281-8.

71. Geffroy, P.M., et al., Chemical Engineering Science, 2013. **87**(Supplement C): p. 408-33.

72. Chen, C.S., et al., Solid State Ionics, 1995. **76**(1): p. 23-8.
73. Chen, C.S., et al., Solid State Ionics, 1996. **86-88**(Part 1): p. 569-72.
74. Kim, J. and Y.S. Lin, Journal of Membrane Science, 2000. **167**(1): p. 123-33.
75. Luo, H., et al., Industrial & Engineering Chemistry Research, 2011. **50**(23): p. 13508-17.
76. Luo, H., et al., Chemistry of Materials, 2012. **24**(11): p. 2148-54.
77. Liang, F., et al., Chemical Communications, 2014. **50**(19): p. 2451-4.
78. Pippardt, U., et al., Journal of Ceramic Science and Technology, 2014. **5**(4): p. 309-16.
79. Kniep, J., et al., Solid State Ionics, 2010. **180**(40): p. 1633-9.
80. Yun, K.S., et al., Journal of Membrane Science, 2015. **486**(Supplement C): p. 222-8.
81. Joo, J.H., et al., ACS Applied Materials & Interfaces, 2015. **7**(27): p. 14699-707.
82. Fang, W., et al., Angewandte Chemie International Edition, 2015. **54**(16): p. 4847-50.
83. Dong, X., et al., Chemical Communications, 2011. **47**(39): p. 10886-902.
84. Kyriakou, V., et al., Applied Catalysis B: Environmental, 2016. **186**: p. 1-9.
85. Coors, W.G., Journal of The Electrochemical Society, 2004. **151**(7): p. A994-A7.
86. Gahleitner, G., International Journal of Hydrogen Energy, 2013. **38**(5): p. 2039-61.
87. BAN, M., et al., Journal of Modern Power Systems and Clean Energy, 2017. **5**(3): p. 337-49.
88. Schiebahn, S., et al., International Journal of Hydrogen Energy, 2015. **40**(12): p. 4285-94.
89. Guandalini, G., et al., Applied Energy, 2015. **147**(Supplement C): p. 117-30.
90. Qadrdan, M., et al., International Journal of Hydrogen Energy, 2015. **40**(17): p. 5763-75.
91. Varone, A. and M. Ferrari, Renewable and Sustainable Energy Reviews, 2015. **45**(Supplement C): p. 207-18.
92. Zhang, X., et al., Applied Energy, 2017. **190**(Supplement C): p. 326-38.

93. Balachandran, U., et al., International Journal of Hydrogen Energy, 2007. **32**(4): p. 451-6.
94. Wang, H., et al., Electrochimica Acta, 2011. **56**(20): p. 6989-96.
95. Evdou, A., et al., Journal of Membrane Science, 2008. **325**(2): p. 704-11.
96. Murashkina, A., et al., International Journal of Hydrogen Energy, 2014. **39**(24): p. 12472-9.
97. Wu, X.-Y., et al., AIChE Journal, 2016. **62**(12): p. 4427-35.
98. Fang, W., et al., Angewandte Chemie International Edition, 2016. **55**(30): p. 8648-51.
99. Franca, R.V., et al., Journal of Membrane Science, 2012. **389**(Supplement C): p. 173-81.
100. Park, C.Y., et al., International Journal of Hydrogen Energy, 2011. **36**(15): p. 9345-54.
101. Li, J., et al., International Journal of Hydrogen Energy, 2012. **37**(21): p. 16006-12.
102. Göransson, K., et al., Renewable and Sustainable Energy Reviews, 2011. **15**(1): p. 482-92.
103. Zhang, L., et al., Energy Conversion and Management, 2010. **51**(5): p. 969-82.
104. Babakhani, E.G., et al., J. Nat. Gas Chem., 2012. **21**(5): p. 519-25.
105. Zhang, Y., et al., Fuel, 2011. **90**(1): p. 324-30.
106. Liao, Q., et al., Chemical Engineering Journal, 2014. **237**(Supplement C): p. 146-52.
107. Yang, Z., et al., Journal of Membrane Science, 2014. **470**(Supplement C): p. 197-204.
108. Song, S., et al., International Journal of Hydrogen Energy, 2015. **40**(34): p. 10894-901.
109. Sadykov, V., et al., Catalysis Today, 2010. **156**(3): p. 173-80.
110. Yaremchenko, A.A., et al., Physical Chemistry Chemical Physics, 2007. **9**(21): p. 2744-52.
111. Zhu, X., et al., Journal of Membrane Science, 2010. **360**(1): p. 454-60.
112. Liu, J.-j., et al., Journal of Power Sources, 2012. **217**(Supplement C): p. 287-90.
113. Ruiz-Trejo, E., et al., Chemical Engineering Science, 2015. **127**(Supplement C): p. 269-75.

114. Jin, Y., et al., Catalysis Today, 2016. **264**(Supplement C): p. 214-20.
115. Park, C.Y., et al., International Journal of Hydrogen Energy, 2010. **35**(9): p. 4103-10.
116. Arora, S. and R. Prasad, RSC Advances, 2016. **6**(110): p. 108668-88.
117. Luo, Y., et al., Materials Letters, 2012. **86**(Supplement C): p. 5-8.
118. Zhang, K., et al., Journal of Membrane Science, 2014. **471**(Supplement C): p. 9-15.
119. Wang, W. and Y.S. Lin, Journal of Membrane Science, 1995. **103**(3): p. 219-33.
120. Othman, N.H., et al., Journal of Membrane Science, 2015. **488**(Supplement C): p. 182-93.
121. Chiang, P.H., et al., Journal of the Electrochemical Society, 1991. **138**(6): p. L11-L2.
122. Chiang, P.-H., et al., Solid State Ionics, 1993. **61**(1): p. 99-103.
123. Liu, Y., et al., Industrial & Engineering Chemistry Research, 2006. **45**(11): p. 3782-90.
124. Rebeilleau-Dassonneville, M., et al., Catalysis Today, 2005. **104**(2): p. 131-7.
125. Dalmon, J.-A., et al., Applied Catalysis A: General, 2007. **325**(2): p. 198-204.
126. Cao, Z.W., et al., Angew. Chem.-Int. Edit., 2013. **52**(51): p. 13794-7.
127. Liu, S., et al., Journal of Catalysis, 2003. **220**(1): p. 57-65.
128. Ma, H., et al., Catalysis Letters, 2005. **104**(1): p. 63-6.
129. Skutil, K. and M. Taniewski, Fuel Processing Technology, 2006. **87**(6): p. 511-21.
130. Rönsch, S., et al., Fuel, 2016. **166**(Supplement C): p. 276-96.
131. Ghaib, K. and F.-Z. Ben-Fares, Renewable and Sustainable Energy Reviews, 2018. **81**(Part 1): p. 433-46.
132. Meylan, F.D., et al., Journal of Energy Storage, 2017. **11**(Supplement C): p. 16-24.
133. Müller, K., et al., Environmental Earth Sciences, 2013. **70**(8): p. 3771-8.
134. Stangeland, K., et al., Energy Procedia, 2017. **105**(Supplement C): p. 2022-7.
135. Zhang, L., et al., Journal of Energy Chemistry, 2017. **26**(4): p. 593-601.

136. Lim, R.J., et al., Catalysis Today, 2014. **233**(Supplement C): p. 169-80.

137. Xie, K., et al., Journal of Materials Chemistry, 2011. **21**(1): p. 195-8.

138. Kalaitzidou, I., et al., Journal of Catalysis, 2015. **331**(Supplement C): p. 98-109.

139. Vasileiou, E., et al., Solid State Ionics, 2015. **275**: p. 110-6.

140. Marnellos, G., et al., Journal of Catalysis, 2000. **193**(1): p. 80-7.

141. Li, Z., et al., Science and Technology of Advanced Materials, 2007. **8**(7): p. 566-70.

142. Murakami, T., et al., Journal of the Electrochemical Society, 2005. **152**(5): p. D75-D8.

143. Xu, G., et al., Science in China Series B: Chemistry, 2009. **52**(8): p. 1171-5.

144. Tsipis, E.V. and V.V. Kharton, Journal of Solid State Electrochemistry, 2011. **15**(5): p. 1007-40.

145. Fabbri, E., et al., Science and Technology of Advanced Materials, 2010. **11**(4): p. 044301.

146. Ito, N., et al., Journal of Power Sources, 2005. **152**(Supplement C): p. 200-3.

147. Yamaguchi, S., et al., Solid State Ionics, 2003. **162-163**(Supplement C): p. 291-6.

148. Hibino, T., et al., Journal of The Electrochemical Society, 2002. **149**(11): p. A1503-A8.

149. Bathe, K.-J., *Finite Element Procedures*. 2nd ed. 2012.

150. Mimura, K., et al., *CFD Analysis of a Single Palladium Membrane Tube Reactor for the Dehydrogenation of Cyclohexane as a Chemical Hydrogen Carrier*. Vol. 43. 2010. 757-66.

151. Mimura, K., et al., *CFD Analysis and Design of Multi-tubular Membrane Reactor for Dehydrogenation of Cyclohexane*. Vol. 53. 2010. 283-91.

152. Byron Smith, R.J., et al., Chemical Engineering Research and Design, 2011. **89**(11): p. 2448-56.

153. Said, S.A.M., et al., International Journal of Hydrogen Energy, 2015. **40**(8): p. 3158-69.

154. Habib, M.A., et al., Journal of Membrane Science, 2013. **446**: p. 230-43.

155. Ahmed, P., et al., Energy, 2014. **77**: p. 932-44.

156. Roses, L., et al., International Journal of Hydrogen Energy, 2010. **35**(22): p. 12668-79.
157. Marchisio, D.L., et al., AIChE Journal, 2006. **52**(5): p. 1877-87.
158. Janardhanan, V.M. and O. Deutschmann, Journal of Power Sources, 2006. **162**(2): p. 1192-202.
159. Autissier, N., et al., Journal of Power Sources, 2004. **131**(1): p. 313-9.
160. Andersson, M., et al., International Journal of Heat and Mass Transfer, 2012. **55**(4): p. 773-88.
161. Murthy, S. and A.G. Fedorov, Journal of Power Sources, 2003. **124**(2): p. 453-8.
162. Lockett, M., et al., Journal of Power Sources, 2004. **131**(1): p. 243-6.
163. Huang, C.M., et al., Journal of Power Sources, 2008. **183**(1): p. 205-13.
164. Ni, M., International Journal of Hydrogen Energy, 2012. **37**(8): p. 6389-99.
165. Hawkes, G., et al., International Journal of Hydrogen Energy, 2009. **34**(9): p. 4189-97.
166. Lee, G., et al., Korean Journal of Chemical Engineering, 2017. **34**(9): p. 2366-73.
167. Ahmed, P., et al., Energy, 2014. **77**(Supplement C): p. 932-44.
168. Farooqui, A.E., et al., International Journal of Energy Research, 2013. **37**(11): p. 1265-79.
169. Coroneo, M., et al., Industrial & Engineering Chemistry Research, 2010. **49**(19): p. 9300-9.
170. Subrenat, A., et al., Chemical Engineering Science, 2003. **58**(22): p. 4965-73.
171. Breault, R.W. and E.D. Huckaby, Applied Energy, 2013. **112**(Supplement C): p. 224-34.
172. Ji, G., et al., Chemical Engineering Science, 2014. **111**(Supplement C): p. 142-52.
173. Mei, D., et al., International Journal of Hydrogen Energy, 2013. **38**(35): p. 15488-99.
174. Li, T., et al., Industrial & Engineering Chemistry Research, 2010. **49**(15): p. 6780-9.
175. Ghasemzadeh, K., et al., International Journal of Hydrogen Energy, 2017. **42**(43): p. 26914-23.
176. Chen, W.-H., et al., Fuel, 2017. **199**(Supplement C): p. 358-71.

177. Hla, S.S., et al., Chemical Engineering Journal, 2015. **276**(Supplement C): p. 289-302.
178. Ghasemzadeh, K., et al., International Journal of Hydrogen Energy, 2016. **41**(20): p. 8745-54.
179. Xuan, J., et al., International Journal of Hydrogen Energy, 2009. **34**(22): p. 9076-86.
180. Huang, H., et al., International Journal of Hydrogen Energy, 2016. **41**(1): p. 208-18.

4. EXPERIMENTAL METHODOLOGY

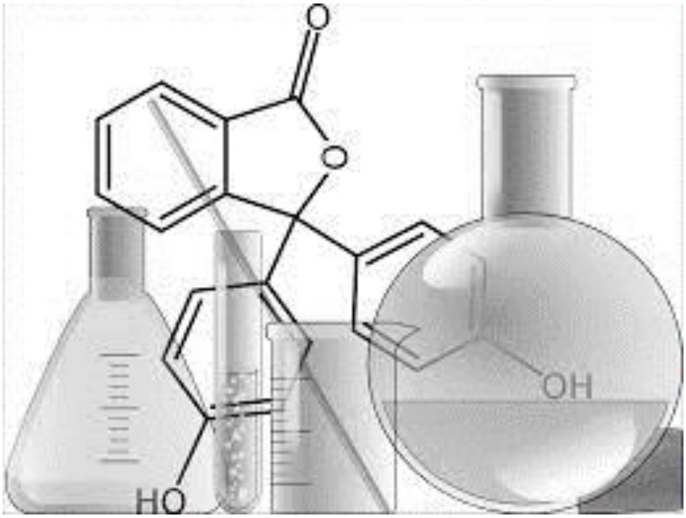

In this chapter, the procedures to synthesize the materials and developing the experimental characterization of these materials are thoroughly described. First, the different pathways to synthesize the different materials are described. Then, the methods to characterize the synthesized materials are defined. Finally, the experimental procedures and techniques to evaluate the behavior of the material are carefully defined.

Finite elements models built for this thesis present very differentiated methods and, therefore, an overall methods section would be tedious, and, in any case, each model would need its respective specifications. Therefore, each finite element-based study chapter presents its methods section where the model to simulate each respective phenomenon of the multiphysic process are carefully described.

4.1.Materials synthesis

The first experimental research of this thesis is focused in the development of copper-based electrodes for tubular membrane reactors based on protonic conducting ceramic materials. The procedures are defined in general terms. That means, although the procedures are cautiously described, the specific parameters of each method to synthesize the material or to optimize the behavior of the material are indicated in this chapter and detailed in the respective chapter.

4.1.1.Sol-gel method

Sol-gel method, also called Pechini method, is a technique that combines different metal nitrates to obtain the final oxide combination (Figure 4.1) [1]. The sol-gel method overcomes possible problems with the stoichiometry of precipitation methodologies when one or more ions are left in solution because the reactants never precipitate out [2, 3]. Considering the final stoichiometry of the final desired compound, stoichiometric nitrate amounts are mixed in distilled water. The mixture keeps under stirring using a magnetic stirrer. The typical chelating agent is citric acid (but EDTA is also used), and it is added to stabilize the metal complexes during the reaction step. Ethylene glycol (EG) is introduced for the polymerization process. Then, the temperature is increased until 100 – 130ºC to accelerate the combination of citric acid and EG in a polyester while the water is gradually evaporated. That causes a gelation of the solution followed by foaming. Afterwards, the solution is introduced in a heater at 220ºC to accelerate the process. The oxides form at temperatures above of 500ºC, therefore the powder obtained from the heater is calcined at higher temperatures to achieve the pure crystalline compound.

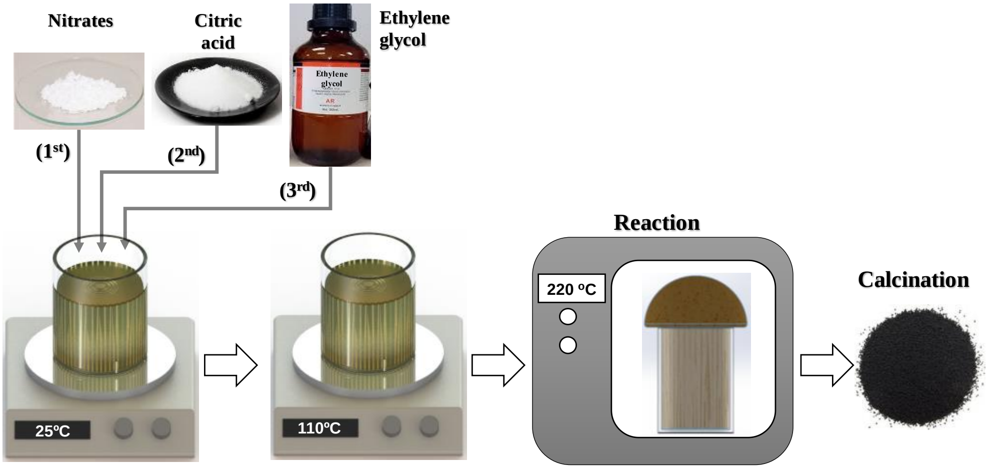

Figure 4.1. Sol-gel method for pure multicomponent formation.

4.1.2. Solid state reaction

Solid state reaction (SSR) is technique that combines non-volatile solids in a solid reaction system to achieve the desired compound. The process is accelerated using high temperatures due to the increasing of the reactivity system and, specially, the solid diffusion [4]. The temperature must be lower than the lowest melting point of the solids to avoid material losses and to keep the desired stoichiometry in the final compound.

Considering the doping agents, the reagents have to decompose before or during the reaction. The nucleation rate can be optimized using reactants with similar crystal structure.

SSR is a widely technique employed because its simplicity and low manufacturing costs. However, the method requires a good optimization in order to maximize the solid diffusion, to avoid secondary phases and to maximize the homogeneity of the final ceramic [5]. Further, SSR typically generates materials with small surface area due to its high sintering temperature [6].

The stoichiometric amounts of the metal oxides (although the method allows to use carbonates or sulphates) are mixed with zirconia balls (2mm of diameter) and acetone. The mixture is grinded in a ball mill to homogenize and to decrease the particle sizes minimizing the distance the reactants that have to diffuse. The dried powder is sieved and pelletized to maximize the contact between the different components. Finally, the pellets are heated in a furnace for several hours. This annealing must be conscientiously controlled to obtain the desired single phase. Figure 4.2 shows an illustration of the different steps of this technique.

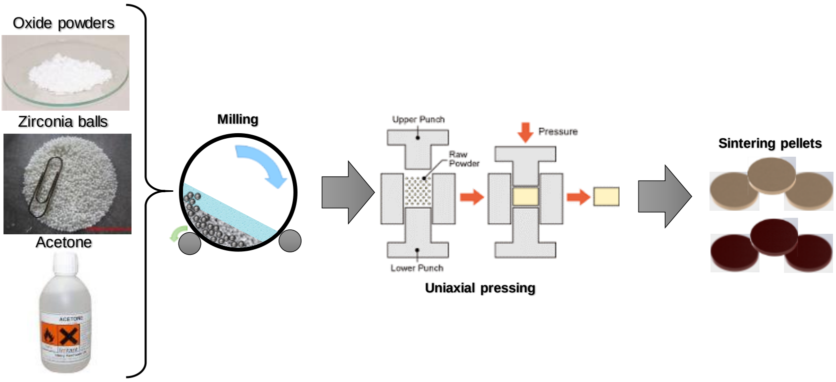
Oxide powders
Zirconia balls
Acetone
Milling
Upper Punch
Raw Powder
Pressure
Lower Punch
Uniaxial pressing
Sintering pellets

Figure 4.2. Solid State Reaction procedure.

4.1.3. Co-precipitation method

Co-precipitation technique allows obtaining metal oxides from soluble precursor of these metals using the change solubility of the metal compound (hydroxides, oxalates, carbonates, etc.) at different pH [7]. The particle size and shape are strongly dependent on the process conditions like the nature and method of dosing of ingredients, mixing and stirring. Therefore, these conditions have to be accurately controlled throughout the precipitation process [8].

Nitrate powders are dissolved in distilled water to achieve a specific concentration. The solution is kept in stirring while the pH of the solution is decreased using NaOH. The concentration of the NaOH should be optimized to fit the microstructure of the final oxide. The saturated solution is filtered with a vacuum filtration system and the resultant cake, dried. Vacuum filter used is Filter Papers 41 Ashless diameter 150mm 100 circles from Whatman^{TM}. Finally, the resultant powder is treated at different temperature in order to obtain the final particle size. Figure 4.3 shows the main steps of the co-precipitation method.

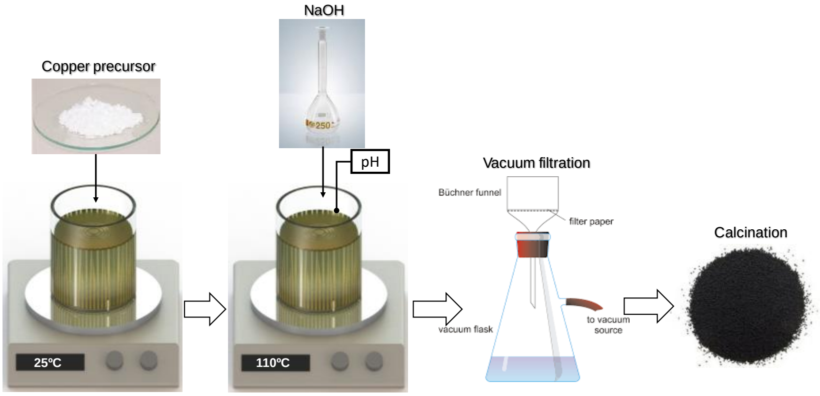
NaOH
Copper precursor
pH
Vacuum filtration
Büchner funnel
filter paper
Calcination
vacuum flask
to vacuum source
25ºC
110ºC

Figure 4.3. Co-precipitation methodology.

4.2.Deposition techniques

Materials synthetized using the described methods were used to developed copper-based electrodes and to deposit it on tubular half-cells.

4.2.1. Tubular support tested

Several tubular supports based on BZCY perovskite were tested and they were obtained from Coorstek Membrane Sciences. The characteristics of the different tubes are shown in the table 4.1. These tubes have 8.2 mm and 9.8 mm for internal and external diameters.

Table 4.1. Composition and thicknesses of the tubular half-cell electrochemical support.

Initial composition	**Layer**		**Thickness (mm)**
NiO-BZCY/BZCY	NiO-BZCY	Porous cermet	0.775
	BZCY	Dense layer	0.025
Ni-BZCY/BZCY	Ni-BZCY	Porous cermet	0.775
	BZCY	Dense layer	0.025

4.2.2. Dip-coating

The dip-coating method was developed to deposit thin and porous electrode layers on the described tubular half-cells. In this process, a liquid layer remains on the substrate with a thickness profile that is determined by the effect of different forces (mainly viscous force, gravity, and surface tension) on its flow [9]. Initial ceramic powders were mixed in acetone in ball milling during 12h. The dried powder was sieved. The slurry was prepared by mixing ethanol and different mixtures of terpineol and ethylcellulose (EC). Then polyvinyl pyrrolidone (PVP) was added to the solution. Finally, the ceramic powder was added to the slurry and the slurry was homogenized by stirring. Table 4.2 shows the composition of the slurries.

Table 4.2. Slurry compositions.

Ethylcellulose slurry		**Ethylcellulose free slurry**	
	wt %		**wt %**
Ethanol	23.5%	**Ethanol**	23.5%
Terpineol with 6 %wt EC	31.0%	**Terpineol**	31.0%
PVP	8.0%	**PVP**	8.0%
CuO-BZCY mixture powder	37.5%	**CuO-BZCY mixture powder**	37.5%

Tubes were dipped in the slurry and dried at temperatures between 65 – 80 °C. The procedure of dipping and drying was repeated several times to fit the thickness of the final cermet layer. Finally, dipped tubes were sintered at high temperatures. Figure 4.4 shows the summary of the dip-coating methodology with all the steps from the initial powders until the final reduction.

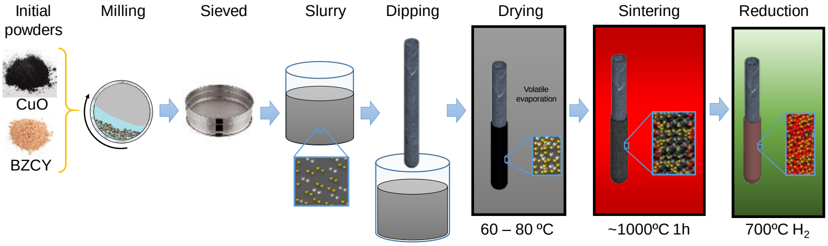
Initial powders
Milling
Sieved
Slurry
Dipping
Drying
Sintering
Reduction
CuO
BZCY
Volatile evaporation
60 – 80 ºC
~1000ºC 1h
700ºC H_2

Figure 4.4. Dip-coating methodology.

Pt catalyst was introduced in the sintered electrode layer using the infiltration method. Chloroplatinic acid was used as platinum precursor. It was dissolved in acetone and was dropped on reduced copper-based electrode until the full wetness of the layer.

4.2.3. Sputtering

The most basic and well-known glow-discharge technique to deposit thin films is sputtering. The ejection of surface atoms from an electrode surface (target) by momentum transfer from bombarding ions to surface atoms until the substrate surface (Figure 4.5). From this definition, sputtering is clearly an etching process and, is used as such for surface cleaning and for pattern delineation. Since sputtering produces a vapor of electrode material, it is frequently used as a method of film deposition. Sputter deposition has become a generic name for a variety of processes [10].

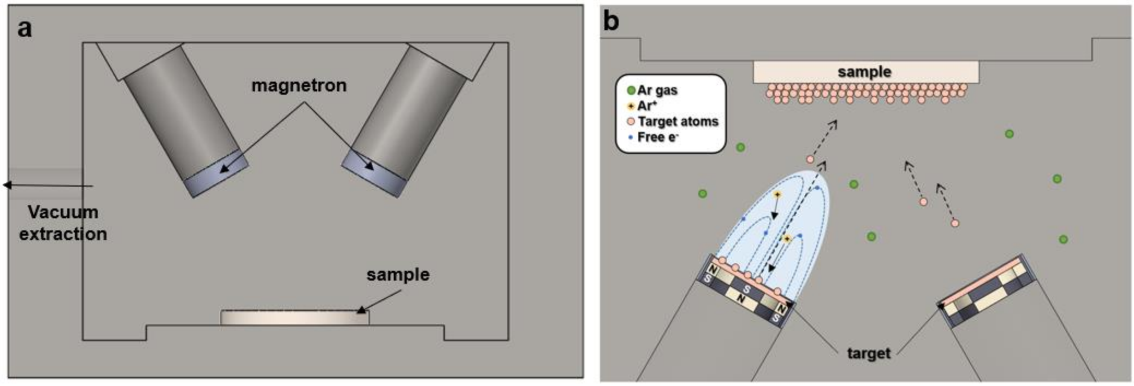

Figure 4.5. Sputtering technique. (a) Setup view; (b) detailed view of the sputter deposition on flat supports.

In this thesis, conventional sputtering system was adapted to be able to deposit copper on a tubular support. For that end, the tube is rotating during the deposition using an electric motor to ensure a homogeneous deposition. Further, to improve the deposition, the sputtering was developed at room temperature and at high temperatures. The heat to achieve the desired temperature during the sputtering deposition was supplied by an electrical resistance placed in the interior of the tube beside of a thermocouple to control the temperature. Figure 4.6 shows a drawing of this setup.

Cu films were deposited with a radio frequency (13.56 MHz) Pfeiffer Classic 250 deposition system. The copper films were obtained by sputtering 1 inch Cu sputtering target with r.f. power of 25 W. The base pressure of the chamber before the deposition was $2 \cdot 10^{-6}$ mbar or lower. The working vacuum pressure was $2.1 \cdot 10^{-2}$ mbar by using pure Ar.

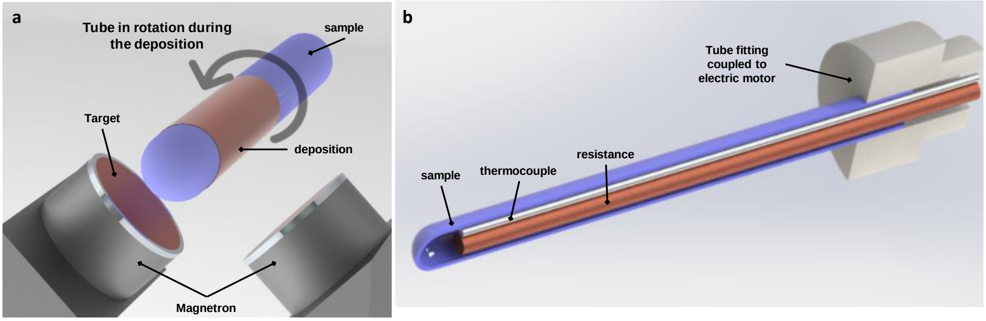
a
Tube in rotation during the deposition
sample
Target
deposition
Magnetron
b
Tube fitting coupled to electric motor
resistance
sample
thermocouple

Figure 4.6. Sputtering setup for tubular supports. (a) View of the rotating technique to deposit the layer by sputtering; (b) View of the resistance for the heating and the themocouple on the sputtering assembly to deposit copper on tubular supports.

4.2.4. Screen-printing

The deposition over flat supports was made by means of the screen-printing technique. In general, properties of final films depends on printer settings, screen options, substrate preparation and ink rheology [11]. Screen-printing inks were prepared by mixing suitable amounts of inorganic powders with a solution of ethylcellulose in terpineol (6%-wt.) and subsequently refined using a three-roller mill (Exakt) (Figure 4.7). The proportion powder-liquid (i.e. solution of ethylcellulose in terpineol (6%-wt.)) is 50%-wt. Finally, the inks were deposited on the BZCY72 disc pellets and sintering at high temperatures.

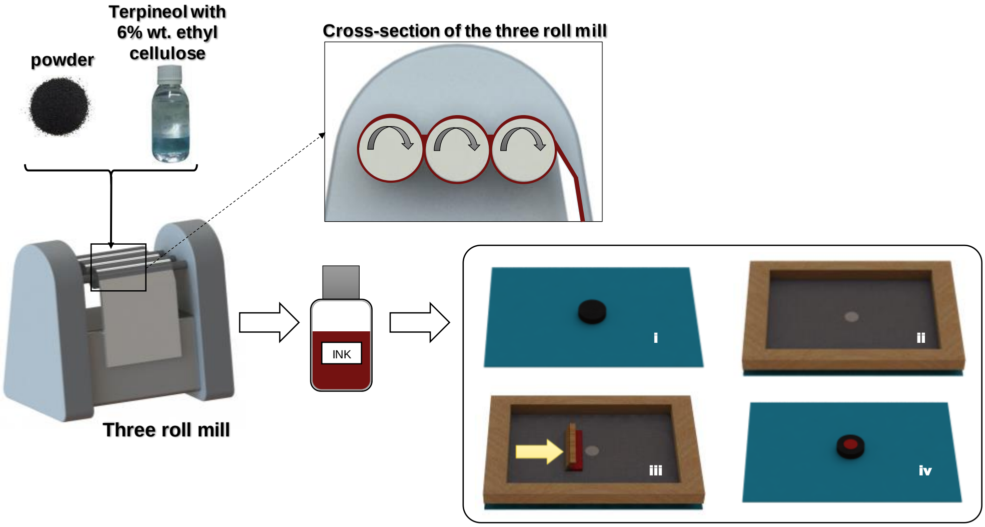
Terpineol with 6% wt. ethyl cellulose
powder
Cross-section of the three roll mill
Three roll mill
INK
i
ii
iii
iv

Figure 4.7. Screen-printing technique methodology.

4.3.Structural characterization

4.3.1. X-ray powder diffraction

X-ray diffraction (XRD) is a non-destructive technique mainly used for determining the crystalline phases and orientation of crystalline materials and material related properties such as lattice parameters, strain, crystallite size and thermal expansion.

X-ray are transverse electromagnetic radiations, similar to visible light, with shorter wavelength produced via interactions of the accelerated electrons of high energy with a heavy metal target (anode). X-ray than appears because of the hit of the electrons with this material and it is radiated in all directions.

This technique is based on the Bragg law (equation 4.1). This law says if the incident X – rays of wavelength (λ) strike a crystal where all atoms are placed in a regular periodic array with interplanar spacing d', diffraction beam of sufficient intensity is detected only when:

$$2 \cdot d' \cdot \sin\theta = n \cdot \lambda \tag{4.1}$$

where n is called the order of reflection and is equal to the number of wavelengths in the path difference between diffracted X-rays from adjacent crystal planes (see Figure 4.8).

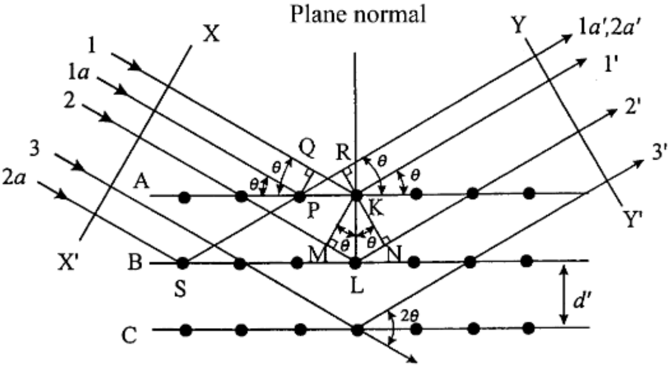

Figure 4.8. Schematic diagram of diffraction of X-rays by a crystal (Bragg condition). Image obtained from [12].

In general, the n^{th} order reflection from a certain crystal plane (h k l) with the interplanar spacing of d could be considered the first-order reflection from a plane (nh nk nl). Since the (nh nk nl) plane is parallel to the (h k l) plane, reflection from (nh nk nl) plane is equivalent to the first order reflection from planes spaced at the distance ($d = d'/n$). From such a point of view, 2θ is called the diffraction angle in many cases.

The diffraction angle 2θ of any set of planes (h k l) can be computed by combining Bragg law equation with the plane-spacing equations that relate distance between providing the relationship among the distance of adjacent planes to Miller indices and lattice parameters for each crystal system. Therefore, information about the geometry of the crystal can be obtained from the diffraction of X-ray. (Table 4.3)

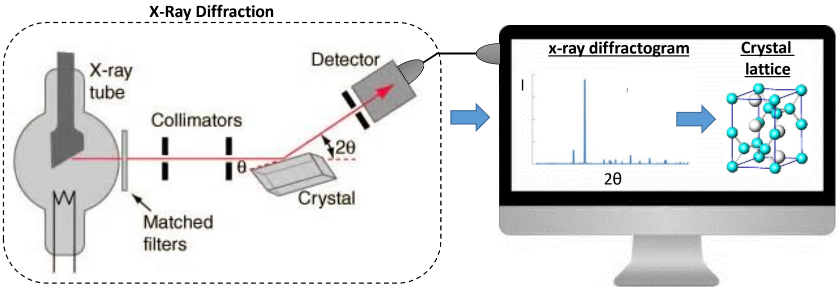

Figure 4.9. X-ray diffraction setup: from diffractometer until crystal structure.

In a diffraction testing, an incident wave is directed into a material and a detector is typically moved about to record the directions and intensities of the outgoing diffracted waves. Therefore, considering each crystal structure and chemical composition causes their singular patterns, comparing the results with the database it is possible to determine the composition and crystal structure (Figure 4.9).

The measurements developed during the present thesis were carried out by a Cubix fast diffractometer, using $CuK\alpha_{1,2}$ radiation (λ_1=1.5406 Å) and an X'Celerator detector in Bragg-Brentano geometry. XRD patterns were recorded in the 2θ range from 2° to 90° and analyzed using X'Pert Highscore Plus software.

Table 4.3. The fourteen Bravais lattices. From [12].

System	Lengths and angles	Geometries			
		Primitive	Body-centered	Face-centered	Side-centered
Cubic	$a = b = c$ $\alpha = \beta = \gamma = 90°$	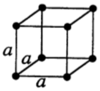	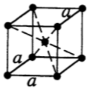	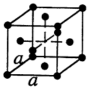	
Tetragonal	$a = b \neq c$ $\alpha = \beta = \gamma = 90°$	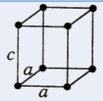	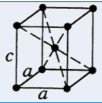		
Orthorombic	$a \neq b \neq c$ $\alpha = \beta = \gamma = 90°$	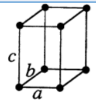	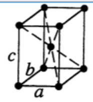	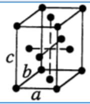	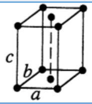
Hexagonal	$a = b \neq c$ $\alpha = \beta = 90°$ $\gamma = 120°$	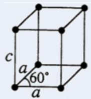			
Monoclinic	$a \neq b \neq c$ $\alpha = \gamma = 90°$ $\beta \neq 120°$	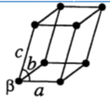	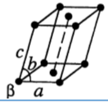		
Triclinic	$a \neq b \neq c$ $\alpha \neq \beta \neq \gamma \neq 90°$	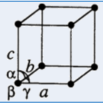			
Trigonal	$a = b = c$ $\alpha = \beta = \gamma = 90°$	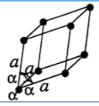			

4.3.2. Scanning electron microscope

The scanning electron microscope (SEM) is one of the most versatile instruments available for the examination and analysis of the microstructure morphology and chemical composition characterizations. SEM uses a focused beam of high-energy electrons to generate a variety of signals at the surface of solid specimens. The signals that derive from electron-sample interactions reveal information about the sample including external morphology (texture), chemical composition, and crystalline structure and orientation of materials making up the sample. In most applications, data are collected over a selected area of the surface of the sample, and a 2-dimensional image is generated that displays spatial variations in these properties.

A primary beam penetrates the specimen surface, it scatters as a variety of signals. The scattered electrons that escape from atoms occupying the top surface specimen, also called secondary electrons, are created by inelastic collisions. The back scattered electrons are scattered from deeper levels and are generated by multiple elastic collisions. Secondary electrons and backscattered electrons are usually used for imaging samples. Whereas secondary electrons are most valuable for showing topography and morphology of samples, back scattered electrons are most common to use it for drawing contrasts in composition in multiphase samples. X-ray is produced by inelastic collisions of the incident electrons with the electrons in the orbitals of the sample. Thus, the X-ray generated depends on the excited element by the electron beam. The X-ray can be used to determine the compositions of the sample, since is well-known the energetic levels of electrons in different shells for a certain element.

The SEM is also capable of performing analyses of selected point locations on the sample; this approach is especially useful in qualitatively or semi-quantitatively determining chemical compositions (using EDS), crystalline structure, and crystal orientations (using EBSD). The design and function of the SEM is very similar to the EPMA and considerable overlap in capabilities exists between the two instruments.

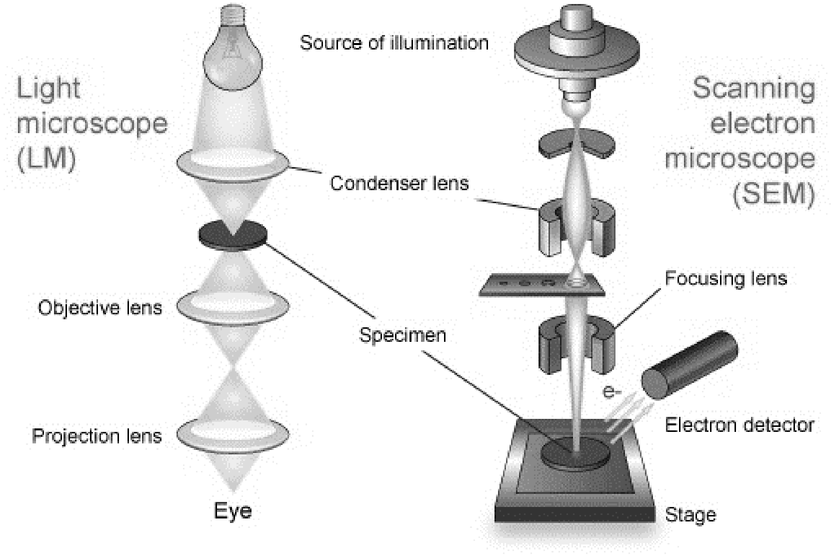
Source of illumination
Light microscope (LM)
Scanning electron microscope (SEM)
Condenser lens
Focusing lens
Objective lens
Specimen
e-
Electron detector
Projection lens
Eye
Stage

Figure 4.10. SEM device description. Image from [13].

The SEM used in the present thesis was a JEOL JSM6300 electron microscope.

4.3.3. Field emission scanning electron microscope

Field emission scanning electron microscope (FESEM) is a special type of SEM with uses different emitter. SEM devices uses thermoionic emitters where an electrical current heats up a filament. When the heat is enough to overcome the work function of the filament material, the electrons can escape from the material itself. Thermionic sources have relative low brightness, evaporation of cathode material and thermal drift during operation. FESEM uses field emission gun also called a cold cathode field emitter, does not heat the filament. The emission is reached by placing the filament in a large electrical potential gradient.

FESEM produces clearer images, less electrostatic distortions than SEM and spatial resolutions < 2 nm.

The FESEM used in the present thesis was a ZEISS Ultra55.

4.4. Chemical characterization

4.4.1. Inductively Coupled Plasma Optical Emission Spectroscopy (ICP-OES)

The Na content in the CuO obtained by coprecipitation (see section 4.1.3) were checked and determined by ICP-OES on a Varian 715-ES. The solid samples in powder (30 mg) were dispersed in a volumetric mixture of HNO_3:HF:HCl, 1:1:3 (vol. ratio). In all cases, the calibration curve was adjusted to the expected analyte concentration and was determined using ICP standard solutions (Aldrich).

4.5. Electrochemical characterization

4.5.1. Electrochemical Impedance Spectroscopy (EIS)

The copper-based materials developed on this thesis have their final application as electrodes for protonic conductor membrane reactors at high temperature. Therefore, their electrochemical behavior has to be analyzed.

The emphasis in electrochemistry has shifted from a time/concentration dependency to frequency-related phenomena because the electrochemistry in solid-based setups is controlled by the triple phase contacts between gas, electrode and electrolyte also called Triple Phase Boundary (TPB). Electrical double layers and their inherent capacities reactances are characterized by their relaxation times, or more realistically by the distribution of their relaxation times. The electrical response of the heterogeneous cell can vary substantially depending on the species of charge present, the microstructure of the electrolyte and the texture and nature of electrodes [14].

Electrochemical impedance spectroscopy is used to evaluate electrical properties of materials and their interfaces with surface-modified electrodes. It may be used to investigate the dynamics of the bound or mobile charge in the bulk or interfacial regions of any kind of solid or liquid material: ionic, semiconducting, mixed electronic-ionic, and even insulators (dielectrics) [14].

Standard impedance spectroscopy tests measure directly in the frequency domain by applying a single-frequency voltage to the interface and measuring the phase shift and amplitude, or real and imaginary parts, of the resulting current at that frequencies. Any intrinsic property that influences the conductivity of an electrode–materials system, or an external stimulus, can be studied by EIS. The parameters derived from an EIS spectrum fall generally into two categories:

a) those pertinent only to the material itself: conductivity, dielectric constant, mobilities of charges, equilibrium concentrations of the charged species, and bulk generation–recombination rates
b) those pertinent to an electrode–material interface: adsorption–reaction rate constants, capacitance of the interface region, and diffusion coefficient of neutral species in the electrode itself.

Therefore, a monochromatic signal of potential *v(t)* (equation 4.2), involving the single frequency (f) ($\omega = 2\pi f$), is applied to the cell and the resulting steady state current measured *i(t)* (equation 4.3).

$$v(t) = V_m \cdot \sin(\omega t) \tag{4.2}$$

$$i(t) = I_m \cdot \sin\,(\omega t + \theta) \tag{4.3}$$

Here, θ is the phase difference between the voltage and the current (zero for pure resistive behavior). The relation between system properties and response to periodic voltage or current excitation is very complex in the time domain. In general, the solutions of a system of differential equations is required. Response of capacitive and inductive elements is given (equations 4.4 and 4.5, respectively), with C and L correspondingly, and combinations of many such elements can produce an intractable complex problem.

$$i(t) = \left[\frac{dv(t)}{dt}\right] C \tag{4.4}$$

$$v(t) = \left[\frac{di(t)}{dt}\right] L \tag{4.5}$$

Fourier transformation allows to become these complex differential expressions in a simpler system and defining the impedance (Z) as a complex function (equation 4.6). Here, it is critical to can assume the linearity between the voltage and the current to carry out this analysis [14].

$$Z(\omega) = \frac{V}{I} = \frac{V_m \cdot \sin\,(\omega t)}{I_m \cdot \sin\,(\omega t + \theta)} = Z_0 \cdot \exp(j\theta) = Z' + Z''j \tag{4.6}$$

Where *Z'* and *Z''* are the real and complex contributions of the impedance, respectively and $j = \sqrt{-1}$. In general, Z is frequency-dependent, as defined above. Conventional EIS consists of the (nowadays often automated) measurement of Z as a function of n or ω over a wide frequency range. It is from the resulting structure of the $Z(\omega)$ vs. ω response that one derives information about the electrical properties of the full electrode–material system [14].

For nonlinear systems, i.e. most real electrode–material systems, EIS measurements are useful and meaningful in general only for signals of magnitude such that the overall electrode–material system response is electrically linear. This requires that the response to the sum of two separate input-measuring signals applied simultaneously be the sum of the responses of the signals applied separately. Therefore, the application of a monochromatic signal, one involving sin(ωt), results in no generation of harmonics in the output (or at least negligible), that is components with frequencies nv for n = 2, 3, … Electrochemical systems tend to show strong nonlinear behavior, especially in their interfacial response, when applied voltages or currents are large. But so long as the applied potential difference amplitude V_m is less than the thermal voltage, $V_T = \frac{R \cdot T}{F} = \frac{k_b \cdot T}{p}$, about 83 mV at 700 °C, it can be shown that the basic differential equations which govern the response of the system become linear to an excellent approximation. Here k_b is Boltzmann’s constant, T the absolute temperature, p the proton charge, R the gas constant, and F the faraday constant. Thus, if the applied amplitude V_m is appreciably less than V_T, the system will respond linearly. Note that in the linear regime it is irrelevant as far as the determination of $Z(\omega)$ is concerned whether a known $v(\omega t)$ is applied and the current measured or a known $i(\omega t)$ applied and the resulting voltage across the cell measured. When the system is nonlinear, this reciprocity no longer holds. Additionally, the applied potential difference amplitude V_m must be enough to avoid that the signal is on the range of white noise.

EIS can contribute to the interpretation of fundamental electrochemical and electronic processes. Table 4.4 shows briefly the advantages and limitations of this technique.

Table 4.4. Advantages and limitations for the EIS [14].

Advantages	Limitations
Readily automated	Possible ambiguities in interpretation
Easy correlation between electrical response and process variables (mass transport, reaction rates, corrosion, and dielectric properties, to defects, microstructure, and compositional influences on the conductance of solids)	Several options for the equivalent circuit (even infinites)
Characterization of sensors and fuel cells	

Finally, EIS technique introduces an AC voltage (or current) and recover the response of the system in the respective AC current (or voltage). Figure 4.11 shows the typical results when an AC voltage is introduced with the different diagram and plots for obtaining the information of the electrochemical processes.

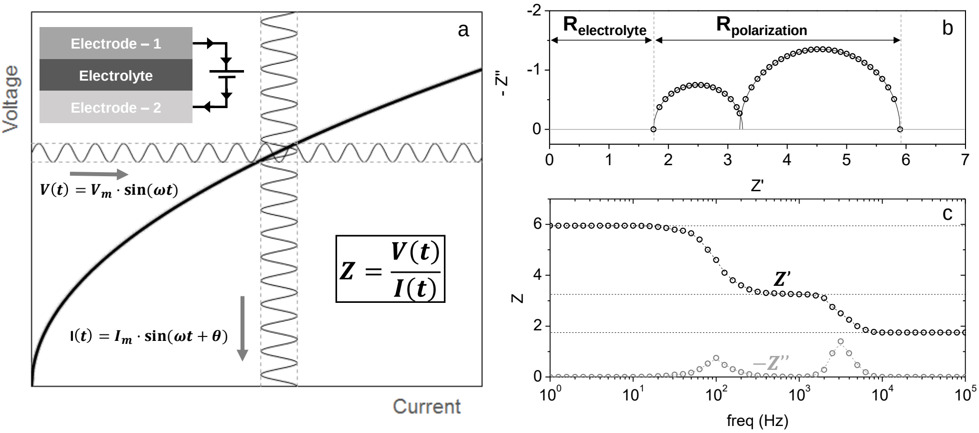

Figure 4.11. Impedance spectroscopy applied to an electrochemical setup. (a) Description of the general response of the system; (b) Nyquist plot of the impedance; (c) Bode plots for the real contribution of the impedance (Z') and the imaginary contribution of the impedance (Z'').

The different reactions occurred in the cell take place at different velocities. As EIS makes the analysis in the complex plane using different frequencies is possible to separate the different processes and to analyze them separately.

Solartron 1470E was used for obtaining the data, generating the sinusoidal current/voltage signals. 1455A module was connected for the frequency analysis (*frequency response analyzer*, or FRA). The electric connections are presented in the Figure 4.12. The connections from the Solartron modules consist of two couples of cables as measuring terminal: a couple that transports the current (+ CE and – WE) and the other couple for measuring the voltage (+ Re1 and + Re2 of reference ones). These terminals are connected to the electrodes by means of copper wires. Each current terminal is connected with the respective reference terminal in the electrode to remove possible contributions in the response of impedance of the terminals and wires. Finally, the electrochemical impedance spectroscopy tests were developed with 20 mV of amplitude in the frequency range of 30 mHZ until 1 GHz.

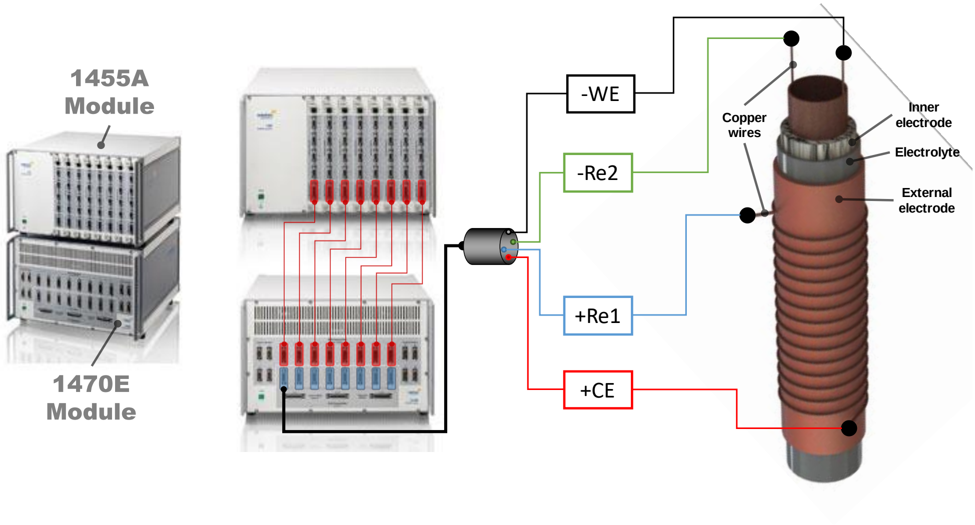

Figure 4.12. Connection of the Solartron modules with the sample.

The diagram of the experimental setup is shown in the Figure 4.13. Gas flows and composition are regulated using the flowmeters for hydrogen, argon and methane. Moist conditions were achieved using a gas bubbler at room temperature where the inlet gas takes water until the saturation conditions (~ 4 – 5 % of steam content). Ar line is connected with a by-pass system to remove the air of all lines before to the start. The reactor is heated using an electric furnace controlled using a thermocouple placed between the reactor and the furnace. An additional thermocouple was placed close of the sample to ensure the temperature in the tube is desired. Both wires and the thermocouple placed close of the sample are introduced in the reactor using alumina multibores ensuring thermocouple was not connected with the electric wires.

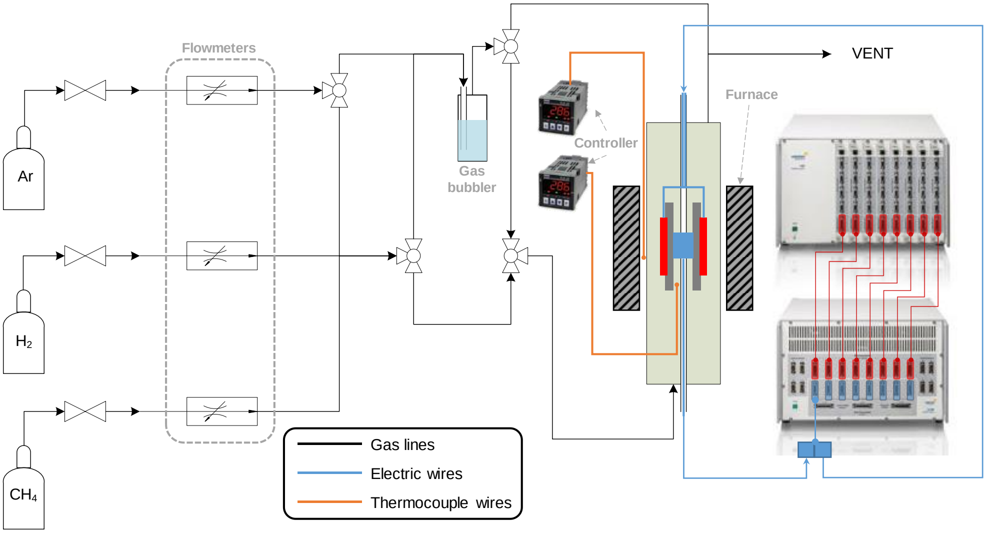

Figure 4.13. Diagram of the experimental setup to make electrochemical impedance spectroscopy tests.

4.6.References

1. Sakka, S., *Chapter 11.1.2 - Sol–Gel Process and Applications A2 - Somiya, Shigeyuki*, in *Handbook of Advanced Ceramics (Second Edition)*. 2013, Academic Press: Oxford. p. 883-910.
2. E.Smart, L. and E. A.Moore, *Solid state chemistry: an introduction. Third Edition*. 2005.

3. Schubert, U., *Chemistry and Fundamentals of the Sol–Gel Process*, in *The Sol-Gel Handbook*. 2015, Wiley-VCH Verlag GmbH & Co. KGaA. p. 1-28.
4. Rao, C.N.R. and K. Biswas, *Essentials of Inorganic Materials Synthesis*. 2015, New York, UNITED STATES: John Wiley & Sons, Incorporated.
5. Ecija, A., et al., *Synthetic methods for perovskite materials – structure and morphology*. Vol. 19. 2012. 485-505.
6. *Perovskite Oxide for Solid Oxide Fuel Cells*. 2009: Springer.
7. Cotler, V.F., *Nanopowders and Nanocoatings: Production, Properties and Applications*. 2010, Hauppauge, UNITED STATES: Nova Science Publishers, Inc.
8. Lok, M., *Coprecipitation*, in *Synthesis of Solid Catalysts*. 2009, Wiley-VCH Verlag GmbH & Co. KGaA. p. 135-51.
9. Guglielmi, M., *Glass: Sol–Gel Coatings A2 - Buschow, K.H. Jürgen*, in *Encyclopedia of Materials: Science and Technology (Second Edition)*, R.W. Cahn, et al., Editors. 2001, Elsevier: Oxford. p. 3575-9.
10. Seshan, K., *Handbook of Thin-Film Deposition. Processes and Techniques. Second Edition*, ed. M.C.o.N.C. Gary E. McGuire, et al. 2002.
11. Somalu, M.R., et al., Renewable and Sustainable Energy Reviews, 2017. **75**(Supplement C): p. 426-39.
12. Waseda, Y., et al., *X-Ray Diffraction Crystallography. Introduction, Examples and Solved Problems*. 2011: Springer.
13. *Australian Microscopy & Microanalysis Research Facility*. [cited 2018; Available from: http://www.ammrf.org.au/myscope/sem/background/#detail.
14. Barsoukov, E. and J.R. Macdonald, *Impedance Spectroscopy : Theory, Experiment, and Applications*. 2005, Hoboken, UNITED STATES: John Wiley & Sons, Incorporated.

5. DIP-COATING METHOD TO DEVELOP COPPER BASED ANODES FOR HIGH TEMPERATURE MEMBRANE REACTORS

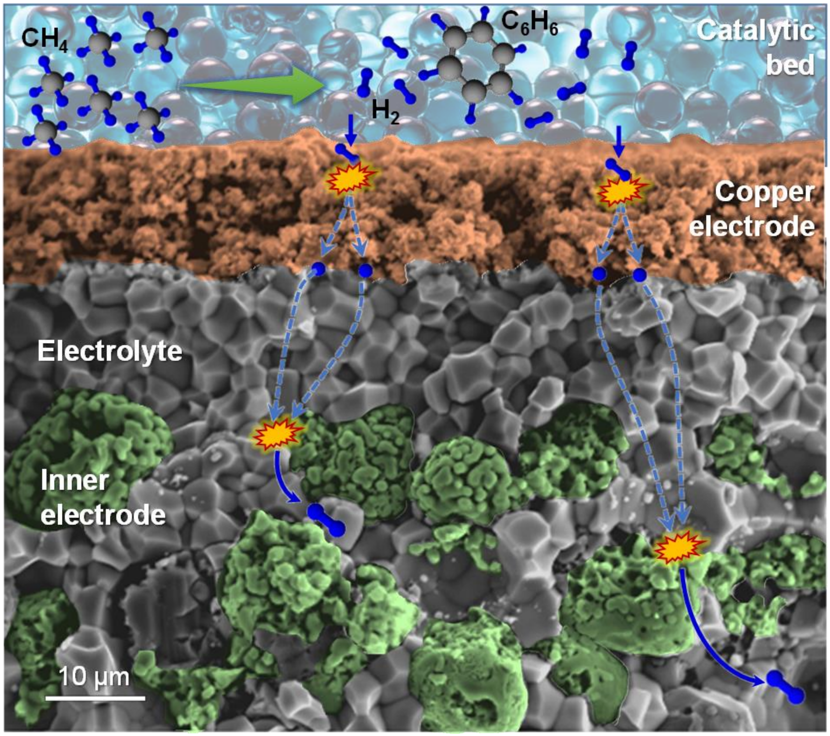
CH_4
C_6H_6
Catalytic bed
H_2
Copper electrode
Electrolyte
Inner electrode
10 µm

5.1.Introduction

In the last years, the development of high-temperature ceramic ionic conductors has experienced notable advances in the fields of fuel cells, electrolysis and electrochemical membrane reactors. Solid oxide fuel or electrolysis cells (SOFC and SOEC) offer better power and efficiencies than conventional low temperature electrochemical cells [1]. The last advances in the electrolyte materials for SOFC applications allow operating at intermediate temperatures (500 – 800 °C) with suitable conductivity response [2]. The operation temperature for the electrochemical cell will depend to a large extent on the application [2].

High temperature proton conducting materials [3] have a high potential as electrochemical membrane reactors for selective hydrogen separation. Thermodynamic analysis show that SOFCs based on proton conducting electrolytes may have essential advantages compared to SOFCs based on oxygen-ion conductors, regarding the efficiency of the transformation of chemically stored energy to electrical energy [4-6]. Additionally, proton conducting materials are able to work at lower temperatures (400 – 800°C) than oxygen-ion conducting materials. The benefits of using proton conductors in high temperature electrochemical membrane reactors have been demonstrated in different catalytic processes such as methane dehydroaromatization to produce benzene, methane steam reforming or ammonia synthesis [7-10].

Most of the anodes for protonic based SOFC devices are mixtures of NiO and the electrolyte material [10-13]. However, Ni electrodes tend to coke under hydrocarbon-rich non-oxidative operation leading to extensive coke formation which is the cause of deactivation for catalyst-based and electrochemical processes [12]. In order to find suitable alternatives for nickel electrodes for membrane reactors must accomplish certain series of conditions that depend on the process. In general, anodes materials need to (i) fulfill high electrical conductivity; (ii) suitable thermal expansion coefficient; (iii) no coke formation; (iv) low particle size (in the nanometer range); (v) no chemical interactions with electrolyte material; (vi) large triple-phase boundary length, i.e. surface area for the gas-solid reaction (vii); proper porosity for fast gas transport; and (viii) good ionic conductivity [14]. Due to this large list of requirements, only few alternatives to Ni have been reported for protonic high temperature electrochemical cells so far. For instance, the overpotentials of the Pd-loaded FeO anode and the $Ba_{0.5}Pr_{0.5}CoO_3$ cathode at 600 °C were less than one-fourth those of a Pt electrode [15].

To develop protonic high temperature electrochemical cells fed with hydrocarbon fuels, the use of Fe or Cu as anode materials may represent other valid alternative to Ni-based anodes, due to the reduced coke formation [11]. Here, metallic copper is one of the most promising materials as does not catalyze carbon formation, is stable at typical SOFC non-oxidant conditions and does not catalyze hydrocarbon oxidation at intermediate temperatures that could cause diffusion problems [16]. One of the disadvantages of Cu is its low melting point (1083 °C) as compared to Ni (1453 °C), implying that Cu electrodes may lose porosity under operation at high temperature. Process temperatures above 800 °C are not recommended with regard to coarsening and sintering of Cu particle [16]. Considering the melting temperatures of CuO (1201 °C) and Cu_2O (1235 °C), conventional firing procedures are not applicable for the manufacture of Cu-based electrodes. Copper has already been used as anode for electrochemical membrane reactors in previous works [7, 8]. Finally, layers of Cu-Pd were deposited using sputtering on disc pellets for hydrogen permeation assemblies [17].

In this work, Cu-based cermet has been deposited on tubular proton conducting electrochemical cells using dip-coating technique to reach well-attached electrodes. This study involves different tubular supports to find a robust methodology to achieve a suitable external copper-based layers.

5.2.Results

5.2.1. Characterization of synthesized materials

Synthesis of CuO

CuO was obtained by coprecipitation methodology (details in chapter 4). The obtained powders were characterized by XRD, ICP and SEM. The single phase CuO can be observed in the Figure 5.1 for different sintering temperatures. ICP analysis revealed the final powder is free of Na presence (from NaOH used to precipitate the copper nitrate).

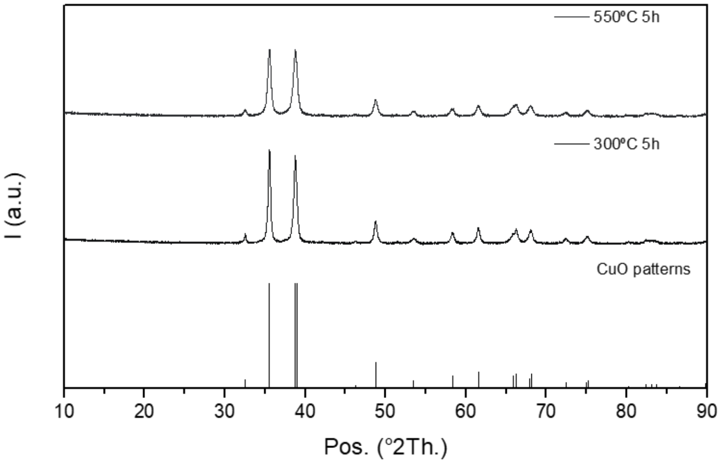

Figure 5.1. XDR patterns of coprecipitated CuO at different temperatures.

However, considering the microstructure, the precipitation methodology can affect significantly to the CuO particles. The difference observed in the Figure 5.2 between the types of CuO microparticles obtained comes from the NaOH concentration: for high NaOH concentrations, the CuO obtained forms needles (Figure 5.2a) while if the NaOH concentrations have lower concentrations than 2M, the CuO obtained presents spherical particles (Figure 5.2b). Considering spherical particles with similar sizes than BZCY is requested, the NaOH concentration used has to be lower than 2M. Consequently, using solutions with lower concentrations increases the volume of solution needed to precipitate all the copper and the water necessary for the filtration.

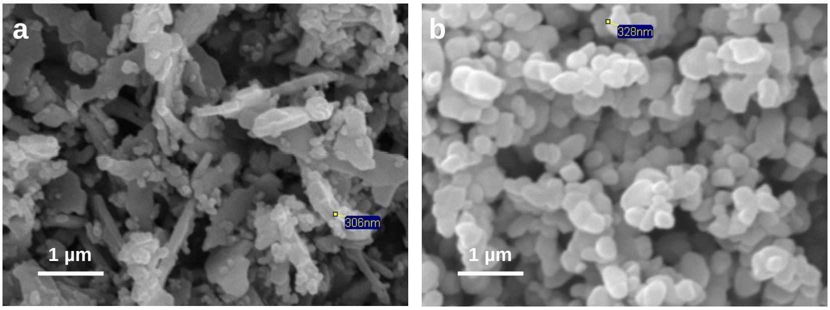

Figure 5.2. (a) CuO from coprecipitation with NaOH solutions > 2 M; (b) CuO from coprecipitation with NaOH solutions 2 M

Finally, Figure 5.3 shows that CuO particle size (precipitated using 2M NaOH solutions) increases when the sintering temperature increases, especially when the sintering temperature increase above 700°C.

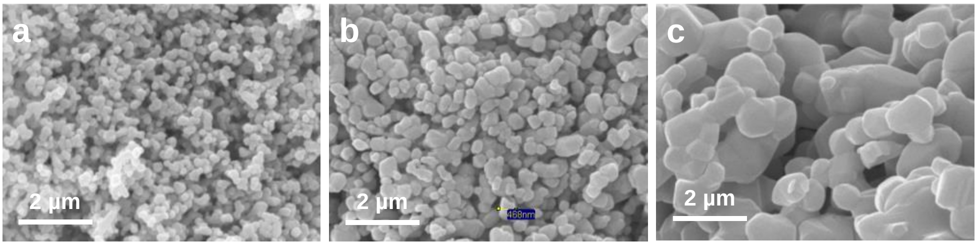

Figure 5.3. CuO sintered at 600 °C (a), 700 °C (b) and 800 °C (c).

Synthesis of BZCY

The BZCY powder obtained by Solid State Reaction (SSR) method, was characterized by XRD. As can be ascribed from the XRD patterns (Figure 5.4), a single phase is obtained when the synthesized powder is sintered first at 1550ºC 15 hours (Figure 5.2 black) and when the synthesized powder is sintered at 1600ºC 10 hours (Figure 5.2 gray).

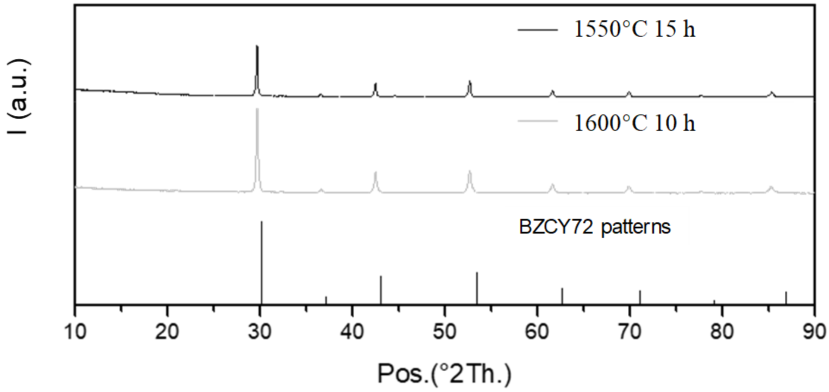

Figure 5.4. XDR patterns of BZCY72 single phase. Black: SSR sintering at 1550ºC 15h; gray: SSR sintering at 1600ºC 10h; black patterns: BCZY27 patterns.

5.2.2. Optimization of the dip-coating methodology

CuO particles plays a critical role in the final electrode and, therefore, the geometry of the initial CuO must be spherical and similar to the BZCY to ensure the optimal distribution of the particles in the cermet. BZCY was sintered at higher temperatures than the cermet sintering step and, therefore, it was expected the annealing slightly affects to the size of the BZCY size. CuO particles were sintered at lower temperatures and, thus, the sintering step of the cermet causes significant changes in the size of the copper particles.

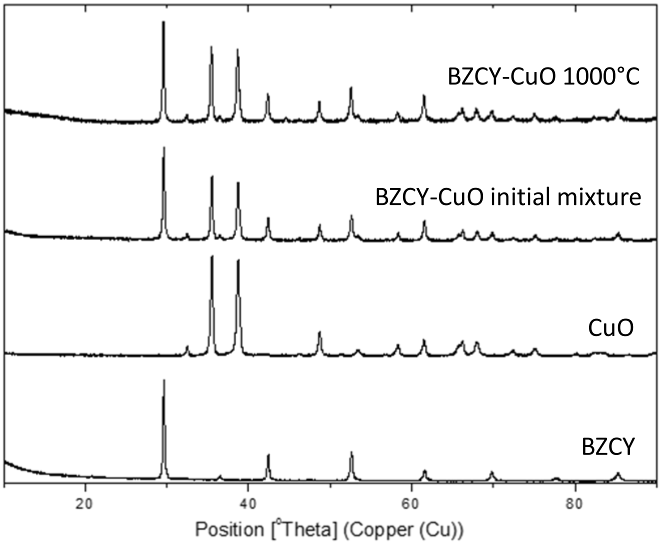

Figure 5.5. XDR patterns of the different sintered phases. BZCY72: sintering at 1550 °C; CuO: sintering at 550 °C; BZCY-CuO: mixture before the sintering; BZCY-CuO final: sintering at 1000 °C 2 hours.

Figure 5.5 shows the XRD patterns of the sintered BZCY powders, CuO powders, the initial CuO–BZCY powder mixture and CuO-BZCY final sintered cermet. These results show that there are no additional peaks in the final sintered cermet as compared with the initial mixture or the initial powders of BZCY and CuO. Therefore, the sintering step at 1000 °C 2 hours does not cause reactivity between the different compounds of the cermet. This is in agreement with Patki et. al. which did not observe interactions between Cu and BCZY in their study of copper deposition on this kind of tubes using electroless plating methodology [18].

However, considering a more aggressive final sintering step of the CuO-BZCY mixture, in this case at 1050 °C 5 hours, the final XDR patterns shows the presence of $BaCeO_3$ (Figure 5.6). Therefore, the sintering step have to carry out at temperatures below 1050 °C and with shorter times.

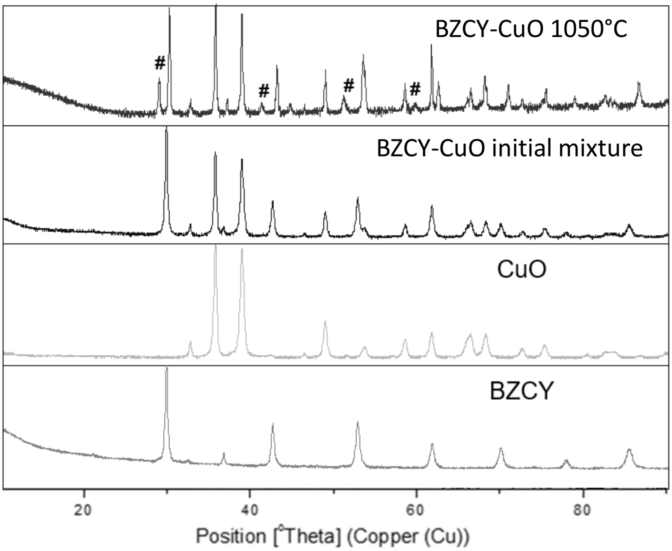

Figure 5.6. XDR patterns of the different sintered phases. BZCY72: sintering at 1550 °C; CuO: sintering at 550 °C; BZCY-CuO: mixture before the sintering; BZCY-CuO final: sintering at 1050 °C 5h. #: $BaCeO_3$ peaks.

The conditions of the pre-sintering of the copper oxide were controlled to achieve similar distribution and sizes as the BZCY initial. The size particle distribution of the co-precipitated CuO (blue, red and green boxplots), the initial BZCY72 (grey band) and the CuO particles of the final sintering cermet (grey boxplot) are presented in Figure 5.7 as a function of the sintering temperature (of CuO powder and dipped tube). The temperature of the sintering of the co-precipitated CuO leads to the gradual grain growth from 200 – 300 nm at 600 °C until 500 – 1500 nm at 800 °C. The pre-sintering temperature of the CuO was fixed between

550 and 600 °C to achieve similar size distribution to the initial BZCY72. The distribution of CuO oxide particles in the composite after final sintering at 1000 °C ranges 1.75 – 3.5 µm.

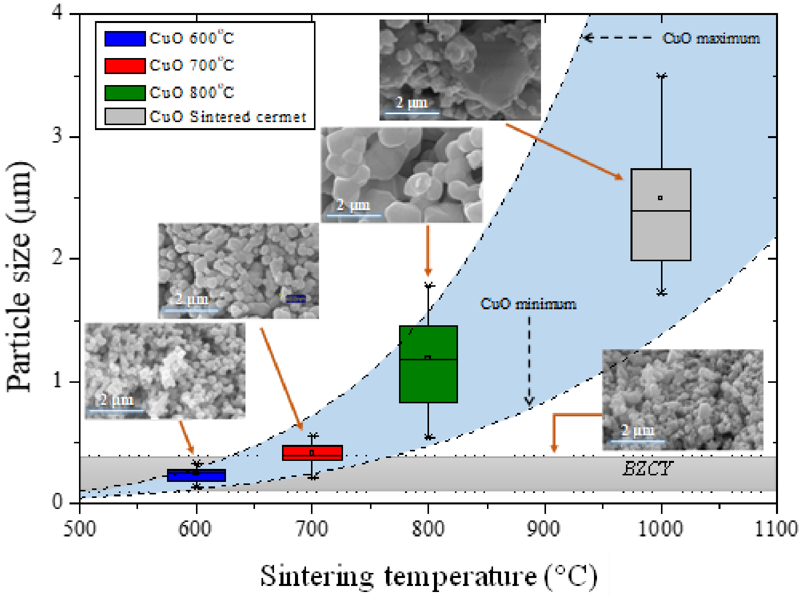

Figure 5.7. Size particle distribution of the sintered phases (CuO and final sintering cermet) with the SEM images. Each size distribution is shown using boxplots. Images was acquired at 25 kV

Figure 5.8 shows SEM images of the electrodes-electrolyte interfaces and electrodes overviews in both as-sintered and reduced state of a tube that was dipped once using a slurry with ethylcellulose. The dipped tube was sintered at 1000 °C for 2 h and reduced at 700 °C in H_2. CuO or Cu grains, for as sintered or reduced electrodes, respectively, are much bigger than those of BZCY72. The sintering process (Figure 5.8a and c) induced the CuO particles growth (see also Figure 5.7) from 250 – 400 nm initial until 2 – 3.5 µm. As was expected, the reduction of the electrode slightly decreases Cu particle size (Figure 5.8b and d), but they are still much larger than BZCY72 particles (Cu particles of 1.5–2.5 µm). It can also be inferred that both sintering and reduction processes do not affect the BZCY72 particle size, ranging 250 – 400 nm in both cases.

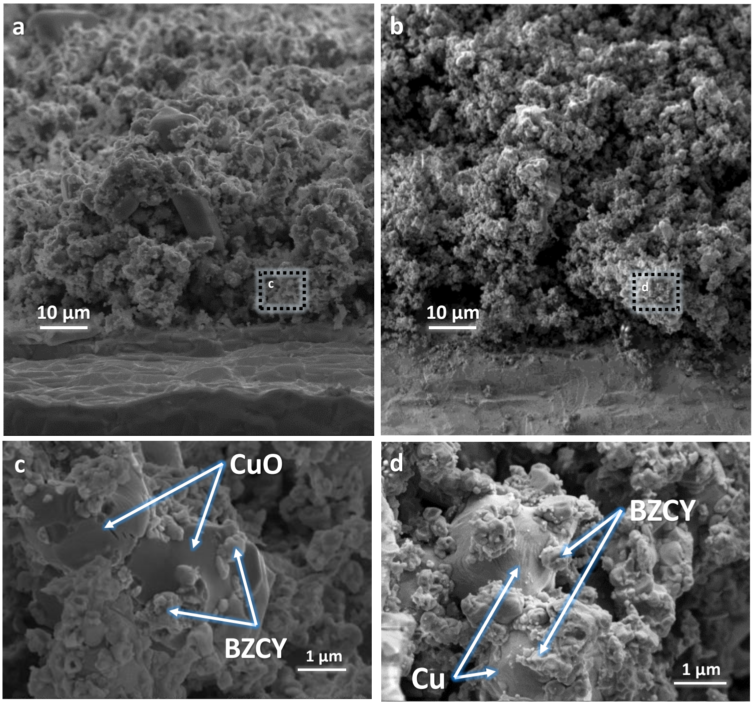

Figure 5.8. FESEM micrograph of cermet CuO/Cu– BZCY27: (a) as sintered electrode at 1000 °C in air (Image acquired at 5.00 kV); (b) as-sintered electrode at 1000 °C in air (Image acquired at 20.00 kV); (c) as-sintered electrode at 1000 °C in air (Image acquired at 3.00 kV); (b) reduced electrode at 700 °C in H_2 (Image acquired at 3.00 kV).

Several options were studied in order to reduce the copper particle size in the electrode. The size of the initial BZCY72 was varied to attempt blocking the growing of CuO particles during the sintering step in the reduced cermet electrode. With that purpose, three batches of BZCY were obtained changing the milling times of the BZCY sintered. Figure 5.9 shows images of the reduced electrodes with different BZCY72 initial particle sizes. The size of the initial BZCY does not affect to the copper particle sizes in the final sintered (or reduced) electrode.

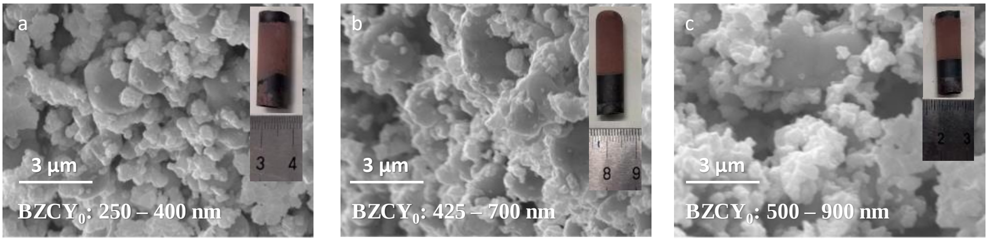

Figure 5.9. Reduced cermet on tubes using different BZCY initial particle sizes. Sintering at 1000ºC 2h and reduced at 700ºC in H$_2$. BZCY initial particle sizes: (a) 250-400 nm; (b) 425-700nm; (c) 500-900 nm.

The effect of the sintering time (at 1000 °C) on the microstructure of the copper layer is presented in Figure 5.10. In these images, copper particle size does not seem to be affected by the increase in the sintering time. That means that the growing of the CuO during the sintering steps occurs relatively fast.

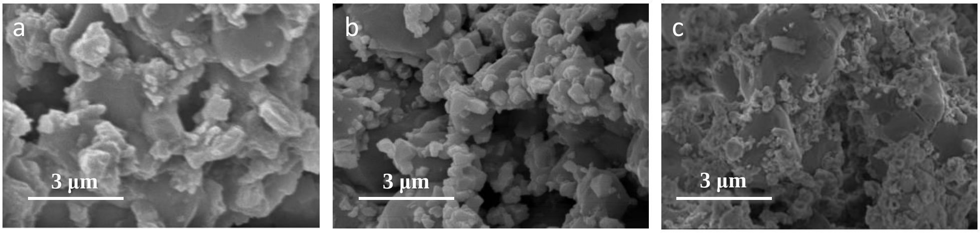

Figure 5.10. Sintering cermet on tubes sintering at 1000ºC with different times. (a) 1h; (b) 2h; (c) 4h.

5.2.3. Effect of the sintering process in the cermet microstructure

The procedure was refined in order to find the best conditions to deposit the layer by dip-coating technique. Figure 5.11 shows SEM images of electrode-electrolyte interfaces for reduced electrodes for different sintering temperatures. The copper electrode sintered at temperatures from 1000 (but lower than 1025°C) has larger copper particles and lower overall cermet porosity compared with electrodes sintered at temperatures lower than 1000 °C. Sintering at higher temperatures improves the adhesion and necking between the Cu and BZCY72 particles.

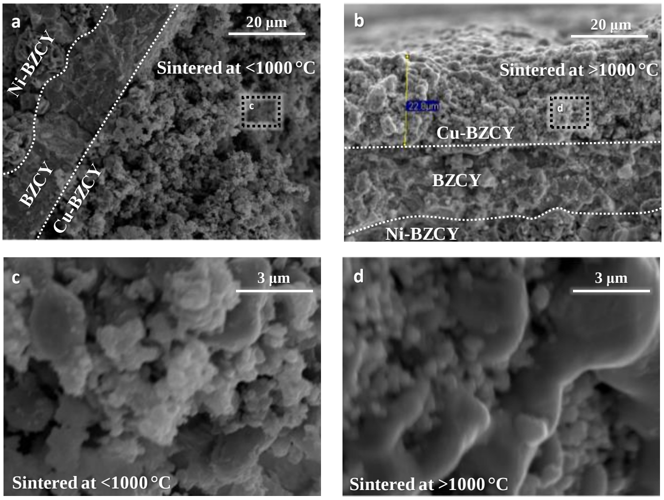
a
20 µm
Sintered at <1000 °C
c
Ni-BZCY
BZCY
Cu-BZCY
b
20 µm
Sintered at >1000 °C
22.0µm
d
Cu-BZCY
BZCY
Ni-BZCY
c
3 µm
Sintered at <1000 °C
d
3 µm
Sintered at >1000 °C

Figure 5.11. Reduced cermet on asymmetric initially unreduced tubes. Tubes were dipped once on slurry with ethylcellulose, sintered 1 h and reduced at 700 °C in H_2. (a) cermet sintered at temperatures < 1000 °C; (b) cermet sintered at temperatures > 1000 °C. (c) zoom view cermet sintered at temperatures < 1000 °C; (d) zoom view of the cermet sintered at temperatures >1000 °C.

The observed differences between the sintered electrodes at temperatures lower and higher than 1000°C may be caused by phenomena that take place at these temperatures. The phase diagram for the Cu-Cu_2O-CuO system (Figure 5.12) as a function of temperature and oxygen partial pressure [19] reveals that sintering in air leads to the reduction of the CuO to Cu_2O between 1020 °C and 1050 °C. As a consequence, it can be hypothesized that the observed differences between the copper particles in the electrode sintered at temperatures above 1000 °C may be linked with this reduction step that further activates the grain growth.

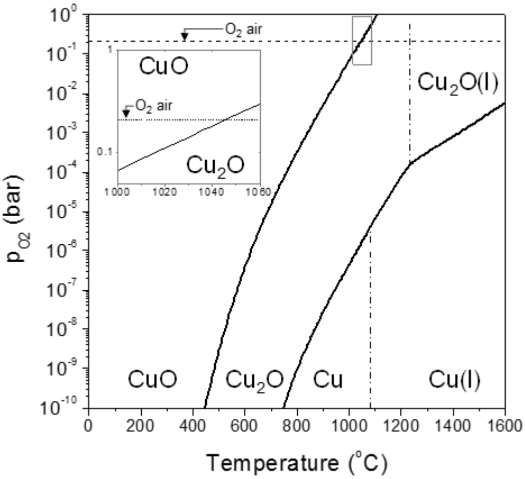

Figure 5.12. Copper oxide phase diagram [19]

Regarding the adhesion of the layer, the electrodes sintered at temperatures from 1000°C showed good adhesion to the tubes (Scotch tape test passed), while at lower temperatures, the layer adhesion is insufficient. At temperatures higher than 1025 °C the reduced electrode did not present in-plane electronic conductivity at room temperature.

At that point, after fitting the sintering conditions for stable and well-attached layer with electronic conductivity (at least, at room temperature), the microstructure of the assembly was analyzed. Figure 5.13 shows the fracture cross-section SEM image and the EDS analysis of the complete and reduced tubular electrochemical cell (internal electrode, electrolyte, external electrode). The EDS analysis shows a homogeneous Cu-BZCY layer onto the BZCY electrolyte. This electrode presents enough porosity and homogeneous particle sizes. The electrolyte, with thickness in the range of 15-20 µm, does not contain detectable amounts of copper or nickel. As can be observed, the support electrode beneath the electrolyte comprises brain-shaped nickel particle aggregates while BZCY grains presents the same microstructure as the electrolyte. Furthermore, hydrogen chemisorption analysis revealed that the nickel surface area of the internal support is 0.186 m^2/g.

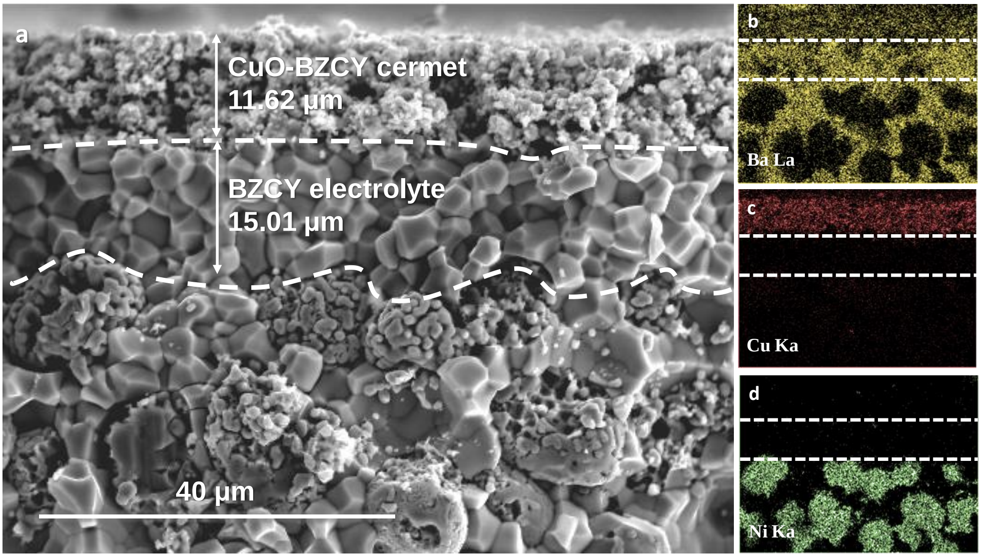

Figure 5.13: (a) Cross-section SEM image of reduced cermet on asymmetric tube initially unreduced. Sintered at 1015 °C 1h. (b–d) EDS analysis (Ba represents the BZCY).

Finally, the complete cells were characterized by impedance spectroscopy. Figure 5.14 shows the polarization resistance results under dry and wet pure hydrogen at 700 °C corresponding to copper-based electrodes sintered at different temperatures. The samples sintered at temperatures above 1000 °C present lower polarization resistances. This can be ascribed to the better copper connectivity, necking with BZCY and improved attachment to the electrolyte, despite the lower specific surface area achieved when the sintering temperature is higher than 1000 °C.

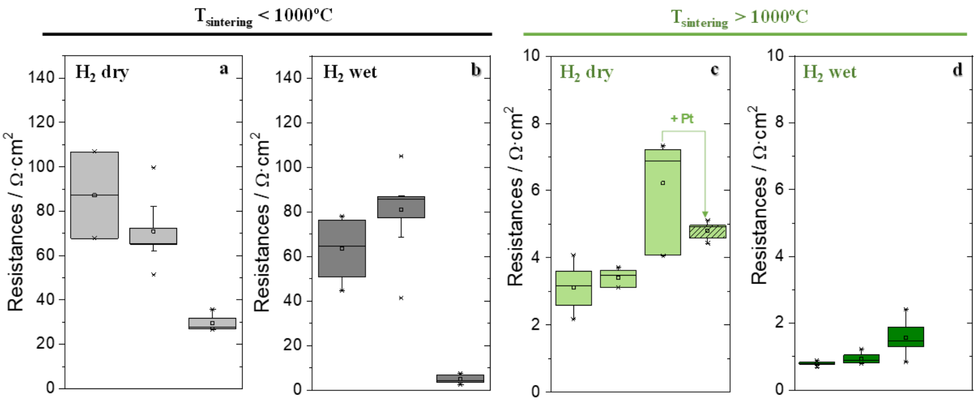

Figure 5.14. Polarization resistances at 700 °C under different conditions for copper-based cermets deposited on asymmetric initially unreduced tubes with copper electrodes sintered at temperatures < 1000 °C (a-b) and > 1000 °C (c-d). The polarization resistances distribution for each sample was plotted using boxplots.

5.2.4. Effect of the dipping conditions

The sintering conditions determines significantly the microstructure of the deposited layer. However, it may be optimized considering the dipping procedure. To further improve porosity and electrochemical performance, the dip-coating was further modified by varying the slurry composition and the number of successive coatings. Figure 5.15 shows cross-section images of two reduced electrodes with coating conditions adjusted to reach a final thickness around 20μm. There is a decrease of the thickness when the ethylcellulose was not included in the slurry composition. Ethylcellulose induces a rise of the viscosity in the slurry and, consequently, the thickness of the layer is higher. Indeed, in order to achieve similar thickness with ethylcellulose-free slurries, three sequential dipping steps were needed.

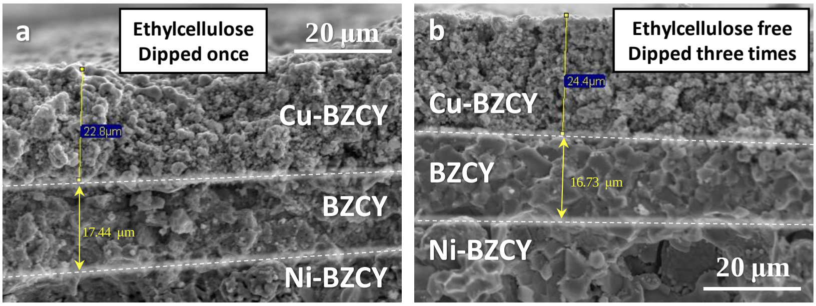
a
Ethylcellulose
Dipped once
20 µm
22.8µm
Cu-BZCY
17.44 µm
BZCY
Ni-BZCY
b
Ethylcellulose free
Dipped three times
24.4µm
Cu-BZCY
BZCY
16.73 µm
Ni-BZCY
20 µm

Figure 5.15. Cross section SEM images for reduced cermets on asymmetric tubes initially unreduced. The sintering step was developed at 1000 – 1025 °C 1h. (a) tube dipped once on slurry with ethylcellulose; (b) tube dipped three times on free-ethylcellulose slurry.

Finally, all dipped electrodes showed good adhesion to the tubes and passed the so-called ‘Scotch tape’ test. Figure 5.16 shows camera photos of the tube cells along the different preparation steps from the initial clean tube until the final reduced electrode. The asymmetric initially-unreduced tube was dipped three times using a ethylcellulose-free slurry. The electrode was sintered at 1000 °C for 1 h and reduced at 700 °C using 5% H_2 on Ar for 5 h.

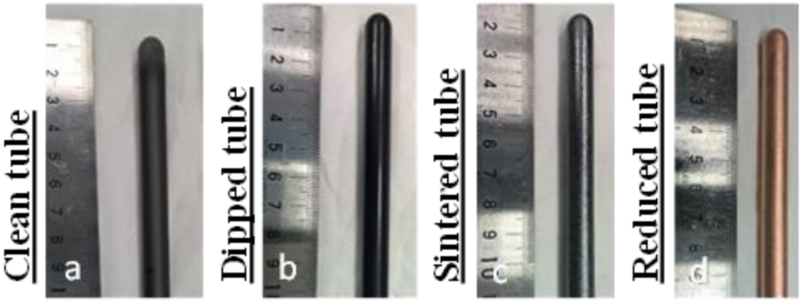

Figure 5.16. Images of the tube in the different steps across the dip-coating methodology. (a) clean asymmetric initially unreduced tube; (b) dipped tube; (c) sintered tube; (d) reduced tube).

5.2.5. Electrochemical characterization

Once the layer was deposited on the tubes, the electrochemical behavior was characterized using electrochemical impedance spectroscopy (EIS) at 700°C under H_2 based atmospheres. Figure 5.17 shows the electrochemical results of an asymmetric tube that was dipped three times using an ethylcellulose-free slurry and sintered at 1000 °C 1h in air. The ohmic contribution of the overall resistance (Figure 17a and b) at 700 °C decreases substantially under moist conditions. Additionally, fast performance recovery was observed when switching back to wet H_2 from wet CH_4 – H_2 mixtures. Higher polarization resistance values (Figure 17c and d) are reached at 700 °C under dry H_2 rather than under wet H_2 conditions while the electrode performance is recovered upon switching back to wet H_2 from wet CH_4-H_2 mixtures. Both contributions –ohmic and electrode polarization– showed stable behavior for 170 hours.

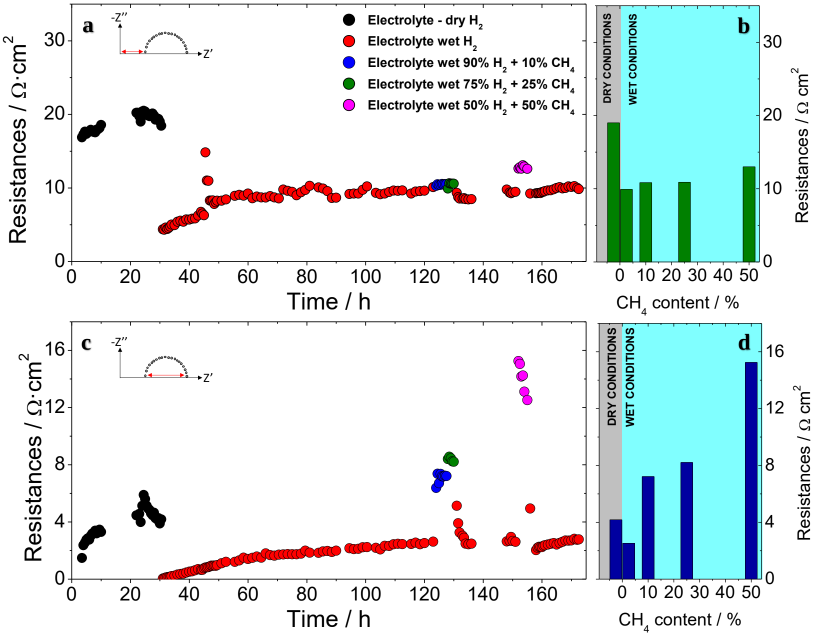

Figure 5.17. Impedance spectroscopy results at 700 °C under different atmospheres. Sample dipped three times on free-ethylcellulose slurry on an asymmetric initially unreduced tube. The electrode was sintered at 1015 °C 1h. (a and c) Ohmic contribution; (b and d) polarization resistances.

Once analyzed the overall resistances, additional analysis allowed characterizing the phenomena and their respective importance in the electrochemical behavior of the sample. The normalized Nyquist plot (Figure 5.18a) reveals that two arcs are appearing under dry H_2 conditions while a single arc is detected under wet H_2 conditions. One arc disappears when it changes at moist H_2 conditions. Electrode polarization resistance values of 4 and 2 $\Omega\cdot cm^2$ are reached in dry and wet H_2, respectively. Regarding wet $CH_4 – H_2$ mixtures, the polarization resistance values of 6, 7 and 12 $\Omega\cdot cm^2$ were reached for 10%, 25%, 50% of CH_4 content (H_2 balance) under wet conditions, respectively. After 5 hours under wet 50% CH_4 the polarization resistance decreased until 10 Ω·cm^2. The imaginary Bode plot (Figure 5.17c) reveals that the measurement under dry H_2 presents a specific contribution at low frequencies (0.1 Hz) together with a contribution at high frequencies (9 kHz). Low-frequency contributions are usually attributed to electrode surface processes while high-frequency contributions to bulk processes, in this case, probably related to the low hydration degree of the BZCY in the cermet [20-24] Under wet conditions, only one contribution at medium frequencies appears (80-200 Hz) and may be related to coupled surface processes and transport of protons within the composite grains towards the electrolyte.

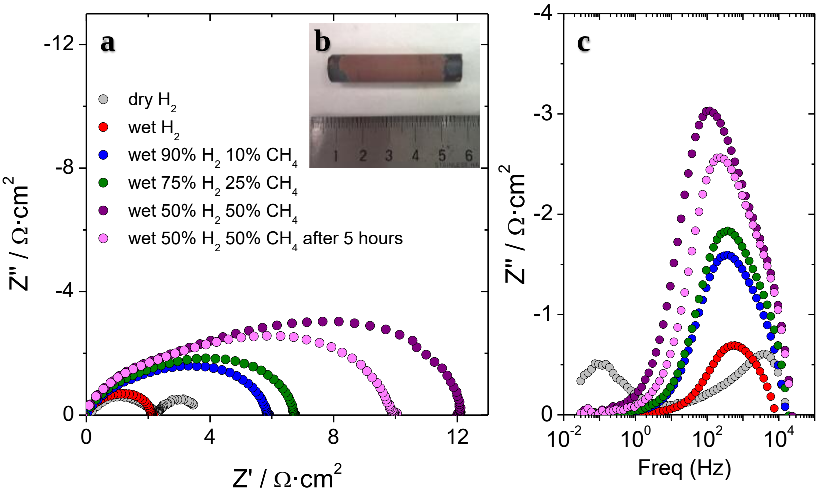

Figure 5.18. Impedance spectroscopy results at 700 °C under different conditions. Sample dipped three times on free-ethylcellulose slurry. The electrode was sintered at 1000 °C 1h. (a) Normalized Nyquist plot; (b) view of the sample; (c) Imaginary bode plot.

Figure 5.19a shows the polarization resistance and their respective contributions (at low and high frequencies) for different mixtures of Ar-H_2 in dry conditions at 700 °C. Decreasing the H_2 concentrations leads to higher polarization resistances. Taking into account the double-arc contribution appearing in dry conditions, the H_2 dilution increases the low frequency contribution while the high frequency contribution keeps constant. This supports that the present low frequency contribution is related to surface reaction processes. The cell study under different CH_4–H_2 mixtures in wet conditions (Figure 5.19b) shows that the polarization resistance augments with increasing CH_4 contents in agreement with results observed in previous studies with methane mixtures [25-27].

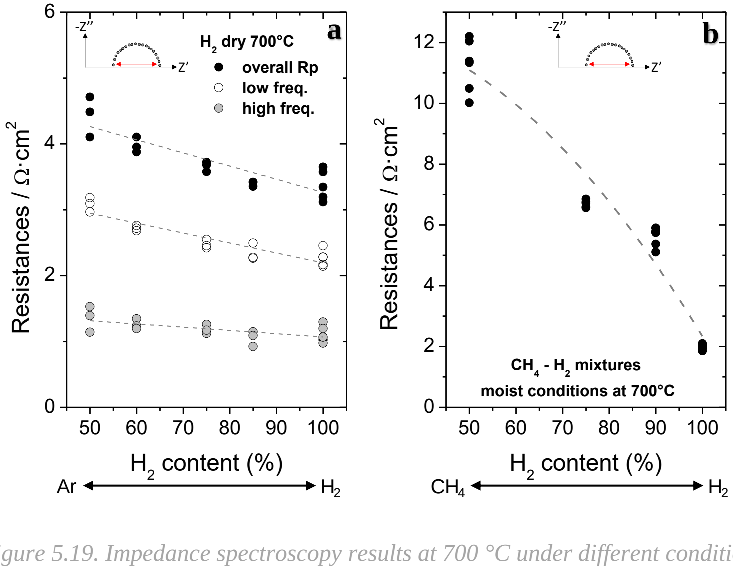

Figure 5.19. Impedance spectroscopy results at 700 °C under different conditions. Sample dipped three times on free-ethylcellulose slurry. The electrode was sintered at 1000 °C 1h. (a) Dry H_2-Ar mixtures at 700 °C. (b) Wet H_2-CH_4 mixtures at 700 °C.

Considering the surface limitations under dry conditions, the effect of the catalytic promotion of the electrode was investigated by infiltrating a Pt aqueous solution into a copper cermet. Under dry H_2 at 700 °C, Pt infiltration enables to reduce significantly the low frequency arc (Figure 5.20) Pt dispersion on the electrode effectively seems to promote surface reaction processes.

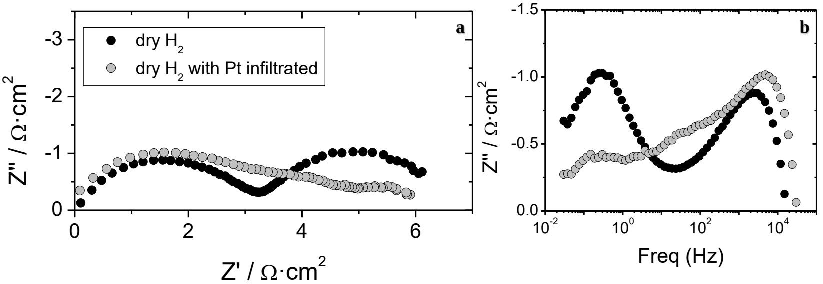

Figure 5.20. Impedance spectroscopy results at 700 °C under hydrogen in dry conditions. Sample dipped three times on free-ethylcellulose slurry. The electrode was sintered at 1000 °C 1h. (a) Normalized Nyquist plot (b) Bode plot.

Finally, Figure 5.21 shows the polarization resistances for all tubes measured for the electrodes sintered at temperatures higher 1000 °C on asymmetric initially unreduced tubes. Under dry H_2 conditions, the polarization resistance values are lower than 7.5 Ω·cm^2 for all cases and lower than 5 Ω·cm^2 for most of the samples. Under wet H_2 at 700 °C, the polarization resistance is below 2.5 Ω·cm^2 for all cases, and around 1 Ω·cm^2 for half of the cases. In addition, from the comparison among the different samples, a high reproducibility in the electrode preparation and testing can be ascertained.

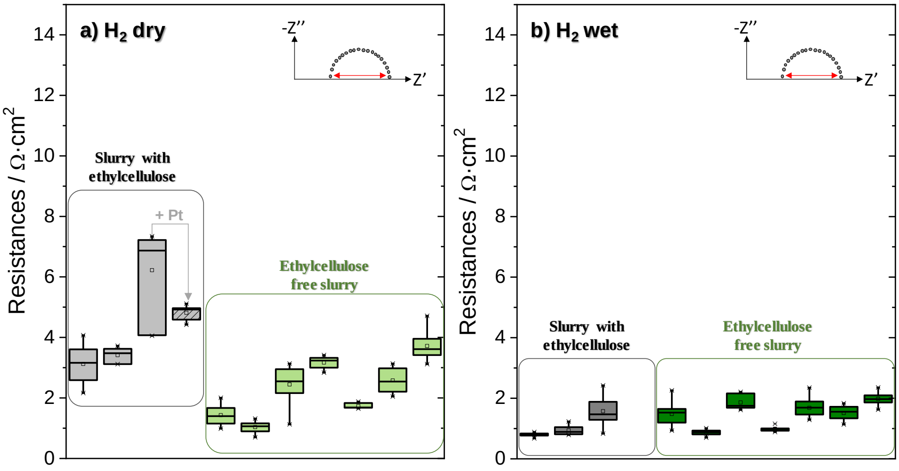

Figure 5.21. Impedance spectroscopy results at 700 °C under different conditions. The electrodes were deposited on asymmetric initially unreduced tubes and sintered at 1000°C 1h. (a) Polarization resistances for dry hydrogen at 700 °C; (b) Polarization resistances for wet hydrogen at 700 °C.

5.2.6. Stability of the cermet electrode

The stability of the electrode was evaluated under dry H_2 at 750 °C and 800 °C. Here, a Cu – BZCY72 electrode deposited by double dipping on asymmetric initially-unreduced tubes, sintered at 1015 °C 1 h and reduced at 700 °C in H_2 for 2 h was employed. SEM analysis (Figure 5.22) of the electrode before and after annealing shows that there are no significant differences between the microstructure and particle sizes before (Figure 5.22a and d) and after test at 750 °C (Figure 22b and e) for 2 weeks. However, the microstructure of the copper cermet after annealing at 800 °C (Figure 5.22c and f) shows agglomeration/sintering of the copper particles. Therefore, the microstructure of the copper cermet electrode remains fairly stable at 750 °C but evolves by copper sintering at 800 °C under dry H_2 atmospheres.

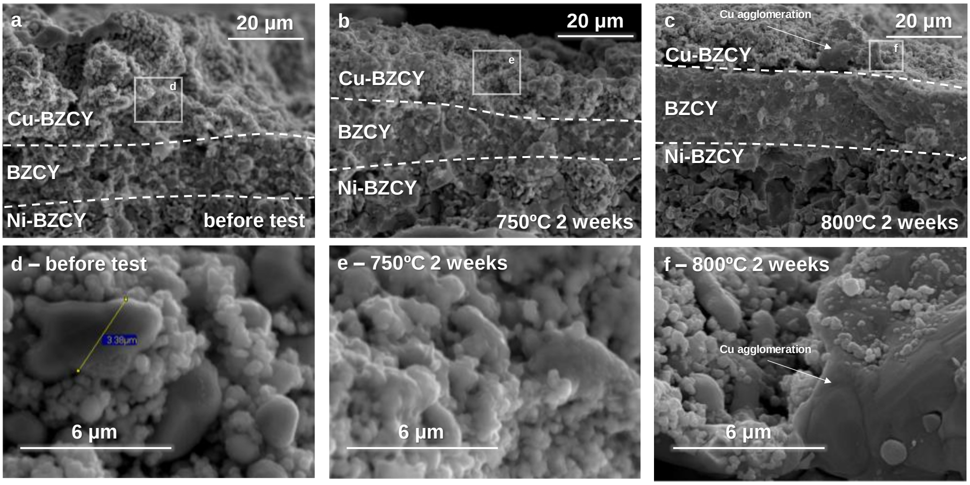
a
20 µm
d
Cu-BZCY
BZCY
Ni-BZCY
before test
b
20 µm
e
Cu-BZCY
BZCY
Ni-BZCY
750°C 2 weeks
c
Cu agglomeration
20 µm
f
Cu-BZCY
BZCY
Ni-BZCY
800°C 2 weeks
d – before test
3.38µm
6 µm
e – 750°C 2 weeks
6 µm
f – 800°C 2 weeks
Cu agglomeration
6 µm

Figure 5.22. Cross section SEM images for the reduced cermet on asymmetric tube initially unreduced. The tube was dipped twice on slurry with ethylcellusose and sintered at 1000 – 1025 °C 1h. (a) Before the accelerating aging test; (d) zoom view of the sample before the aging test; (b) after the accelerating aging test at 750 °C (e) zoom view of the sample after the aging test at 750 °C; (c) after the accelerating aging test at 800 °C, (f) zoom view of the sample after the aging test at 800 °C.

5.2.7. Dip-coating on asymmetric initially reduced tubes

The dip-coating methodology was transferred for asymmetric tubular support with the internal electrode initially reduced (asymmetric initially-reduced tubes). The sintering step was accomplished by using dual atmosphere (air for the external electrode and 5% H_2 in Ar for the internal electrode) to avoid the oxidation of the internal electrode. After the annealing, the external electrode presents a brown color and the layer fold with the minimal friction contact. Figure 5.23a-d show the cross section SEM image and the EDS analysis after the adapted sintering step at 1000 °C. The EDS analysis did not show copper presence in the external cermet layer. Additionally, Figure 5.23e-h shows the cross-section SEM image and the EDS analysis of the internal electrode-electrolyte interface. This analysis reveals that copper fully diffused into the inner Ni-based electrode during the dual-atmosphere annealing. Figure 5.23g shows how the copper concentration decreases with the distance from the BZCY electrolyte within the inner electrode.

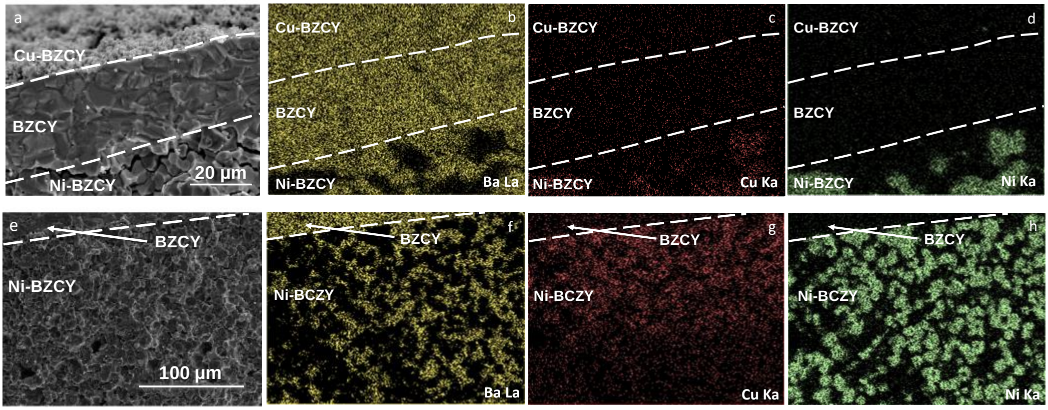
a
Cu-BZCY
BZCY
Ni-BZCY
20 µm
b
Cu-BZCY
BZCY
Ni-BZCY
Ba La
c
Cu-BZCY
BZCY
Ni-BZCY
Cu Ka
d
Cu-BZCY
BZCY
Ni-BZCY
Ni Ka
e
BZCY
Ni-BZCY
100 µm
f
BZCY
Ni-BCZY
Ba La
g
BZCY
Ni-BCZY
Cu Ka
h
BZCY
Ni-BCZY
Ni Ka

Figure 5.23. Tube dipped twice on slurry with ethylcellusose and sintered at 1000 °C 1h. (a) Cross-section SEM image of reduced cermet on asymmetric tube initially reduced; (b–d) EDS analysis; (e) Cross section SEM image of the reduced cermet on asymmetric tube initially reduced in the internal electrode – electrolyte interphase; (f – h) EDS analysis of the internal electrode.

Taking into account the absence of copper in the outer electrode, two possible mechanisms may be possible for the copper diffusion: (i) diffusion across the bulk of BZCY electrolyte grains; and (ii) diffusion across grain boundaries of BZCY electrolyte. To shed further light on this mechanism a new experiment was designed. A symmetrical assembly of Cu-BZCY electrodes on BZCY flat disc pellets was elaborated by screen-printing sintering the layer at 1000°C 2hours.

However, when this assembly was reduced in H_2 at 700 °C, the electrodes on both sides of the pellet were in electric contact even at room temperature. The EDS-SEM analysis of the copper-based cermet on symmetrical cells (Figure 5.24) revealed that both electrodes were connected because copper diffused along cracks and defects along the electrolyte thickness (Figure 5.24c and Figure 5.24f). This effect suggests that copper transport in reducing conditions or dual-phase atmospheres takes places through electrolyte defects and/or grain boundaries and these mechanisms are facilitated by the high mobility of the copper oxides in these conditions. Therefore, dense electrolytes without any defect are necessary for copper-based electrodes to avoid the copper diffusion between electrodes or to avoid short-circuits at high sintering temperatures.

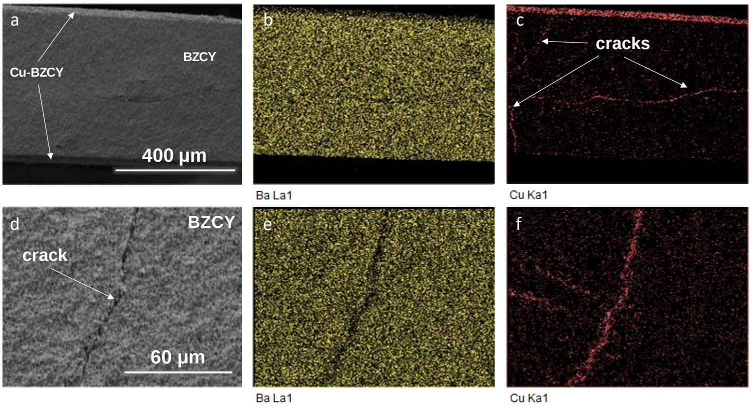

Figure 5.24. (a) Cross-section SEM image of symmetric Cu-BZCY screen-printed on BZCY disc. (b–c) EDS analysis (Ba represents BZCY). (d) Zoom view of the crack; (e-f) EDS analysis (Ba represents BZCY). Both electrodes were deposited on the disc pellets using screen printing technique. The electrode was sintered at 1000 °C 2h and reduced at 700 °C 2h with H_2.

5.3. Summary

Dip-coating procedures were developed to deposit copper-based electrodes on proton-conducting electrochemical tubular cells. The sintering step was found to be the most critical step due to the fast sintering of copper particles.

In the electrode deposition on asymmetric tubes with the inner Ni-based electrode initially-unreduced, sintering temperatures between 1000 and 1025 °C causes bigger copper particles and better attachment between BZCY72 and copper particles and, hence, a better interconnection of the copper network. These electrodes present high stability regarding microstructure and electrochemical results at 700 °C under different conditions based on H_2 atmospheres. On asymmetric tubes with inner electrode initially-reduced, copper migrates into internal electrode during dual-phase sintering step through grain boundary and defects in the electrolyte layer.

The copper-based electrodes deposited using dip-coating technique on proton-conducting tubular cells present specific resistances lower than 2.5 $\Omega \cdot cm^2$ for more than 150 hours on stream at 700 °C under different application-oriented atmospheres (H_2-CH_4). The operation in wet conditions ameliorates both surface reaction processes and solid diffusion transport of protons thanks to the improved BZCY hydration. The best electrode performances were reached in moist H_2-rich gas environments while increasing CH_4 concentration leads to higher electrode polarization resistances.

5.4. References

1. Laguna-Bercero, M.A., Journal of Power Sources, 2012. **203**: p. 4-16.

2. Brett, D.J.L., et al., Chemical Society Reviews, 2008. **37**(8): p. 1568-78.

3. Fabbri, E., et al., Chemical Society Reviews, 2010. **39**(11): p. 4355-69.

4. Sundmacher, K., et al., Catalysis Today, 2005. **104**(2–4): p. 185-99.

5. Demin, A. and P. Tsiakaras, International Journal of Hydrogen Energy, 2001. **26**(10): p. 1103-8.

6. Jamsak, W., et al., Chemical Engineering Journal, 2006. **119**(1): p. 11-8.

7. Morejudo, S.H., et al., Science, 2016. **353**(6299): p. 563-6.

8. Kyriakou, V., et al., Applied Catalysis B: Environmental, 2016. **186**: p. 1-9.

9. Vasileiou, E., et al., Solid State Ionics, 2015. **275**: p. 110-6.

10. Malerød-Fjeld, H., et al., Nature Energy, 2017.

11. Fabbri, E., et al., Advanced Materials, 2012. **24**(2): p. 195-208.

12. Atkinson, A., et al., Nat Mater, 2004. **3**(1): p. 17-27.

13. Fabbri, E., et al., Science and Technology of Advanced Materials, 2010. **11**(4): p. 044301.

14. Shaikh, S.P.S., et al., Renewable and Sustainable Energy Reviews, 2015. **51**: p. 1-8.

15. Hibino, T., et al., Journal of the Electrochemical Society, 2002. **149**(11): p. A1503-A8.

16. Ge, X.-M., et al., Advanced Energy Materials, 2012. **2**(10): p. 1156-81.

17. Escolástico, S., et al., ACS Applied Materials & Interfaces, 2017. **9**(41): p. 35749-56.

18. Patki, N.S., et al., International Journal of Hydrogen Energy, 2017. **42**(27): p. 16911-9.

19. Pelton, A.D., *Thermodynamics and Phase Diagrams*. 2011, Centre de Recherche en Calcul Thermodynamique (CRCT) Montreal.

20. Primdahl, S. and M. Mogensen, Journal of the Electrochemical Society, 1997. **144**(10): p. 3409-19.

21. Lee, C.-H., et al., Solid State Ionics, 1997. **98**(1): p. 39-48.

22. Savaniu, C.D., et al., Journal of Materials Chemistry, 2005. **15**(5): p. 598-604.

23. Haile, S.M., et al., Journal of Materials Science, 2001. **36**(5): p. 1149-60.

24. Baumann, F.S., et al., Solid State Ionics, 2006. **177**(11): p. 1071-81.

25. Vernoux, P., et al., Solid State Ionics, 2000. **135**(1): p. 425-31.

26. Li, M., et al., Journal of Materials Chemistry A, 2015. **3**(43): p. 21609-17.

27. Coors, W.G., Journal of Power Sources, 2003. **118**(1): p. 150-6.

6. COPPER SPUTTERED ANODES FOR MEMBRANE REACTORS AT HIGH TEMPERATURE

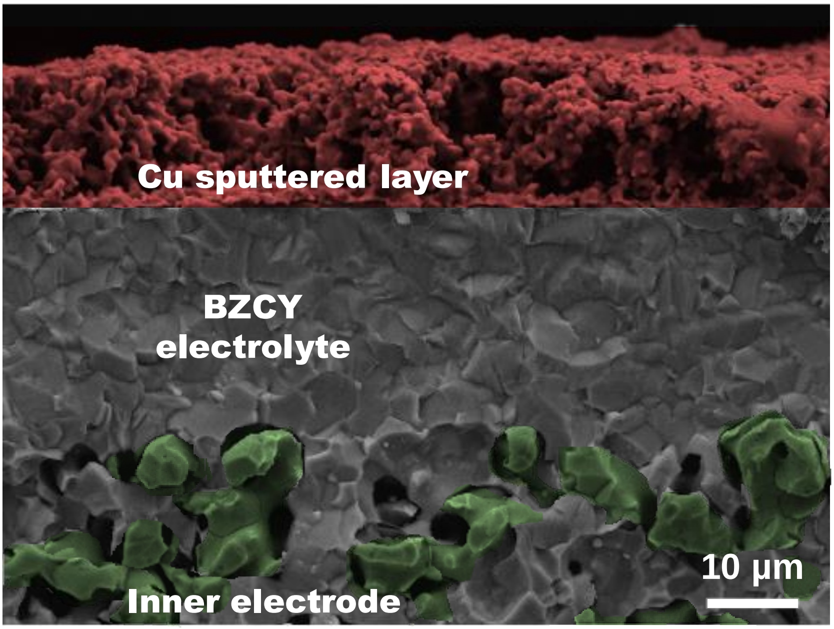
Cu sputtered layer
BZCY
electrolyte
Inner electrode
10 µm

6.1.Introduction

The development of ion-conducting ceramics for high temperature applications is allowing the intensification of several processes. This intensification is not only in the energy field (e.g. fuel cell and electrolysis) but in chemical production using membrane reactors integrating these materials as selective separators for the improvement of several processes as methane steam reforming, ammonia synthesis among others [1-3]. These processes involve very differentiated atmospheres and, obviously, the materials for the respective electrochemical assembly must be able to tolerate these conditions. Therefore, the progress in this field is bounded to the development of materials for stable and effective operation of the electrochemical cell.

Typical electrodes for SOFC applications are nickel-based cermets comprising the ionic conducting material [3-6]. However, nickel presents several drawbacks in some atmospheres as coarsening at high temperatures and, specially, coke formation in non-oxidizing hydrocarbon atmospheres [5]. Between different alternatives, copper is a potential material because its high electronic conductivity even at high temperatures and its stability at intermediate temperatures [7]. However, its low melt point makes difficult the deposition under the electrolyte via conventional techniques, e.g. ceramic sintering technique. Further, copper coarsening effect becomes important in the microstructure of the layer at temperatures around 800°C [7]. However, for lower temperatures applications, e.g. methane dehydroaromatization at temperatures around 700°C, copper-based electrodes could be a key to build viable and robust assemblies for the intensification of these processes [8]. Further, the last developments in proton conducting materials allows decreasing the temperature window until intermediate temperature applications (400 – 600°C) [4] where copper could have an excellent behavior as electrode with the suitable deposition method.

Sputtering could be a suitable technique to deposit copper because it does not involve high temperatures, the versatility of the technique and the facility to control the morphology of the deposition [9]. Sputtering has been largely used for SOFC application, for both electrolyte and electrodes depositions [9-13]. Deposition by sputtering at relative low temperatures should minimize the risk of reactivities between electrode and electrolyte material with regard to conventional sintering methods [9]. Nanocomposite electrodes may result in increased triple phase boundary area, reduced thermal stresses and the high-volume fraction of grain boundaries [14-16]. Sputtered materials for ionic ceramic applications have allowed improving not only the yield of these processes but also the understanding of the phenomena those take place [9, 17-21]. Finally, despite of all the reported benefits of sputtering, it presents several drawbacks as the equipment costs and deposition rates (<5 μm/h) that limit the applicability of magnetron sputtering [9, 22].

6.2.Results

Sputtering method is conventionally used to deposit thin-films on planar supports, therefore the sputtering assembly was adapted and optimized to deposit copper electrodes on tubular electrochemical semi-cells (described in Chapter 4). Considering the adapted sputtering assembly, deposition time and temperature were studied to optimize the deposition achieved.

6.2.1. Sputtering at room temperature

Once the sputtering assembly was adapted for tubular supports, the first sputtering deposition attempts were developed at room temperature. The adapted assembly consist of oriented magnetron guns towards the surface of the tube while the tube is rotating. Therefore, copper particles are being incorporated gradually on the external surface of the tube.

The copper layer deposited on tubular half-cells did not show good adhesion to the electrolyte and, consequently, these layers did not pass the “Scotch test”. Figure 6.1 shows several images of the microstructure of the copper deposited layer on tubes. The layer presents a thickness around 0.85 – 1 µm. Further, although the images show well-defined layers without interphases or reactivities between the different layers, the deposited film is not continuous and dense while presenting cracks (Figure 6.1.c)

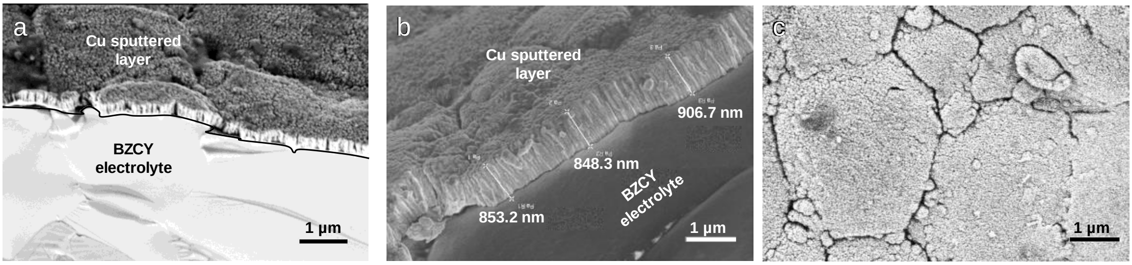

Figure 6.1. FESEM images of the copper sputtered electrode at room temperature. (a-b) View of the interphase electrode-tube (image adquisition at 2.00 kV); (c) frontal view of the copper layer (image adquisition at 3.00kV)

The electrochemical behavior was characterized using impedance spectroscopy because, although the deposited layer does not present perfect mechanical attachment with the tube, it may present a good electrochemical connection, nevertheless. EIS results at 700 °C in H_2 atmospheres are presented in the Figure 6.2.

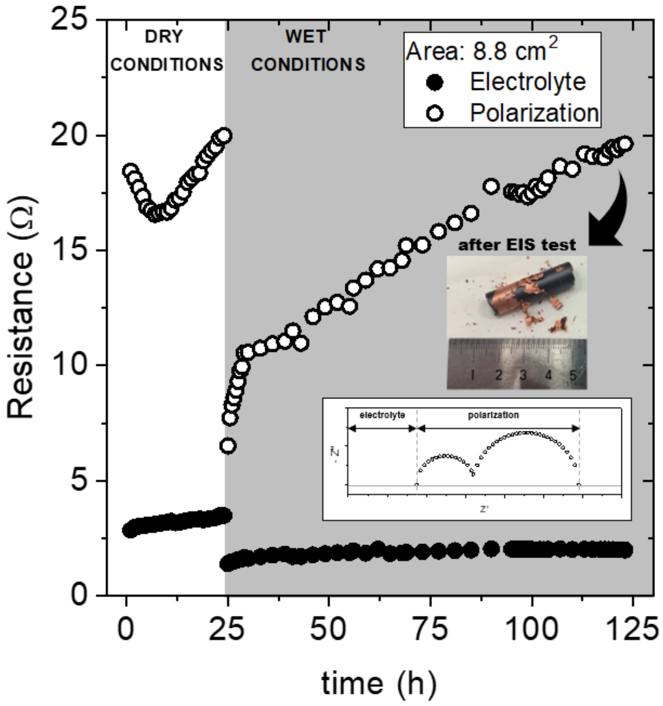

Figure 6.2. Polarization resistance and electrolyte resistance for impedance spectroscopy test developed on H_2 atmospheres at 700 °C.

While the electrolyte contribution keeps approximately constant with time under dry and wet H_2, the polarization resistance increases gradually, even when it changed until wet atmospheres. Finally, for dry conditions where the polarization resistance was between 16 – 20 Ω, the specific polarization resistance ranges 140 – 175 Ω·cm^2. For wet conditions, the polarization resistance was between 6 – 20 **Ω**, the specific polarization resistance would be among 50 – 175 **Ω**·cm^2. When the experiment finished it was observed (photo in the Figure 6.2) that the electrode was almost peeled off. Therefore, the increase of the polarization resistance is ascribed to the loss of adhesion and, thus, active electrode area rather than to degradation of the material.

In summary, copper depositions on tubular supports by sputtering at room temperature present important limitations due to the poor attachment.

6.2.2. Sputtering at high temperature

The sputtering step was made at higher temperature to improve the adhesion of the copper particles on the tubular support and overcoming the limitations observed in room temperature sputter electrodes.

The sputtering deposition was developed at 400 – 450 °C 5 hours. After deposition step, the deposited layer passes the Scotch test and it presents electronic conductivity at room temperature (checked by multimeter). Therefore, increasing the temperature during the deposition by sputtering improves the adhesion of the copper on the tubular support. Figure 6.3 shows the microstructure of the copper sputtered layer on tubular supports. The thickness of the sputtered layers sizes ranges 10 – 15 µm (Figure 6.3.a), which means a deposition rate of 2 – 3 µm/h. This deposition rates for copper target in sputtering are similar to the reported in previous works [23-25]. The detailed view of the deposited copper layer shows well-defined porous copper network (Figure 6.3.b and c).

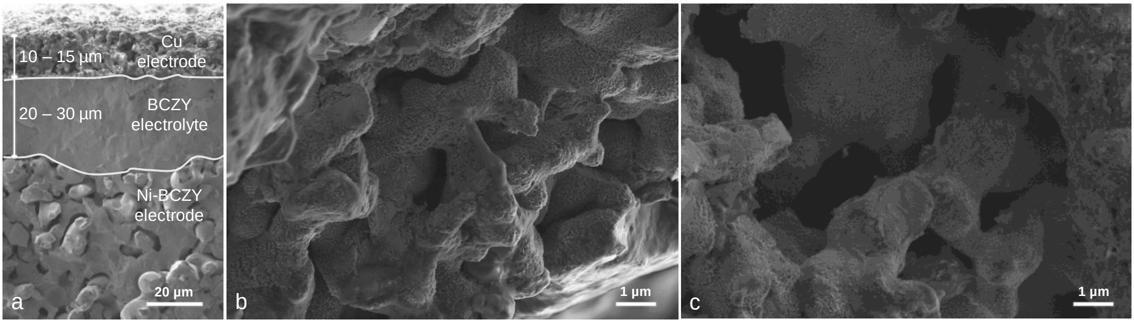
10 – 15 µm
Cu electrode
20 – 30 µm
BCZY electrolyte
Ni-BCZY electrode
20 µm
a
b
1 µm
c
1 µm

Figure 6.3. FESEM images of the copper electrode sputtered on tubes at high temperature. (a) View of cross section of the tube; (b-c) Zoom view of the copper electrode. Images adquired at 2.00kV.

An advanced analysis of the microstructure and composition of the different layers was made. Figure 6.4 shows the microstructure of the cross-section of the inner electrode – electrolyte – sputtered electrode and the EDS analysis. EDS analysis shows a homogeneous copper layer above the electrolyte (Figure 6.4.b). The electrolyte layer is free of nickel or copper (Figure 6.4.c).

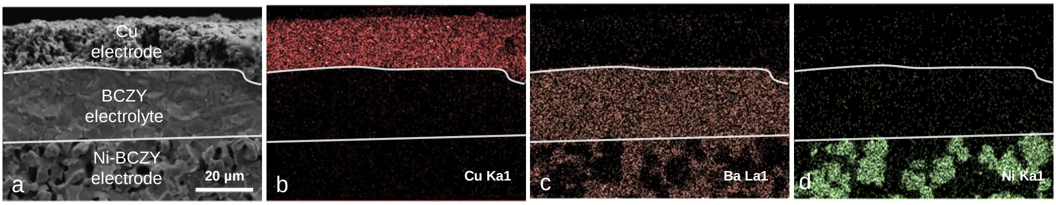
Cu electrode
BCZY electrolyte
Ni-BCZY electrode
20 µm
a
b
Cu Ka1
c
Ba La1
d
Ni Ka1

Figure 6.4. EDS analysis of the copper sputtered on a tubular support at high temperature. (a) View of the cross section of external electrode - electrolyte - internal electrode; EDS results about copper (b), Ba (c) and Ni (d). Ba denotes all BCZY phase.

The copper layer deposited by sputtering at high temperature presents well-attached and well-defined porous layer above the electrolyte. The sample was characterized by EIS to evaluate its electrochemical behavior. Figure 6.5 shows the EIS results at 700°C under H_2-CH_4-H_2O atmospheres. The steam absence increases dramatically the polarization resistances two orders of magnitude from dry to wet conditions. Furthermore, the steam presence modifies the electrolyte resistance changes with around 1 Ω·cm^2 in moist conditions and around 4 Ω·cm^2 in dry conditions.

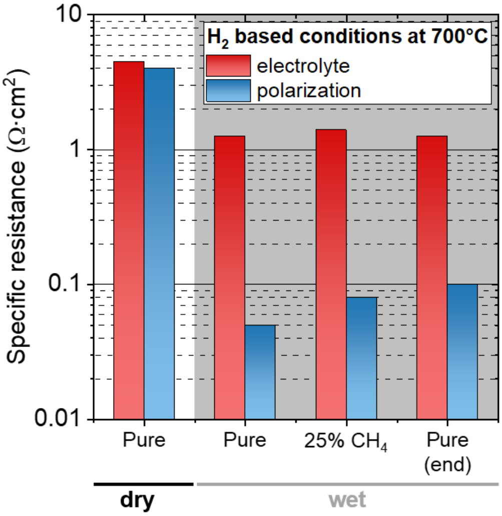

Figure 6.5. Polarization resistance and electrolyte resistance for impedance spectroscopy test developed in H_2 atmospheres at 700 °C.

Figure 6.6 shows the EIS results depending on the experimental time. The test was developed at 700°C under H_2-CH_4-H_2O atmospheres. When the steam is removed or added, the results recover its previous values rapidly. Methane presence in wet conditions did not affect significantly the results, but after around 10 hours in methane conditions, the polarization contribution increases gradually until stabilization for 90 hours. The results after 100 hours lay around 4 Ω·cm^2 for electrolyte and polarization contributions in dry conditions and, for the wet conditions, 0.04 – 0.1 Ω·cm^2 for the polarization contribution and around 1.5 Ω·cm^2 for the electrolyte contribution. These electrolyte contributions give conductivities around 0.044 – 0.067 S/m on dry H_2 and 0.16 – 0.24 S/m on moist H_2. These conductivities are in the range of the reported for previous works [26-28].

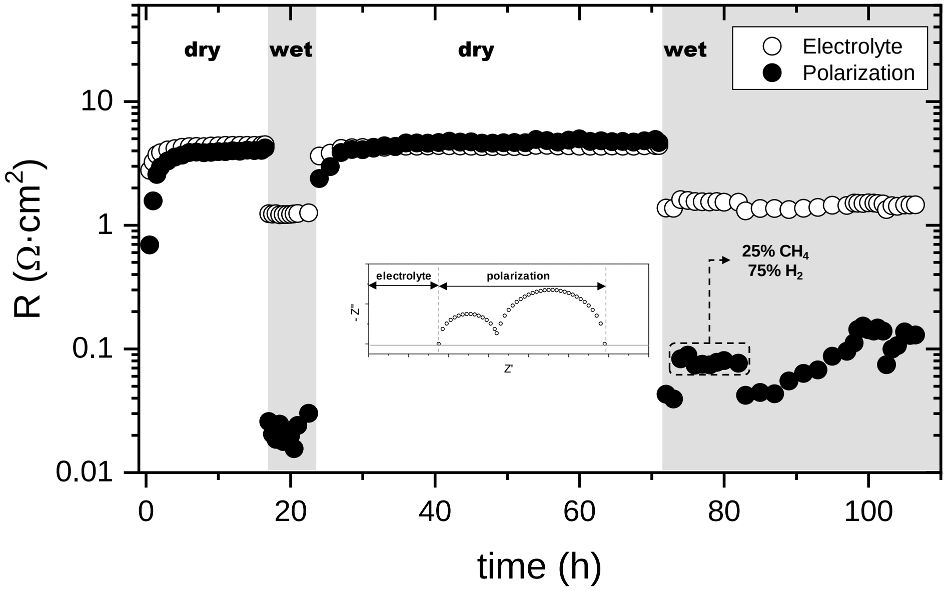

Figure 6.6. Stability of the specific resistance contributions of the impedance spectroscopy test developed in H_2 atmospheres at 700 °C.

Figure 6.7 shows the Nyquist plots for the copper sputtered on tubular support sample at high temperature. The electrode under dry H_2 presents a double arc contribution at lower and higher frequencies, related to surface and bulk processes, respectively. The results in wet conditions only show a single arc at high frequencies. Furthermore, results show the polarization resistances significative lower in wet conditions than in dry conditions. The electrolyte contribution increases from around 1.45 Ω·cm^2 until 1.5 Ω·cm^2 when the methane is introduced in the test conditions (Figure 6.8b). Finally, Figure 6.8c show the initial single arc when the conditions where changed until wet conditions.

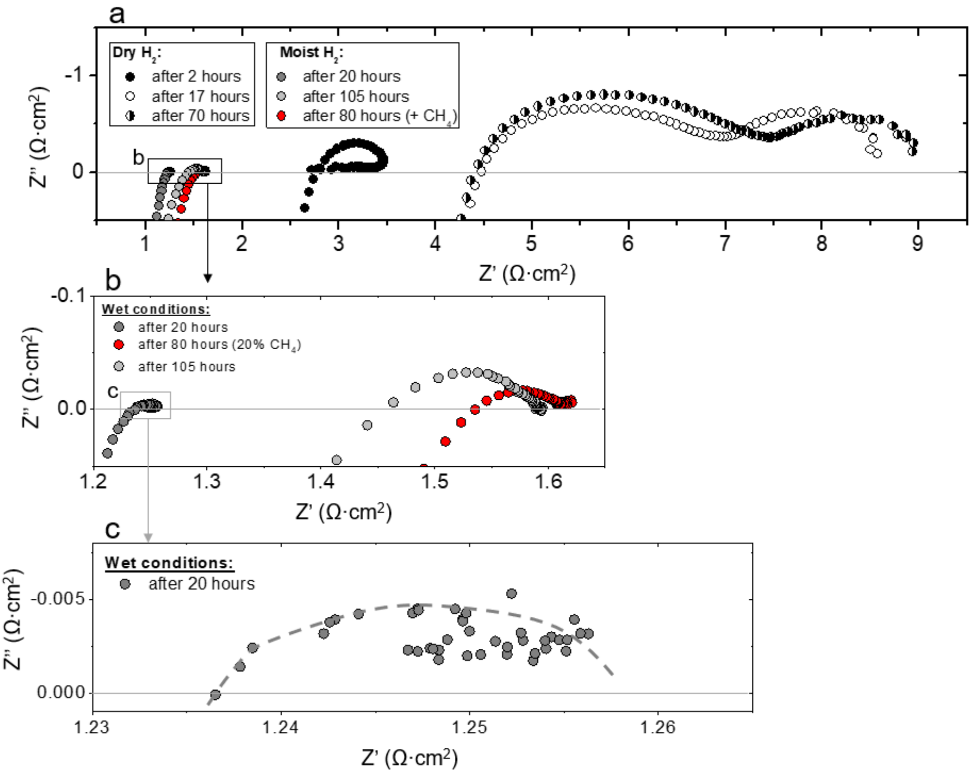

Figure 6.7. Impedance spectroscopy test with hydrogen atmospheres at 700 °C. (a-c) Nyquist plots

The imaginary Bode plots (Figure 6.8) shows the frequency of each arc contribution observed in the previous picture. The results obtained under dry H_2 shows the first arc at low frequencies, between 0.1 – 1 Hz, and the second arc at high frequencies, 100 – 1000 Hz (Figure 6.8a). At wet conditions (pure H_2 or mixture CH_4-H_2) illustrate the single arc observed in the Nyquist plot at around 1000 Hz.

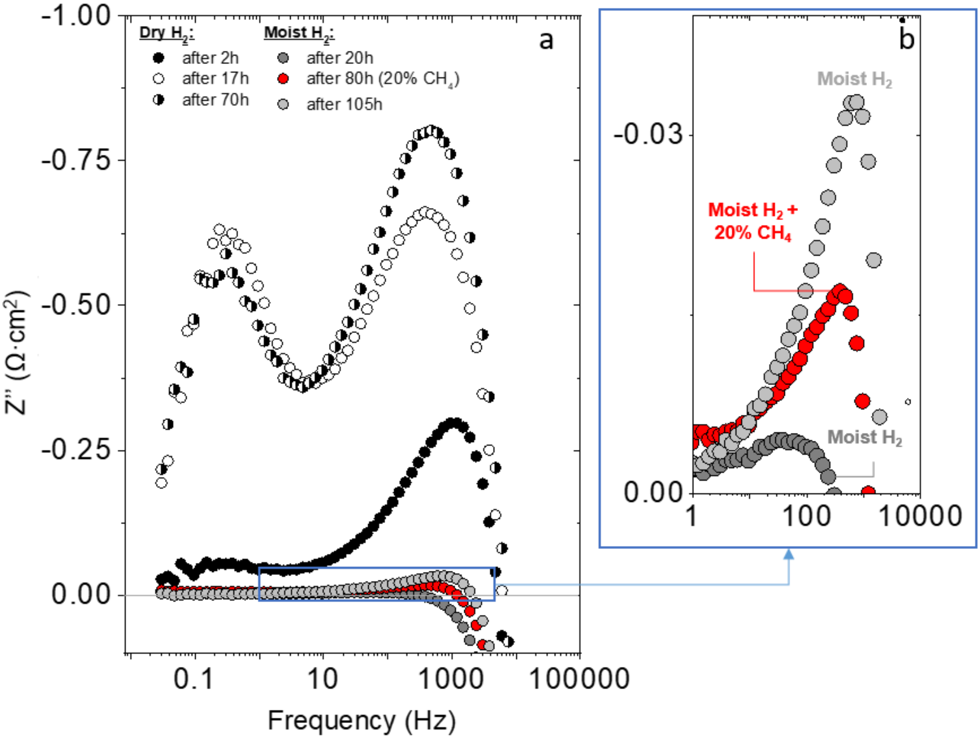

Figure 6.8. Impedance spectroscopy test with hydrogen atmospheres at 700 °C. (a) Bode plot of the imaginary contribution; (b) zoom of the Bode plot of the imaginary contribution.

Finally, the Figure 6.9 shows the images of the electrode after the sputtering step and after the EIS test in hydrogen atmospheres at 700 °C.

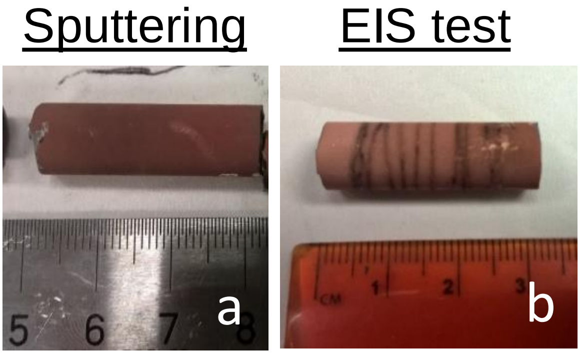

Figure 6.9. Images of the tube: (a) after sputtering of Cu at high temperature; (b) after impedance spectroscopy test at 700 °C.

6.3.Future works

Considering the excellent electrochemical behavior of the cell when the copper is deposited by sputtering at high temperature, next works are going to check the cell in reaction conditions: (i) checking the hydrogen pumping of the cell, i.e. to evaluate the faradic efficiency ; (ii) checking the behavior of the cell under reaction conditions: between the reaction proposed are methane dehydroaromatization, methane steam reforming and electrosynthesis of ammonia.

6.4.Summary

Copper layers for tubular electrochemical supports were developed and optimized using magnetron sputtering as deposition technique. Attachments problems were observed when the sputtering process was developed at room temperature. The electrode was detached at reaction conditions (700°C in hydrogen rich atmospheres). These problems were solved when the sputtering was carried out at high temperatures (400 – 450 °C). The resulting electrochemical cells shows very low polarization resistances (0.01 – 0.1 Ω cm^2) while the final sputtered layer is distributed as porous thin layer above the electrolyte.

6.5.References

1. Fang, W., et al., Angewandte Chemie International Edition, 2015. **54**(16): p. 4847-50.
2. Morejudo, S.H., et al., Science, 2016. **353**(6299): p. 563-6.
3. Malerod-Fjeld, H., et al., Nat. Energy, 2017. **2**(12): p. 923-31.
4. Fabbri, E., et al., Advanced materials, 2012. **24**(2): p. 195-208.
5. Atkinson, A., et al., Nature Materials, 2004. **3**: p. 17.
6. Emiliana, F., et al., Science and Technology of Advanced Materials, 2010. **11**(4): p. 044301.
7. Ge, X.M., et al., Advanced Energy Materials, 2012. **2**(10): p. 1156-81.
8. Patki, N.S., et al., International Journal of Hydrogen Energy, 2017. **42**(27): p. 16911-9.
9. Pederson, L.R., et al., Vacuum, 2006. **80**(10): p. 1066-83.
10. Froitzheim, J., et al., Journal of Fuel Cell Science and Technology, 2010. **7**(3): p. 031020--7.
11. Huang, H., et al., Journal of The Electrochemical Society, 2007. **154**(1): p. B20-B4.
12. Wang, L.S. and S.A. Barnett, Solid State Ionics, 1993. **61**(4): p. 273-6.
13. Nagata, A. and H. Okayama, Vacuum, 2002. **66**(3): p. 523-9.
14. Litzelman, S.J., et al., Fuel Cells, 2008. **8**(5): p. 294-302.

15. Litzelman, S.J., et al., Journal of Electroceramics, 2009. **22**(4): p. 405-15.
16. Labrincha, J.A., et al., Materials Research Bulletin, 1993. **28**(2): p. 101-9.
17. Radhakrishnan, R., et al., Journal of The Electrochemical Society, 2005. **152**(1): p. A210-A8.
18. Hertz, J.L. and H.L. Tuller, Journal of Electroceramics, 2004. **13**(1): p. 663-8.
19. Briois, P. and A. Billard, Surface and Coatings Technology, 2006. **201**(3): p. 1328-34.
20. Escolástico, S., et al., ACS Applied Materials & Interfaces, 2017. **9**(41): p. 35749-56.
21. Solís, C., et al., The Journal of Physical Chemistry C, 2014. **118**(42): p. 24266-73.
22. Isenberg, A. *Cost reduction in fabrication processes for SOFC cell components, vol. 2*. in *Lucern, Switzerland: European Fuel Cell Forum*. 2000.
23. Lee, K. and Y.K. Lee, Journal of Materials Science, 2000. **35**(23): p. 6035-40.
24. Thornton, J.A., Journal of Vacuum Science and Technology, 1975. **12**(4): p. 830-5.
25. Chan, K.-Y. and B.-S. Teo, Journal of Materials Science, 2005. **40**(22): p. 5971-81.
26. Heras-Juaristi, G., et al., Journal of Power Sources, 2017. **364**: p. 52-60.
27. Sawant, P., et al., International Journal of Hydrogen Energy, 2012. **37**(4): p. 3848-56.
28. Ricote, S., et al., Solid State Ionics, 2009. **180**(14): p. 990-7.

7. CHARACTERIZATION OF OXYGEN TRANSPORT ON BSCF MEMBRANES ASSISTED BY FLUID DYNAMIC SIMULATIONS

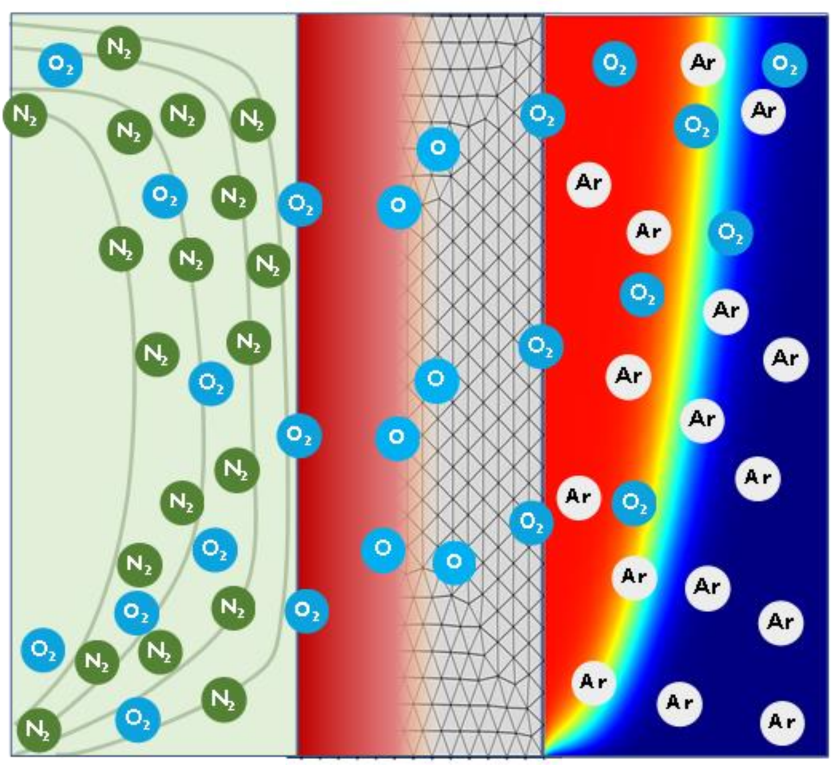

7.1.Introduction

Oxygen Transport Membranes (OTMs) represent a very appealing option for conducting an in-situ and low cost O_2 generation in small and medium-scale industrial applications with an O_2 demand, e.g. partial oxidation and combustions in cement, ceramic, glass and power generation industries [1–3]. Currently, these industries utilize vacuum pressure swing adsorption (VPSA) or cryogenic O_2 thus requiring a periodic bulk transport and storage implying a high cost and an external dependence. The economic and process advantages of implementing OTM-based O_2 supply systems have been largely studied, demonstrating benefits in O_2 production costs and a gain in process efficiency due to the thermal integration of OTM systems within processes presenting waste heat streams [4–6]. Amongst all the considered materials for OTM, $Ba_{0.5}Sr_{0.5}Co_{0.8}Fe_{0.2}O_{3-d}$ (BSCF) is that presenting the highest permeation values with O_2 production capabilities of up to 62ml·min^{-1}·cm^{-2} at 1000 °C [7] despite the limited stability. Some studies have set a permeation threshold of at least 10 ml·min^{-1}·cm^{-2} O_2 for considering the feasible utilization of OTM modules in oxy-fuel applications [8], therefore, membrane modules based on BSCF would be suitable for being integrated in such applications.

The configuration of OTM modules for integration within an industrial process can follow a 3-end or a 4-end approach [9]. In the latter, a hot gas stream belonging to the process (typically a flue gas stream) is used for heating up the module and for conducting the O_2 separation as sweep gas, whereas for the 3-end mode the permeated O_2 is collected by inducing vacuum. As BSCF is very sensitive to environments containing CO_2 and H_2O [10–12], it is considered a 3-end approach for BSCF-based OTM production systems. O_2 permeation performance is affected by several parameters such as temperature, O_2 concentration at feed and permeate sides, feed and sweep gas flow rates and membrane thickness. OTM module integration into an industrial process requires a preliminary design phase where plant layout, elements and devices are dimensioned. In this stage, process simulations are conducted for checking mass and energy transfer balances and thus perform the most precise definition of the different elements. Amongst all the existing equipment, the OTM module is the most difficult to simulate, since the most commonly used process simulation software do not include pre-defined algorithms for simulating the OTM module performance. It is then necessary to build an accurate permeation model that takes into account the aforementioned parameters as well as permeation mechanisms such as oxygen surface reactions and oxygen ions diffusion through the bulk material.

Regarding the development of these materials, modelling helps to improve the understanding of the permeation process as it provides a physical explanation from the raw empirical results. Furthermore, the achievement of an accurate model describing the O_2 transport across the membrane is critical to design the assemblies for the demanded O_2 considering the suitable membrane area. Most of the defined algorithms for these processes consider 0D models [13–16]. Modelling of O_2 permeation typically assumes local electroneutrality and the idealization of the ionic conduction and gas diffusion as hypothesis [17]. The applicability of the simulation results is limited by the considered assumptions. The most-frequently considered models are based on the surface reactions [18–24], chemical potential transport [13,25] and effective medium transport [26]. The development of these models allows the conduction of advanced studies by using computational techniques for higher analysis of the O_2 permeation process. On one side, commercial process simulation software such as Aspen Plus permits the evaluation of the process viability [9,27–34]. On the other side, Computational Fluid Dynamics methodology (CFD) has been utilized as strong visualization tool to simulate the effects of reactions in membrane reactors [33,35–38]. In summary, although several of the developed models are suitable to numerous applications, the continuous development of O_2 permeation models is necessary especially when these membranes are integrated in reactive systems such as oxy-combustion reactors.

In the present chapter, the joint effect of the fluid dynamics conditions and operating conditions (feed concentration and temperature) on the oxygen transport was studied by using a model that specifically takes into account the most relevant phenomena implied in the oxygen transport through MIEC membranes, i.e. formation and diffusion of oxygen vacancies and surface resistance to transport as proposed by Zhu et al. [13]. The model implementation was carried out using a Multiphysics software for finite element analysis (COMSOL Multiphysics) that made possible to handle complex geometries. The results herein obtained will permit the understanding and interpretation of the different factors governing the oxygen permeation and subsequently, the definition of strategies for the optimization of the oxygen production with ceramic MIEC materials. Therefore, the main objective of this work is providing a tool for researchers on the definition of tests and interpretation of experimental results involving permeation of oxygen, as well as helping of more advanced and applied research oriented to the design and the upscaling of processes in the field of OTM technology.

7.2.Methods

7.3.1. Experimental procedure

In order to obtain the necessary information to fit the membrane parameters from experimental data, permeation experiments were carried out in an experimental set-up for a wide range of operating conditions (i.e. temperature, flow rates, O_2 partial pressure, sweep gas type). Permeation tests were conducted on 0.8 mm-thick disk-shaped BSCF membranes. Dense membrane specimens were produced from $Ba_{0.5}Sr_{0.5}Fe_{0.2}Co_{0.8}O_3$ commercial powder (IKTS Fraunhofer, Germany) after uniaxial pressing in a 26 mm diameter steel die and subsequent sintering at 1100 ºC in air for 5 hours. These samples were tested in a quartz lab-scale reactor in which synthetic air (21%, vol. O_2) or O_2/N_2 mixtures were fed into the O_2-rich chamber, while Ar and different Ar/CO_2 mixtures were used as sweep gases on the permeate side chamber, in a 4-end mode configuration. Both streams were fed at atmospheric pressure. Inlet gases were preheated in order to ensure the correct gas temperature for contact with the membrane surface. This is particularly important when high gas flow rates are employed. All streams were individually mass flow controlled. The temperature was measured by a thermocouple attached to the membrane. Membrane gas leak-free conditions were achieved using gold rings, which were heated to 1060 ºC for 4 h immediately prior to the measurement. The permeate was analyzed at steady state by online gas chromatography using a micro-GC Varian CP-4900 equipped with Molsieve5A, Pora-Plot-Q glass capillary, and CP-Sil modules. Membrane gas leak-free conditions were ensured by continuously monitoring the N_2 concentration in the product gas stream. An acceptable sealing was achieved when the ratio between the O_2 flow leak and the O_2 flux was lower than 1%. The data reported here were achieved at steady state after 1 h in the reaction stream. Each test was repeated three times to minimize the analysis error. The experimental analytical error was below 0.5%.

A one-dimensional implementation of the model was additionally performed for diminishing the computational time required for fitting. This enabled an objective function performing significantly faster than the objective function for the multidimensional model considering the exact system geometry. Therefore, it was possible to use a genetic algorithm for the minimization of the objective function, a technique which is suitable for seeking for global optima, but highly time-consuming. Once the model parameters were fitted, the model was able to predict the O_2 permeation flux using as inputs the O_2 partial pressure on both sides of the membrane and the operating conditions. Subsequently, the fitting parameters obtained with the one-dimensional model were used as starting point for the minimization of the objective function based on the full set-up geometry (COMSOL model) by using a direct optimization method.

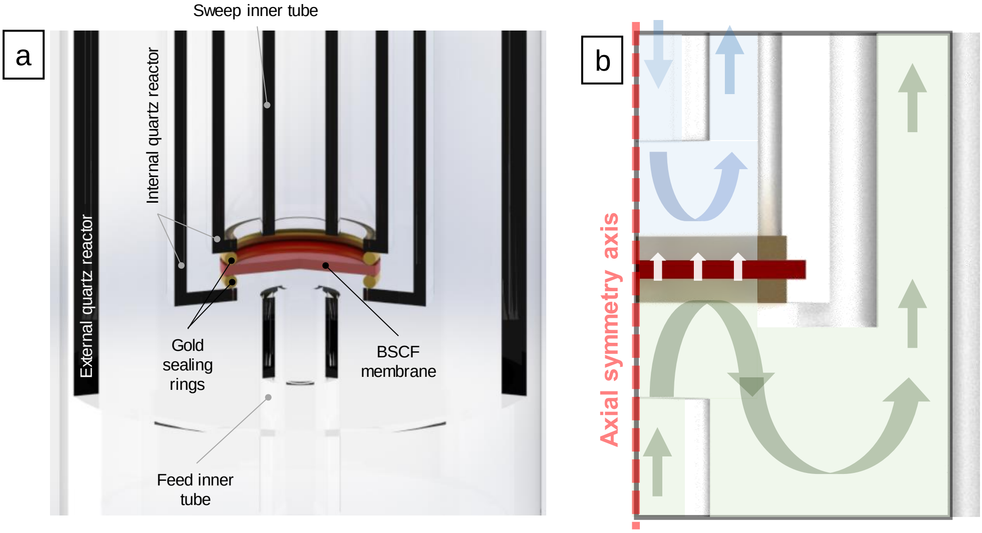
a
Sweep inner tube
Internal quartz reactor
External quartz reactor
Gold sealing rings
BSCF membrane
Feed inner tube
b
Axial symmetry axis

Figure 7.1. Experimental set-up. (a) View of the general set-up; (b) adaptation of the geometry to 2D axial symmetry

Once the parameters were refined for a base case, the effects of membrane thickness, feed and sweep flow were studied in a range around reference conditions. In addition, the effect of dilution and shear conditions in the sweep side and the study of the limiting case of sweep vacuum conditions were thoroughly characterized. Finally, it was built a specific permeation model for the considered setup geometry by using dimensionless numbers and the whole set of CFD results.

7.3.2. Modelling

7.3.2.1. Model equations

The developed model describes the O_2 transport through a MIEC membrane taking into account bulk diffusion and surface resistances, both based on empirical parameters, together with model equations that account for fluid dynamics and component transport in gaseous phases, assuming isothermal conditions. Table 7.1 summarizes the equations used to describe the transport through the membrane bulk and across the gas-membrane interfaces. According to the simplified scheme shown in Figure 7.2, five regions are distinguished, where the O_2 flux is expressed in a different manner as a function of the oxygen potentials in each region.

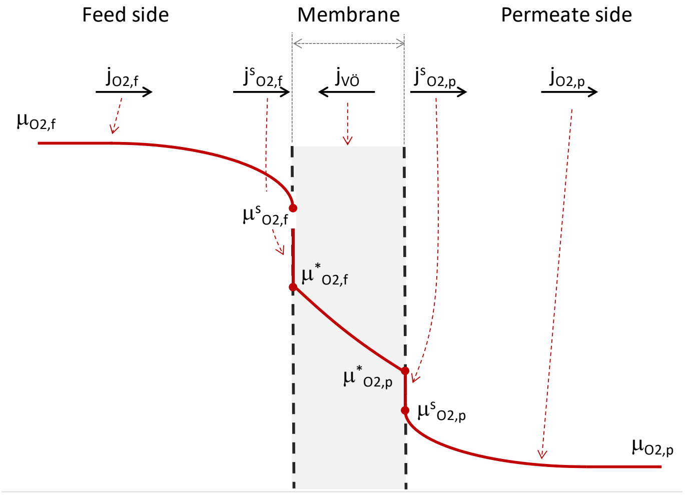

Figure 7.2. Scheme of the oxygen chemical potential gradient for the oxygen permeation process through the MIEC membrane

The O_2 transport through the membrane bulk occurs throught the diffusion of oxygen vacancies (Eq. (1)). In this equation, the diffusion coefficient of oxygen vacancies is assumed to follow an Arrhenius behavior (Eq. (2)). The equilibrium between the effective O_2 pressure on the gas side and the oxygen vacancies (oxygen non-stoichiometry) is expressed by a Langmuir-like equation (Eq. (3)) with temperature-dependent coefficients (Eq. (4) and (5)).

Table 7.1. Model equations

Equation	id
$j_{V_{\ddot{O}}} = -D_{V_{\ddot{O}}} \nabla C_{V_{\ddot{O}}}$	(1)
$D_{V_{\ddot{O}}} = A_v \exp\left(-\frac{E_{a,v}}{T}\right)$	(2)
$\delta = \frac{3\,K\,p_{O_2}^m}{1 + K\,p_{O_2}^m}$	(3)
$\ln K = C_1 - \frac{C_2}{T}$	(4)
$m = C_3 + C_4\,T$	(5)
$j_{O_2,f}^s = \frac{1}{4^2\,F^2} \cdot \frac{\mu_{O_2,f}^s - \mu_{O_2,f}^*}{r_f}$	(6)
$j_{O_2,p}^s = \frac{1}{4^2\,F^2}\,\frac{\mu_{O_2,p}^* - \mu_{O_2,p}^s}{r_p}$	(7)
$r_f = r_{f,0} \cdot \left(\frac{P_{O_2,f}}{P_0}\right)^{-\frac{1}{n}}$	(8)
$r_{f,0} = A_f \exp\left(-\frac{E_{a,f}}{T}\right)$	(9)
$r_p = r_{p,0} \cdot \left(\frac{P_{O_2,p}}{P_0}\right)^{-\frac{1}{n}}$	(10)
$r_{p,0} = A_p \exp\left(-\frac{E_{a,p}}{T}\right)$	(11)

The transport of O_2 in the gaseous phases depends on the fluid dynamics. In the model, the Navier–Stokes equations were used under the assumptions of stationary and isothermal flow, negligible volume forces, density independent from composition, and Newtonian gas behavior.

The O_2 transfer in the feed gas was modeled using the Maxwell–Stephan diffusion approach, as the O_2 fraction is far from dilute conditions. This equation requires the estimation of the diffusivity matrix in terms of binary diffusion coefficients. In the sweep-gas compartment, as the O_2 concentration is low, the Fick’s law accurately describes the O_2 mass transfer in the gas phase. The binary diffusion coefficients were obtained from the Chapman-Enskog theory as a function of the temperature and molecular properties.

The flux on both membrane interfaces is proportional to the drop in chemical potential and inversely proportional to the transport surface resistances (r_f) and (r_p) in Eqs. (6) and (7), respectively. The drop in chemical potential through the membrane-gas interface is calculated with the O_2 effective pressure (in equilibrium with the concentration of oxygen vacancies in the membrane) and the gas O_2 pressure in contact with the membrane. According to the surface resistance model proposed by Zhu et al. [13], the resistances follow a pressure power-law (Eqs. (8) and (10)) with coefficient n = 0.5. The specific resistances of the feed side ($r_{f,0}$) and permeation side ($r_{p,0}$) followed an Arrhenius-like expression (Eqs. (9) and (11).

In the case of the one-dimensional implementation of the model, it was assumed that the only relevant gradients were those along the axial coordinate z. The equations resulting from this simplification are shown in Table 7.2.

Table 7.2. Equations used for the unidimensional model.

Equations	**id**
$j_{V_{\ddot{O}}} = -D_{V_{\ddot{O}}} \frac{C_{V_{\ddot{o}}}\Big\|_{z=0} - C_{V_{\ddot{o}}}\Big\|_{z=\Delta z}}{\Delta z}$	(12)
$j_{O_2,f} = k_f \cdot \frac{P_{O_2,f} - P_{O_2,f}^{s}}{R\,T}$	(13)
$j_{O_2,p} = k_p \cdot \left[\frac{P_{O_2,p}^{s}}{R\,T} - \left(\frac{P_{O_2,p}}{R\,T} + \frac{j_{O_2,p} \cdot A_{mod}}{2\,Q_p}\right)\right]$	(14)

Thereby, the O_2 flux caused by the diffusion of oxygen vacancies is simplified to Eq. (12). In this case, the Navier-Stokes and the rigorous transport equations cannot be used to obtain the O_2 transport in the gas phase domains. Instead, these equations were replaced by phenomenological expressions using a mass transfer coefficient (Eq. (13), (14)). Note that the latter equation takes into account an average O_2 pressure in the permeate compartment being expressed in its implicit form. In both equations, the mass transfer coefficients k_f and k_p were obtained from mass transfer simulations performed with the Multiphysics software for the gas compartments specific geometries as a function of gas inlet flow, temperature and gas composition.

Table 7.3. Values of the factors for the oxygen transport model.

Parameter	**Value**
C1	-1.0534
C2	-4170.7094 K
C3	$3.9175 \cdot 10^{-3}$
C4	$-2.2739 \cdot 10^{-5}$ K^{-1}
Molecular volume for BSCF	38.3 mol m^{-3}

7.3.2.2. Boundary conditions

The solution of the system of equations requires imposing proper conditions at the boundaries of the five considered regions. For the outmost boundaries, the pO_2 in the feed and sweep gas bulk must be imposed. For the innermost boundaries, flux-matching conditions at the gas-membrane interfaces were used (Eqs. (15) and (16)). At the feed side membrane surface, the flux from the feed gas must be equal to O_2 flux in terms of the surface resistance to transport (defined by Eq. (6)) and the O_2 flux caused by the filling of oxygen vacancies at the membrane surface. Apparently, at the permeate side, the O_2 flux originated by the formation of oxygen vacancies must equate the flux given by Eq. (7) and the O_2 flux from the gas in contact to the membrane side to the sweep-gas bulk.

$$j_{O_2,f}\Big|_{z=0} = j^{s}_{O_2,f} = \frac{1}{2}\, j_{V_{\ddot{O}}}\Big|_{z=0} \tag{15}$$

$$\frac{1}{2}\, j_{V_{\ddot{O}}}\Big|_{z=\Delta z} = j^{s}_{O_2,p} = j_{O_2,p}\Big|_{z=\Delta z} \tag{16}$$

In the case of the simplified one-dimensional approach, as there are not any flux components different from the axial one, all the fluxes for Eq. (6), (7), (12), (13) and (14) are equal.

7.3.2.3. Model equation

The equations of the multidimensional model (Table 7.1) were implemented in the software COMSOL Multiphysics v4.4. As the axial geometry permits using 2D computational domains, then the model complexity can be greatly reduced from a computational point of view if only radial and z-components of the equations are considered [39].

Therefore, three interconnected domains were considered: permeate, membrane, and feed compartments.

Figure 7.3 shows the meshing performed for the different domains. The membrane domain used a mesh based on quadratic elements using a mapped mesh type, while the gas phases were meshed using free triangular elements. For the boundary layers it was used a special type of meshing suitable for contours. The final mesh has an average quality mesh of 0.9316. The calculations were carried out using the Parallel Direct Solver (PARDISO) with parameter continuation to warrantee convergence, fixing the tolerance of the method at 0.001.

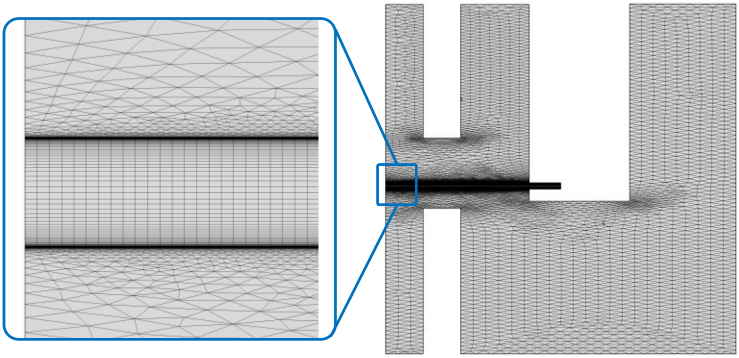

Figure 7.3. Mesh of the geometry

The simplified one-dimensional model was implemented in MATLAB and used the software numeric capabilities to solve the set of non-linear algebraic equations corresponding to the flux identity between domains. All scalar equations of Table 7.1 were used in the one-dimensional model. The expression for flux of oxygen vacancies was simplified to Eq. (12). The flux equations were expressed as a function of the inlet O_2 pressure, O_2 pressure in the gas in contact with the membrane surface and effective pressure in equilibrium with the oxygen vacancies. The application of the boundary equations required the calculation of these pressures and, consequently, of the O_2 fluxes.

7.3.3. Fitting procedure

The model equations include many parameters. To simplify the problem, the equilibrium related parameters of Eqs. (4) and (5) were taken from [40]. Even so, the amount of the remaining temperature dependent parameters was high. However, the quantity of parameters to be fitted becomes smaller if the fitting is performed independently for each temperature. Once the parameters for each temperature are obtained, they can be fitted to determine their temperature-dependent correlations.

According to this procedure, the experiments were divided into subsets for each temperature. Figure 7.4 schematized a procedure for the fitting of the parameters to the set of experimental results. The fitting procedure is based on the minimization of absolute value of the deviations of the values predicted for the model and the experimental points as a function of the parameters. However, this fitting procedure has the problem that many local minima can occur. To increase the possibilities to obtain a global optimum, optimization technique based on genetic algorithms was used although a large number of evaluations of the objective function were required. This optimization approach can be very time-consuming in the case of 2D models solved by a Multiphysics software.

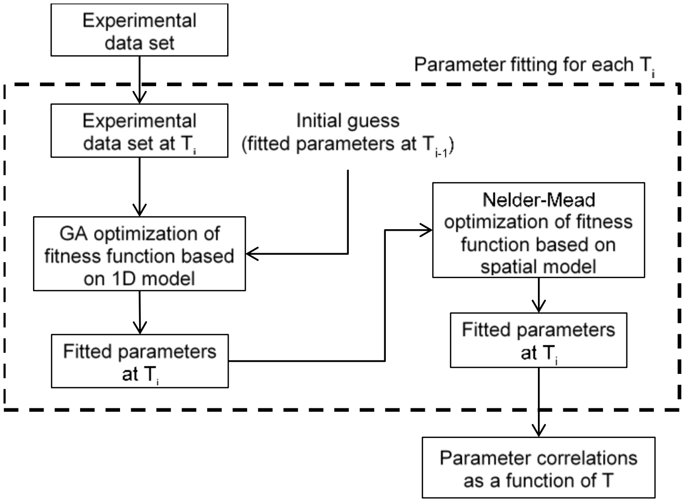
Experimental data set
Parameter fitting for each T_i
Experimental data set at T_i
Initial guess (fitted parameters at T_{i-1})
GA optimization of fitness function based on 1D model
Fitted parameters at T_i
Nelder-Mead optimization of fitness function based on spatial model
Fitted parameters at T_i
Parameter correlations as a function of T

Figure 7.4. Overall fitting procedure of the model parameters

The genetic algorithm used was a single genetic algorithm for real-coded parameters as described by Haupt and Haupt [41]. The individuals took the form of the parameter vector to be fitted and the objective function to be minimized was the medium square error (MSE) obtained between the calculated values for the present parameter vector and the experimental values at constant temperature. The algorithm starts from an initial population randomly generated around typical values for the parameters found in the literature [41]. The initial population size was 45. The population was improved for a number of generations of 800.

The values of the parameters obtained using the one-dimensional model were used as starting values for the fitting procedure using an objective function based on the 2D model. In this case, a direct method (Nelder-Mead) was sequentially applied to minimize the objective function by sequentially using the results given by COMSOL. The whole procedure was repeated for each temperature. Afterwards, linear fitting was applied between the logarithm of the parameters and the inverse of temperature to obtain the law of temperature dependence for each parameter. The fitting procedure of the vector of parameters was based on the minimization of the medium square relative error (MSRE) of the oxygen flux at given operating conditions (Eq (17)).

$$MSRE(\vec{p}) = \frac{1}{N}\sum_{i}^{N}\left(1 - \frac{j_{O2,i}^{calc}(\vec{p},\vec{y}_i)}{j_{O2,i}^{exp}}\right)^2 \qquad (17)$$

7.3.4. Description of the simulation studies

By using the fitted parameters, several studies were performed in order to analyze the influence of the main variables of the membrane and separation process. In addition, the use of vacuum pressure was studied as an alternative to using a sweep gas for many industrial applications. The conditions of the reference case used in the simulations are shown in Table 7.4. In the following sections, the specific conditions and ranges studied are described while keeping the rest of the conditions as depicted in Table 7.4.

Table 7.4. Conditions for the reference case. STP: Standard Temperature and Pressure

Parameter	Units	Values
Feed inlet composition	-	Air
Feed inlet flow	mL_{STP}/min	300
Pressure in the feed compartment	bar	1
Sweep inlet composition	-	Ar⁽¹⁾
Sweep inlet flow	mL_{STP}/min	300
Pressure in the sweep chamber	bar	1
Membrane thickness	µm	800
Temperature	°C	700, 800, 900, 1000

(1) Ar with $2\cdot10^{-5}$ bar of O_2

7.3.4.1. *Effect of the membrane thickness*

The membrane thickness was varied from 10 to 5000 µm to assess the relative importance of the bulk transport with respect to the other transport mechanisms involved in O_2 separation. The study was performed with and without considering surface-exchange resistances.

7.3.4.2. *Effect of the feed inlet flow*

The flow rate of the air feed was varied from 10 to 1250 mL_{STP}/min to characterize the fluid dynamic behavior in the feed compartment and to determine its impact in the O_2 flux as a function of temperature.

7.3.4.3. *Effect of the sweep inlet flow*

The gas sweeping causes different effects that influence the magnitude of the net O_2 flux. Namely, the gas sweeps the O_2 from the membrane surface and simultaneously dilutes the swept O_2 gas. Both effects enable to increase the driving force for oxygen transport. Both effects were investigated through the fluid-dynamics simulation in the permeate (sweep gas) compartment, i.e. by varying the sweep inlet flow rate in the range from 10 to 1000 mL_{STP}/min.

7.3.4.4. *Effect of the sweep gas composition*

He, CO_2 and steam were used as sweep gases for comparison with the reference gas (Ar). For all the three sweep gases, a pO_2 of $2 \cdot 10^{-5}$ bar was assumed at the inlet. CO_2 and steam may be adsorbed on the BSCF membrane surface, leading to changes in the O_2 surface-exchange kinetics and in the material microstructure, thus affecting negatively the O_2 permeation [9,11,12,42,43]. However, the model does not consider this specific surface phenomena and, therefore, the simulation only will account for fluid dynamic effects related with molecular mass, viscosity and differences of oxygen diffusion in these gases.

7.3.4.5. *Apparent activation energy*

Taking into account the simulation results obtained by varying the feed and sweep inlet flow rates, two situations according to the magnitude of the concentration polarization were studied for all sweep gases: (i) situation with relative low sweep gas flow; and (ii) situation of high sweep gas flow, i.e. the effect of concentration polarization may be negligible. The comparison of both situations made possible to determinate the effect of the concentration polarization on oxygen flux and the associated (apparent) activation energy. Indeed, the apparent activation energy is usually determined experimentally and is used as a good indicator of the most probable rate-limiting step in O_2 separation with ionic membranes.

7.3.4.6. *Fluid-dynamic dimensionless studies*

The analysis of the CFD results on the effect of the sweep gas in the oxygen transport across the membrane was made considering correlations of dimensionless numbers. For this kind of processes where the permeation is governed by the oxygen transference across the membrane, a correlation is needed to correlate gas transference, gas diffusions and fluid-dynamics. The typical correlation for this kind of phenomena uses the equation (18) [44–49], which relates the Sherwood number ($Sh = \frac{k_m \cdot L_c}{D}$), Reynolds number $\left(Re = \frac{\rho \cdot u \cdot L_c}{\mu}\right)$ and Schmidt number $\left(Sc = \frac{\mu}{\rho \cdot D}\right)$.

$$Sh = a \cdot Re^{b} \cdot Sc^{c} \tag{18}$$

Where a, b, and c are the constants of the correlation. A typical value for c for this correlation is 1/3. The material transference coefficient (k_m) was measured considering:

$$J_{O2} = k_m \cdot \Delta C_{O2} \tag{19}$$

$$k_m = \frac{J_{O2}}{\Delta C_{O2}} \tag{20}$$

Where ΔC_{O2} is the oxygen concentration gradient in the surroundings of the membrane.$\Delta C_{O2,feed} = C_{O2,chamber} - C_{O2,membr}$ for the feed chamber and $\Delta C_{O2,sweep} = C_{O2,membr} - C_{O2,chamber}$ for the sweep chamber.

7.3.4.7. Vacuum extraction system

The simulation of a vacuum extraction system in the same set-up required the implementation of several changes in the model. The sweep gas inlet was removed, and the sweep gas outlet was replaced by the vacuum extraction tool included in the COMSOL software at the corresponding pressure. The composition of the compartment was adapted according to O_2 properties. The considered vacuum pressures ranged from 10 to 200 mbar. The feed inlet for all cases was 500 mL$_{STP}$/min of standard air.

7.3.Results

7.3.5. Fitting results

Figure 7.5 shows the fitting results for D_V, r_f and r_p as a function of temperature. The diffusion coefficient of oxygen vacancies (D_V) fits an Arrhenius expression (Figure 7.5a) with a correlation factor of > 0.99. The temperature dependence of the parameters associated to gas-exchange surface resistance (Figure 7.5b) was different for each membrane side. In the case of the feed – membrane surface, the resistance parameter r_f decreases with temperature and the results fit to an Arrhenius equation (Figure 7.5b). For the membrane – sweep surface, the resistance parameter rp decreases until 800 °C, and it almost stabilizes its value above this temperature. The results after fitting to an Arrhenius expression are shown in Table 7.5. The activation energy values of D_V are similar to those obtained elsewhere but the surface resistances present lower values because of a small pre-exponential factor [24,50–55].

Table 7.5. Parameter fitting as a function of the temperature $f(T) = A \cdot \exp\left(-\frac{Ea}{RT}\right)$

Coefficient	**A**	**units**	**E_a**	**Units**
D_{Vo}	8.471E-5	m^2/s	63.853	kJ/mol
$r_{f,0}$	2.700E-6	$\Omega \cdot cm^2$	-78.133	kJ/mol
$r_{p,0}$ **(T < 800 °C)**	7.223E-5	$\Omega \cdot cm^2$	-33.035	kJ/mol
$r_{p,0}$ **(T > 800 °C)**	3.770E-3	$\Omega \cdot cm^2$	2.272	kJ/mol

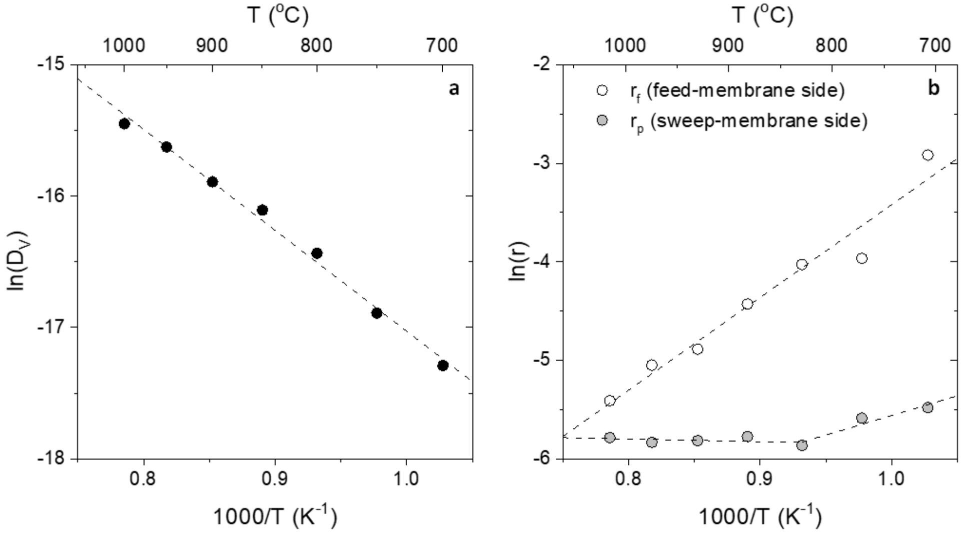

Figure 7.5. Fitting results (a) diffusion coefficient of oxygen vacancies (b) Pre-exponential factors for surface resistances.

Figure 7.6 compares the experimental results (data points) of O_2 flux (J_{O2}) with model simulations (solid lines) using the fitted parameters as a function of the pO_2 of each chamber. In the studied range, the experimental data have similar values to those reported in other works [54,56–61] for BSCF membranes. In Figure 7.6a, the pO_2 of the feed inlet is varied at different temperatures while the sweep inlet composition remains fixed, as can be seen, the obtained CFD model fits the experimental results with a high degree of accuracy. Similarly, Figure 7.6b illustrates the goodness of the fitting when the pO_2 of the sweep gas is varied at a fixed feed inlet composition.

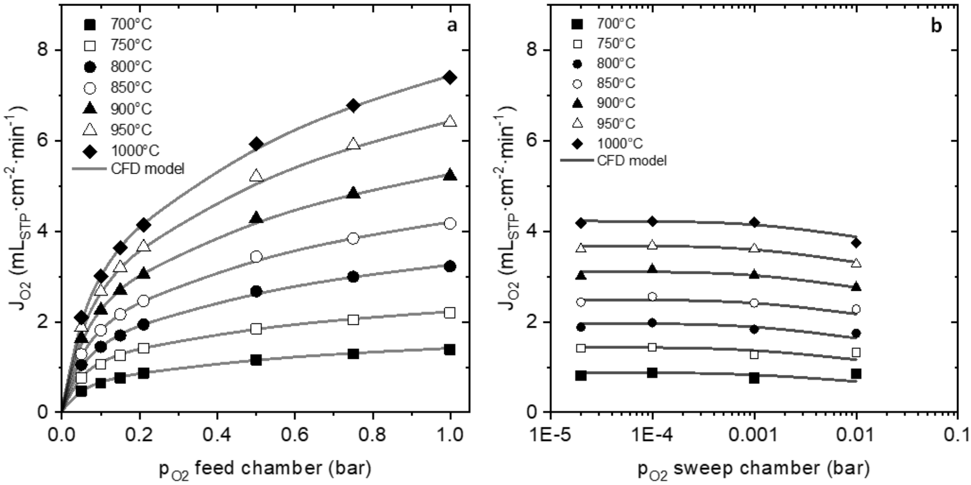

Figure 7.6. Comparison of experimental results (points) and model simulations using the fitted parameters (full lines) for oxygen flux at different temperatures (a) Effect of the oxygen partial pressure of the feed inlet; (b) Effect of the oxygen partial pressure of the sweep gas inlet (feed inlet conditions: air, 300 mL_{STP}/min; sweep inlet conditions: argon, 300mL_{STP}/min, membrane thickness: 1mm).

7.3.6. Results of the CFD simulations of the 3D permeation setup

7.3.6.1. Effect of membrane thickness

As a general rule, the higher the membrane thickness the higher the bulk-transport resistance towards O_2 permeation, hence an improvement in J_{O2} can be expected when reducing thickness as long as bulk-transport governs the O_2 separation. Figure 7.7 shows the J_{O2} calculated by using the CFD model from the fitted parameters as a function of the membrane thickness at different temperatures. On one hand, if gas-exchange surface resistances are considered in addition to bulk-transport resistances, J_{O2} does not increase (solid lines) when reducing membrane thickness below 100 µm. On the other hand, if the effect of surface resistance is neglected in the model and only bulk-transport is considered, the flux increases as the membrane thickness is decreased in the considered range. Therefore, for thicknesses around 100 µm, the surface resistances fully control the permeation process, with no beneficial effects in J_{O2} if thickness is reduced. At thicknesses above 100 µm, both model considerations lead to a similar J_{O2} behavior with a performance worsening with thickness increments, since the process is mainly controlled by the bulk transport of oxygen vacancies.

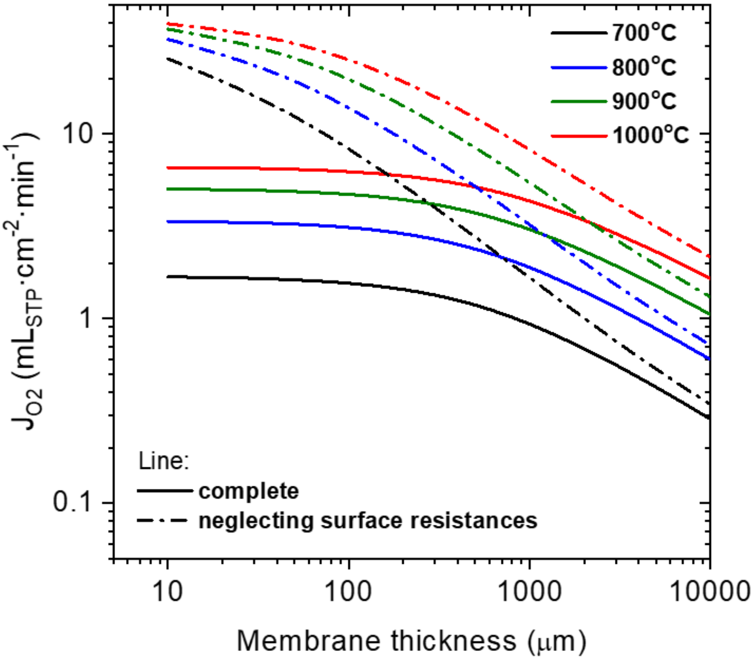

Figure 7.7. Effect of thickness on the average oxygen flux (Feed inlet conditions: air, 300mL$_{STP}$/min; sweep inlet conditions: argon ($2·10^{-5}$ bar O_2), 300mL$_{STP}$/min).

From the CFD model it was also possible to determine the contribution of the different resistances in dependence of thickness and temperature.

Figure 7.8 shows the relative distribution of the different resistances in a thickness range from 10 to 10000 µm at 1000, 850 and 700 ºC. As it can be seen and as it was previously mentioned, for thicknesses below 100 µm the bulk resistance effect is not significant in comparison with the gas-exchange surface resistances in both feed and sweep sides for all the considered temperatures.

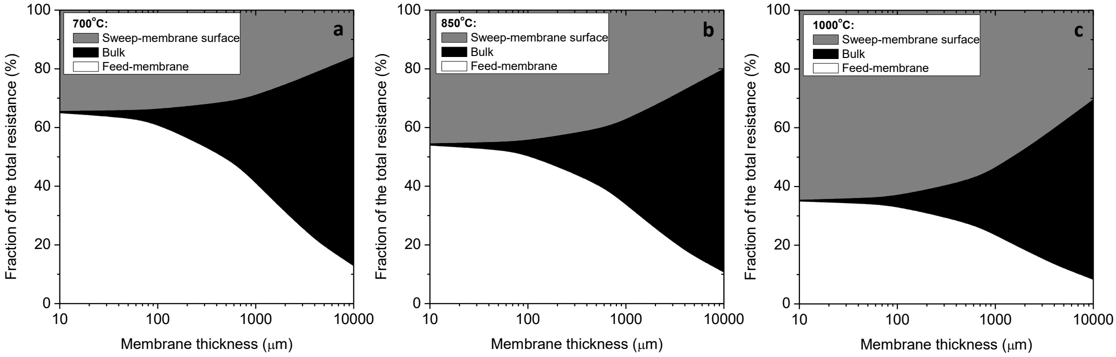

Figure 7.8. Contribution of the different resistances to the total resistance to oxygen permeation (a) 700 °C, (b) 850 °C, (c) 1000 °C. Feed inlet flow 300mL$_{STP}$/min, feed inlet: air, sweep inlet flow 300mL$_{STP}$/min, sweep inlet: Ar ($2\cdot10^{-5}$ bar O_2)

Concerning the contribution of the surface resistances, there is a stronger limiting effect of sweep side surface exchange reactions at higher temperatures and low thicknesses, whereas at lower temperatures the surface reactions at feed side become more dominant. The latter is due to oxygen reduction reactions occurring at feed side are more dependent on temperature, being then slower at low temperatures with respect to oxygen oxidation reactions. The state-of-the-art BSCF asymmetric membranes considered for practical applications present thicknesses in the range from 10 to 60 µm, therefore it is necessary the conduction of surface activation strategies for optimizing the O_2 permeation performance [7,62]. For the highest thickness values studied, the bulk resistance becomes comparable to the surface resistances. At 700 °C (Figure 7.8a) and 850 °C (Figure 7.8b), the resistances of the three contributions are similar, while at 1000 °C (Figure 7.8c), the surface resistance on sweep side represents almost half of the total resistance. Other authors have reported similar resistance distribution [13,54].

7.3.6.2. *Effect of the feed flow*

Figure 7.9 shows the effect of feed flow rate in J_{O2} for a 0.8 mm-thick BSCF membrane at different temperatures. For the considered membrane thickness, both the gas-exchange surface and the bulk resistances are in the same order of magnitude. As can be seen in Figure 8, the influence of feed flow rate is significant at low values, with a sharp J_{O2} decrease below 100 mL_{STP}/min for all the considered temperatures, whereas at flow rates above this value the O_2 fluxes are barely improved. This is due to concentration polarization phenomena occurring at feed side surface when the provided O_2 is insufficient for satisfying the high transport of O^{2-} through the bulk. Therefore, for high-permeating materials such as BSCF, if the amount of O^{2-} transported through the oxygen vacancies is higher than the supplied O_2 (this happening at low feed flows), then a significant decrease of the local pO_2 occurs at the membrane feed side surface due to an O2 depletion in the gas phase. This produces a reduction in the driving force through the membrane and subsequently in the O_2 permeation. Instead, at higher feed flow rates the O_2 supply is sufficiently high for ensuring the O^{2-} bulk diffusion and therefore no significant gain in $J(O_2)$

is obtained by increasing the feed flow. This polarization concentration resistance takes place at all the temperatures, but it is more limiting at higher temperatures due to the higher O^{2-} bulk diffusion, as can be seen for the 1000 ºC results. The same behavior was reported for Zhu et. al. [13] and Wang et. al. [58].

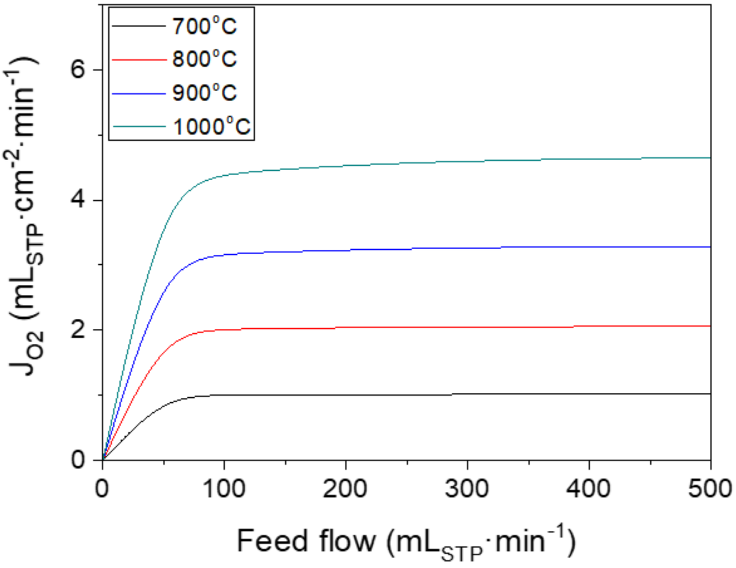

Figure 7.9. Effect of the feed inlet flow on the average oxygen flux for different temperatures. (Feed conditions: air , Sweep inlet conditions : Ar ($2\cdot10^{-5}$ bar O_2) 300 ml$_{STP}$/min, membrane thickness: 0.8mm).

7.3.6.3. *Effect of the sweep inlet flow*

Similarly to the feed side, the permeate side is also affected by concentration polarization resistances in the way that an accumulation of O_2 on membrane surface generates an increase in the pO_2 thus lowering the pO_2 gradient across the membrane and, as previously explained, the J_{O2}. Such an accumulation arises from a poor O_2

desorption from the membrane surface due to an inefficient sweeping. The sweep inlet flow causes velocity gradients on the membrane surface that depend on the module geometry. The gas velocity gradients determine the O_2 concentration profile in the sweep gas compartment that, at the same time, influence the oxygen transport. Therefore, it is of great importance to study the effect of the sweep flow rates on the pO_2 profiles for understanding its influence on the maximization of J_{O2}. Figure 7.10 shows the effect of the sweep inlet flow on the average O_2 flux, the average pO_2 and the average shear rate on the membrane surface. The pO_2 is calculated as the average values at 2 mm from the membrane surface. From the obtained results it is confirmed that as the sweep inlet flow rate increases, the O_2 in the sweep compartment is more diluted, and therefore, the J_{O2} increases as a consequence of the increased driving force. For sweep gas flow rates greater than 300 mL_{STP}/min (approximately 10^4 s^{-1} of average shear rate) the sweep inlet flow does not significantly influence the oxygen flux, thus setting the optimal value for 0.8 mm-thick BSCF membranes.

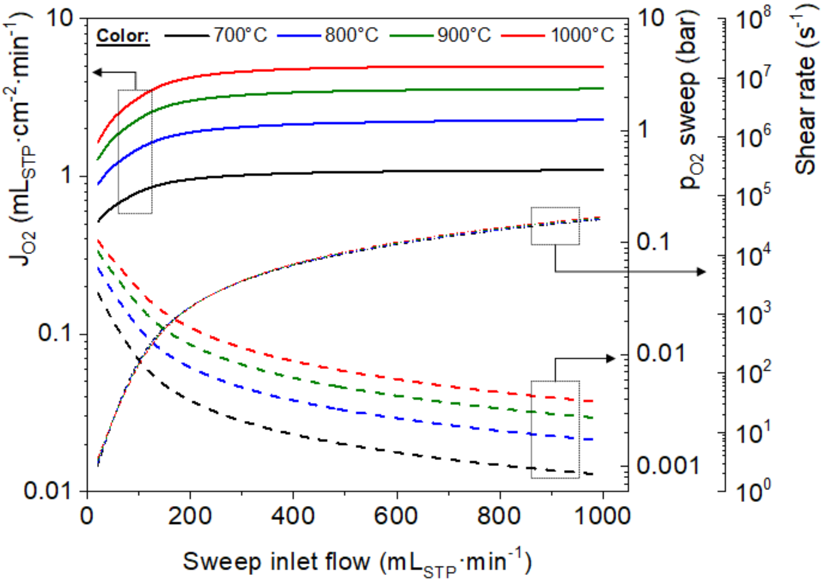

Figure 7.10. Effect of the sweep flow on the average oxygen flux, partial pressure over the membrane surface and shear rate. Feed inlet flow: 300mL_{STP}/min; feed inlet: air, sweep inlet: Ar ($2\cdot10^{-5}$ bar O_2), membrane thickness: 0.8mm.

Figure 7.11 shows the pO_2 profile for different sweep inlet flows at 1000 °C. Regarding the pO_2 in the feed compartment, the polarization effects were not significant, even for the highest sweep inlet flows studied. However, in the sweep compartment, the polarization effect is important at low sweep inlet flows, since (i) the sweep stream does not dilute sufficiently the permeated O_2 and (ii) the velocity close to the membrane is not high enough to sweep the O_2 and to properly mix with it the main gas stream.

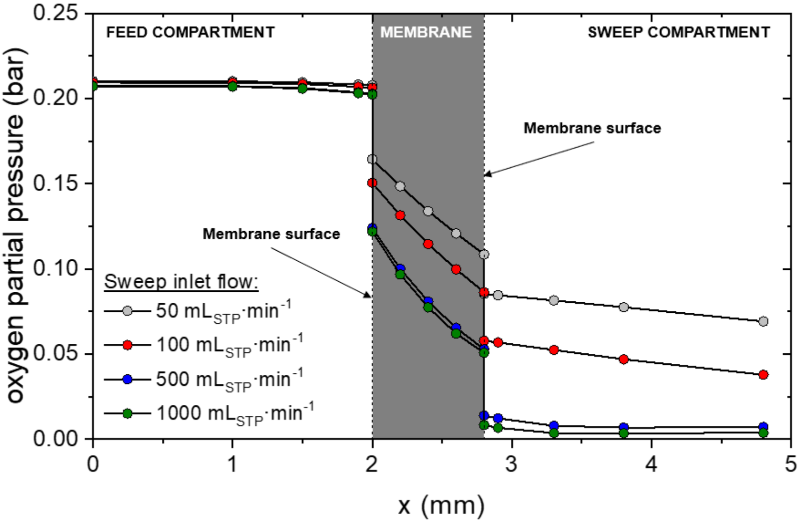

Figure 7.11. Oxygen partial pressure profile at different sweep inlet flows and 1000 °C. Feed inlet flow: 300mL$_{STP}$/min; feed inlet: air, sweep inlet: Ar ($2\cdot10^{-5}$ bar O_2), membrane thickness: 0.8 mm.

7.3.6.4. *Analysis of the apparent activation energy*

Taking into account the previous results, the effect of the thickness in the apparent activation energies related to the O_2 flux was studied for three cases according the fluid dynamic regime: (i) the reference case; (ii) a case with low concentration polarization; and (iii) a case with high concentration polarization. The conditions of each case are described in Table 7.6.

Table 7.6. Conditions for the activation energies study

Case	**Feed inlet flow**	**Feed inlet**	**Sweep inlet flow**	**Sweep inlet O_2**
Units	*mL$_{STP}$/min*	-	*mL$_{STP}$/min*	*bar*
Reference	300	Air	300	$2\cdot10^{-5}$
Low polarization	300	Air	500	$2\cdot10^{-5}$
High polarization	50	Air	50	$2\cdot10^{-5}$

Figure 7.12 shows the O_2 flux for three different membrane thicknesses (10, 100 and 1000 microns) in dependence of temperature. It is commonly found that the apparent activation energies (E_A) for oxygen permeation change their values above a certain temperature [19,63,64]. In our case, the results showed a change in E_A at a temperature near to 800 °C.

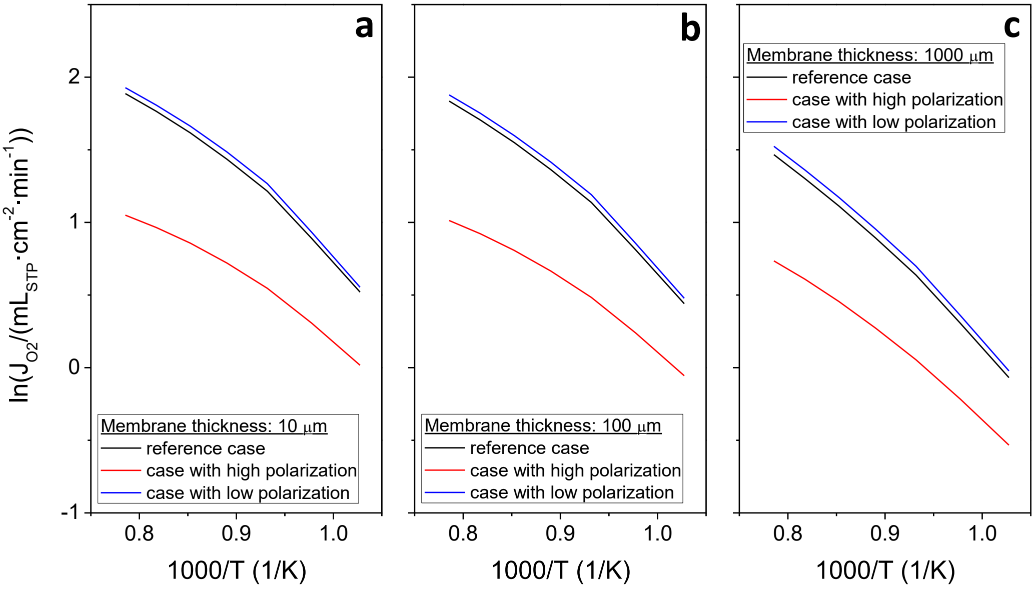

Figure 7.12. Oxygen flux. Thickness: 0.8mm, feed inlet: air, sweep inlet: Ar ($2 \cdot 10^{-5}$ bar O_2). R = Reference case, LP = case with low polarization, HP = case with high polarization

Figure 7.13 shows the results of the E_A for the considered cases. The case with high polarization has the lowest E_A values, while the reference case and the case with low polarization present similar results. For all cases, the E_A is lower at high temperatures (HT) than at lower temperatures (LT). At LT the E_A for the reference and low polarization cases do not significantly vary with the membrane thickness, while for the high polarization case, it increases with the membrane thickness (specially above of 100 µm). At HT, there is a notable raise in the E_A with the thickness. These results are in line with previous experimental works [13,54] and enables to quickly interpret typical experimental results in O_2 permeation.

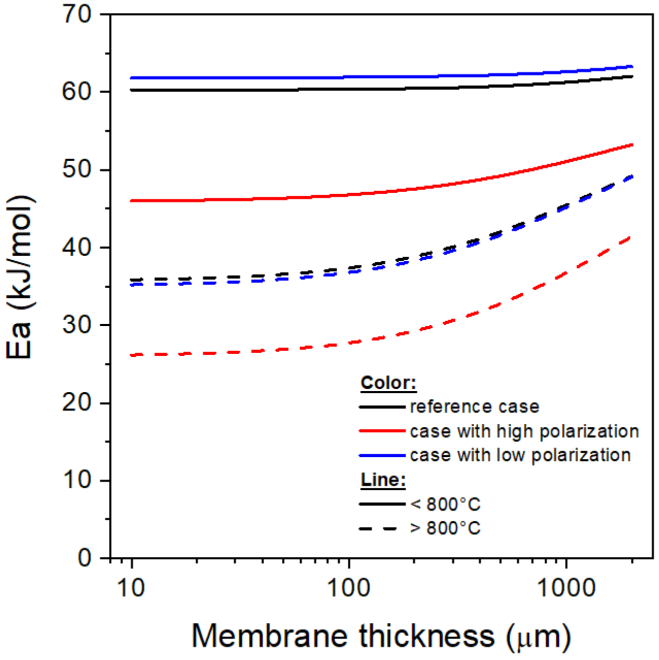

Figure 7.13. Apparent activation energies at LT (low temperature, <800 °C) and at HT (high temperature, >800 °C). Feed inlet: air, sweep inlet: Ar ($2\cdot10^{-5}$ bar O_2).

Figure 7.14 does not show a linear relation between $ln(p_{O2,feed}/p_{O2,sweep})$, considered as apparent driving force of the oxygen flux. At this thickness (0.8 mm), there is not a single phenomenon that controls the process, but all the phenomena have significant contributions in the process.

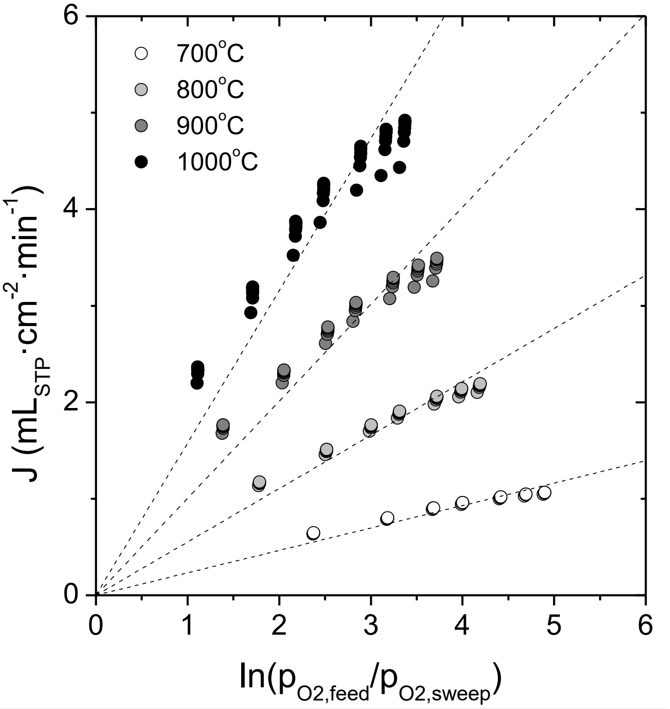

Figure 7.14. Apparent driving force. Thickness: 0.8mm; feed inlet flow: 50 – 500 mL$_{STP}$/min; feed inlet: air; sweep inlet flow: 50 – 500 mL$_{STP}$/min; sweep inlet: Ar ($2\cdot10^{-5}$ bar)

Figure 7.15 compares the *pO2* profiles for the high and low polarization cases. In Figure 7.15a (high polarization case) it can be observed a considerable *pO2* gradient in the sweep compartment near to the membrane surface. Furthermore, the O_2 profile in the feed compartment shows that the permeated O_2 causes the pO_2 in contact with the membrane to be lower than the pO_2 in the inlet feed. Otherwise, Figure 7.15b (low polarization case) shows that the pO_2 on the membrane surface has practically the same value than in the feed. In this case, the streamlines indicate the formation a swirl close to the membrane.

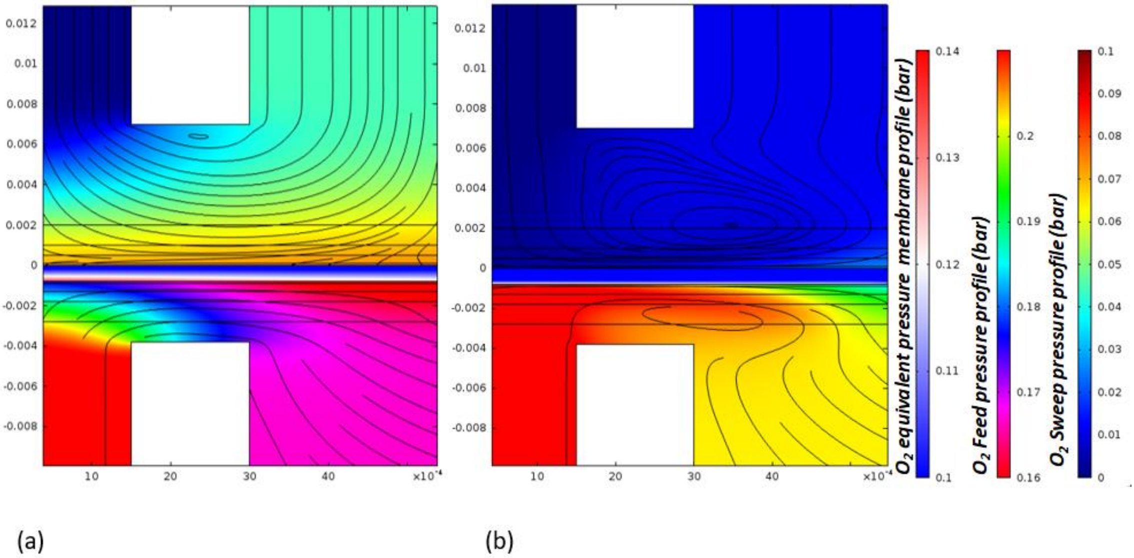

(a) (b)

Figure 7.15. Oxygen pressure profile for the high polarization case (a) and the low polarization case (b) at 1000ºC. Streamlines: speed pathways.

7.3.6.5. *Effect of the sweep gas composition on the oxygen transport in the gas phase*

Considering the model established from the experimental data (obtained by using Ar as sweep), it was studied the effect of varying the type of sweep gas on the O_2 transport in the gas phase. For conducting this study, it was considered the sweeping of a BSCF membrane with Ar, CO_2, H_2O and He. Note that the possible effects on the surface resistance due to gas composition are not considered in the study (e.g., CO_2 and H_2O completive adsorption on the surface of ionic membrane), i.e., only the fluid dynamic and diffusional characteristics are considered. Figure 7.16a shows the results of O_2 flux at different temperatures and sweep inlet flow for the four gases studied. The O_2 flux obtained using He as sweep is lower than that obtained with the other gases for values of sweep inlet flow higher than 100 mL_{STP}/min, whilst the J_{O2} tends to the same value for all gases at very high values of sweep gas flow. As the molecular mass of He is notably smaller than the other considered gases, therefore its ‘sweeping capacity’ is also smaller. Figure 7.16b shows the shear rate on the membrane surface from the same simulations as an indicator of the ‘sweeping capacity’ in the way that the higher the shear rate the more effective the sweeping. At low sweep gas flows (high concentration polarization), all gases lead to similar shear rate values, but at high sweep flow values (high concentration polarization), the use of Ar, CO_2 or steam leads to shear rates two orders of magnitude higher than those of He, thus explaining the J_{O2} results observed in Figure 7.16a.

Figure 7.17 shows the apparent activation energy for the different gases. At low temperature ($T < 800$ °C) all gases have the same behavior. However, at high temperatures, He has higher activation energy than the rest of the gases.

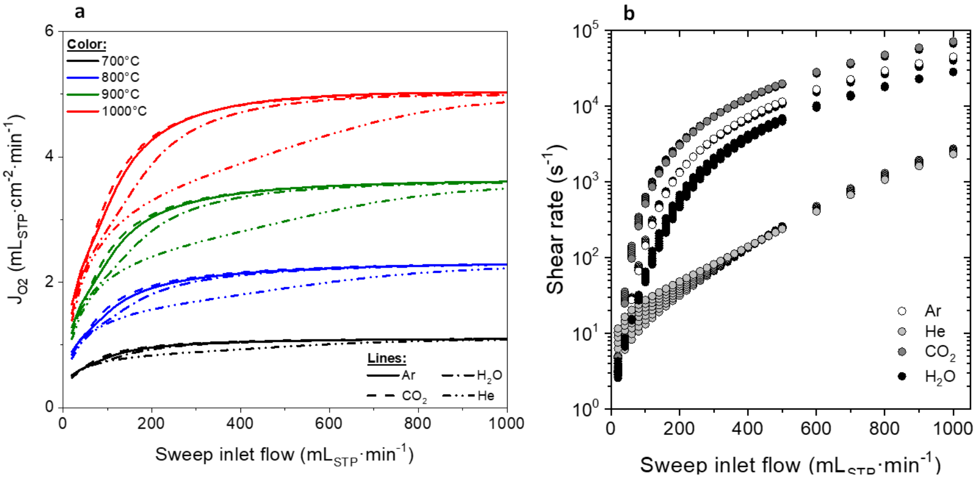

Figure 7.16. (a) Oxygen flux for different sweep gases (reference case) (b) shear rate in the sweep – membrane surface using different sweep gases (different sweep gas flow at reference conditions)

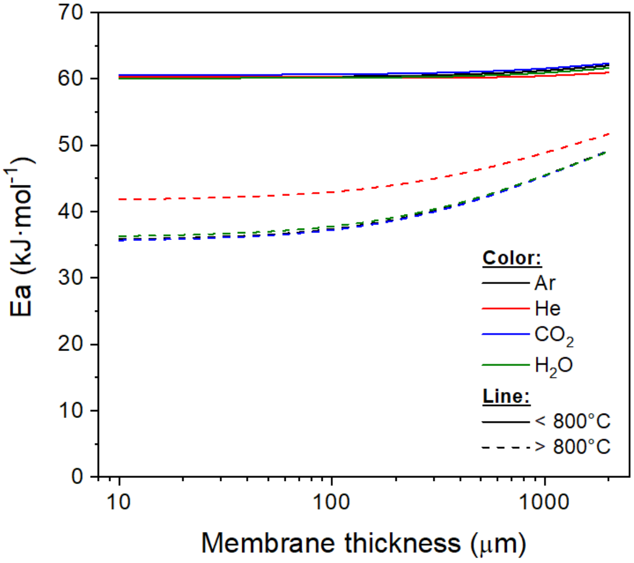

Figure 7.17. Activation energy at LT (low temperature, T < 800 °C) and at HT (high temperature, T > 800 °C)

Finally, Figure 7.18 shows results of fitting the correlation between Sherwood (*Sh*), Reynolds (*Re*) and Schmidt (*Sc*) numbers (equation 18). Plot shows the relation Sh/Sc^c, with c = 1/3 depending on Reynolds number, as expected for mass transport processes in gases. This plot provides an idea about the effect of the inertial forces effect on the permeation. At Reynolds lower than around 8 – 10, the inertial forces do not present any effect in the oxygen transport, thus for these lower values, the oxygen transport is due only for the difference of partial pressures and it is expected polarization close of the membrane appear due to that low inertial strength of the gas. At Reynolds higher than 8 – 10, the increase of the inertial forces in the gas improves the oxygen transference and, as consequence, the inertial forces enable to improve the sweeping of the oxygen permeated.

Table 7.7 shows the comparison of the values for the fluid dynamic correlation for this study (before the fitting and after the fitting) and previous works [44–49]. The correlation values are in line with those reported elsewhere while the fitted constants are similar to the reported in the bibliography [44,45,47,48] using this correlation (eq. 18).

Table 7.7. Comparison of the values for the fluid dynamic correlation ($Sh=a \cdot Re^b \cdot Sc^c$).

Composition	***a***	***b***	***c***
O_2 - Ar	0.4361	0.9318	1/3
O_2 - steam	0.3577	1.0026	1/3
O_2 - CO_2	0.5121	0.8936	1/3
O_2 – Global (sweep)	0.4394	0.9323	1/3
O_2 – Air (feed)	0.5309	0.697	1/3

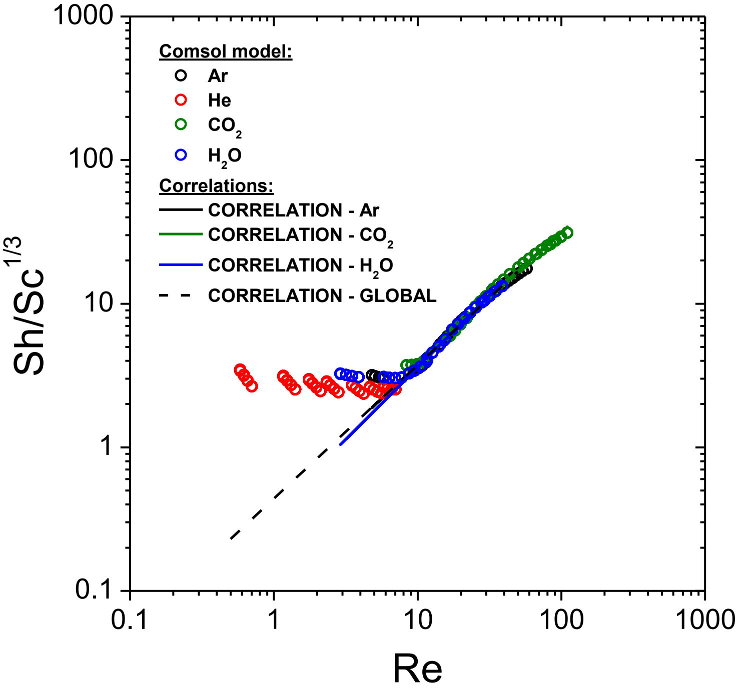

Figure 7.18. Evaluation of the fluid dynamic effect in the oxygen permeation using correlations of Sherwood, Reynolds and Schmidt dimensionless numbers.

However, and although it is expected that the dilution effect has a higher effect in the O_2 permeation than the inertial effect (or sweep effect). This analysis reveals the importance of the sweep gas in the oxygen transport process. Therefore, in order to avoid polarizations in this chamber, the suitable gas compositions and flow shall be chosen carefully. These considerations could be critical when upscaling the permeation system to minimize the required membrane surface area, and thus the related capital expenses.

7.3.6.6. Vacuum system

Finally, the performance of a vacuum system was compared with that of case using sweep gas at an inlet flow for which low concentration polarization is obtained (500 mL_{STP}/min). Figure 7.19a shows that similar O_2 flux values to those of the sweep gas case are obtained for a vacuum pressure of 10 mbar. For this vacuum pressure, the O_2 flux is higher than that of the sweep gas case at temperatures higher than 800 °C and smaller under this temperature. The reason of this behavior can be seen in Figure 7.19b. Under this temperature value, the average pO_2 on the membrane surface is higher using vacuum pressure and, consequently, the driving force is smaller.

As it can be seen, compared with the situations in which a sweep gas is used, there is not significant changes in the slope if vacuum pressure is used. A previous work reported similar results for tubular devices [58].

Figure 7.20 shows the pO_2, velocity profiles and streamlines for a vacuum pressure of 10 mbar at 1000 °C. Comparing the pO_2 profiles (Figure 7.20a) with one obtained using sweep gas, it can be observed that the vacuum systems achieve a more homogeneous O_2 profile in the sweep compartment. Therefore, by using vacuum pressure there is not stagnant flow near to the corners and all the membrane surface is active for transport.

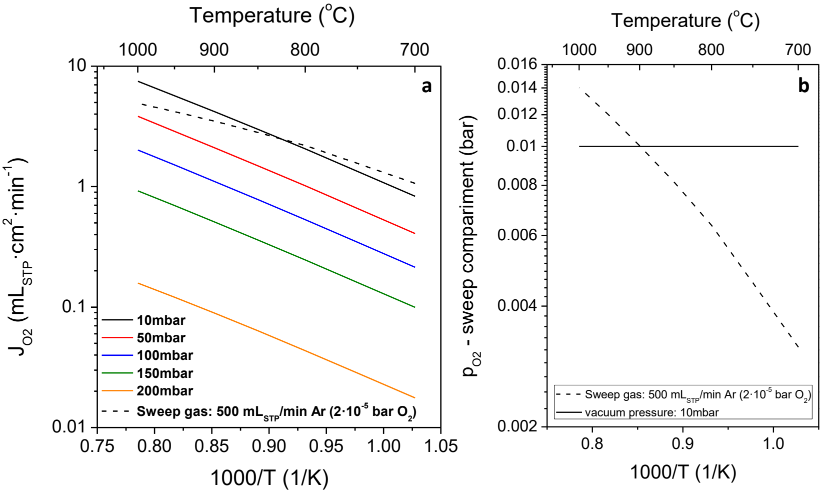

Figure 7.19. Vacuum results. (a) Oxygen flux results; (b) oxygen partial pressure in the sweep compartment. Feed inlet flow: 300mL$_{STP}$/min; feed inlet: air; thickness: 0.8mm

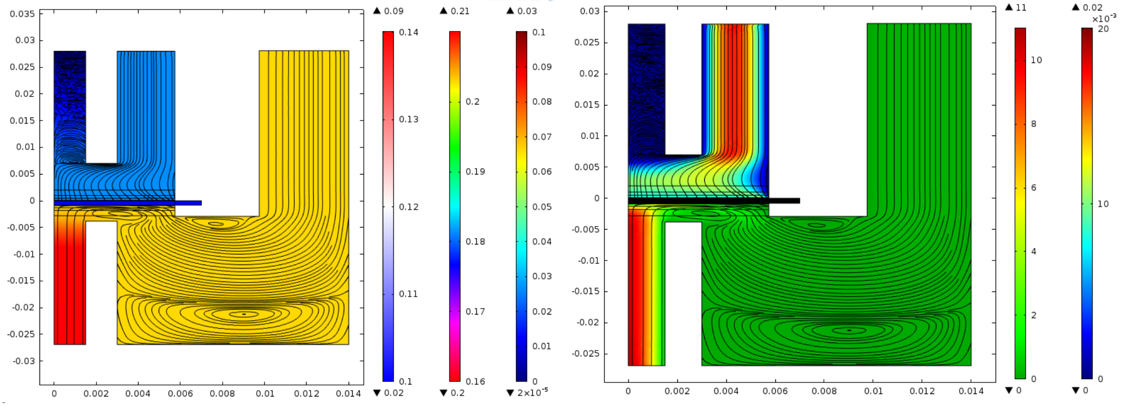

Figure 7.20. contour plots. (a) O_2 partial pressure profile (left bar: pressure profile in the vacuum compartment; middle bar: O_2 partial pressure in the feed compartment; right bar: O_2 equivalent pressure in the membrane; streamlines: speed pathways); (b) speed profile (left bar: O_2 flow profile in the membrane; middle bar: speed profile in the feed compartment; right bar: speed profile in the vacuum compartment; streamlines: speed pathways). Feed inlet flow: 500 mL$_{STP}$/min; feed inlet: air; vacuum pressure: 50 mbar; 1000 °C.

7.4.Summary

Finite element model was built to evaluate the oxygen transport across MIEC ceramics at high temperature. This methodology allows to evaluate locally all the phenomena involved on the oxygen permeation process. A fitting of the model to experimental results was done with the parameters of the surface and bulk diffusion parameters of the model. The advantage of this methodology is conventional 0D methodology can be influenced for polarization phenomena while this methodology evaluates locally all the phenomena.

The exploitation of the fitted model has revelated the oxygen permeation are controlled (or limited) for the bulk diffusion for the high thicknesses of the membrane (>2mm). Polarization effect causes higher limitations on the oxygen transport when appears on the sweep side. The polarization can be presented on the sweep chamber for a not suitable sweep of the oxygen permeated. As this work reveals, the bas sweep is due to the inert gas used to sweep the oxygen does not have enough force to gather the oxygen. The study reveals that, although the diluting effect of the sweep gas have higher influence on the oxygen transport, the sweep effect is not neglectable (mainly due to the appearance of polarization problems). Finally, a comparison with vacuum extraction of the oxygen permeated was performed. This last study allows to evaluate how high vacuums are needed to achieve similar oxygen results than using sweep gas.

List of symbols

A_f	Pre-exponential factor of the feed-membrane surface resistance
A_p	Pre-exponential factor of the permeate-membrane surface resistance
A_v	Pre-exponential factor of the diffusion coefficient of oxygen vacancies
A_{mod}	Membrane active area
$C_{V\ddot{o}}$	Molar concentration of oxygen vacancies
C_i	Coefficients for equilibrium equation
$D_{V\ddot{o}}$	Diffusion coefficient of oxygen vacancies
E_A	Activation energy
$E_{a,f}$	Activation energy factor of the feed-membrane surface resistance
$E_{a,p}$	Activation energy of the permeate-membrane surface resistance
$E_{a,v}$	Activation energy of the diffusion coefficient of oxygen vacancies
F	Faraday constant

j_{O2}	Molar flux of oxygen
$j_{Vö}$	Molar flux of oxygen vacancies
J_{O2}	Flux of oxygen
k	Mass-transfer coefficient
K	Temperature dependent coefficient of the oxygen non-stoichiometry
m	Temperature dependent exponent of the oxygen non-stoichiometry
n	Exponential coefficient for oxygen pressure dependence of surface resistance
P_{O2}	Oxygen partial pressure
P_0	Reference pressure
Q_p	inlet flow of sweep gas
R	Universal gas constant
Re	Reynolds number
r_f	resistance parameter at the feed-membrane surface
r_p	resistance parameter at the permeate-membrane surface

$r_{f,0}$	Pre-exponential factor of surface resistance at the feed-membrane surface
$r_{p,0}$	Pre-exponential factor of surface resistance at the permeate-membrane surface
Sc	Schmidt number
Sh	Sherwood number
T	Absolute temperature

Greek letters:

δ	Oxygen non-stoichiometry
Δz	Membrane thickness
μ_{O2}	Oxygen chemical potential

Subscripts

f	Feed side
p	Permeate side
z	z-direction

Superscripts

*	Gas property calculated in equilibrium with the oxygen vacancies

s	Gas-membrane surface

7.5.References

[1] M.A. Habib, H.M. Badr, et al., A review of recent developments in carbon capture utilizing oxy-fuel combustion in conventional and ion transport membrane systems, Int. J. Energy Res. 35 (2011) 741–764. doi:10.1002/er.1798.

[2] S.S. Hashim, A.R. Mohamed, et al., Oxygen separation from air using ceramic-based membrane technology for sustainable fuel production and power generation, Renew. Sustain. Energy Rev. 15 (2011) 1284–1293. doi:10.1016/J.RSER.2010.10.002.

[3] P. Markewitz, J. Marx, et al., Ecological Evaluation of Coal-fired Oxyfuel Power Plants -cryogenic Versus Membrane-based Air Separation-, Energy Procedia. 37 (2013) 2864–2876. doi:10.1016/J.EGYPRO.2013.06.172.

[4] M. Puig-Arnavat, S. Soprani, et al., Integration of mixed conducting membranes in an oxygen–steam biomass gasification process, RSC Adv. 3 (2013) 20843. doi:10.1039/c3ra44509g.

[5] S. Smart, C.X.C. Lin, et al., Ceramic membranes for gas processing in coal gasification, Energy Environ. Sci. 3 (2010) 268. doi:10.1039/b924327e.

[6] R. Castillo, Thermodynamic analysis of a hard coal oxyfuel power plant with high temperature three-end membrane for air

separation, Appl. Energy. 88 (2011) 1480–1493. doi:10.1016/J.APENERGY.2010.10.044.

[7] S. Baumann, J.M. Serra, et al., Ultrahigh oxygen permeation flux through supported Ba0.5Sr0.5Co0.8Fe0.2O3−δ membranes, J. Memb. Sci. 377 (2011) 198–205. doi:10.1016/J.MEMSCI.2011.04.050.

[8] M.J. den Exter, W.G. Haije, et al., Viability of ITM Technology for Oxygen Production and Oxidation Processes: Material, System, and Process Aspects, in: Inorg. Membr. Energy Environ. Appl., Springer New York, New York, NY, 2009: pp. 27–51. doi:10.1007/978-0-387-34526-0_2.

[9] S. Engels, F. Beggel, et al., Simulation of a membrane unit for oxyfuel power plants under consideration of realistic BSCF membrane properties, J. Memb. Sci. 359 (2010) 93–101. doi:10.1016/J.MEMSCI.2010.01.048.

[10] Z. Shao, W. Yang, et al., Investigation of the permeation behavior and stability of a Ba0.5Sr0.5Co0.8Fe0.2O3−δ oxygen membrane, J. Memb. Sci. 172 (2000) 177–188. doi:10.1016/S0376-7388(00)00337-9.

[11] M. Arnold, H. Wang, et al., Influence of CO2 on the oxygen permeation performance and the microstructure of perovskite-type (Ba0.5Sr0.5)(Co0.8Fe0.2)O3−δ membranes, J. Memb. Sci. 293 (2007) 44–52. doi:http://dx.doi.org/10.1016/j.memsci.2007.01.032.

[12] J. Yi, M. Schroeder, High temperature degradation of

Ba0.5Sr0.5Co0.8Fe0.2O3−δ membranes in atmospheres containing concentrated carbon dioxide, J. Memb. Sci. 378 (2011) 163–170. doi:10.1016/j.memsci.2011.04.044.

[13] X. Zhu, H. Liu, et al., Permeation model and experimental investigation of mixed conducting membranes, AIChE J. 58 (2012) 1744–1754. doi:10.1002/aic.12710.

[14] K. Gerdes, D. Luss, Oxygen transport model for layered MIEC composite membranes, Solid State Ionics. 177 (2006) 2931–2938. doi:10.1016/J.SSI.2006.09.002.

[15] H. Xie, Y. Wei, et al., Modeling of U-shaped Ba0.5Sr0.5Co0.8Fe0.2O3−δ hollow-fiber membrane for oxygen permeation, Chinese J. Chem. Eng. 25 (2017) 892–897. doi:10.1016/J.CJCHE.2017.02.002.

[16] Y. Zhu, W. Li, et al., Selection of oxygen permeation models for different mixed ionic-electronic conducting membranes, AIChE J. 63 (2017) 4043–4053. doi:10.1002/aic.15718.

[17] C. Li, J.J. Chew, et al., Modelling of oxygen transport through mixed ionic-electronic conducting (MIEC) ceramic-based membranes: An overview, J. Memb. Sci. 567 (2018) 228–260. doi:10.1016/J.MEMSCI.2018.09.016.

[18] Y.-S. Lin, W. Wang, et al., Oxygen permeation through thin mixed-conducting solid oxide membranes, AIChE J. 40 (1994) 786–798. doi:10.1002/aic.690400506.

[19] S.J. Xu, W.J. Thomson, Oxygen permeation rates through ion-conducting perovskite membranes, Chem. Eng. Sci. 54 (1999)

3839–3850. doi:10.1016/S0009-2509(99)00015-9.

[20] B. Zydorczak, K. Li, et al., Mixed conducting membranes - Macrostructure related oxygen permeation flux, AIChE J. 56 (2010) 3084–3090. doi:10.1002/aic.12216.

[21] S. Li, W. Jin, et al., Synthesis and oxygen permeation properties of La0.2Sr0.8Co0.2Fe0.8O3−δ membranes, Solid State Ionics. 124 (1999) 161–170. doi:10.1016/S0167-2738(99)00136-8.

[22] Z. Wang, H. Liu, et al., Improvement of the oxygen permeation through perovskite hollow fibre membranes by surface acid-modification, J. Memb. Sci. 345 (2009) 65–73. doi:10.1016/J.MEMSCI.2009.08.024.

[23] H. Pan, L. Li, et al., Improvement of oxygen permeation in perovskite hollow fibre membranes by the enhanced surface exchange kinetics, J. Memb. Sci. 428 (2013) 198–204. doi:10.1016/J.MEMSCI.2012.10.020.

[24] A. Ghadimi, M.A. Alaee, et al., Oxygen permeation of BaxSr1 − xCo0.8Fe0.2O3 − δ perovskite-type membrane: Experimental and modeling, Desalination. 270 (2011) 64–75. doi:http://dx.doi.org/10.1016/j.desal.2010.11.022.

[25] S. Kim, Y.L. Yang, et al., Oxygen surface exchange in mixed ionic electronic conductor membranes, Solid State Ionics. 121 (1999) 31–36. doi:10.1016/S0167-2738(98)00389-0.

[26] B. Van Hassel, T. Kawada, et al., Oxygen permeation modelling of perovskites, Solid State Ionics. (1993). doi:10.1016/0167-2738(93)90419-4.

[27] Y. Jin, Z. Rui, et al., Sequential simulation of dense oxygen permeation membrane reactor for hydrogen production from oxidative steam reforming of ethanol with ASPEN PLUS, Int. J. Hydrogen Energy. 35 (2010) 6691–6698. doi:10.1016/J.IJHYDENE.2010.04.042.

[28] N.D. Mancini, S. Gunasekaran, et al., A Multiple-Compartment Ion-Transport-Membrane Reactive Oxygen Separator, Ind. Eng. Chem. Res. 51 (2012) 7988–7997. doi:10.1021/ie202433g.

[29] D.M. Turi, P. Chiesa, et al., High fidelity model of the oxygen flux across ion transport membrane reactor: Mechanism characterization using experimental data, Energy. 96 (2016) 127–141. doi:10.1016/J.ENERGY.2015.12.055.

[30] N.D. Mancini, A. Mitsos, Ion transport membrane reactors for oxy-combustion – Part I: intermediate-fidelity modeling, Energy. 36 (2011) 4701–4720. doi:10.1016/J.ENERGY.2011.05.023.

[31] V. Spallina, T. Melchiori, et al., Auto-Thermal Reforming Using Mixed Ion-Electronic Conducting Ceramic Membranes for a Small-Scale H2 Production Plant, Molecules. 20 (2015) 4998–5023. doi:10.3390/molecules20034998.

[32] C.D. Fischer, O.A. Iribarren, Oxygen integration between a gasification process and oxygen production using a mass exchange heuristic, Int. J. Hydrogen Energy. 41 (2016) 2399–2410. doi:10.1016/J.IJHYDENE.2015.12.124.

[33] A. Hunt, G. Dimitrakopoulos, et al., Measuring the oxygen

profile and permeation flux across an ion transport ($La_{0.9}Ca_{0.1}FeO_{3-\delta}$) membrane and the development and validation of a multistep surface exchange model, J. Memb. Sci. 468 (2014) 62–72. doi:10.1016/J.MEMSCI.2014.05.043.

[34] J. Hong, P. Kirchen, et al., Numerical simulation of ion transport membrane reactors: Oxygen permeation and transport and fuel conversion, J. Memb. Sci. 407–408 (2012) 71–85. doi:10.1016/J.MEMSCI.2012.03.018.

[35] M.A. Habib, R. Ben Mansour, et al., Modeling of oxygen permeation through a LSCF ion transport membrane, Comput. Fluids. 76 (2013) 1–10. doi:10.1016/J.COMPFLUID.2013.01.007.

[36] M.A. Nemitallah, A study of methane oxy-combustion characteristics inside a modified design button-cell membrane reactor utilizing a modified oxygen permeation model for reacting flows, J. Nat. Gas Sci. Eng. 28 (2016) 61–73. doi:10.1016/J.JNGSE.2015.11.041.

[37] M.A. Nemitallah, M.A. Habib, et al., Experimental and numerical study of oxygen separation and oxy-combustion characteristics inside a button-cell LNO-ITM reactor, Energy. 84 (2015) 600–611. doi:10.1016/J.ENERGY.2015.03.022.

[38] P. Ahmed, M.A. Habib, et al., Investigation of oxygen permeation through disc-shaped BSCF ion transport membrane under reactive conditions, Int. J. Energy Res. 41 (2017) 1049–1062. doi:10.1002/er.3696.

[39] J.M. Gozálvez-Zafrilla, A. Santafé-Moros, et al., Fluid dynamic modeling of oxygen permeation through mixed ionic-electronic conducting membranes, J. Memb. Sci. 378 (2011) 290–300. doi:10.1016/j.memsci.2011.05.016.

[40] R. Kriegel, R. Kircheisen, et al., Oxygen stoichiometry and expansion behavior of Ba0.5Sr0.5Co0.8Fe0.2O3 - δ, Solid State Ionics. (2010). doi:10.1016/j.ssi.2009.11.012.

[41] R.L. Haupt, S.E. Haupt, Practical genetic algorithms, John Wiley & Sons, Hoboken, New Jersey, 2004.

[42] J. Yi, M. Schroeder, et al., Behavior of Ba(Co, Fe, Nb)O $_{3-\delta}$ Perovskite in CO $_2$ -Containing Atmospheres: Degradation Mechanism and Materials Design, Chem. Mater. 22 (2010) 6246–6253. doi:10.1021/cm101665r.

[43] A. Leo, S. Liu, et al., Production of pure oxygen from BSCF hollow fiber membranes using steam sweep, Sep. Purif. Technol. 78 (2011) 220–227. doi:10.1016/J.SEPPUR.2011.02.006.

[44] S. LEE, Applicability of Sherwood correlations for natural organic matter (NOM) transport in nanofiltration (NF) membranes, J. Memb. Sci. 240 (2004) 49–65. doi:10.1016/j.memsci.2004.04.011.

[45] Makaka S., Aziz M., et al., Copper recovery in a bench-scale carrier facilitated tubular supported liquid membrane system, J. Min. Metall. Sect. B Metall. 46 (2010) 67–73. doi:10.2298/JMMB1001067M.

[46] J. Catalano, M. Giacinti Baschetti, et al., Influence of the gas phase resistance on hydrogen flux through thin palladium–silver membranes, J. Memb. Sci. 339 (2009) 57–67. doi:10.1016/j.memsci.2009.04.032.

[47] L. Giani, G. Groppi, et al., Mass-Transfer Characterization of Metallic Foams as Supports for Structured Catalysts, Ind. Eng. Chem. Res. 44 (2005) 4993–5002. doi:10.1021/ie0490886.

[48] G. Groppi, L. Giani, et al., Generalized Correlation for Gas/Solid Mass-Transfer Coefficients in Metallic and Ceramic Foams, Ind. Eng. Chem. Res. 46 (2007) 3955–3958. doi:10.1021/ie061330g.

[49] R.B. Bird, W.E. Stewart, et al., Transport Phenomena, Wiley, New York, 1960.

[50] L. Wang, R. Merkle, et al., Oxygen tracer diffusion in dense Ba0.5Sr0.5Co0.8Fe0.2O3−δ films, Appl. Phys. Lett. 94 (2009). doi:http://dx.doi.org/10.1063/1.3085969.

[51] A. Berenov, A. Atkinson, et al., Oxygen tracer diffusion and surface exchange kinetics in Ba0.5Sr0.5Co0.8Fe0.2O3−δ, Solid State Ionics. 268 (2014) 102–109. doi:10.1016/j.ssi.2014.09.031.

[52] M. Kessel, R.A. De Souza, et al., Oxygen diffusion in single crystal barium titanate, Phys. Chem. Chem. Phys. 17 (2015) 12587–12597. doi:10.1039/C5CP01187F.

[53] T. Antonini, K. Gallucci, et al., Oxygen transport by ionic membranes: Correlation of permeation data and prediction of

char burning in a membrane-assisted biomass gasification process, Chem. Eng. Process. Process Intensif. 94 (2015) 39–52. doi:10.1016/j.cep.2014.11.009.

[54] A. Behrouzifar, A.A. Asadi, et al., Experimental investigation and mathematical modeling of oxygen permeation through dense Ba0.5Sr0.5Co0.8Fe0.2O3−δ (BSCF) perovskite-type ceramic membranes, Ceram. Int. (2012). doi:10.1016/j.ceramint.2012.02.068.

[55] D. Chen, Z. Shao, Surface exchange and bulk diffusion properties of Ba0.5Sr0.5Co0.8Fe0.2O3−δ mixed conductor, Int. J. Hydrogen Energy. 36 (2011) 6948–6956. doi:10.1016/j.ijhydene.2011.02.087.

[56] H. Wang, W. Yang, et al., Diffusion Fundamentals, Diffus. Fundam. (Online Journal). 1 (2005) 1–17. http://www.uni-leipzig.de/diffusion/contents_vol1.html.

[57] D. Gao, J. Zhao, et al., Influence of high-energy ball milling of the starting powder on the sintering; microstructure and oxygen permeability of Ba0.5Sr0.5Co0.5Fe0.5O3−δ membranes, J. Memb. Sci. (2011). doi:10.1016/j.memsci.2010.10.001.

[58] H. Wang, R. Wang, et al., Experimental and modeling studies on Ba0.5Sr 0.5Co0.8Fe0.2O3-δ (BSCF) tubular membranes for air separation, J. Memb. Sci. 243 (2004) 405–415. doi:10.1016/j.memsci.2004.07.003.

[59] S. Baumann, F. Schulze-Küppers, et al., Influence of sintering conditions on microstructure and oxygen permeation of

Ba0.5Sr0.5Co0.8Fe0.2O3−δ (BSCF) oxygen transport membranes, J. Memb. Sci. (2010). doi:10.1016/j.memsci.2010.02.002.

[60] L. Tan, X. Gu, et al., Influence of powder synthesis methods on microstructure and oxygen permeation performance of Ba0.5Sr0.5Co0.8Fe0.2O3−δ perovskite-type membranes, J. Memb. Sci. (2003). doi:10.1016/S0376-7388(02)00494-5.

[61] J. Vente, S. McIntosh, et al., Properties and performance of BaxSr1−xCo0.8Fe0.2O3−δ materials for oxygen transport membranes, J. Solid State Electrochem. (2006). doi:10.1007/s10008-006-0130-2.

[62] R. Hoffmann, U. Pippardt, et al., Impact of sintering temperature on permeation and long-term development of support structure and stability for asymmetric oxygen transporting BSCF membranes, J. Memb. Sci. 581 (2019) 270–282. doi:10.1016/J.MEMSCI.2019.03.066.

[63] M.P. Lobera, M. Balaguer, et al., Catalytic Oxide-Ion Conducting Materials for Surface Activation of $Ba_{0.5}Sr_{0.5}Co_{0.8}Fe_{0.2}O_{3-\delta}$ Membranes, ChemistrySelect. 2 (2017) 2949–2955. doi:10.1002/slct.201700530.

[64] J.M. Serra, J. Garcia-Fayos, et al., Oxygen permeation through tape-cast asymmetric all-La0.6Sr0.4Co0.2Fe0.8O3−δ membranes, J. Memb. Sci. 447 (2013) 297–305. doi:10.1016/J.MEMSCI.2013.07.030.

8. ENERGETIC EVALUATION OF SOLID OXIDE ELECTROLYSER USING PROTONIC CONDUCTORS

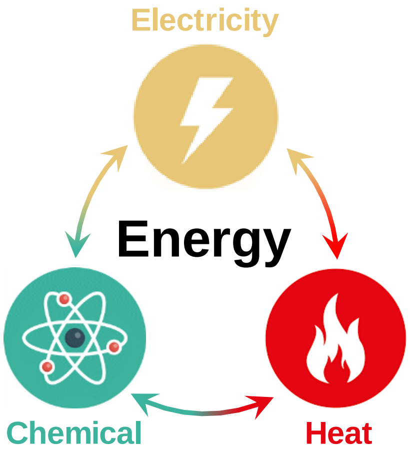
Electricity
Energy
Chemical
Heat

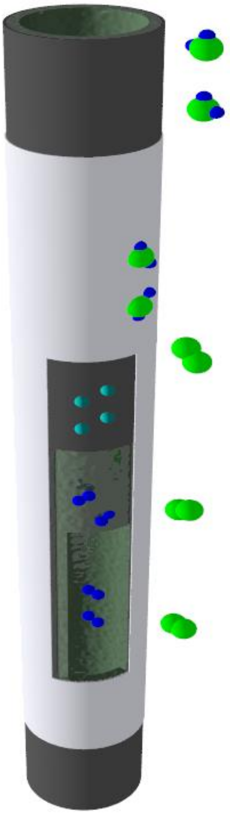

8. ENERGETIC EVALUATION OF SOLID OXIDE ELECTROLYSER USING PROTONIC CONDUCTORS 205

8.1. INTRODUCTION 208
8.2. METHODS 210
8.2.1. METHODOLOGY TO EVALUATE THE THERMOFLUID DYNAMIC OF THE ELECTROLYSIS PROCESS BY FINITE ELEMENTS 210
8.2.2. METHODOLOGY TO EVALUATE THE EFFICIENCY OF THE ELECTROLYSIS PROCESS 221
8.3. RESULTS 227
8.3.1. EVALUATION OF THE THERMOFLUID DYNAMIC OF ELECTROLYSIS BASED ON PROTONIC CONDUCTING MATERIALS AT HIGH TEMPERATURE 227
8.3.2. EVALUATION OF THE EFFICIENCY OF ELECTROLYSIS PROCESS BASED ON PROTONIC CONDUCTING MATERIALS AT HIGH TEMPERATURE 244
8.4. SUMMARY 254
8.5. REFERENCES 257

8.1.Introduction

At present, the concerning about to develop eco-friendly facilities is growing because the awareness of the environment warnings status and of the intensification of the legislations, especially in occidental countries [1, 2]. Among the alternatives, hydrogen is a clean source of energy and presents the with highest energy density (143 kJ/kg) [3]. Furthermore, hydrogen presents large demands for different industries such as petrochemicals, pharmaceutical and, especially, ammonia synthesis among others [4]. However, it presents several drawbacks mainly because its low density makes difficult its storage [5, 6] and from its production because there is not hydrogen deposits in the nature and, consequently, it requires to be synthetized. Although storage problems would lead to the hydrogen viability to be obtained in situ, the conventional (and most-practiced) method to generate hydrogen is from steam reforming processes. These processes need large plants to reach economic viability [7, 8]. For this reason, the hydrogen status in these days are focused to satisfice the industry demands [9]. Finally, as consequence to obtain hydrogen from fossil fuels and energy, the hydrogen is marked with considerable CO_2 footprints (around 8 – 12 kg CO_2 eq./kg H_2) [2, 10, 11].

Electrolysis can be potentially viable and competitive for the hydrogen production comparing with the reforming process, mainly for small scale productions [9]. However, high operation costs make necessary further efforts. That high operation cost is mainly due to the high electrical demands, therefore, in these days there is a high interest to integrate renewable energy sources with electrolysis to obtain hydrogen

[3, 4, 12]. These projects are known as Power to gas (*P2g*) and they are focused in storage in form of H_2 or CH_4 the energy from renewable sources (mainly wind and solar) when they work in overplus situation, i.e. the plant generates higher amounts of energy than the demand [12-16]. Here, there is a big potential in using hydrogen as energy storage using this kind of technology.

Alternative to the reforming processes, electrolysis allows obtaining hydrogen from water and electricity. This technology is typically classified depending on the material used as electrolyte. Further, the different electrolyte materials work in very different conditions (mainly temperature), leading to very differentiated processes. Although high temperature electrolysers based on ion-conducting ceramics materials are not in the market, they present the theoretical highest efficiencies between the different electrolyser technologies [11, 17, 18]. Among these materials, protonic conducting materials present the highest efficiencies for electrolysers in comparison conventional oxygen ion conducting ceramics [19, 20]. Additionally, protonic conductor electrolyser allows obtaining pure hydrogen while for oxygen ion conducting electrolysers the hydrogen is diluted with water.

Finite element approach has been used to enhance the understanding of this kind of processes and advanced analysis about the integration of the phenomena which take place in the process [21-25]. Three different modes of operation were confirmed for electrolysis considering its heat balance: (i) endothermic operation, working at potentials lower than thermo-neutral potential; (ii) isothermal, working at thermo-neutral potential; (iii) exothermic, working at higher potentials than thermoneutral potential; depending of the difference between the heat demands (reaction) and electrochemical heats [26-28]. Thermoneutral voltage is the voltage where the heat demands of water dissociation carry out by electrolysis is covered for the overpotentials of the electrochemical circuit. Heat transference of additional phenomena may limit the electrochemistry because the marked temperature-dependency of the conductivities for these materials (both oxygen ion conductors and protonic conductors) [29].

8.2.Methods

This chapter present the evaluation of the electrolysis process based on protonic conducting materials at high temperatures. This evaluation has been developed using finite elements and the efficiency of the overall process. Finite elements method allows evaluating the performance of the process. The efficiency of the process allows to evaluate the theoretical yield of the system expressed in energy terms.

8.2.1. Methodology to evaluate the thermofluid dynamic of the electrolysis process by finite elements

8.2.1.1. Equations and properties

The software used to evaluate the electrolyser with finite elements methodology was Comsol Multiphysics v4.4. Electrolysis using protonic conductor ceramics is a process which holds several interacting phenomena. The phenomena of this process are: (i) gas flow, (ii) gas diffusion, (iii) electrochemistry, (iv) heat transference. Table 8.1 shows the governing equations of all phenomena. Navier-Stoke equations were used to model gas flows in the internal and in the external chamber considering the respective correction for the porous domains. Averaged-mixture equations were used to model gas diffusions where Ar, H_2O and O_2 were considered for the external chamber and Ar and H_2 for the internal chamber. Secondary current distribution was considered to model the electrochemistry. The electrochemical kinetics of electrodes were modelled using Butler-Volmer method (eq 13) considering the exchange current density at 0.1 $A \cdot cm^{-2}$ and anodic and cathodic transference coefficients at 0.5. Finally, the faradaic efficiency considered was 100%. For the heat transference, it was model considering an adiabatic assembly with radiative heat transference and considering the heats from the reaction and electrochemical circuit as heat sources.

The properties of pure gases were collected from literature [30]. Gas density was calculated considering ideal gas mixtures (eq 19). The viscosity and the thermal conductivity for the gas mixtures (both internal and external gas mixtures) were calculated using the wilke model (eq 20, 21 and 28). The heat capacity and the heat capacity ratio for gas mixtures was estimated considering the molar average (eq 30 and 31). For risers of the tube and the interconnectors, alumina properties were considering. For the tube, Ni properties were used for the thermal properties and density of the material. For the external tube stainless steel properties were considered.

Table 8.1. Governing equations for the CFD model.

Governing equation	id	Property equations	id
Navier-Stokes			
$\rho(u\cdot\nabla)u=\nabla\cdot\left[-pI+\mu(\nabla u+(\nabla u)')-\frac{2}{3}\mu(\nabla\cdot u)I\right]$	(1)	$\rho=\frac{p}{R\cdot T}\cdot M_n$	(19)
$\nabla\cdot(\rho u)=0$	(2)	$\mu=\sum_i\frac{\mu_{g,i}}{1+\frac{1}{x_i}\cdot\sum_{j,j\neq i}x_j\cdot\phi_{i,j}}$	(20)
$\frac{\rho}{\epsilon_p}\left((u\cdot\nabla)\frac{u}{\epsilon_p}\right)=\nabla\cdot\left[-pI+\frac{\mu}{\epsilon_p}(\nabla u+(\nabla u)')-\frac{2\mu}{3\epsilon_p}(\nabla\cdot u)I\right]-\left(\mu\kappa^{-1}+\beta_F\lvert u\rvert+\frac{Q_{br}}{\epsilon_p^2}\right)u$	(3)	$\phi_{i,j}=\frac{\left(1+\left(\frac{\mu_{g,i}}{\mu_{g,j}}\right)^{\frac{1}{2}}\cdot\left(\frac{M_j}{M_i}\right)^{\frac{1}{4}}\right)^2}{4/\sqrt{2}\cdot\left(\frac{M_i}{M_j}\right)^{\frac{1}{2}}}$	(21)
$\nabla\cdot(\rho u)=Q_{br}$	(4)	$\kappa=\frac{d_p^2\cdot\epsilon_p^3}{150\cdot\left(1-\epsilon_p\right)^2}$	(22)
Averaged-mixture for transport of specie			
$\nabla\cdot j_i+\rho(u\cdot\nabla)w_i=r_i\cdot M_i$	(5)	$D_i^m=\frac{1-w_i}{\sum_{k\neq i}\frac{x_k}{D_{i,k}}}$	(23)
$N_i=j_i+\rho u w_i$	(6)	$M_n=\left(\sum_i\frac{w_i}{M_i}\right)^{-1}$	(24)
$j_i=-\left(\rho D_i^m\nabla w_i+\rho w_i D_i^m\frac{\nabla M_n}{M_n}\right)$	(7)	$D_{i,j}=k_{diff}\cdot\frac{T^{1.75}\cdot\left(\frac{1}{M_i}+\frac{1}{M_j}\right)^{1/2}}{p\cdot\left(v_i^{1/3}+v_j^{1/3}\right)^2}$	(25)
Charge transport (electrochemistry			
$\nabla i_I=Q_I$	(8)	$E_{eq}=E_{eq}^0+\frac{R\cdot T}{z\cdot F}\ln\left(\prod p_i^{n_i}\right)$	(26)
$i_I=-\sigma_I\nabla\phi_I$	(9)	$E_{eq}^0=-\frac{\Delta G^0}{z\cdot F}$	(27)
$\nabla i_S=Q_S$	(10)		
$i_S=-\sigma_S\nabla\phi_S$	(11)		
$\eta=\phi_S-\phi_I-E_{eq}$	(12)		
$i=i_o\left(\exp\left(\frac{-\beta zF\eta}{RT}\right)-\exp\left(\frac{(1-\beta)zF\eta}{RT}\right)\right)$	(13)		
Thermal transport			
$\rho Cpu\cdot\nabla T=\nabla(k\cdot\nabla T)+Q_{term}$	(14)	$k=\sum_i\frac{k_{g,i}}{1+\frac{1}{x_i}\cdot\sum_{j,j\neq i}x_j\cdot\phi_{i,j}}$	(28)
$\rho Cpu\cdot\nabla T=\nabla(keq\cdot\nabla T)+Q_{term}$	(15)	$keq=\theta_p\cdot k_p+\left(1-\theta_p\right)\cdot k$	(29)
$Heat_{REACTION}=-(0.5\cdot\Delta H_{O2}+\Delta H_{H2}-\Delta H_{H2O})\cdot\frac{I_{tot}}{z\cdot F}$	(16)	$Cp=\sum_i x_i\cdot Cp_{g,i}$	(30)
$Heat_{ELEC}=E_{cell}\cdot I_{tot}$	(17)	$\gamma=\sum_i x_i\cdot\gamma_{g,i}$	(31)

The porosity and permeability are two key factors that govern the fluid flow in the porous region and the permeability for a packed bed with randomly distributed spherical particles was calculated using the Carman-Kozeny model and the stated particle size and porosity model [31]. As previously was determined for this kind of tubes, the porosity of the internal electrode was fixed at 25% with a particle size of 10 μm [32, 33]. Additionally, the tortuosity of the system was evaluated considering the inverse of the square root of the porosity of the domain considering the electrode as a packed bed with randomly distributed spherical particles [34, 35]. Finally, the gas diffusion coefficient was corrected for the internal porous electrode considering the porosity and the tortuosity.

To simplify the complexity of the problem and considering it could not distinguished between anode and cathode contribution in the experimental polarization resistance, the total electric resistance was introduced in the electrolyte layer as an Arrhenius expression considering 3 $\Omega\ cm^2$ at 600ºC with an activation energy of 0.5 *eV* based on the experimental results.

- Radiation heat transference evaluation

The influence of radiation heat transference in SOFC has been a topic of large discussion in the last decades [36-45]. Although the conventional way to consider the heat transference on finite elements studies for these processes is neglecting radiative effects, the high temperatures of these processes indicate the radiative could have significant effects under the overall heat transference and, consequently, it would have significant effects in temperature distributions. Considering the marked effect of the temperature in the electrical charge resistances of the high temperature ceramic ionic conductors, seems critical to characterize all the phenomena those can have relevant effects in the temperature distribution. Therefore, in this study, the radiative heat transference has been evaluated.

Previous studies including radiative heat transference revealed that, for planar stacks the effect of the radiative effect is negligible or with minor effects [37, 38, 40-42, 45]. For the tubular configurations, the radiative effect causes a mitigation of the heats of the process and, consequently, a decrease of the temperatures along length of the tube, and a distribution of temperature more homogeneous [39, 44-47].

In addition to the surface-to-surface radiative transference, there is to take into account that the asymmetrical gas molecules gases (H_2O, CO, CO_2, hydrocarbons, etc.) which could play a role in the radiative performance while symmetrical and monoatomic are transparent to thermal radiation (O_2, N_2, etc. and Ar, He, etc.) [48]. Therefore, between the surfaces of the internal chamber: alumina risers surface and the internal electrode surface the radiative model considering only the surface-to-surface radiative transference. On the other hand, for the external chamber, H_2O interacts with the radiation emitted for the external surfaces of the tubular alumina risers, the external surface of the external electrode, and the internal surface of the reactor.

Finally, considering the porous domain of the internal electrode, the radiation heat has been considered using the equivalent thermal conductivity (k_{ef}) [49-51]. That equation replaces the equation 29 for the thermal conductivity for porous domains.

$$k_{eq} = k_{eq}^{0} + 0.111 \cdot k_{gas} \cdot \frac{Re_p \cdot Pr^{1/3}}{1 + 46 \cdot \left(\frac{dp}{d_{eq}}\right)^2} \tag{32}$$

$$k_{eq}^{0} = \epsilon_p \cdot \left(k_{gas} + 0.95 \cdot \alpha_{ru} \cdot dp\right) + \frac{0.95 \cdot (1 - \epsilon_p)}{\frac{2}{3 \cdot k_p} + \frac{1}{10 \cdot k_{gas} + \alpha_{rs} \cdot dp}} \tag{33}$$

$$\alpha_{ru} = \frac{0.8171 \cdot \left(\frac{T}{100}\right)^3}{1 + \left(\frac{\epsilon_p}{2 \cdot (1 - \epsilon_p)} \cdot \left(\frac{1 - \varepsilon}{\varepsilon}\right)\right)} \left[\frac{kJ}{h \cdot m^2 \cdot K}\right] \tag{34}$$

$$\alpha_{rs} = 0.8171 \cdot \left(\frac{\varepsilon}{2 - \varepsilon}\right) \cdot \left(\frac{T}{100}\right)^3 \left[\frac{kJ}{h \cdot m^2 \cdot K}\right] \tag{35}$$

Where Re_p, Pr and ε are the Reynolds number for the particles of the internal electrode, the Prant number and the emittance of the material, respectively. *dp* and d_{eq} are the particle size for the porous domain and the diameter of the chamber, respectively.

$$Re_p = \frac{dp \cdot u_{gas} \cdot \rho_{gas}}{\mu_{gas}} \tag{36}$$

$$Pr = \frac{c_{p,gas} \cdot \mu_{gas}}{k_{gas}} \tag{37}$$

Considering the overall heat transference, the equations to model that phenomenon is:

$$\rho \cdot c_p \cdot u \cdot \nabla T = \nabla \cdot \left(k_{eq} \nabla T\right) + Q_{term} \tag{38}$$

$$S_i \nabla I_i = \kappa_r I_b(T) - \beta I_i + \frac{\sigma_{sc}}{4\pi} \sum_{j=1}^{N} \omega_j I_j \phi\left(S_j, S_i\right) \tag{39}$$

$$I_b(T) = \frac{\sigma_B \cdot n \cdot T^4}{\pi} \tag{39}$$

Where S_i are the surface *i*, I_i is the spectra radiation intensity of the surface S_i, β is the extinction coefficient, κ_r is the absorption coefficient, σ_{sc} is scattering coefficient (zero for this study), σ_B is the Stefan-Boltzmann constant ($5.67 \cdot 10^{-8}$ W m^{-2} K^{-4}), ω_j is angular range and ϕ is the phase function between the surfaces S_j and S_i, and n is the refractive index (fixed at 1). The equation 39 is a balance between the irradiation transferred, the absorbed and the scattered. All solids (alumina risers, electrochemical tube cell, stainless steel) were considered as opaque solids.

Considering the surface-to-surface radiative heat transference for the surfaces of the internal chamber (that means, these equations are applied in the respective surfaces), the equations describing the heat transference are:

$$-n \cdot (-k\nabla T) = \varepsilon \cdot \left(G - e_b(T)\right) \tag{40}$$

$$e_b(T) = n^2 \sigma_B \cdot T^4 \tag{41}$$

$$G = G_m(J) + G_{amb} \tag{42}$$

$$G_{amb} = F_{amb} \cdot e_b(T_{amb}) \tag{43}$$

Where ε is the surface emissivity of the surface (0.8 for riser surfaces, and 0.75 for the tube), G is the irradiation, e_b is the irradiation of a black body, J is the radiosity, G_m is mutual irradiation coming from other surfaces, G_{amb} is ambient irradiation, and F_{amb} is the ambient factor.

$$G_m = \int_{S'} \frac{(-n' \cdot r)(n \cdot r)}{\pi |r|^4} J' dS \tag{44}$$

$$F_{amb} = 1 - \int_{S'} \frac{(-n' \cdot r)(n \cdot r)}{\pi |r|^4} dS \tag{45}$$

Where *S* is the wall surface, n' is the unit normal factor of m' *(x', y', z')* in solid surface. *r* is the vector from the point *m (x,y,z)* to *m (x', y', z')*, *n* is the normal unit factor of *m (x, y, z)* and *J'* is the radiosity of m' *(x', y', z')*. For this study, it works in radial coordinates, therefore each *(x, y, z)* becomes in *(r, z, θ)*.

Finally, considering the radiative heat transference with participating media for the external chamber, the heat emitted for the surfaces of the chambers with the participating media (equation for external chamber surfaces) is:

$$-n \cdot (-k\nabla T) = \varepsilon\sigma_B\left(T_{amb}^4 - T^4\right) \tag{46}$$

And the equations to model the heat transference are for participating media domains (external chamber volume) are:

$$\rho \cdot c_p \cdot u \cdot \nabla T = \nabla \cdot (k\nabla T + k_R\nabla T) + Q_{term} \tag{47}$$

$$k_R = \frac{16 \cdot n^2 \cdot \sigma_B \cdot T^3}{3 \cdot \beta_R} \tag{48}$$

Where k_R is the radiative equivalent thermal conductivity, evaluated using the Rosseland approximation, β_R is the extinction radiation coefficient which is equal to the absorption coefficient for this case. The absorption coefficient (κ_{H2O}) for the gases was considered as follow:

$$\kappa_{H2O} = p_{H2O} \cdot a_{H2O} \tag{49}$$

$$a_{H2O} = -0.23093 - 1.1239 \cdot \left(\frac{1000}{T}\right) + 9.4153 \cdot \left(\frac{1000}{T}\right)^2 - 2.9988 \cdot \left(\frac{1000}{T}\right)^3 + 0.513882 \cdot \left(\frac{1000}{T}\right)^4 - 1.8684 \cdot 10^{-5} \cdot \left(\frac{1000}{T}\right)^5 \quad (50)$$

Where p_{H2O} is the steam partial pressure, and a_{H2O} is the Planck mean absorption coefficient in m·atm^{-1} [52-55].

8.2.1.2. Geometries

The reference geometry for the finite element study presents the same dimensions of the experimental setup. To simplify the complexity of the system, 2D axial symmetry was considered. The electrochemical cell and risers have an internal diameter of 8.2 *mm* and an external diameter of 9.8 *mm*. The tube cell has a length of 5cm where the external electrode has a 2.*9cm* of length centered in the tube. The reactor has an internal diameter of 16.5 *mm* and an external diameter of 20 *mm*. Experimental setup is an isothermal assembly where the temperature was ensured using a controlled electric furnace. The risers have a total length of 10 *cm*.

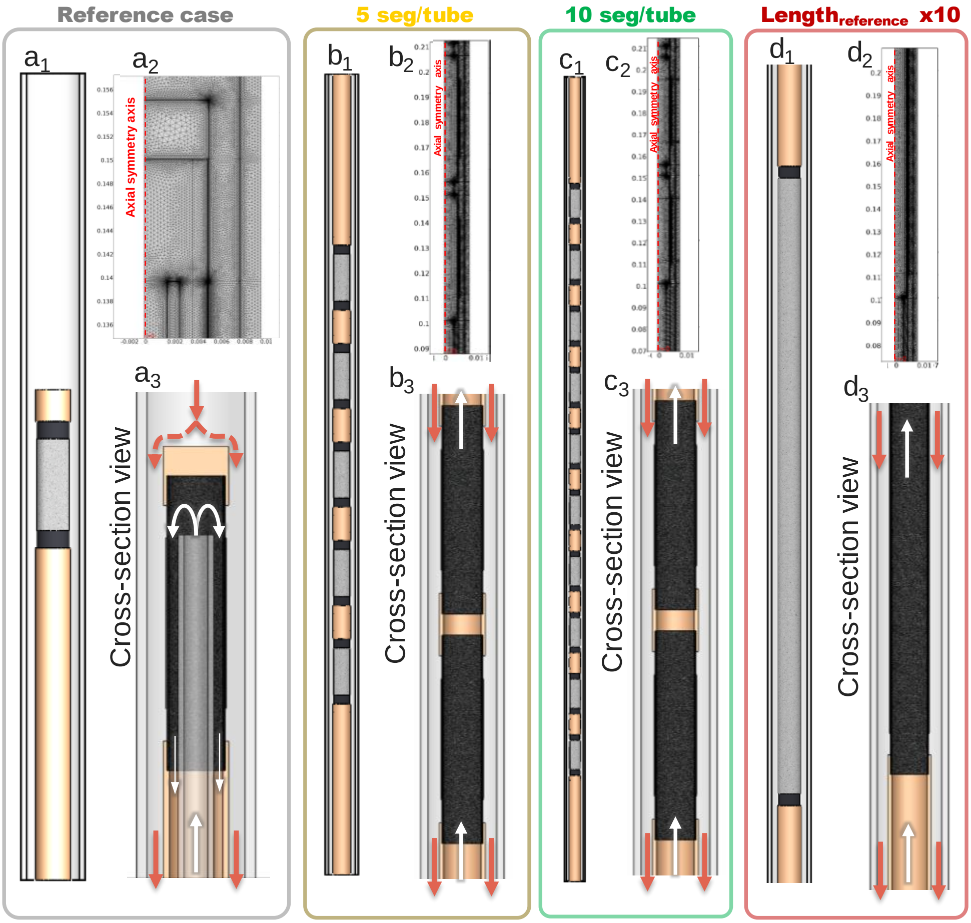
Reference case
5 seg/tube
10 seg/tube
Lengthreference x10
a1
a2
a3
b1
b2
b3
c1
c2
c3
d1
d2
d3
Axial symmetry axis
Cross-section view

Figure 8.1. Different geometries for this study: (a) expterimental setup (2.9cm electrode length); (b) geometry with 5 segments with 2.9cm electrode length per segment than expeimental setup; (c) geometry with 10 segments with 2.9cm electrode length per segment than expeimental setup; (d) geometry using a external electrode with 29cm electrode length. Meshes (a_2, b_2, c_2, d_2); flow directions (a_3, b_3, c_3, d_3).

The evaluation of the scalability of the assembly was studied considering assemblies with 1 (experimental setup), 5 and 10 segments cells and with an additional setup with an external electrode with 10 times the length of the experimental setup (Figure 8.1). The interconnectors between segments have a length of 5 *mm*. For the experimental setup, the inlet is introduced using an internal tube in the internal chamber because it is a closed tube assembly. However, for the rest of the assemblies, for the internal chamber, the inlet is introduced in the bottom and extracted from the top. For the external chamber, the gas is introduced in the top and extracted from the bottom.

8.2.1.3. Conditions and inlets

The reference conditions and inlets for the CFD study present the same values of the experimental tests. The inlet for the external chamber was 150 $NmL \cdot min^{-1}$ of a mixture of H_2O, O_2 and Ar considering a total pressure of 3 bar and the partial pressures in the inlet of the H_2O and O_2 are 1.5 and 0.08 *bar*, respectively. Finally, the external gas flow is introduced at 600*ºC*. For the internal chamber, the inlet gas is 50 $NmL \cdot min^{-1}$ of a mixture of H_2 and Ar were the total pressure is 3 *bar* and the partial pressure of the H_2 in the inlet is 0.3 *bar*. The inlet gas for the internal chamber is introduced at 600*ºC*.

For the evaluation of the scalability of the process, the study keeps the inlet compositions for the reference case (both internal and external chambers). For the total inlet flow of both chambers are increased proportional to the increase of the area (as shows the Table 8.2).

Table 8.2. Total inlet flow in each chamber for each geometry considered.

Setup	**Segments**		**Feeding (*NmL/min*)**	
	Nº	**Length (*cm*)**	**Internal chamber**	**External chamber**
Experimental	1	2.9	50	150
5 segments	5	2.9	250	750
10 segments	10	2.9	500	1500
Larger segment	1	29.0	500	1500

8.2.1.4. Solver and meshing

Figure 8.1 shows the meshing performed for the different geometries. The mesh was optimized using tetragonal division of the different domains. Adaptive mesh refinement was used to optimize the mesh. The calculations were carried out using the Parallel Direct Solver (PARDISO) with parameter continuation to assure convergence. The relative tolerance of the method is 0.001. A consistent stabilization criterion was chosen for all phenomena using streamline diffusion and crosswind diffusion. To improve the convergence of the system, the process was solved under isothermal conditions and then the solution was used as initial values for the complete process.

8.2.2. Methodology to evaluate the efficiency of the electrolysis process

The evaluation of the process considering finite elements is based on results of experimental setup. However, these results were obtained for low pressures (both steam-oxygen chamber and hydrogen chamber). Therefore, the evaluation of the effect of the pressures of each chamber is developed considering the effect of these pressures on the thermodynamic energy of the electrolysis and the different additional units required for the electrolysis at high temperatures and pressures.

8.2.2.1. Study of the effect of the hydrogen and steam chamber pressures

There was no experimental information available about the effect to increase the pressures on the steam and/or the hydrogen chambers (at higher pressures > 5bar), especially on the overall specific resistance, a thermodynamic evaluation was done.

For study the effect of the hydrogen pressure in the electrolysis process a simple 0D model was considered. The reversible potential (E_{rev}), thermoneutral potential (E_{th}) and cell potential (E_{cell}) were calculated using the equations 51, 52 and 53, respectively.

$$E_{rev} = \frac{\Delta G_r}{z \cdot F} \tag{51}$$

$$E_{th} = \frac{\Delta H_r}{z \cdot F} \tag{52}$$

$$E_{cell} = E_{rev} + i \cdot ASR \tag{53}$$

The overall reaction Gibbs energy (ΔG_r) and overall reaction enthalpy (ΔH_r) were calculated using the equations:

$$\Delta G_r = \Delta G_{H2}(T, p^{II}) + 0.5 \cdot \Delta G_{O2}(T, p^{I}) - \Delta G_{H2O}(T, p^{I}) \tag{54}$$

$$\Delta H_r = \Delta H_{H2}(T, p^{II}) + 0.5 \cdot \Delta H_{O2}(T, p^{I}) - \Delta H_{H2O}(T, p^{I}) \tag{55}$$

Where p^I is the pressure in the steam-oxygen chamber, p^{II} is the pressure in the hydrogen chamber, ΔG_i is the gibbs energy of the pure *i* compound and ΔH_i is the enthalpy of the pure i compound. The pure compounds energies where obtained from [30].

- Effect of the hydrogen chamber pressure

The increase of the pressure of the hydrogen chamber allows obtaining the hydrogen at high pressure. This pressurization is performed by a regulator valve and it has its energy losses. However, in this study these energy losses were not considered. Figure 8.2 shows the overall process considered for the study of the pressure of the hydrogen chamber. First the water is vaporized from 25°C and 1 *bar* of pressure. Then a heat exchanging system is considered. It was considered that there is enough heat in the outlet streams to heat the inlet stream until the working temperature. Finally, the electrolysis was considered at adiabatic conditions working at thermoneutral voltage. This allows working at isothermal regime.

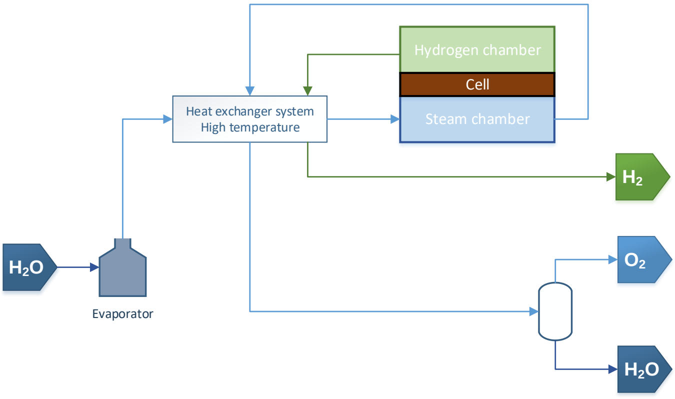

Figure 8.2. Diagram of the overall electrolysis process for the study of the effect of the pressure of the hydrogen chamber.

The energies of upstream units of the electrolyser were obtained from Aspen Plus v8.8. In this case, electrolysis energy and vaporization energy are required to evaluate the energy demand of the process. Finally, the energies collected from Aspen plus were corrected to obtain energies in *kWh/kg* H_2 obtained. For that purpose, the steam conversion in the electrolysis units was considered (*XH2O*).

$$H(evap) = \frac{H(evap)}{F0_{H2O}} \cdot \frac{M_{H2O}}{M_{H2}} \cdot \qquad (56)$$

Where *H(evap)* is the energy to perform the water evaporation in terms of *kWh/kg*. $F0_{H2O}$ is the inlet water stream (*kg/h*). Mi is the molecular weight of the i compound.

8.2.2.2. Study of efficiency of the process

Finally, considering the experimental results, the energy stored efficiency was evaluated. The aim is to evaluate the energy of the hydrogen production.

For that purpose, different hypotheses were made considering the energy demand of the process:

1) Only considering the electric energy demanded by the electrolysis.
2) Adding the heat demand of the water dissociation when the cell works at lower potentials than the thermoneutral voltage.
3) Adding the heat of the water evaporation.

For this approach, the energy to heat the stream until the operation temperature has not been considered. The energy efficiencies (η_{energy}) for each case are defined in the follow equations:

Considering only the electricity for the electrolysis

$$\eta_{energy} = \frac{P(H_2)}{P(elec)} = \frac{LHV_{H2} \cdot F_{H2}}{E_{cell} \cdot I_{tot}} = \frac{LHV_{H2} \cdot \frac{I_{tot} \cdot \eta_{Far}}{z \cdot F}}{E_{cell} \cdot I_{tot}} \tag{57}$$

$$\boldsymbol{\eta_{energy} = \frac{LHV_{H2} \cdot \eta_{Far}}{E_{cell} \cdot z \cdot F}} \tag{58}$$

Where *P(H₂)* is the energy of the hydrogen obtained, *P(elec)* is the electricity required for the electrolysis, LHV_{H2} is the Low Heating value for hydrogen (241.8 kJ/mol); F_{H2} is the hydrogen molar flow, η_{Far} is the faradaic efficiency.

Adding the heat demand of the water dissociation when the process works at endothermal operation mode

$$\eta_{electric} = \frac{P(H_2)}{P(elec) + H(elec)} \tag{59}$$

$$\eta_{electric} = \frac{LHV_{H2} \cdot \frac{I_{tot} \cdot \eta_{Far}}{z \cdot F}}{E_{cell} \cdot I_{tot} + I_{tot} \cdot \eta_{Far} \cdot (E_{th} - E_{cell}) \cdot (E_{cell} < E_{th})} \tag{60}$$

$$\boldsymbol{\eta_{electric} = \frac{LHV_{H2} \cdot \eta_{Far}}{(E_{cell} + \eta_{Far} \cdot (E_{th} - E_{cell}) \cdot (E_{cell} < E_{th})) \cdot z \cdot F}} \tag{61}$$

Where *H(elec)* is the heat demand of the electrolysis process when the cell works at voltages lower than thermoneutral voltage.

Adding the water evaporation heat

$$\eta_{electric} = \frac{P(H_2)}{P(elec) + H(elec) + H(H_2O, XH2O)} \tag{62}$$

$$\eta_{electric} = \frac{LHV_{H2} \cdot \frac{I_{tot} \cdot \eta_{Far}}{z \cdot F}}{E_{cell} \cdot I_{tot} + I_{tot} \cdot \eta_{Far} \cdot (E_{th} - E_{cell}) \cdot (E_{cell} < E_{th}) + \lambda_{H2O} \cdot F_{H2O}} \tag{63}$$

$$\eta_{electric} = \frac{LHV_{H2} \cdot \frac{I_{tot} \cdot \eta_{Far}}{z \cdot F}}{E_{cell} \cdot I_{tot} + I_{tot} \cdot \eta_{Far} \cdot (E_{th} - E_{cell}) \cdot (E_{cell} < E_{th}) + \lambda_{H2O} \cdot \frac{I_{tot}}{z \cdot F} \cdot \frac{\eta_{Far}}{XH2O}} \tag{64}$$

$$\boldsymbol{\eta_{electric} = \frac{LHV_{H2} \cdot \eta_{Far}}{(E_{cell} + \eta_{Far} \cdot (E_{th} - E_{cell}) \cdot (E_{cell} < E_{th})) \cdot z \cdot F + \frac{\lambda_{H2O} \cdot \eta_{Far}}{XH2O}}} \tag{65}$$

Where $H(H_2O,XH2O)$ is the heat to vaporize the water of the process, λ_{H2O} is the latent heat of the water, F_{H2O} is the water molar flow, $XH2O$ is the water conversion of the electrolysis process.

8.3. Results

8.3.1. Evaluation of the thermofluid dynamic of electrolysis based on protonic conducting materials at high temperature

Figure 8.3 shows the mesh refinement study of the experimental setup. This study was developed in adiabatic regime neglecting the radiation heat transference. The temperature distribution shows slight differences (around 2 – 3 *°C*) when the mesh was gradually improved. Additionally, there is not signal of influence in the mesh used in the electrochemical results. Therefore, the mesh optimal strategy (around $0.5 \cdot 10^6$ *gl*) was kept for the other geometries analyzed this work.

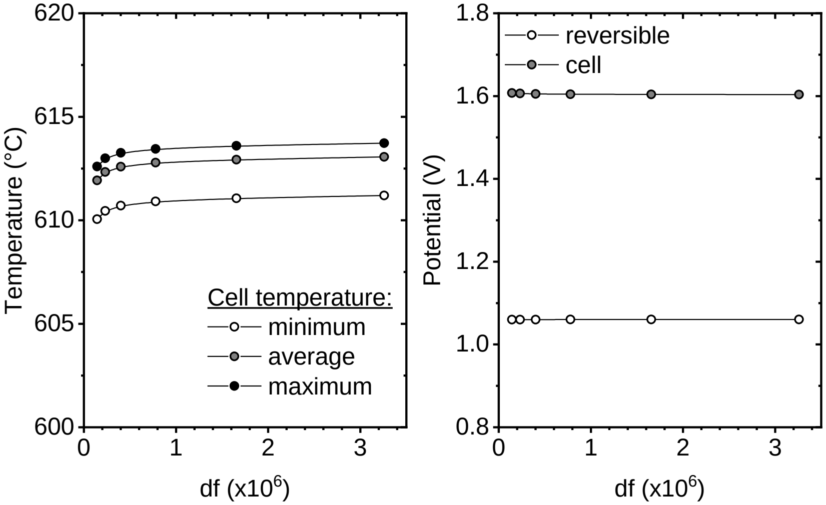

Figure 8.3. Effect of increasing the mesh complexity on specific modelling results (T, V). df: degrees of freedom of the computational study

8.3.1.1. Evaluation of the fluid dynamic of the process in isothermal conditions

The first evaluation of the built model was made in isothermal conditions. This study allows to evaluate the process without the influence of the heat exchanging phenomena. Figure 8.6 shows the results of the model working in isothermal conditions as a function of the current density. The molar fraction of the H_2O and H_2 for the outlet streams of the external chamber and internal chamber, respectively, shows how the process obey the material balance (Figure 8.4a). The cell potential increases almost lineally with the current density (Figure 8.4b). This indicates that the cell voltage is determined by the cell resistance.

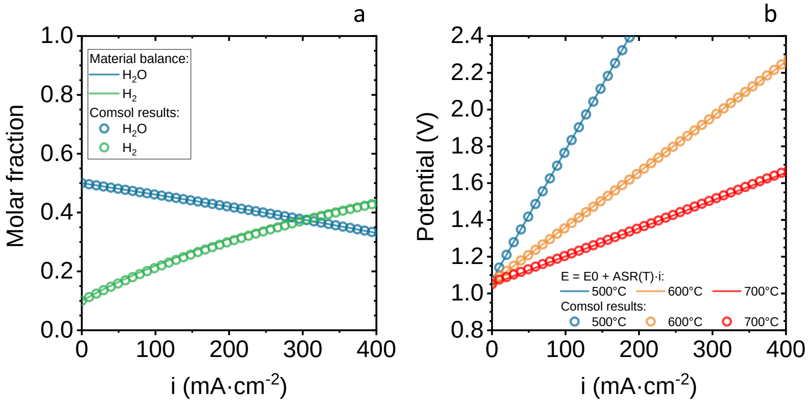

Figure 8.4. Results of the isothermal model. (a) Molar fractions of the steam (external chamber) and H_2 (internal chamber) regarding the current density applied; (b) Cell potential regarding the current density applied at different temperatures.

Gas speed profile for both chambers is depicted in Figure 8.5a and 8.5b when the process works isothermally at 600°C and 99 $mA \cdot cm^{-2}$. These profiles show that the gas presents laminar distribution and there is not signal of local turbulences. Additionally, Figure 8.5c and Figure 8.5d show the molar fraction profiles for steam and hydrogen for the external chamber and the internal chamber, respectively. These profiles show how the steam is converted gradually along the external electrode. Furthermore, there is not important radial contributions for these profiles. Likewise, there are practically no radial concentration gradients, i.e. the proper gas-phase transport for the chosen cell geometry is confirmed, while the spatially-progressive steam conversion and dilution with the formed oxygen can be recognized.

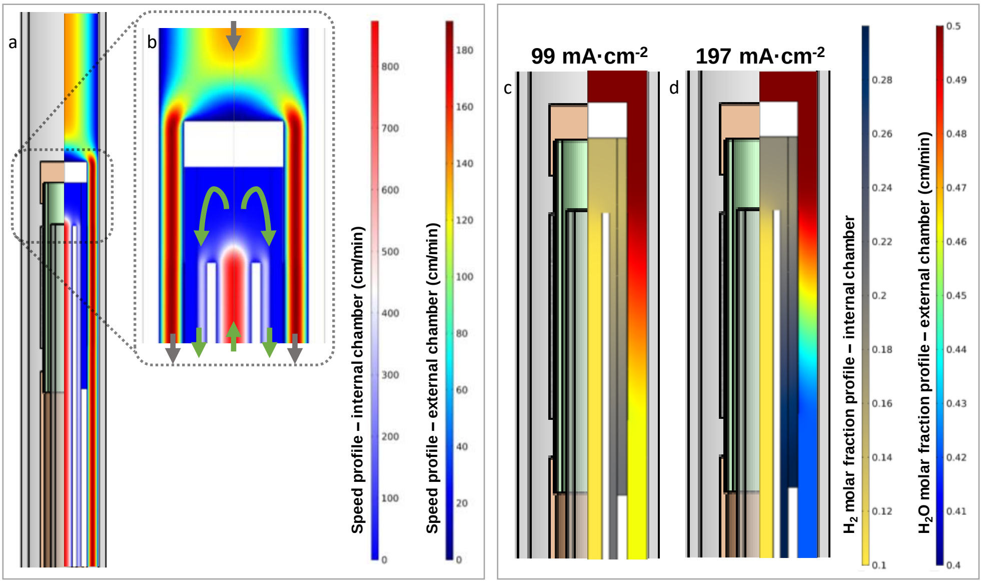

Figure 8.5. Results of the model in isothermal conditions at 600°C. (a) Gas speed profile in both chambers when the current density is 99 mA·cm^{-2}; (b) zoom of the gas speed profile; (c) Molar fraction profiles of H_2O and H_2 when the current density is 99 mA·cm^{-2}; (d) Molar fraction profiles of H_2O and H_2 when the current density is 197 mA·cm^{-2}.

Figure 8.6 shows the current profiles for the ionic contribution and electronic when the cell works isothermally at 600°C and 99 mA·cm^{-2}. These profiles show how the current is exchanged between electronic and ionic in the electrodes. Therefore, the electronic current decreases with the distance to the electrolyte decreases because the electronic current is gradually becoming in ionic current across the electrochemical reactions. Then, the ionic current crosses the electrolyte in the radial direction until reaching the other electrode.

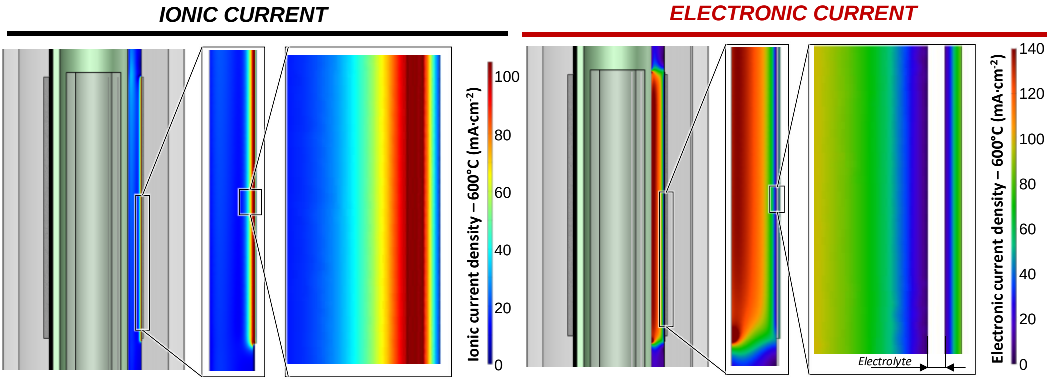

Figure 8.6. Profiles of the current density distribution at 600°C when the cell works isothermally with 99 mA·cm^{-2}.

Finally, as Figure 8.7 has shown, the cell potential is dominated by the ohmic losses. In this model, the overall resistance observed in the experimental setup was introduced in the electrolyte layer because the impossibility to switch the overall resistance in the contribution of each layer (i.e. electrodes, electrolyte, and contact between each layer). Figure 8.7 shows the ionic potential profile when the cell works isothermally at 600°C and 99 mA·cm^{-2}. This profile shows how the potential jump is gathered in the electrolyte layer.

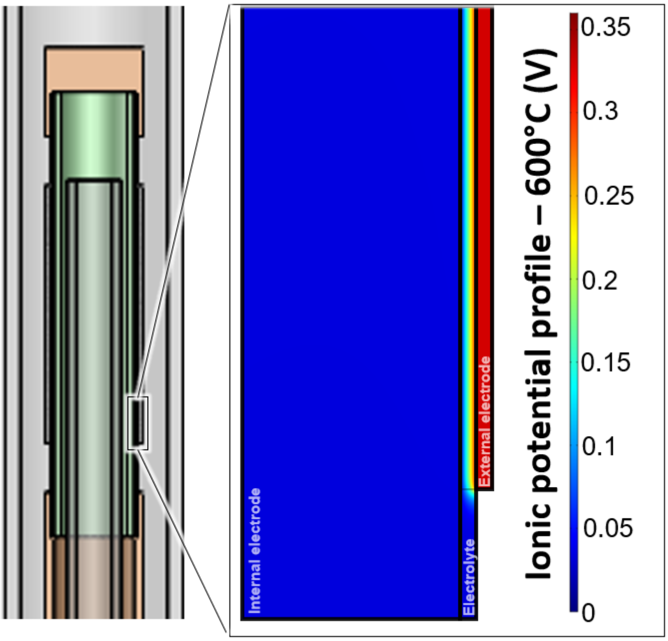

Figure 8.7. Results of the isothermal model: potential profile when the cell works isothermally at 600°C and 99 mA·cm^{-2}.

8.3.1.2. Analysis of the cell assembly working at the thermoneutral voltage

The finite element model was built to evaluate how the tubular cell works around the thermoneutral voltage in adiabatic conditions. Considering that all electrochemical energy exchanges are balanced, the process would work isothermally.

Figure 8.8 shows the results of the model when the cell works in the thermoneutral point. The model considers adiabatic conditions with surface-to-surface radiation contribution and media participating radiation for the external chamber. Temperature profile (Figure 8.8.c) shows no important temperature gradient profiles along the cell. The highest temperatures are gathered in the central zone of the cell. This is a consequence of the fact that top and bottom of the cell are refrigerated by inlet streams (steam feed for the external chamber and sweep for the internal chamber). Furthermore, molar fraction profiles (Figure 8.8.d) shows how the electrochemical reaction takes place gradually along the cell. As it was mention in the isothermal analysis, there is no important radial gradients that could limit the process.

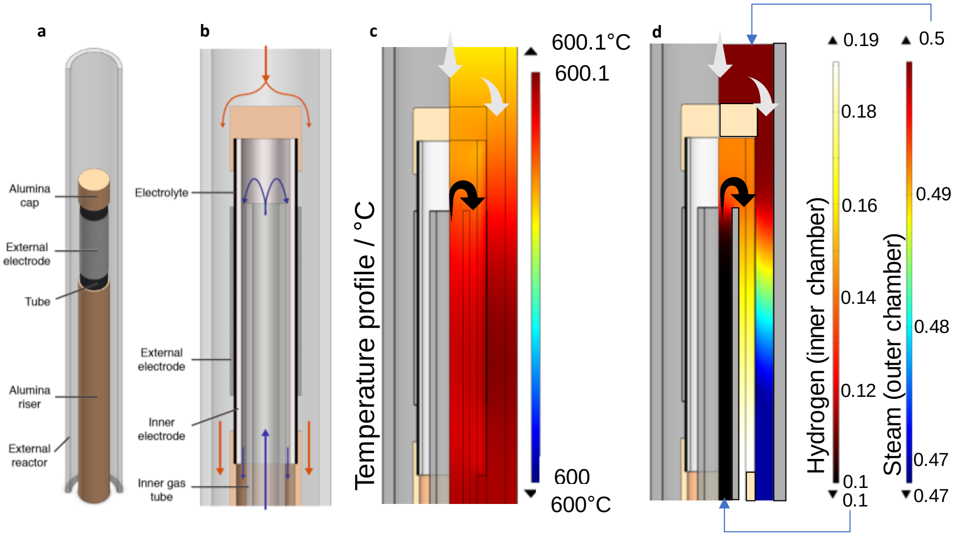
a
b
c
d
Alumina cap
External electrode
Tube
Alumina riser
External reactor
Electrolyte
External electrode
Inner electrode
Inner gas tube
Temperature profile / °C
600.1°C
600.1
600
600°C
0.19
0.18
0.16
0.14
0.12
0.1
0.1
Hydrogen (inner chamber)
0.5
0.49
0.48
0.47
0.47
Steam (outer chamber)

Figure 8.8. Results of the CFD model for the electrolysis working at the thermoneutral voltage. (a) General view of the setup, (b) cross section view of the setup; (c) Temperature profile of the electrolyser working at the thermoneutral voltage; (d) Molar fractions profile for the steam (external chamber) and hydrogen (internal chamber).

This first analysis shows how the built CFD model offers coherent results regarding the thermoneutral mode operation for the electrolyser at 600°C.

8.3.1.3. Effect of the radiation heat transference

The temperature plays a critical role in electrolysis mainly because its remarked influence on the conductivities of the electrochemical cell and, on the gas flows and gas diffusion. Considering the heat exchanging of electrolysis, the heat transference must be thoroughly characterized to avoid temperature polarizations that can lead to local inefficiencies. Therefore, in view of the range of the temperatures of this process works, the effect of the radiation heat transference has been evaluated. The results of the analysis of the radiation heat transference with the CFD model are in the Figure 8.9.

On one hand, when the radiation contribution is neglected, the low heat transference between the cell and the external gas flow makes the temperature in the cell is higher (Figure 8.9.a and b). This low heat transference is because the low contact area between the solid and the external gas. Otherwise, in the internal chamber, the internal porous domain improves the heat transference because: (i) the contact area is higher; (ii) the hydrogen is released at the cell temperature in this domain.

On the other hand, when radiation is considered, peak temperatures decrease comparing the radiation neglecting case (Figure 8.9c) because this contribution causes a mitigation of the heat sources of the process [39, 44-47]. Furthermore, the temperature distribution is more homogeneous. Including the radiation in the heat transference (as the radiation starts to play a significant influence in the heat transference), improves the way as the heat is transferred for the setup and, consequently, it causes the temperatures are more homogeneous.

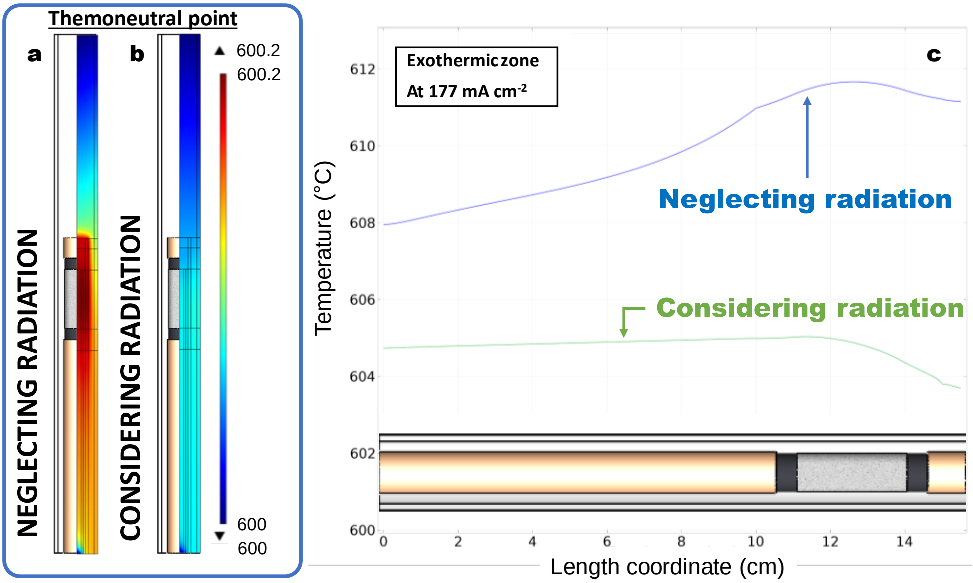

Figure 8.9. Evaluation of the radiation effect in the temperature distributions for an electrolyser working at the thermoneutral point. (a) Temperature profile neglecting the radiation heat transference; (b) Temperature profile considering radiation; (c) Temperature distributions along the tube of the electrolysis setup working in the exothermic zone.

Furthermore, the heat transference of this process involves different radiation contribution: (i) surface-to-surface between the different surfaces of the setup and (ii) participating media from the steam of the external chamber. Furthermore, the thermal conductivity of the porous domains was corrected. Considering the different contribution in the radiative heat transference, Figure 8.10 shows the different temperature profiles of the CFD model working in the exothermic zone (at around 100 mA cm^{-2}). Although the conventional implementation in the radiation implies neglecting the media participating contribution, the present results shows significant differences in the temperature distribution.

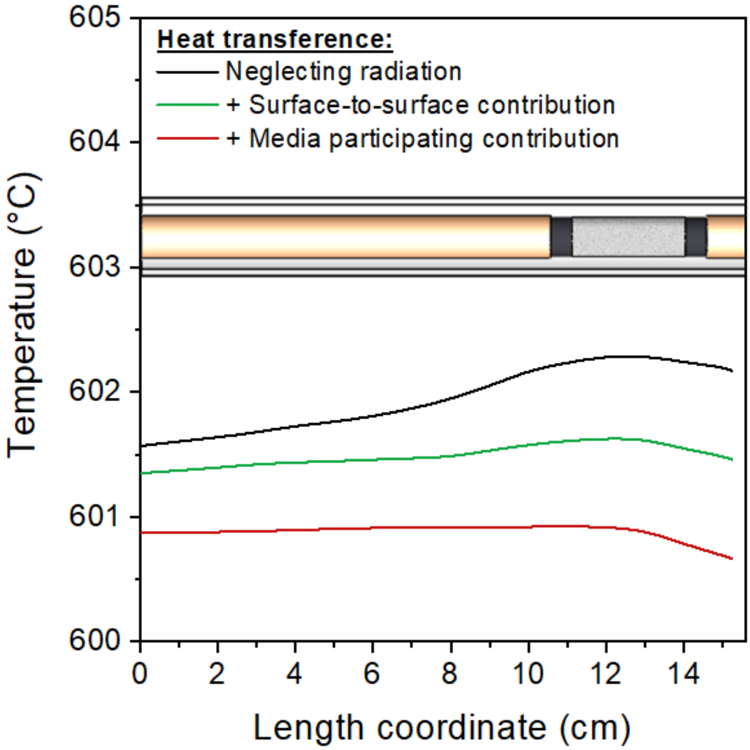

Figure 8.10. Evaluation of the effect of the different radiation phenomena in the electrolysis temperature distribution.

Figure 8.11 shows a comparison of the experimental results with the results of the model considering and neglecting the radiation contribution.

Experimental results for the cell potentials presents a stabilization as the current density increases. This stabilization is commonly attributed to an improvement of the electrochemical phenomena which turns in a decrease of the specific electrochemical resistance when the current density increases. However, comparing with results of the adiabatic model, the decreasing of the overall specific resistance could be simultaneously due an increase of the temperature in the cell, because the controller only reads the temperature locally in the place of the thermocouple. Considering that the electrolysis process implies high-energy exchanges (and the stabilization occurs in the exothermic zone (soft red zone in Figure 8.11a)), it can ascertain that the electrochemical process may causes a local increase of the temperature without the thermocouple realizes.

Finally, the model shows that there are no significant differences between neglecting or considering the radiative heat transference in the average temperature of the cell (even at cell potentials up to 1.8 V) but yes in the temperature distribution where the radiation improves the heat transference generating more homogeneous profiles. 600°C is not a very high temperature for the radiative heat transference causes significant changes.

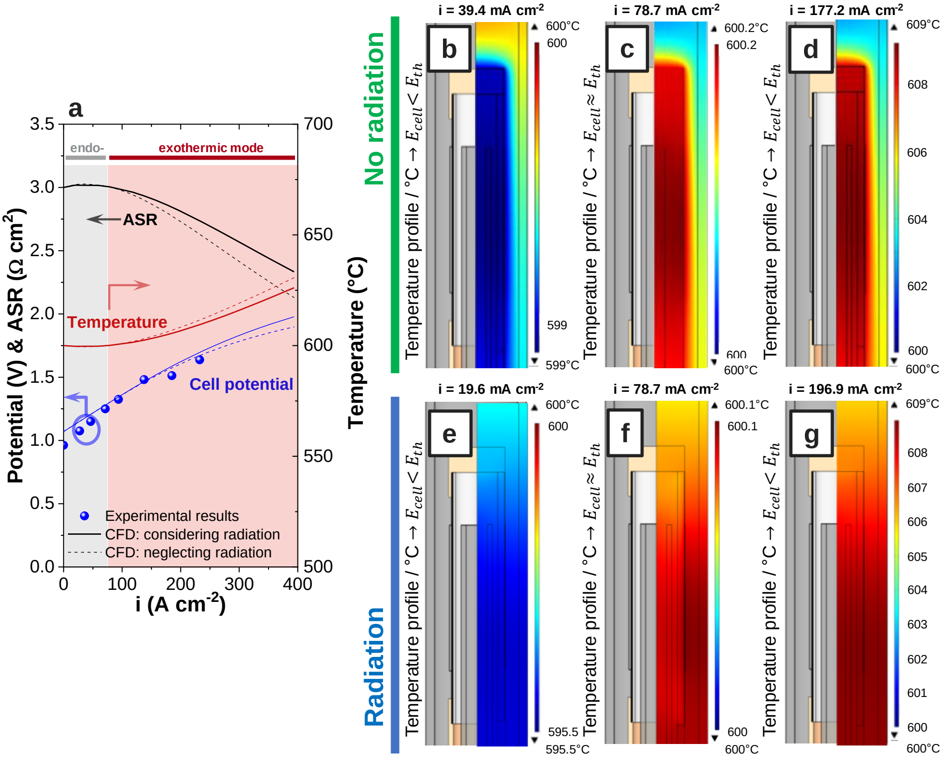

Figure 8.11. Final comparison of the CFD model. (a) Electrochemical results and average temperature for the CFD model (grey zone: endothermic mode operation, red zone: exothermic mode operation). Temperature profiles of the CFD model neglecting radiation for the endothermic mode (b), thermoneutral (c) and exothermic (d). Temperature profiles for the CFD model considering the radiation for the endothermic mode (e), thermoneutral (f) and exothermic zone (g)

8.3.1.4. *Upscaling effect in the heat transference*

One of the principal advantages for the conventional membrane processes is its easy scaling because it only supposes an increase of the membrane area. Therefore, the scaling was studied using different membrane areas considering the same inlet compositions and keeping the relation between the total inlet flow and the cell. Four setups were compared: (i) one cell with 2.9 cm of external electrode (experimental setup), (ii) one cell with 29 cm of external electrode (reference length x10), (iii) five cells with 2.9 cm of external electrode per cell and (iv) ten cells with 2.9 cm of external electrode per cell. The temperature profiles for cell working close of thermoneutral voltage are depicted in the Figure 8.12. These images show that increasing the area does not change significantly the temperatures when the heat sources are balanced. As can be observed the central zones are at higher temperatures than the bottom or the top. These zones are refrigerated by the inlet streams. Therefore, as the electrochemical area is higher, the temperature differences along the cell (for a larger electrode) or cells working at different temperatures (when the area is switched in several segments) is higher.

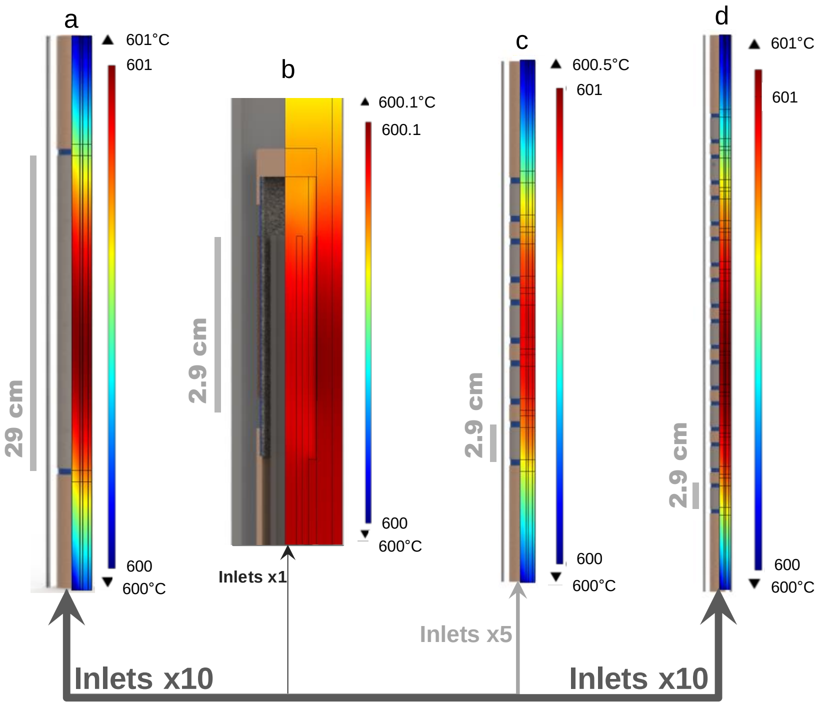

Figure 8.12. Results of the scaling study increasing the area of the cell working close the thermoneutral point. (a) Geometry of 29 cm of electrode length; (b) Experimental setup (2.9cm); (c) Geometry of 5 segments of 2.9cm of electrode length per segment; (d) Geometry of 10 segments of 2.9cm of electrode length per segment.

Considering the final application, working in the thermoneutral voltage only would require keeping well isolated the cell. However, working at higher voltages could bring problems due to there are zones or cells working with different temperatures due to the effect of the temperature in the conductivity of the cell (Figure 8.13). In a multisegmented configuration unit, if the segments are connected in series, then the current distribution in the segments is homogeneous, but the heat released not. The heat released would be higher in the segments where the temperature is lower and, consequently, this consequence brings the setup until to more isothermal distribution (Figure 8.13a). However, for segments connected in parallel, the current could not be perfectly distributed in the segments. This would be due to the current would be higher in segments with lower resistances (Figure 8.13b).

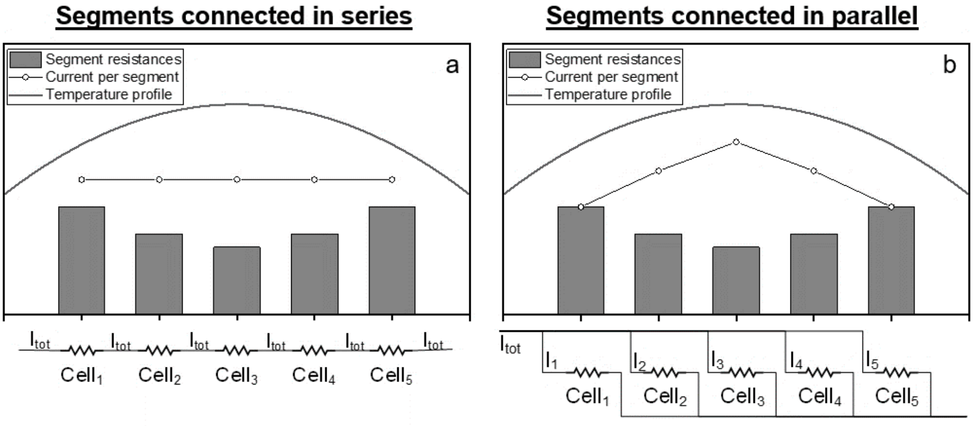
Segments connected in series
Segments connected in parallel
Segment resistances
Current per segment
Temperature profile
a
b
Itot
Cell1
Cell2
Cell3
Cell4
Cell5
I1
I2
I3
I4
I5

Figure 8.13. View of the different types of electric connection when the total area is switched in several segments; (a) segments connected in series; (b) segments connected in parallel.

Figure 8.14 shows results of the potential, the average temperature of the setup and the overall specific resistance of each cell for the different geometries considered in the study of the scaling-up. The results show how the temperature increases when the total area increases. This increase of the temperature causes a decrease in the resistance of the cell and, consequently, the potentials are lower. For the geometries which have different segments, the difference in the cell potential of each segment for the same current density is because each segment works at different temperature.

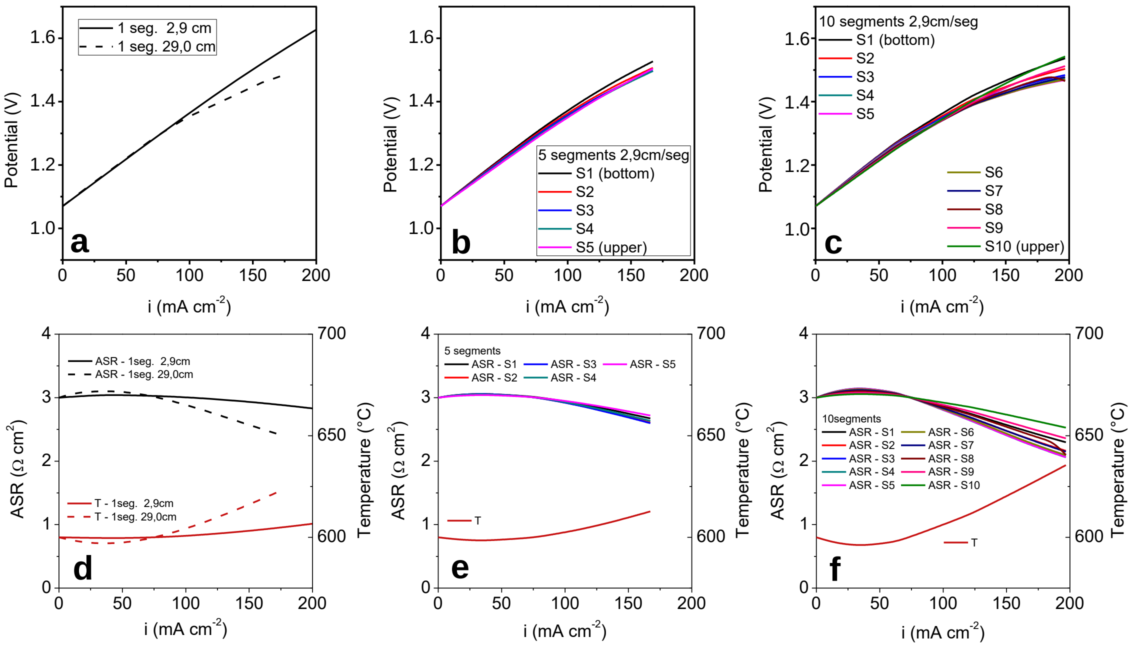

Figure 8.14. Results of the scaling study about tubular electrolyser. 1 segment: potentials depending the current density (a); ASR and temperature depending on current density (d); 5 segments/tube: potentials depending on the current density (b); ASR and temperature depending on current density (e); 10 segments/tube: potentials depending on the current density (c); ASR and temperature on depending current density (f).

Additionally, note that the scaling of the reactor systems, the heat problems are usually enlarged (usually caused by the difficult evacuation of heat leading to higher temperatures). When the electrolyser should be scale up for the final application working at the thermoneutral voltage should be the best way to avoid heat problems of and peak temperatures.

8.3.1.5. Effect of the specific resistance

The Joule effect can govern the electrolysis process until overcontrol temperature situations when the process works at high voltages (above of the thermoneutral voltage). The Joule effects originate rightly from the electrochemical resistance of the cell. Therefore, a study of the effect of this resistance is necessary to evaluate the Joule effect influence on the heat transference and overall thermal behavior.

Figure 8.15 shows the average temperatures for the electrolysers considering a total resistance at 600°C of 1, 2 and 3 Ω·cm^2 (keeping the energy activation). Electrochemical cell with lower specific resistance reaches the thermoneutral voltage at higher current densities because the potential drop is lower. The thermoneutral voltage is reached at 77 mA·cm^{-2}, 115 mA cm^{-2} and 225 mA·cm^{-2}, when the overall resistance at 600°C ($ASR_{600°C}$) is 1 Ω·cm^2, 2 Ω·cm^2 and 3 Ω·cm^2, respectively. Furthermore, the increase of the endothermal zone (cell potential lower than thermoneutral voltage) may allow integrating the setup on other process with present an excess of heat. In general, as the overall specific resistance is lower, the temperatures are being lower.

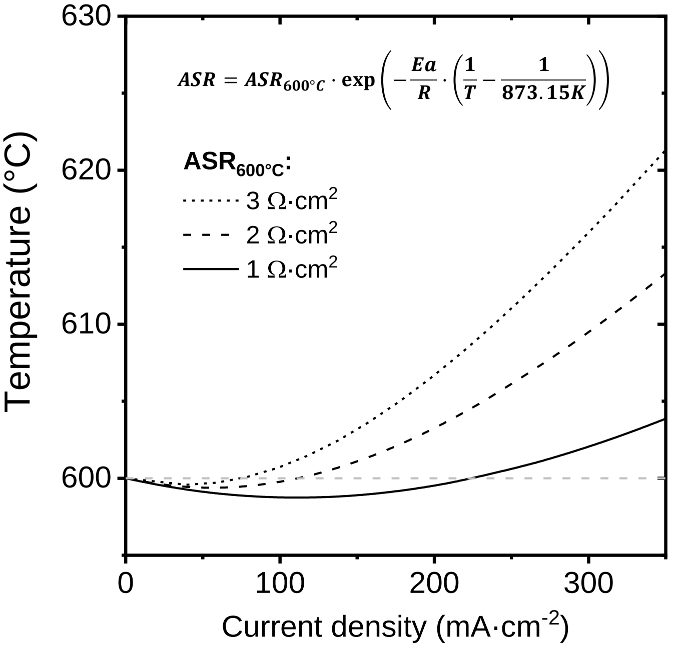

Figure 8.15. Results of the average temperature of the study of the overall specific resistance with the CFD model.

Figure 8.16 shows the cell potential when the current density is increased for several specific resistance. As the overall electrical resistance becomes higher, the temperature rise reaching faster the exothermal mode of the electrolysis (cell potential higher than thermoneutral voltage). As a consequence of this increase of the temperature, the overall resistance decreases slightly (considering the Arrhenius expression) and, thus, the deviation of the cell potential linearity is higher as the overall electric resistance increases.

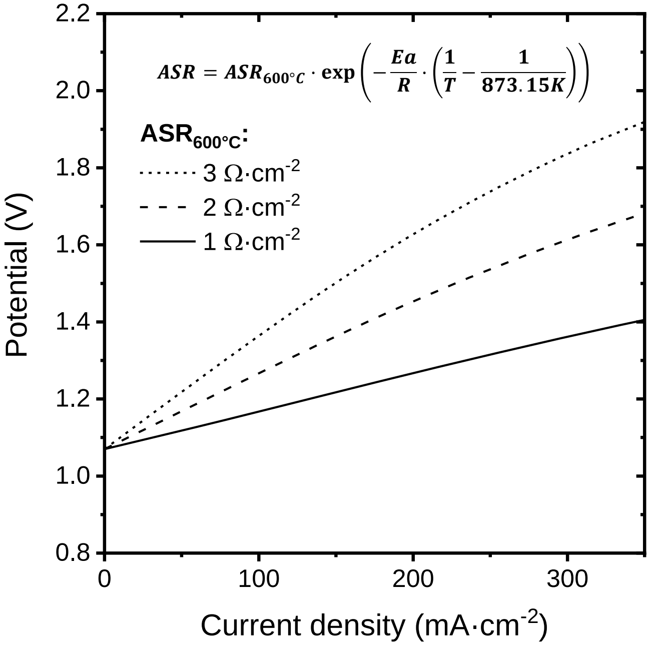

Figure 8.16. Cell potential results depending of the current density applied. Study of the overall specific resistance in the CFD model.

8.3.2. Evaluation of the efficiency of electrolysis process based on protonic conducting materials at high temperature

Electrolysis converts electric energy in chemical energy, in this case in form of hydrogen. Considering electrolysis based on protonic ceramics at high temperature, the conditions (i.e. temperature and pressure) plays a critical role under the behavior of the process. These sections make a detailed study of the effect of these conditions under the theoretical behavior of the process.

8.3.2.1. Thermodynamics of the hydrogen pressurization in electrolysis working in the thermoneutral potential

One of the advantages of the electrolysis in protonic cells is the possibility to produce pressurized hydrogen in situ. Electrolysis does not imply a conventional gas pressurization where the hydrogen (or other gas or fluid) goes from an initial pressure p_1 until a pressure p_2 ($p_2 > p_1$). In electrolysis, hydrogen is generated from water (steam for these conditions) across the electrochemical reactions. Then, in electrolysis we cannot talk formally about compression or pressurization of the hydrogen. However, it is necessary to identify where the electrochemical energy exchange takes place when the hydrogen pressure is increased.

The Figure 8.17 shows the theoretical reversible and thermoneutral voltages at different temperatures, hydrogen pressures and different steam pressures. As can be observed, increasing the hydrogen pressure increases the reversible voltage. Thermodynamically, increasing the pressure of the hydrogen it causes a decrease of the entropy of the overall electrochemical reaction and, thus, the Gibbs energy increases. It becomes in the observed increase of the reversible potential. Therefore, when the hydrogen pressure increases, the difference between the reversible voltage and the thermoneutral voltage decreases. If this difference decreases, the current density to reach the thermoneutral voltage decreases (considering the same overall specific resistance). The decrease in the current density leads a decrease of the hydrogen productivity considering the same electrochemical membrane area. Increasing the electrochemical area allows to keep the hydrogen productivity. Otherwise, an increase of the pressure of the steam causes an increase of the entropy of the electrochemical reaction and the opposite effect to the increase of the pressure in the hydrogen pressure.

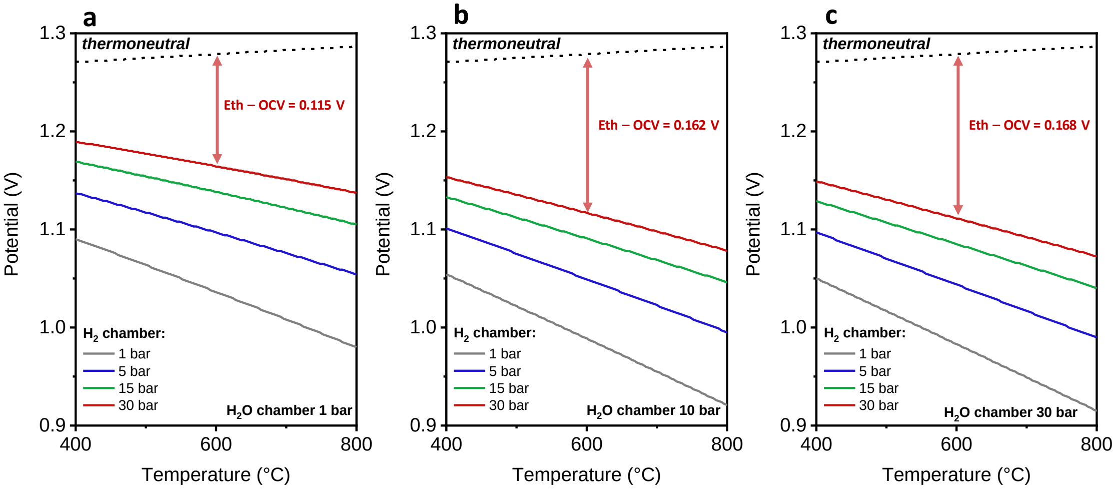

Figure 8.17. Thermoneutral and reversible voltages for water electrolysis depending on the temperature with different pressures for the hydrogen chamber and steam chamber. (a) Results at atmospheric pressure for the steam chamber; (b) Results at 10 bar for the steam chamber; (c) Results at 30 bar for the steam chamber.

Additionally, increasing the pressure for the steam chamber could improve the protonic conductivity of the material and, hence, the resistance of the overall cell decreases. Figure 8.18a shows the effect of the pressure of the steam neglecting its effect on the protonic conductivity of the electrolyte. Figure 8.18b shows the coupled effect (both reversible voltage and resistance of the cell) of the steam pressure. Finally, the increase of the steam pressure causes a decrease in the reversible voltage and in the resistance of the cell that imply an increase of the current density working at the same potential.

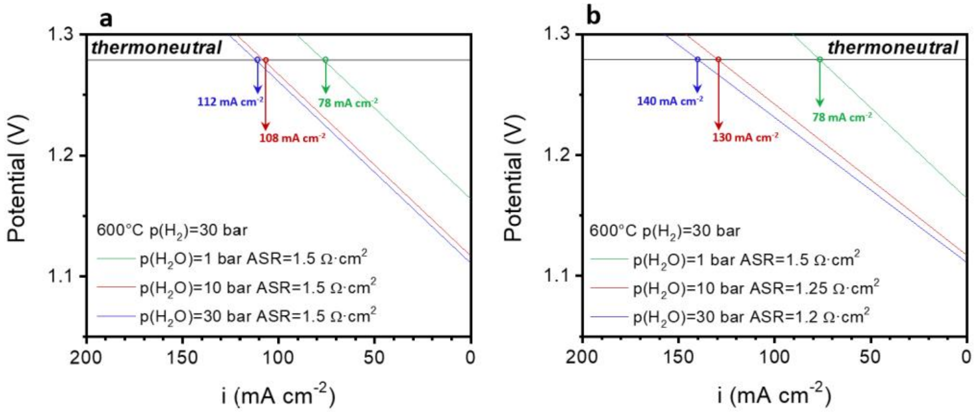

Figure 8.18. Electrolysis curves for different hydrogen pressures at 600°C. (a) Considering a fixed overall specific resistance; (b) simulating the improve of the conductivity when the steam partial pressure increases.

8.3.2.2. Thermodynamic study of the effect of the hydrogen pressure in the overall energy

In this section the effect of the pressure of the hydrogen on the energy to obtain hydrogen from protonic-based electrolysers at high temperature is analyzed.

Figure 8.19 shows the electrochemical results of the cell working at 600°C and at the thermoneutral voltage when the hydrogen pressure is increased. The overall resistance considered of the cell was 3 $\Omega \cdot cm^2$ and the faradaic efficiency was considered 100%. The increase of the hydrogen pressure does not change the thermoneutral voltage because it does not affect to the enthalpy of the reaction. However, as it was mention before, it supposes an increase of the reversible potential and a decrease of the current density to keep the potential. Therefore, although the energy cost per hydrogen is the same, the hydrogen produced per area of electrolyser decreases.

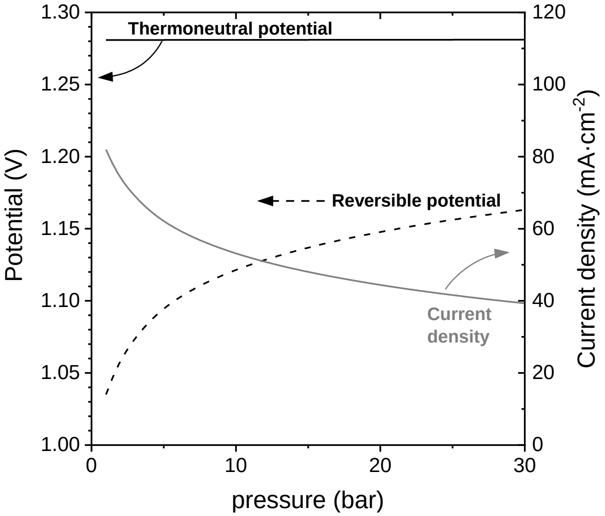

Figure 8.19. Effect of the hydrogen pressure on the electrochemical results when the cell works at the thermoneutral voltage at 600°C.

For the same electrolysis setup (keeping the electrochemical area), the hydrogen produced, and the steam converted decrease. The decrease of the steam converted could affects to the efficiency if the feeding is not controlled suitability.

Figure 8.20 shows the energy cost contribution of the electrolysis process when the hydrogen pressure increases, the cell works in the thermoneutral voltage and the feeding of steam keeps constant. In this case, keeping the feeding of steam causes the unconverted fraction increases. Although, the electrolysis work keeps constant with the hydrogen pressure (dark gray contribution), the evaporation contribution (light gray) increases with the hydrogen pressure. The decrease of the steam conversion implies the energy to transform the water to steam is lost for the non-reacted water fraction.

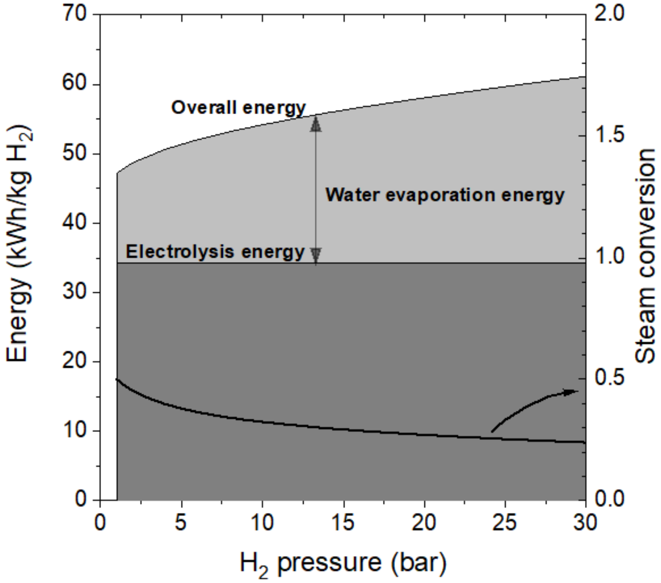

Figure 8.20. Effect of the hydrogen pressure in the energy contributions of the electrolysis process and in the steam conversion when the steam conversion is 90% at 1 bar of hydrogen.

Therefore, considering these results, the increase of the overall energy of the process when the hydrogen pressure increases can be offset decreasing the inlet flow to keep constant the steam conversion. Figure 8.21 shows the results of the different contribution of the process and the efficiency of the process regarding the steam conversion with the cell is working at the thermoneutral voltage. In this case, it was considered the inlet flow is controlled to keep the steam conversion. Once again, the electrolysis energy is not affected by the steam conversion in terms of energy unit per hydrogen obtained while the evaporation contribution increases when the steam conversion decreases. As can be observed, water evaporation represents around 25% of the energy required when the steam conversion is around 1. However, when the steam conversion is lower than 0.5, this contribution reaches around the 33% of the overall demand. This causes, the energy efficiency of the process (expressed in the energy of the hydrogen obtained regarding the energy of the process) could decrease around a 10% due to the steam conversion. Therefore, controlling the inlet flow to keep the steam conversion is critical for the efficiency of the process.

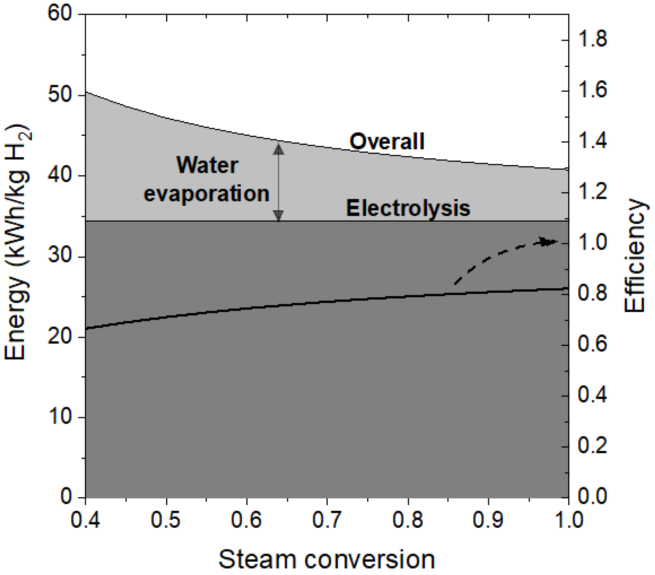

Figure 8.21. Efficiency in the stored energy in the hydrogen depending on steam conversion when the cell works at the thermoneutral voltage at 600°C.

8.3.2.3. Study of the effect of the faradaic efficiency in the energy stored efficiency

The last analysis studies the energy of the hydrogen obtained considers 100% faradaic efficiency. For the evaluation of the faradaic efficiency effect in the efficiency of the process, experimental results were used. Figure 8.22 shows the summary of the experimental results. Cell potential increases when the current applied increases due to the different resistances of the electrochemical cell. Faradaic efficiencies are quite high for low cell potentials and 500 – 600 °C.

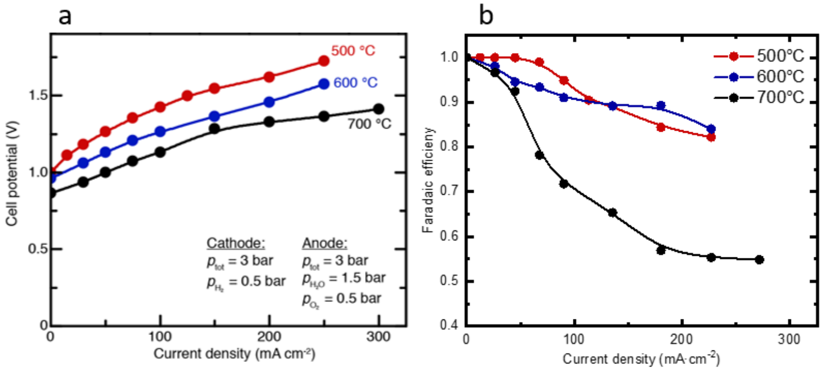

Figure 8.22. Summary of the experimental results at several temperatures. (a) Cell potential regarding the current density applied; (b) Faradaic efficiency regarding the current density applied.

Figure 8.23 shows the results of the energy stored efficiency for different energy demands. Results shows how the energy efficiency decreases when the current density increases. That is because two main reasons: (i) the increase of the overpotentials with the current density; (ii) the faradaic efficiency decreases with the current density.

Electrolysis is a process where water dissociation takes place. Water dissociation is a reaction which requires high amounts of energy. Part of this energy is applied in form of electricity (*P(elec)*), but it is not the overall energetic demand of this reaction. The entropic contribution of this reaction ($-T \cdot \Delta S$) must be added in form of heat. Therefore, considering endothermic operation mode (where this heat demand, *H(elec),* is not balanced with the heat from the Joule effect), if an additional source of heat is considered, the process could reach energy efficiencies higher than 100% (only taking into account the electrolysis). This is possible when, for example the electrolysis is integrated with a process with an excess of heat regarded as “free heat”. However, it is more suitable considering this heat demand in the balance in the cases the Joule effect cannot overcome this demand (i.e. endothermic operation mode). Additionally, the vaporization of water ($H(H_2O)$) supposes a significant decrease of the energy efficiency. That decrease could be higher than 20% considering the water utilization in the electrolyser at low potentials.

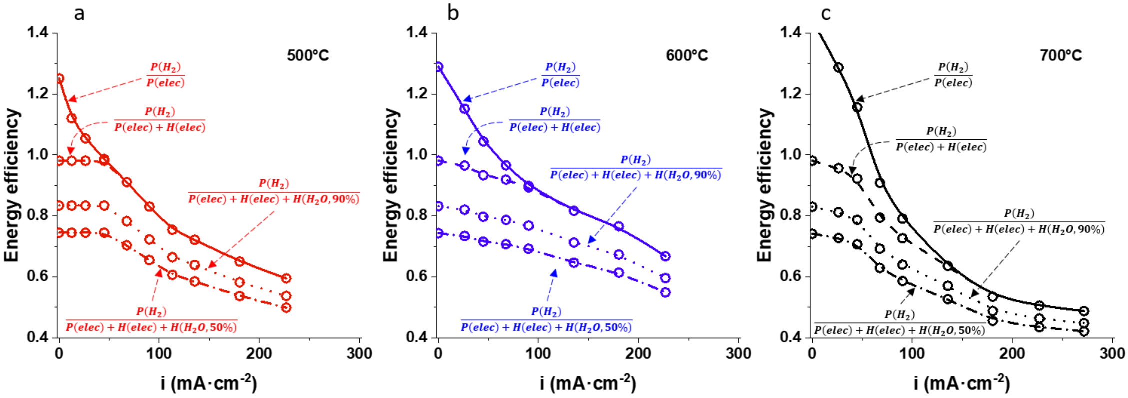

Figure 8.23. Results of the energy efficiency of the electrolysis. (a) results at 500°C; (b) results at 600°C; (c) results at 700°C.

Figure 8.24 shows the results of the energy efficiency considering the electricity and the heat demand of the electrolysis for different temperatures. The effect of the resistances is higher at lower temperatures as the conductivities improves with the temperature. Additionally, the faradaic efficiency declines significantly above 600°C. Therefore, for this cell, above 600°C the decline of the energy efficiency is caused mainly by the rise of the electronic leaks. Below this temperature, the decrease of the efficiency is due to the increase of the resistance contribution of the electrochemical cell.

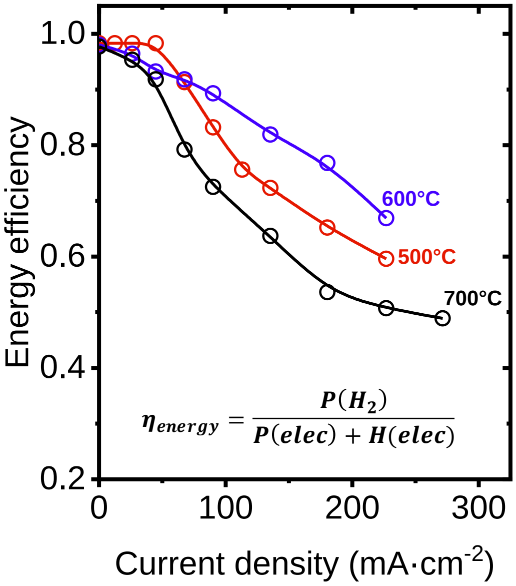

Figure 8.24. Energy efficiency for different temperatures.

8.4. Summary

Electrolysis using proton conducting materials at high temperatures has been analyzed considering different points of views.

A CFD model was built to evaluate the electrolysis using protonic conductor ceramic cells. The radiative heat transference contribution was evaluated in this study detecting slightly lower temperatures and more homogeneous temperature than if this heat contribution is neglected. Working in the thermoneutral voltage, there are not important temperature gradients in the process.

Considering the scaling up, the overall electric resistance of the electrochemical cell (or cells for multisegment) is the most critical factor because the heat from the Joule effect can cause overheatings in the system. Additionally, if the tube cell presents an electrochemical area switched in different segments, the parallel connection between these segments could cause the heterogeneous distribution of the current. If this happens the heat released in each local point changes proportionally with the current density and, consequently, the efficiency of the overall process could be dramatically affected.

Thermodynamic evaluation of the overall plant for the electrolysis process is considered focusing the study in the pressures of the different streams. An increase the hydrogen pressure causes an increase of the reversible potential. Then the thermoneutral voltage is reached at lower overpotentials, consequently, the current density at this point decrease considering the same overall specific resistance. This effect can be mitigated increasing the steam pressure, because it counteracts the entropy effect to increase the hydrogen pressure (at least partially). Additionally, considering the overall process, electrolysis energy is the highest energy demand of the process. However, the vaporization energy demand is not insignificant and, consequently, the steam conversion in the electrolyser must be optimized and controlled in order to avoid inefficiencies in the process.

List of symbols

Symbol	Description	Symbol	Description
κ_r	Adsorption coefficient of radiation	v_i	Molecular volume of the i compound (*A*)
F_{amb}	Ambient factor	M_n	Molecular weight of the gas mixture (*g/mol*)
G_{amb}	Ambient irradiation	M_i	Molecular weight of the i compound (*g/mol*)
ω_j	Angular range	Gm	Mutual irradiation coming of other surfaces
ASR	Asymmetric specific resistance ($\Omega\cdot cm^2$)	ϕ_a	Overpotentials (a=I: ionic; a=S: electric) (V)

D_i^m	Average diffusion coefficient for the *i* compound (m^2/s)	η	Overpotentials (V)
E_{cell}	Cell voltage (*V*)	p_i	Partial pressure of the i compound (*bar*)
k_{diff}	Coefficient for the binary gas coefficient (10^{-3} *cm^2/s·atm*)	d_p	Particle size of the porous bed (*m*)
σ_a	Conductivity *(a=I: ionic; a=S: electric) (S/m)*	κ	Permeability of the porous bed (m^2)
R	Constant of the ideal gases (8.314 *J/mol/K*)	$\phi(S_i, S_j)$	Phase function between the surface Si and Sj
i_a	Current density *(a=I: ionic; a=S: electric)* (A/m^2)	ϵ_p	Porosity
ρ	Denisty (kg/m^3)	Pr	Prandt number
d_{eq}	Diameter of the chamber (*m*)	p	Pressure (*bar*)
μ	Dynamic viscosity (*Pa·s*)	k_R	Radiative equivalent thermal conductivity (*W/m/K*)
$P(elec)$	Electric power demanded for the electrolysis process	J	Radiosity
β	Electrochemistry transfer coefficient	r_i	Reaction rate of i ($kg/m^3/s$)
z	Electrons exchanged	n	Refractive index (fixed at 1)
ε	Emmitance of the material	E_{eq}	Reversible potential contribution (V)
η_{energy}	Energy efficiency	E_{eq}^0	Reversible potential in standar conditions (V)
$P(H2)$	Energy of the hydrogen obtained in the electrolysis process (*kWh/kg*)	Re_p	Reynolds number in the porous domain
ΔH_i	Enthalpy of the i compound (*J/mol*)	σ_{sc}	Scattering coefficient
i_0	Exchange current density (A/cm^2)	θp	Solid fraction in a porous domain
β_R	Extinction radiation coefficient	Q_{br}	Source term (kg/m^3/s)
η_{Far}	Faradaic efficiency	I_i	Spectra radiation intensity of the surface Si
F	Faraday constant (96485 C/mol)	σ_B	Stefan-Boltzmann constant (5.67·10-8 $W \cdot m^{-2} \cdot K^{-4}$)
F_i	Flow of the i compound (kg/s)	n_i	Stoichiometric coefficient of the i compound
ΔG^0	Gibbs energy in estándar conditions (J/mol)	Si	Surface i
Cp	Heat capacity (J/kg/K)	T	Temperature (K)
γ	Heat capacity ratio	k	Thermal conductivity (W/m/K)
$H(elec)$	Heat demanded for the electrolysis process	k_{eq}	Thermal conductivity for the porous domain (W/m/K)
$H(H2O)$	Heat of the evaporation of water	E_{th}	Thermoneutral voltage (V)
Q_{term}	Heat source term (W/m^3)	I_{tot}	Total current applied (A)
$Heat_{REACTION}$	Heat source term of the reaction (W/m^3)	$Heat_{ELEC}$	Total electric power

$F0_i$	Inlet flow of the i compound (*kg/s*)	u	Velocity (m/s)
Q_I	Ionic source term (A/m^3)	$XH2O$	Water conversion in the electorlysis
G	Irradiation	*H(evap)*	Water evaporation energy (*kWh/kg)*
e_b	Irradiation of a black body	N_i	Weight flow for the i compound (kg/m^2/s)
β_F	Isothermal compressibility coefficient	j_i	Weight flux for the i compound (kg/m^2/s)
LHV_{H2}	Low Heating Value of hydrogen (241.8 *kJ/mol*)	w_i	Weigth fraction of the i compound
$D_{i,j}$	Maxwell-Stefan diffusivity (m^2/s)	$\phi_{i,j}$	Wilke dimensionless number of the i and j compounds
x_i	Molar fraction of the i compound		

8.5.References

1. Marbán, G. and T. Valdés-Solís, International Journal of Hydrogen Energy, 2007. **32**(12): p. 1625-37.
2. Lymberopoulos, N. *Hydrogen from Renewables*. 2007. Dordrecht: Springer Netherlands.
3. Armaroli, N. and V. Balzani, ChemSusChem, 2011. **4**(1): p. 21-36.
4. Abbasi, T. and S.A. Abbasi, Renewable and Sustainable Energy Reviews, 2011. **15**(6): p. 3034-40.
5. Eberle, U., et al., Angewandte Chemie International Edition, 2009. **48**(36): p. 6608-30.
6. Yang, J., et al., Chemical Society Reviews, 2010. **39**(2): p. 656-75.
7. Hosseini, S.E. and M.A. Wahid, Renewable and Sustainable Energy Reviews, 2016. **57**: p. 850-66.
8. Nikolaidis, P. and A. Poullikkas, Renewable and Sustainable Energy Reviews, 2017. **67**: p. 597-611.
9. Holladay, J.D., et al., Catalysis Today, 2009. **139**(4): p. 244-60.

10. Ruether, J., et al., *Life-cycle analysis of greenhouse gas emissions for hydrogen fuel production in the United States from LNG and coal*. 2005, DOE/NETL-2006/1227. November.
11. Bhandari, R., et al., Journal of Cleaner Production, 2014. **85**: p. 151-63.
12. Ball, M. and M. Weeda, International Journal of Hydrogen Energy, 2015. **40**(25): p. 7903-19.
13. Götz, M., et al., Renewable Energy, 2016. **85**: p. 1371-90.
14. Wang, M., et al., Renewable and Sustainable Energy Reviews, 2014. **29**: p. 573-88.
15. Zhang, X., et al., Applied Energy, 2017. **190**: p. 326-38.
16. Uusitalo, V., et al., Energy Conversion and Management, 2017. **134**: p. 125-34.
17. da Silva Veras, T., et al., International Journal of Hydrogen Energy, 2017. **42**(4): p. 2018-33.
18. Buttler, A. and H. Spliethoff, Renewable and Sustainable Energy Reviews, 2018. **82**: p. 2440-54.
19. Kim, J., et al., Nano Energy, 2018. **44**: p. 121-6.
20. Bi, L., et al., Chemical Society Reviews, 2014. **43**(24): p. 8255-70.
21. Zhang, J.-H., et al., Energy Conversion and Management, 2017. **149**: p. 646-59.
22. Kang, J., et al., Journal of Fuel Cell Science and Technology, 2015. **12**(5): p. 051006--7.
23. García-Camprubí, M., et al., Renewable and Sustainable Energy Reviews, 2014. **33**: p. 701-18.
24. Choi, H.-W., et al., ECS Transactions, 2013. **57**(1): p. 3161-70.
25. O’Brien, J.E., et al., 2005(42223): p. 117-26.
26. Navasa, M., et al., Applied Energy, 2015. **137**: p. 867-76.
27. Klein, J.-M., et al., ECS Transactions, 2009. **25**(2): p. 1305-14.

28. Hawkes, G.L., et al., Nuclear Technology, 2007. **158**(2): p. 132-44.

29. Ni, M., International Journal of Hydrogen Energy, 2012. **37**(8): p. 6389-99.

30. Bruce E. Poling, J.M.P., John O' Connell, *The properties of gases and liquids. 5th edition.* 2000, New York, Chicago, San Francisco, Athens, London, Madrid, Mexico City, Milan, New Delhi, Singapore, Sydney, Toronto: McGraw-Hill Education.

31. Donald A. Nield, A.B., *Convection in Porous Media. Third Edition*. 2006, United States of America: Springer.

32. Kyriakou, V., et al., Applied Catalysis B: Environmental, 2016. **186**: p. 1-9.

33. Malerød-Fjeld, H., et al., Nature Energy, 2017.

34. Matyka, M., et al., Physical Review E, 2008. **78**(2): p. 026306.

35. Pisani, L., Transport in Porous Media, 2011. **88**(2): p. 193-203.

36. Murthy, S. and A.G. Fedorov, Journal of Power Sources, 2003. **124**(2): p. 453-8.

37. Mahcene, H., et al., Energy Procedia, 2014. **50**(Supplement C): p. 229-36.

38. Zeng, M., et al., Journal of Power Sources, 2012. **206**(Supplement C): p. 185-96.

39. Calise, F., et al., International Journal of Hydrogen Energy, 2007. **32**(17): p. 4575-90.

40. Daun, K.J., et al., 2005(47349): p. 183-91.

41. Daun, K.J., et al., Journal of Power Sources, 2006. **157**(1): p. 302-10.

42. Mejri, I., et al., Internatiomal Journal of Heat and Technology, 2016. **34**(3): p. 351-6.

43. DiGiuseppe, G., Journal of Fuel Cell Science and Technology, 2012. **9**(6): p. 061007--9.

44. Pianko-Oprych, P., et al., *Quantification of the Radiative and Convective Heat Transfer Processes and their Effect on*

mSOFC by CFD Modelling, in *Polish Journal of Chemical Technology*. 2014. p. 51.

45. Ong, K.M., et al., 2012(44823): p. 273-80.
46. Hajimolana, S., et al., Fuel Cells, 2012. **12**(5): p. 761-72.
47. VanderSteen, J. and J. Pharoah. *The effect of radiation heat transfer in solid oxide fuel cell modeling*. in *Combustion Institute/Canadian Section, Spring Technical Meeting*. 2004.
48. Lienhard, J.H., *A heat transfer textbook*. 2013: Courier Corporation.
49. de Wasch, A.P. and G.F. Froment, Chemical Engineering Science, 1972. **27**(3): p. 567-76.
50. Elnashaie, S.S., *Modelling, simulation and optimization of industrial fixed bed catalytic reactors*. Vol. 7. 1994: CRC Press.
51. Roses, L., et al., *Computational fluid dynamics (CFD) analysis of membrane reactors: Simulation of a palladium-based membrane reactor in fuel cell micro-cogenerator system*. Vol. 1. 2013. 496-531.
52. Wakatsuki, K., et al., *Determination of Planck Mean Absorption Coefficients for Hydrocarbon Fuels*. Vol. 180. 2008. 616-30.
53. Barlow, R.S., et al., Combustion and Flame, 2001. **127**(3): p. 2102-18.
54. Grosshandler, W., *RADCAL: a narrow-band model for radiation calculations in a combustion environment NIST Tech*. 1993, Note 1402.
55. Mossi, A., et al., Journal of the Brazilian Society of Mechanical Sciences and Engineering, 2012. **34**: p. 112-9.

9. THERMOFLUID DYNAMIC EVALUATION OF THE HYDROGEN EXTRACTION IN A PROTONIC MEMBRANE REFORMER

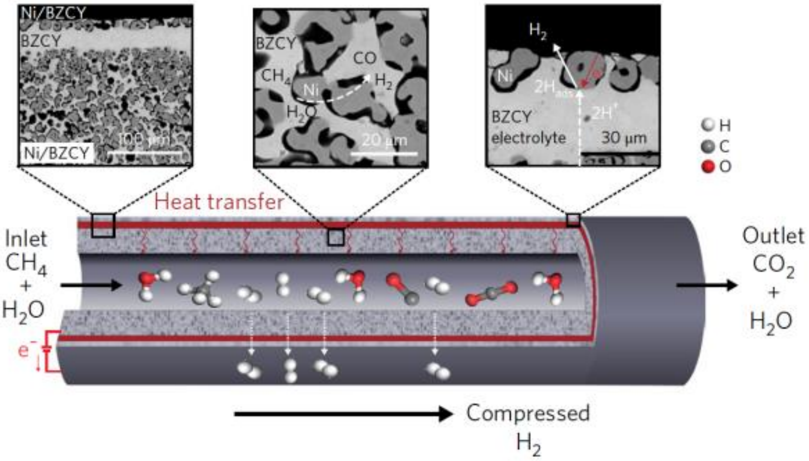
Ni/BZCY
BZCY
Ni/BZCY
100 μm
BZCY
CH_4
Ni
H_2O
CO
H_2
20 μm
H_2
Ni
$2H_{ads}$
$2H^+$
BZCY electrolyte
30 μm
H
C
O
Heat transfer
Inlet CH_4 + H_2O
Outlet CO_2 + H_2O
e^-
Compressed H_2

9. THERMOFLUID DYNAMIC EVALUATION OF THE HYDROGEN EXTRACTION IN A PROTONIC MEMBRANE REFORMER 261

9.1. INTRODUCTION 264
9.2. OBJECTIVES 266
9.3. METHODS 267
9.3.1. DESCRIPTION OF THE PROCESS 267
9.3.2. EXPERIMENTAL PROCEDURE 268
9.3.3. GEOMETRY 268
9.3.4. PHYSICS EQUATIONS 270
9.3.5. STUDIES PERFORMED AND CONDITIONS 281
9.3.6. EFFECT OF THE RADIATION IN THE HEAT TRANSFERENCE .. 288
9.3.7. MESHING AND SOLVER 289
9.4. RESULTS 290
9.4.1. BRIEF DESCRIPTION OF THE EXPERIMENTAL RESULTS 290
9.4.2. VALIDATION OF THE FINITE ELEMENT MODEL 294
9.4.3. ANALYSIS OF THE PMR IN ADIABATIC CONDITIONS 307
9.5. SUMMARY 323
9.6. REFERENCES 327

9.1. Introduction

Nowadays, more than 90% of the worldwide hydrogen production is obtained using steam reforming processes [1, 2]. Conventional production of hydrogen requires large industrial plants to minimize energy losses and capital costs associated with steam reforming, water–gas shift, product separation and compression. Furthermore, although hydrogen is a clean source of energy, as almost the full hydrogen is obtained from fossil fuels, this hydrogen presents an important CO_2 footprint (8.62 kg CO_2 equivalent per each kg of H_2) [1, 3]. Alternative methods are not economically competitive yet and, only power-to-hydrogen projects (using electricity surplus of the renewable sources) seem to have possibilities to take part of the hydrogen market in short/middle-terms [4-11]. Hence, improvements over conventional reforming process are still necessary, e.g. to improve the conversion or to decrease the process energy demand.

Several studies have proposed palladium-based membrane reactors to integrate all the reforming steps of the reforming plant. This unique unit allows hydrocarbon conversion to CO_2, and hydrogen separation simultaneously [12-15]. However, most of these studies show that this kind of membranes does not reach 100% methane conversion and/or hydrogen extractions, mainly due to the difficulty to overcome the hydrogen partial pressure difference as driving force. Previous works using protonic conducting ceramics as catalytic membrane reactor have reported remarkable improvements of the process regarding the conventional fixed bed strategies. Furthermore, high stabilities and benzene selectivity were reported in methane dehydroaromatization process using BZCY based membrane in a catalytic membrane reactor [16]. Electrocatalytic synthesis of ammonia using protonic conducting ceramics shows promising results, although several issues (e.g. faradaic efficiency) [17, 18] need to be overcome. BZCY protonic conducting ceramic was used in the steam reforming process at intermediate temperature to extract hydrogen in an electrochemical assembly with significant advances in terms of conversion [19].

Malerød et. al. proposed a compact steam reforming unit using a proton conducting ceramic to separate hydrogen, simultaneously pressurizing it in an energy-balanced new process (Figure 9.1a) [20]. This study shows full methane conversion in CO_2. It also demonstrates how the thermal balance is not only closed globally, but also locally achieving the microthermal integration of all phenomena which take place in this process. Further, this kind of assembly could be used to extract hydrogen from other reactions as well, i.e. syngas obtained from gasification of biomass.

Finite element methodology was used to reveal the thermal behavior of reforming processes in previous studies such, (i) thermal integration of steam reforming and combustion with different flow configurations [21-25]; (ii) temperature integration across the catalytic pellets in a tube [26-29], (iii) autothermal reforming with membrane reactor [30, 31]. Therefore, this kind of study allows analyzing the reactor design and evaluating the effect of the different phenomena on the yield and efficiencies.

9.2. Objectives

Integrating a protonic membrane reactor with a current assisted hydrogen extraction in a methane steam reforming process, becomes the conventional reformer reactor in a reactor that realizes four process steps simultaneously within a 400 μm length scale (Figure 9.1a). First, it extracts hydrogen from the reforming side and shifts a thermodynamically limited reaction sequence towards full conversion of methane; second, it delivers heat to the strongly endothermic reaction through the electrical operation of the membrane—acting as a separator and a compressor (Figure 9.1b); third, it compresses hydrogen directly at the sweep side of the membrane; and last, it produces high-purity hydrogen.

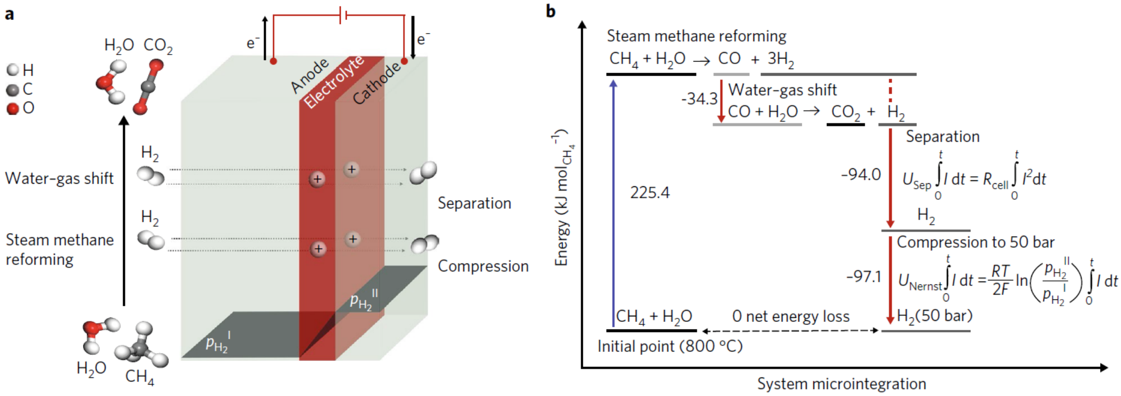
a
H
C
O
H_2O CO_2
Water-gas shift
Steam methane reforming
H_2
H_2
H_2O
CH_4
e^-
e^-
Anode
Electrolyte
Cathode
+
+
+
+
$p_{H_2}^{I}$
$p_{H_2}^{II}$
Separation
Compression
b
Energy ($kJ\ mol_{CH_4}^{-1}$)
Steam methane reforming
$CH_4 + H_2O \rightarrow CO + 3H_2$
-34.3
Water-gas shift
$CO + H_2O \rightarrow CO_2 + H_2$
225.4
Separation
-94.0
$U_{Sep}\int_0^t I\,dt = R_{cell}\int_0^t I^2 dt$
H_2
Compression to 50 bar
-97.1
$U_{Nernst}\int_0^t I\,dt = \frac{RT}{2F}\ln\left(\frac{p_{H_2}^{II}}{p_{H_2}^{I}}\right)\int_0^t I\,dt$
$CH_4 + H_2O$
0 net energy loss
H_2(50 bar)
Initial point (800 °C)
System microintegration

Figure 9.1. (a) Schematic of the protonic membrane reformer; (b) heat balance achieved with the different phenomena of this process. [20]

Therefore, not only the overall heat balance but local heat balance has to be controlled to avoid heat accumulation that can bring high temperature gradients inside the reactor. A finite element model was built to improve the understanding of the heat exchanging of phenomena that take place in this process. Finally, the objective of this study is to check if the integration of all heats is possible not only globally but that the different phenomena do not cause significant temperature gradients to keep the process around 800ºC in the electrochemical tube length. Additionally, several properties of the process was extensively studied to evaluate their effect on the heat balance.

9.3.Methods

9.3.1. Description of the process

The process integrates a protonic conductor ceramic material inside a reforming reactor to extract the hydrogen generated in the reaction and, consequently, shifting the reaction equilibrium towards the products. The electrochemical assembly is based on the protonic conducting material composed of $BaZr_{0.7}Ce_{0.2}Y_{0.1}O_{3-\delta}$ (hereinafter BZCY). The tube consists of three differentiated layers in the radial direction: (i) the internal porous layer, made of a cermet of Ni and BZCY, acts as internal electrode for the electrochemical assembly and as catalyst for the reaction; (ii) the intermediate layer which acts as electrolyte in the electrochemical assembly and, thus, is a dense layer made of the protonic conductor material, BZCY; (iii) the external electrode, centered in the tube, being a thin layer made of Ni and BZCY. The tube is sealed to alumina tubes which act as tube risers and insulators.

Regarding the gas compositions, the pre-reformed inlet gas is a mixture of hydrogen, steam and methane, and it enters the reactor in the internal chamber (hereinafter reforming chamber). The hydrogen extracted from the reforming chamber, due to the current assisted process, is released in the external electrode to the external chamber (hereinafter hydrogen chamber). Finally, the hydrogen pressure is controlled using a pressure regulator valve.

9.3.2. Experimental procedure

The process was studied isothermally at 800°C. The pressure of the internal chamber was fixed at 10 bar, and the pressure of the hydrogen chamber was varied to evaluate its effect on the process. The pre-reforming inlet gas is a mixture of methane, steam, hydrogen and helium. More details about tube elaboration, composition of the different layer and experimental setup, can be found in the published work [20].

9.3.3. Geometry

Figure 9.2 shows a sketch of the Protonic Membrane Reformer (PMR). The setup consists of an external stainless-steel reactor (experimentally 316 SS Swagelok-based system) which contains the electrochemical tube supported by alumina risers. As previously commented, the electrochemical tube is made of a porous internal layer, thin electrolyte layer and thin external layer. The external electrode was modelled as a boundary domain to simplify the geometry. The internal porous layer (Ni-BZCY) acts as catalyst for the reforming process and internal electrode for the electrochemical assembly. The thin electrolyte (BZCY) has around 25μm. The tube possesses the following dimensions: 9.8mm and 8.2mm of outer and inner diameter, respectively, and a length of approximately 12 cm. The above mentioned outer and inner diameters were also fixed for the alumina riser to simplify the geometry. The external stainless steel reactor presents 20mm and 16.5mm of outer and inner diameter, respectively. To simplify the complexity of this study, 2D axial symmetry was considered (Figure 9.3c). Hydrogen pressure is controlled by means of a regulator valve downstream (not viewed in Figure 9.2). The last device is not modelled in the CFD built because the energy release in the hydrogen pressurization is located in the electrochemical cell (as explained section 9.3.4.1).

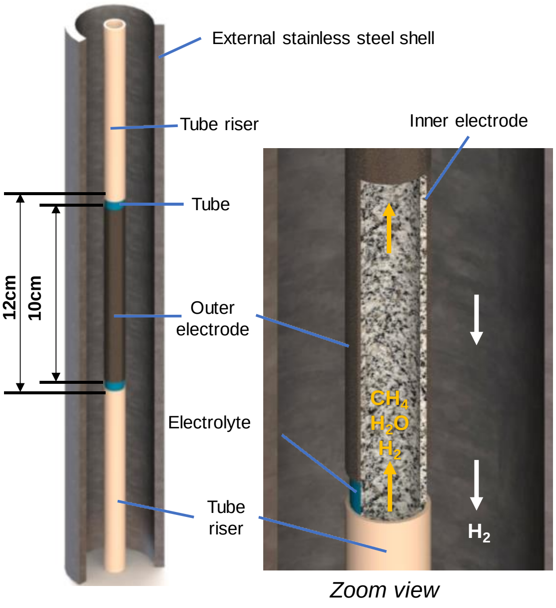
External stainless steel shell
Tube riser
Inner electrode
Tube
12cm
10cm
Outer electrode
Electrolyte
CH_4
H_2O
H_2
Tube riser
H_2
Zoom view

Figure 9.2. View of the PMR setup

9.3.4. Physics equations

As previously mentioned, this process combines several phenomena that take place simultaneously involving heat exchange in the membrane reformer reactor (Figure 9.3a). The process is based on shifting the steam methane reformer reaction (SMR) and water gas shift reaction (WGS) towards the products extracting the generated hydrogen.

$$CH_4 + H_2O \rightleftarrows CO + 3\ H_2 \qquad \text{(SMR)}$$

$$CO + H_2O \rightleftarrows CO_2 + H_2 \qquad \text{(WGS)}$$

The process entails steam methane reformer and water gas shift reactions within the internal porous domain, fluid flows in the reforming and hydrogen chambers, gas diffusion of the reforming species in the reforming chamber, electrochemistry, gas compression and thermal transference. In the reforming chamber (internal gas domain and internal porous electrode domain), chemical reactions, gas flow, gas diffusion process and the electrochemical hydrogen extraction take place. In the external chamber (external gas domain), the gas flow and hydrogen discharging take place. Hydrogen compression and the electrochemistry take place in the electrochemical tube (internal porous domain, electrolyte and external electrode boundary).

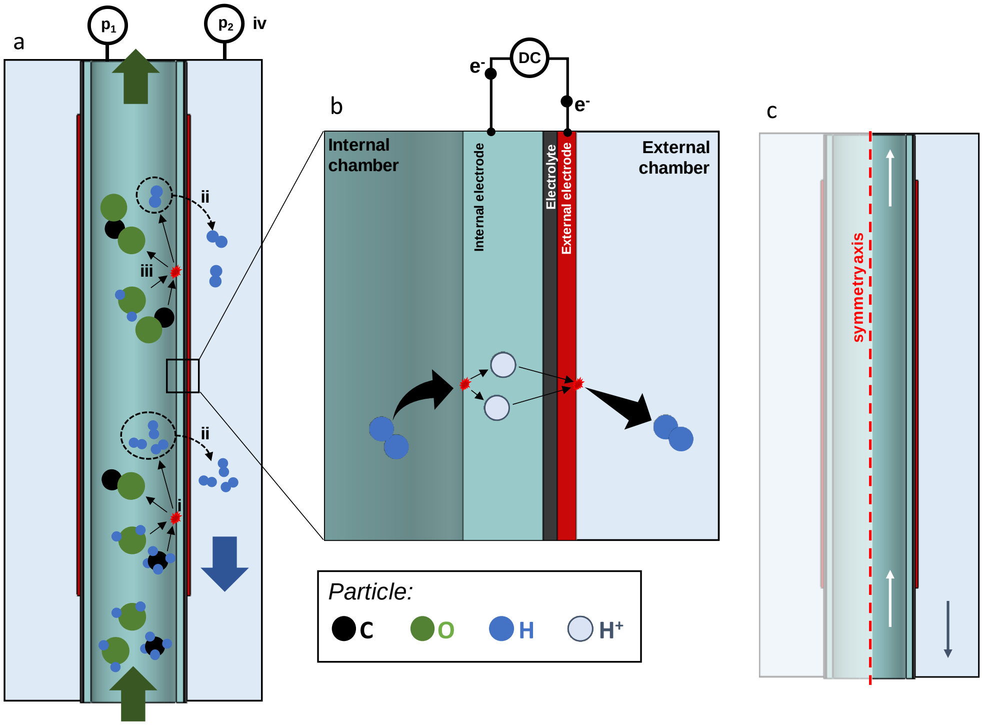
a
p1
p2
iv
ii
iii
ii
i
b
DC
e-
e-
Internal chamber
Internal electrode
Electrolyte
External electrode
External chamber
Particle:
C
O
H
H+
c
symmetry axis

Figure 9.3. description of the process. (a) View of the setup (i: SMR reaction; ii: H_2 pumping; iii: WGS reaction; iv: electrocompression); (b) zoom view of the electrochemical cell; (c) 2D axial symmetry.

Table 9.1 presents the governing equations of the phenomena which take place in this process. The fluid gas flows were modelled with the Navier-Stokes equations (Equations 1-4) for the reforming and hydrogen chambers (with the respective correction for the porous domain). The transport of species in the reforming chamber (CH_4, CO, CO_2, H_2 and H_2O) were modelled using the averaged-mixture model (Equations 5-7). It should be noted that Knudsen diffusion processes were neglected.

Table 9.1. Governing equations of the Finite element model.

Governing equation	id	Property equations	id
Navier-Stokes			
$\rho(u\cdot\nabla)u=\nabla\cdot\left[-pI+\mu(\nabla u+(\nabla u)')-\frac{2}{3}\mu(\nabla\cdot u)I\right]$	(1)	$\rho=\frac{p}{R\cdot T}\cdot M_n$	(20)
$\nabla\cdot(\rho u)=0$	(2)	$\mu=\sum_i\frac{\mu_{g,i}}{1+\frac{1}{x_i}\cdot\sum_{j,j\neq i}x_j\cdot\phi_{i,j}}$	(21)
$\frac{\rho}{\epsilon_p}\left((u\cdot\nabla)\frac{u}{\epsilon_p}\right)=\nabla\cdot\left[-pI+\frac{\mu}{\epsilon_p}(\nabla u+(\nabla u)')-\frac{2\mu}{3\epsilon_p}(\nabla\cdot u)I\right]-\left(\mu\kappa^{-1}+\beta_F\lvert u\rvert+\frac{Q_{br}}{\epsilon_p^2}\right)u$	(3)	$\phi_{i,j}=\frac{\left(1+\left(\frac{\mu_{g,i}}{\mu_{g,j}}\right)^{\frac{1}{2}}\cdot\left(\frac{M_j}{M_i}\right)^{\frac{1}{4}}\right)^2}{4/\sqrt{2}\cdot\left(\frac{M_i}{M_j}\right)^{\frac{1}{2}}}$	(22)
$\nabla\cdot(\rho u)=Q_{br}$	(4)	$\kappa=\frac{d_p^2\cdot\epsilon_p^3}{150\cdot\left(1-\epsilon_p\right)^2}$	(23)
Averaged-mixture for transport of species			
$\nabla\cdot j_i+\rho(u\cdot\nabla)w_i=r_i\cdot M_i$	(5)	$D_i^m=\frac{1-w_i}{\sum_{k\neq i}\frac{x_k}{D_{i,k}}}$	(24)
$N_i=j_i+\rho u w_i$	(6)	$M_n=\left(\sum_i\frac{w_i}{M_i}\right)^{-1}$	(25)
$j_i=-\left(\rho D_i^m\nabla w_i+\rho w_i D_i^m\frac{\nabla M_n}{M_n}\right)$	(7)	$D_{i,j}=k_{diff}\cdot\frac{T^{1.75}\cdot\left(\frac{1}{M_i}+\frac{1}{M_j}\right)^{1/2}}{p\cdot\left(v_i^{1/3}+v_j^{1/3}\right)^2}$	(26)
		$D_{i,j}=\frac{\epsilon_p}{\tau_p}\cdot D_{i,j}$	(27)
Charge transport (electrochemistry)			
$\nabla i_I=Q_I$	(8)	$E_{eq}=E_{eq}^0+\frac{R\cdot T}{z\cdot F}\ln\left(\prod p_i^{n_i}\right)$	(28)
$i_I=-\sigma_I\nabla\phi_I$	(9)		
$\nabla i_S=Q_S$	(10)	$E_{eq}^0=-\frac{\Delta G^0}{z\cdot F}$	(29)
$i_S=-\sigma_S\nabla\phi_S$	(11)		
$\eta=\phi_S-\phi_I-E_{eq}$	(12)	$R_{cell}=0.5\,\Omega\cdot cm^2\cdot \mathrm{e}\hat{}\left(\frac{50.4\frac{kJ}{mol}}{R}\cdot\left(\frac{1}{T}-\frac{1}{1073.15K}\right)\right)$	(30)
Thermal transport			
$\rho Cpu\cdot\nabla T=\nabla(k\cdot\nabla T)+Q_{term}$	(13)	$k=\sum_i\frac{k_{g,i}}{1+\frac{1}{x_i}\cdot\sum_{j,j\neq i}x_j\cdot\phi_{i,j}}$	(31)
$\rho Cpu\cdot\nabla T=\nabla(keq\cdot\nabla T)+Q_{term}$	(14)	$keq=\theta_p\cdot k_p+\left(1-\theta_p\right)\cdot k$	(32)
$Heat_{ri}=-r_i\cdot\Delta H_{ri}$	(15)	$Cp=\sum_i x_i\cdot Cp_{g,i}$	(33)
$Heat_{comp}=R\cdot T\cdot\ln\left(\frac{p^{II}}{x_{H2}\cdot p^I}\right)\cdot\frac{I_{tot}}{z\cdot F}$	(16)	$\gamma=\sum_i x_i\cdot\gamma_{g,i}$	(34)
$Heat_{joule}=\frac{ASR_{cell}(T)}{Area}\cdot I_{tot}^2$	(17)		

Moreover, secondary current distribution was considered for the electrochemistry (Equations 8-12) with 100% of faradaic efficiency.

Considering that the gas compression occurs in a limited space, and as long as this process entails heat exchange with the other phenomena taking place, isothermal compression was accepted to model the hydrogen pressurization (Equation 16, for more details see section 9.3.4.1). The heat transfer model considered the correction for the porous domain, and the full process takes place adiabatically (Equations 13-14).

Considering the gas properties, ideal gas equation was used to calculate the density (Equation 20), considering an ideal gas mixture for the reforming chamber and ideal gas for the hydrogen chamber; viscosity and thermal conductivity for the reforming gas was estimated using the Wilke model (Equations 21, 22, 31), and for the hydrogen chamber pure hydrogen properties were considered. Heat capacity and heat capacity ratio were estimated considering the molar average (Equations 33-34). The properties of pure gases were obtained from [32].

The porosity (ϵ_p) and permeability (κ) are two key factors that govern fluid flow in the porous region. The permeability for a packed bed with randomly distributed spherical particles was calculated using the Carman-Kozeny model, and the average particle size (d_p) and porosity model [33]. As previously was determined for this kind of tubes, the porosity of the internal electrode was fixed at 25% with a particle size of 10 µm [19, 20]. Additionally, the tortuosity of the electrode (τ_p) was evaluated considering the inverse of the square root of the porosity, considering the electrode as a packed bed with randomly distributed spherical particles [34, 35]. Considering this, tortuosity was calculated according the inverse of the square root of the porosity ($\epsilon_p^{-0.5}$). Finally, the gas diffusion coefficient was corrected for the internal porous electrode taking into account the porosity and the tortuosity.

For the solid domains, stainless steel properties were used for the external reactor, alumina properties for the risers, and nickel properties for the porous domain and the electrolyte (except for the electrical and ionic conductivity). In order to reduce the complexity of the system and, considering that experimentally it is not possible to separate each electrical resistance contribution (internal electrode, electrolyte and external electrode), all the electrical resistances were here introduced in the electrolyte layer as ionic conductivity. Hence, the electrical resistance was modelled considering an Arrhenius expression (Equation 30) with 0.5 $\Omega\cdot cm^2$ at 800 *°C* as starting point and an activation energy of 50.4 *kJ/mol*.

The kinetic model includes the reactions of steam methane reforming and the water-gas shift reaction (r_{SMR} and r_{WGS}, respectively). Reactions kinetics are described according to the kinetic model of Xu and Froment [36]. Equilibrium constants of SMR and WGS reactions were calculated from thermodynamic data obtained from [32].

9.3.4.1. Thermodynamics about hydrogen electrocompression

Hydrogen pumping using a current assisted electrochemical device allows the transport of hydrogen from one chamber to other. Considering the overall difference potential to carry out the operation, the theoretical work (reversible contribution) for transporting hydrogen was studied, the potential drops (non-reversible contribution) because the electronic and ionic transport are not considered in this thermodynamic analysis.

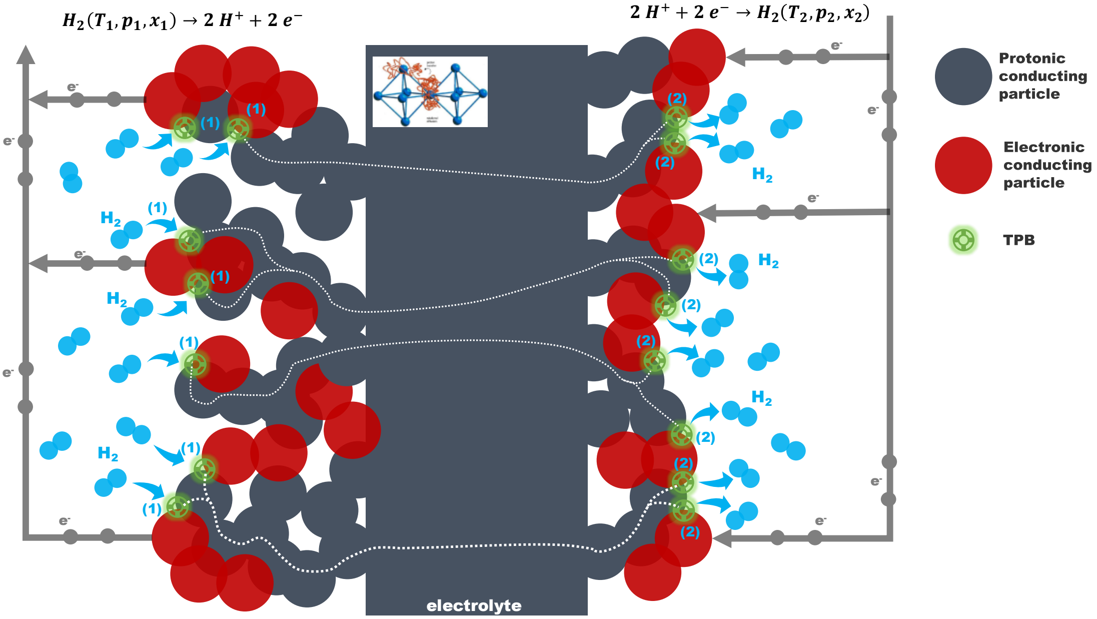
$H_2(T_1,p_1,x_1) \rightarrow 2\,H^+ + 2\,e^-$
$2\,H^+ + 2\,e^- \rightarrow H_2(T_2,p_2,x_2)$
e^-
H_2
(1)
(2)
electrolyte
Protonic conducting particle
Electronic conducting particle
TPB

Figure 9.4. Hydrogen transport across the protonic conducting material.

As Figure 9.4 illustrates, H_2 is incorporated in the TPB point of the anode. H_2 is then transported across the bulk electrolyte and proton conducting particles of electrodes. Finally, the hydrogen is released in the TPB of the cathode. Considering the overall process, the hydrogen is moved from a first chamber, source chamber for this analysis, until a second chamber or final chamber. Both chambers present their own conditions of temperature, pressure and H_2 concentration.

Assuming a perfect ionic and electronic conductor (or, what is the same, neglecting overpotentials), the process exchanges energy to overcome the electrochemical reaction necessities. Electrochemical reactions (*r 1* and *r 2*) are:

$$H_2(T_1, p_1, x_1) \rightarrow 2\,H^+ + 2\,e^- \qquad \text{(r 1)}$$

$$2\,H^+ + 2\,e^- \rightarrow H_2(T_2, p_2, x_2) \qquad \text{(r 2)}$$

Where T_i, p_i and x_i represent the temperature, the total pressure and the hydrogen molar fraction of the chamber *i*. Hence, the overall reaction is:

$$H_2(T_1, p_1, x_1) \rightarrow H_2(T_2, p_2, x_2) \qquad \text{(r 3)}$$

Therefore, the reaction in this direction in terms of energy is defined as the hydrogen chemical potential difference (μ_{H2}) of each chamber.

$$\mu_{H2}(T_2, p_2, x_2) - \mu_{H2}(T_1, p_1, x_1) \qquad (36)$$

$$\mu_{H2}(T, p, x) = \mu_{H2}(T, p_0) + RT \cdot \ln\left(\frac{p \cdot x}{p_0}\right) \qquad (37)$$

Where p_0 is the pressure in standard conditions. Finally:

$$\begin{aligned} &\mu_{H2}(T_2, p_2, x_2) - \mu_{H2}(T_1, p_1, x_1) = \\ &= \mu_{H2}(T_2, p_0) - \mu_{H2}(T_1, p_0) + R \cdot T_2 \cdot \ln\left(\frac{p_2 \cdot x_2}{p_0}\right) - R \cdot T_1 \cdot \ln\left(\frac{p_1 \cdot x_1}{p_0}\right) \end{aligned} \qquad (38)$$

Typically, these assemblies present very thin electrolytes (< 20 μm) and, consequently, the difference of temperature between both sides of the electrolyte should be insignificant. This feature is also met by the experimental cell of this study, therefore, considering $(T_2 - T_1) \rightarrow 0$, then the expression could be rewritten:

$$\mu_{H2}(T,p_2,x_2) - \mu_{H2}(T,p_1,x_1) = \\ = \mu_{H2}(T,p_0) - \mu_{H2}(T,p_0) + RT \cdot \ln\left(\frac{p_2 \cdot x_2}{p_0}\right) - RT \cdot \ln\left(\frac{p_1 \cdot x_1}{p_0}\right) \tag{39}$$

$$\mu_{H2}(T,p_2,x_2) - \mu_{H2}(T,p_1,x_1) = RT \cdot \ln\left(\frac{p_2 \cdot x_2}{p_1 \cdot x_1}\right) \tag{40}$$

This first analysis has evaluated the energy to carry out the pressurization of hydrogen using proton conducting electrochemical cells. However, further analysis is necessary to find how the energy exchange is produced, because in terms of binding energy this process does not suppose any change.

The first law of thermodynamics (Eq. 41) says that in a closed system, the energy can be transformed from one form to another but it can be neither created nor destroyed. Conventional gas compressors pressurize in quasi-isentropic conditions. The isentropic pathway causes the pressurization energy to be absorbed by the gas itself during the pressurization process increasing its internal energy and, consequently, its temperature. However, in the electro-pressurizations, hydrogen is pressurized when it is released in the external electrode. That release is dominated by the electrical current, therefore hydrogen could not increase its internal energy the same way that in a mechanical compressor, because the reaction occurs in the electrode surface.

Additionally, hydrogen is transported through the electrolyte jumping across oxygen lattice sites not in its diatomic molecular form but in the atomic form. Therefore, and considering the low thickness of the electrochemical tube, isothermal pressurization assumption was accepted describing the hydrogen pressurization, where the energy of the process is released as heat. Considering gas pressurization into a compressor, the pressurization does not cause any release of heat (because all the energy of the process is absorbed for the gas).

$$\Delta U = Heat - Work \xrightarrow{isothermal} \Delta U = 0 \tag{41}$$

$$Heat = Work = R \cdot T \cdot \ln\left(\frac{p_2 \cdot x_{H2,2}}{p_1 \cdot x_{H2,1}}\right) \tag{42}$$

For the conventional electrochemical processes, the entropy contribution supposes a heat exchange in the process (heat source for fuel cell mode and heat demand for electrolysis). On the other hand, an electropressurization supposes a change in the pressure of a gas in quasi-isothermal conditions. A pressurization of a gas in isothermal conditions occurs due to a change in its entropy, as theoretically says the thermodynamics.

Finally, although the electrocompression phenomenon takes place isothermally, heat released as consequence of the processes could increase the temperature of the overall process. In this case, the electrical work demanded (and released as heat) would increase with the temperature of the process. The equation 43 shows the 0D balance between the heat released for the process and the inlet stream heat in an electrocompression process.

$$\frac{I}{z \cdot F} \cdot R \cdot T \cdot \ln\left(\frac{p_2 \cdot x_2}{p_1 \cdot x_1}\right) = F_{inlet} \cdot \int_{T_{in}}^{T} cp(T)dT \tag{43}$$

The increase of the temperature of the process would increase the reversible work contribution. The irreversible contributions would decrease as the conductivity of the proton conducting ceramics improves with the temperature. However, both reversible and irreversible contributions entail heat release. To avoid inefficiencies this heat needs to be balanced. For this purpose, several options can be considered: (i) an additional stream to absorb this heat; (ii) integrate the electrocompression in an endothermic process. Using an additional stream would require a high enough flow to mitigate the increase of temperature. Besides, an additional chamber for this stream would be required to avoid hydrogen dilutions in the initial chamber or the final chamber. Therefore, the integration of the electrocompression in an endothermic process seems a suitable path to improve the efficiency of the process.

9.3.4.2. Definition of the reference conditions

Hereinafter, the term “reference conditions” refers to an inlet with a composition expressed in molar fractions of 0.237, 0.614 and 0.148 for methane, steam and hydrogen, respectively. That feed composition always maintains a steam to carbon ratio (S/C) of 2.58. The pressure in the reforming chamber is fixed at 10 *bar*. Porosity and particle size were fixed at 0.25 and 10 μm.

The total volumetric gas flow is usually defined in standard conditions. However, for this inlet composition, water is in liquid state at standard conditions. To solve this, the inlet was defined using the volumetric inlet flow for methane in standard conditions, and the inlet composition. Therefore, the inlet flow of the other inlet compounds (hydrogen and steam) is easily obtained. Finally, the total inlet flow for the reference conditions is 20 *NmL/min* of methane.

9.3.4.3. Definition of the boundary conditions

In this section is defined to describe the boundary conditions used in this model. The Table 9.2 shows the boundary conditions of the model. Figure 9.5 shows the place of the different boundary conditions.

*Table 9.2. Boundary conditions of the model. * number of the domain is referred to the Figure 9.5*

Phenomenon	Domain*	Contour boundary conditions	Domain boundary conditions
Gas flow	1 and 5	- Inlet (flow) - Outlet	Domain 5: H_2 extraction
Transport of species	1 and 5	- Inlet (composition) - Outlet	Domain 5: Reactions and H_2 extraction
Gas flow	3	- H_2 release (Faraday law) - Outlet	
Electrochemistry	5 – 7	- Electric current inlet (internal electrode) - Electric current outlet (external electrode)	
Heat transference	All	- Inlet flow (internal inlet flow): inlet temperature - Outlet flow (flow outlets boundaries)	Domain 5: heat reactions and electrocompression heat Domain 6: Joule effect heat

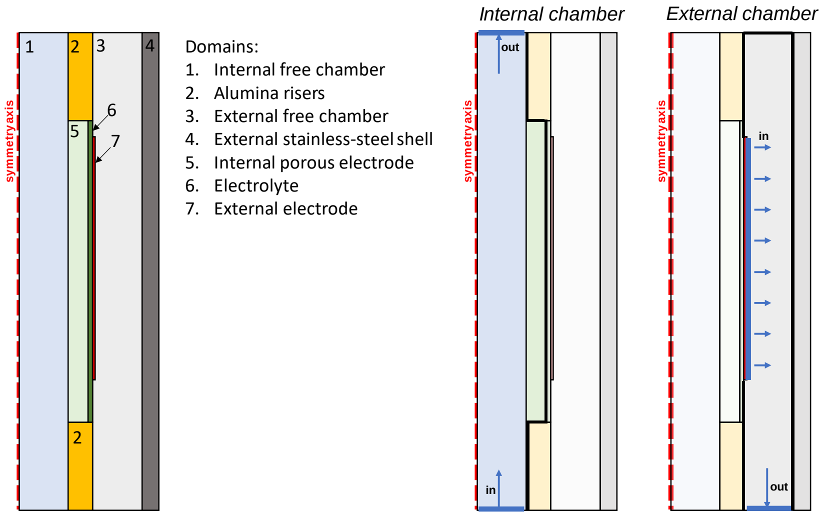
Internal chamber
External chamber
symmetry axis
1
2
3
4
5
6
7
2
Domains:
1. Internal free chamber
2. Alumina risers
3. External free chamber
4. External stainless-steel shell
5. Internal porous electrode
6. Electrolyte
7. External electrode
out
in
in
out

Figure 9.5. Definition of the boundary conditions in the geometry.

9.3.5. Studies performed and conditions

In this section the studies performed in this work are described, detailing the conditions and the range of variables tested in each study. Initially, the mesh of the model was refined to find the optimal mesh for this study. Then, several studies were performed under isothermal conditions to evaluate the process without the effects of the temperature. Finally, additional studies were performed on adiabatic conditions to evaluate the possibility of microthermal integration.

9.3.5.1. Mesh refining methodology

For mesh refining, adiabatic process neglecting the radiation heat transference was considered. According to previous works, radiation heat transference mitigates heats sources (see section 9.3.6). Then, radiation was neglected to maximize the temperature gradients which could appear due to the heat sources of the process and, in this case, the focus of the mesh refining in the surroundings of the heat sources is easier. For mesh refining, the specific tool which the software include was used in order to improve the mesh by adding more nodes where the geometry or the process requires.

9.3.5.2. Reaching the maximum hydrogen extraction

The finite element model allows hydrogen extraction from the reforming chamber. Theoretically, considering the reaction system, maximum hydrogen extraction would lead to the total shifting of the reaction towards hydrogen reactions sides. However, for the finite element model and for the real system, the maximum hydrogen extraction cannot be reached because of diffusion limitations, which are higher or lower depending on geometry and conditions of the process. Figure 9.6 shows the methodology employed to reach the maximum hydrogen extraction for the model evaluated in isothermal conditions and for the model evaluated in adiabatic conditions. Hydrogen Recovery test (*HR* test in Figure 9.6) represents the evaluation of the model results to know the maximum hydrogen extraction. For a specific applied current, if the model did not show incoherencies in the results (i.e. negative fractions of the different species) then the test was repeated increasing the applied current to evaluate if more hydrogen could be extracted. The maximum hydrogen extraction was chosen as the last current without incoherencies. For the adiabatic conditions an additional test was performed in order to fit the temperature on the tube cell length around 800 *°C*. Therefore, considering the temperature distribution shown for the model, the temperature of the inlet of the reforming chamber was varied to fit the temperature in the tube cell around 800 ℃.

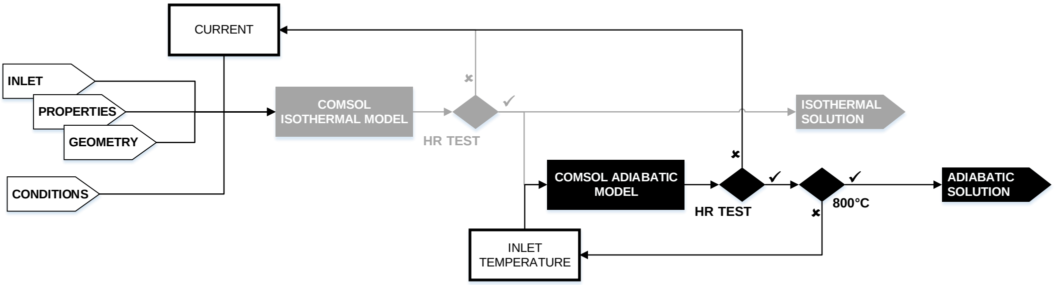
CURRENT
INLET
PROPERTIES
GEOMETRY
CONDITIONS
COMSOL ISOTHERMAL MODEL
HR TEST
✓
✗
ISOTHERMAL SOLUTION
COMSOL ADIABATIC MODEL
HR TEST
✓
✗
800°C
✓
✗
ADIABATIC SOLUTION
INLET TEMPERATURE

Figure 9.6. Methodology of the model. Grey lines: isothermal study; Black lines: adiabatic study. HR test: hydrogen recovery test. 800°C test: fitting the temperature distribution along the tube cell around 800°C.

9.3.5.3. Evaluation of the model in isothermal conditions

1) Hydrogen extraction study

In order to evaluate hydrogen extraction, the current was gradually increased until the maximum hydrogen extraction was obtained.

The total inlet flow studied (expressed with the methane inlet flow) were 10, 15, 20, 25, 30, 40 *NmL* of methane per *min*. The rest of the conditions were kept in the reference conditions. The maximum theoretical current was calculated considering 100% of CO_2 yield. The values are shown in the Table 9.3.

Table 9.3. Theoretical maximum current according regarding the inlet flow.

Inlet NmL CH_4/min	I_{MAX} A	i_{MAX} A·cm^2
10	6.65	0.2160
15	9.90	0.3216
20	13.30	0.4320
25	16.60	0.5392
30	19.90	0.6464
40	26.60	0.8640

$I_{MAX} = \left(4 \cdot F_0(CH_4) + F_0(H_2)\right) \cdot z \cdot F$

2) Study of the porous domain

The porous domain was defined regarding particle size, porosity, permeability and tortuosity. In this work the permeability and tortuosity were defined using particle size and porosity. Therefore, the study of the effect of the porous domain was evaluate considering changes in the particle sizes and porosity. The particle size was varied form 10 µm (to reference conditions) to 20 µm. The porosity was varied from 0.125 to 0.3.

This study was evaluated considering the feeding proposed in the reference conditions, and it compares the maximum hydrogen extraction situations achieved for each combination of particle size and porosity. Therefore, considering the starting point of the study of hydrogen extraction in isothermal conditions for each couple of particle size and porosity, the final current was increased or decreased considering the criteria established for the maximum hydrogen extraction (see section 9.3.5.2).

Variation of the characterization parameters of the porous domain could bring limitations on the hydrogen extraction. Considering this, the implications on the heat balance (if there are any) are a consequence of the decrease of the electric current applied and, consequently, the heats directly related with the hydrogen extraction (i.e. electrocompression and Joule effect) would be reduced. Additionally, the reduction of the hydrogen extraction implies a decrease of the equilibrium shift and, thus, reaction heats are also reduced. This study was evaluated first isothermally to avoid possible thermal interactions (e.g., diffusion if there is a significant decrease of the temperature) and, then, adiabatic study was made for cases where the hydrogen extractions have to be changed.

3) Study of the kinetics of each reaction

The effect of the kinetics on both reactions was evaluate the study was performed using an additional coefficient (a_{ri}), to correct the kinetic coefficient of the respective reaction: $k'_{ri} = a_{ri} \cdot k_{ri}$. Each reaction was analyzed individually.

This study was evaluated considering the inlet proposed in the reference conditions. This study compares the maximum hydrogen extraction situations achieved for each case. Therefore, considering the starting point the results of the study of hydrogen extraction in isothermal conditions the final current was increased or decreased considering the criteria established for the maximum hydrogen extraction.

9.3.5.4. Evaluation of the model in adiabatic conditions

The adiabatic study neglecting radiation was developed for the maximum current applied. The results of the isothermal study were taken as initial solution to improve the convergence. Finally, the inlet temperature was adjusted to fit the temperature on the tube cell centered at around 800°*C* (±30°C). Figure 9.4 shows the methodology for the isothermal and adiabatic studies.

The total inlet flow studied (expressed with the methane inlet flow) were 10, 15 and 20, *NmL/min* methane. The pressure range studied in the hydrogen chamber was 10 – 40 *bar*. The rest of the conditions were kept as in the reference conditions.

1) Adiabatic study considering radiation

The reference conditions were kept for this study, apart from the pressure in the hydrogen chamber that was varied from 10 to 40 *bar*.

2) Study of the porous domain

Considering the solution of this study of the porous domain in isothermal conditions, the study was repeated in adiabatic conditions keeping the inlet temperature of the study of adiabatic study considering radiation with 10 *bar* for the hydrogen chamber.

3) Study of the kinetics

Considering the solution of this study of the kinetics of each reaction in isothermal conditions, the study was repeated in adiabatic conditions keeping the inlet temperature of the study of adiabatic study considering radiation with 10 *bar* for the hydrogen chamber.

4) Study of the specific resistance

The specific resistance depends on the material and conditions. Experimental results show the overall specific resistance was around 0.5 $\Omega \cdot cm^2$. In this study, the specific resistance was varied according

$ASR' = a_{ASR} \cdot ASR$, where ASR is the overall specific resistance to considering the Arrhenius expression, a_{ASR} is the parameter to study the overall specific resistance and ASR' is the new overall specific resistance. The values tested for a_{ASR} were 0.1, 0.25, 0.5, 0.75, 1, 1.25, 1.5, 1.75, 2.

This study was evaluated considering the inlet proposed in the reference conditions. This study compares the maximum hydrogen extraction situations achieved.

9.3.5.5. Characterization of the results

The characterization of the process was made using methane conversion (Equation 43), yield (Equation 44) and hydrogen extraction (Equation 45).

$$X(CH_4) = \frac{F_0(CH_4) - F_{end}(CH_4)}{F(CH_4)_0} \tag{43}$$

$$Y_i = \frac{F_{i,end}}{F_0(CH_4)} \tag{44}$$

$$HR = \frac{F(H_2)_{extracted}}{F(H_2)_{end} + F(H_2)_{extracted}} \tag{45}$$

For the local evaluation of conversion and yields, the molar fractions were used.

$$X_{CH4}(r,z) = 1 - \frac{x_{CH4}(r,z)}{x_{CH4}(r,z) + x_{CO}(r,z) + x_{CO2}(r,z)} \left[\frac{mol\ CH_4\ reacted}{mol\ C\ total}\right] \tag{46}$$

$$Y_{CO2}(r,z) = \frac{x_{CO2}(r,z)}{x_{CH4}(r,z) + x_{CO}(r,z) + x_{CO2}(r,z)} \left[\frac{mol\ CO_2}{mol\ C\ total}\right] \tag{47}$$

Where $X_{CH4}(r,z)$ is the methane conversion in the coordinates *r,z; $x_i(r,z)$* is the molar fraction in the coordinates *r,z; $Y_{CO2}(r,z)$* is the CO_2 yield in the coordinates *r,z*. The coordinates are expressed in radial system: *r,z*.

9.3.6. Effect of the radiation in the heat transference

The explanation about the governing equations to model the radiation heat transference was carefully described in the Chapter 8. In this setup different types of radiation could be considered. Between the surfaces of the external chamber: (i) alumina riser surface, (ii) electrolyte surface, (iii) external electrode with the internal surface of the stainless steel reactor tube the radiative model considering only the surface-to-surface radiative transference. On the other hand, for the internal chamber, H_2O, CO_2, CO and, in minor grade, CH_4 acts as gray gases against the radiation emitted for the internal surfaces of the tubular alumina risers and the internal surface of the internal electrode. In this study, the Planck absorption coefficient were calculated according the equation 48.

$$a_i = \begin{cases} \sum_j c_{i,j} \cdot \left(\frac{1000}{T}\right)^j & for\ H_2O\ and\ CO_2 \\ \sum_j c_{i,j} \cdot T^j & for\ CO\ and\ CH_4 \end{cases} \tag{48}$$

Where a_i is the Planck mean absorption coefficient in $m \cdot atm^{-1}$. The coefficients ($c_{i,j}$) for each gas were obtained from bibliography [53-56] and are presented in Table 9.4.

Table 9.4. Coefficient for the Planck mean absorption coefficient for the reforming gases.

i	**H_2O**	**CO_2**	**CO**		**CH_4**
j			**< 750 K**	**> 750 K**	
0	-0.23093	18.741	4.7869	10.09	4
1	-1.1239	-121.31	-0.06953	-0.01183	$6.57\cdot10^{-3}$
2	9.4153	273.5	$2.95775\cdot10^{-4}$	$4.7753\cdot10^{-6}$	$-1.37\cdot10^{-5}$
3	-2.9988	-194.05	$-4.25732\cdot10^{-7}$	$-5.87209\cdot10^{-10}$	$7.34\cdot10^{-10}$
4	0.513882	56.31	$2.02894\cdot10^{-10}$	$-2.5334\cdot10^{-14}$	$-1.27\cdot10^{-12}$
5	$-1.8684\cdot10^{-5}$	-5.8169			
Range	300–2500 K	300–2500 K	300–750 K	750–2500 K	300–1400 K

9.3.7. Meshing and solver

The 2D axial symmetric model was built using Comsol Multiphysics in steady state (Figure 9.3.c). The mesh uses tetragonal division of the different domains. Adaptive mesh refinement was used to optimize the mesh. The calculations were carried out using the Parallel Direct Solver (PARDISO) with parameter continuation to assure convergence. The relative tolerance of the method is 0.001. Consistent stabilization criterium was chosen for all phenomena using streamline diffusion and crosswind diffusion. To improve the convergence of the system, the process was solved in isothermal conditions (at 800ºC) and then, the solution was used as initial values for the complete process.

9.4.Results

9.4.1. Brief description of the experimental results

Firstly, a summary of the experimental results was made. All these results were extensively described and analyzed in Malerød et. al. [20].

The experimental results about the integration of a protonic membrane reactor in a methane steam reformer are shown in the Figure 9.7. By applying a voltage and hence current across the electrolyte, hydrogen is selectively extracted from the inner steam methane reforming chamber, reaching hydrogen production rates of 25 $Nml \cdot min^{-1} \cdot cm^{-2}$ at 4 $A \cdot cm^{-2}$, operating essentially at the theoretical Faradaic limit (Figure 9.7a). Figure 9.7b shows the evolution of methane conversion to CO and CO_2, and yield, as a function of the imposed hydrogen recovery at 800 *°C* and 10 *bar*. Essentially full equilibrium shift of the steam reforming and WGS reactions (99.9% methane conversion) is accomplished by selectively extracting hydrogen along the reactor length. Methane is completely converted to high-purity hydrogen and wet CO_2 (98% selectivity towards CO_2) in two separate gas streams. The PMR is highly competitive on hydrogen production rate and recovery as well as methane conversion and, advantageously, the PMR delivers compressed hydrogen with an impurity level of < 4 *ppm* at 50 *bar* (Figure 9.7c). Low imperfections in the sealing and/or small spin holes in the electrochemical cell are the cause of the impurities. Nevertheless, the impurities of the obtained hydrogen are low (in the order of *ppm*) and the impurities decrease with the pressure in the hydrogen chamber (Figure 9.7c).

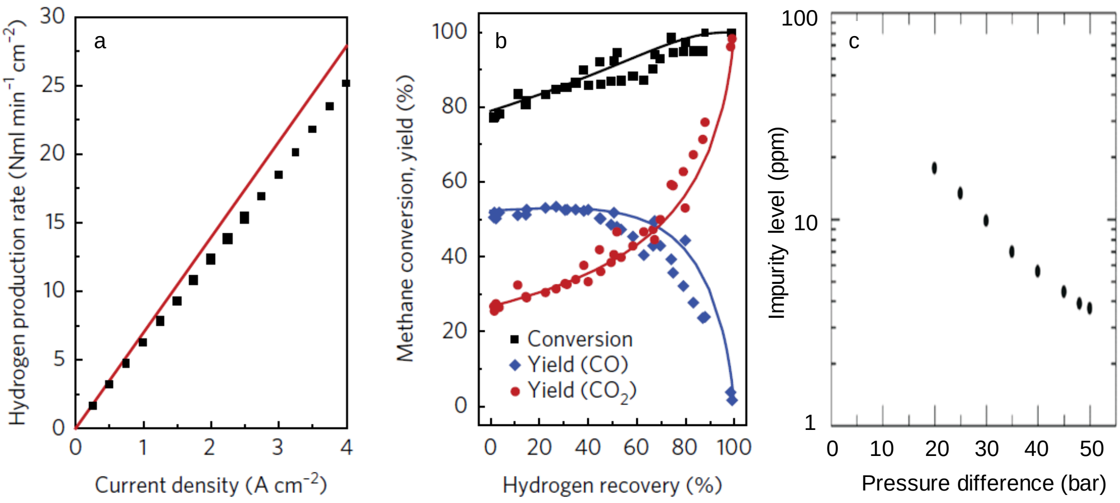

Figure 9.7. Experimental PMR results at 800°C and S/C = 2.5 and reforming pressure of 10bar. (a) hydrogen production rate depending on the current density; (b) methane conversion and yields depending on the hydrogen extraction (points: experimental results; lines: equilibrium); (c) purity of the hydrogen extracted. [20]

The cell voltage (U_{cell}) and associated electrical power required during operation rely on reversible and irreversible terms [57]. The former is described by the Nernst voltage (U_{Nernst}) originating from the hydrogen partial pressure gradient across the proton-conducting electrolyte, and providing a direct estimation of the energy cost of the concomitant hydrogen separation and compression. The irreversible term is related to the overpotential of the resistance to proton migration through the ceramic electrolyte ($U_{\text{electrolyte}}$) and overpotentials related to the kinetics of splitting and re-combining hydrogen at the electrodes ($U_{\text{electrode}}$). When exposed to steam, the oxygen vacancies in the crystal lattice of the BZCY electrolyte annihilate by hydration and are replaced by protonic charge carriers residing as hydroxide ions [58].

$$H_2O + v_O^{\cdot\cdot} + O_O^X = 2\,OH_O^{\cdot} \qquad (49)$$

Under the PMR operating conditions, high steam pressure results in a high concentration of protons and hence high and pure protonic conductivity, even at 800 °*C*, while ceramic proton conductors otherwise must operate below 600 °*C* under ambient humidity [59]. The high-temperature operation exponentially enhances proton mobility, and additionally reduces proton trapping [60] and grain boundary resistance [61], resulting in high protonic conductivity and thus a low $U_{\text{electrolyte}}$.

The electrode composition and microstructure are tailored for high electronic and protonic conduction, and gas transport. Moreover, the Ni electrocatalyst is highly active towards hydrogen redox reactions, altogether providing excellent electrode performance with a total area specific electrode polarization resistance lower than 0.1 $\Omega\ cm^2$ during operation (Figure 9.8a). Figure 9.8c shows the cell voltage breakdown into these different terms, obtained under experimentally optimized conditions. Only U_{Nernst} augments with increasing hydrogen delivery pressure, while $U_{\text{electrolyte}}$ decreases. The latter stems from the simultaneous rise in hydrogen delivery pressure and steam pressure (from 0.1 to 1.6 *bar*, corresponding to a mole fraction of H_2O of 4%) that boosts the electrolyte proton conductivity. The electrode overpotential $U_{\text{electrode}}$ remains essentially constant at ~30 mV, indicating that the hydrogen desorption process is not affected by rising delivery pressures, even up to 40 *bar*.

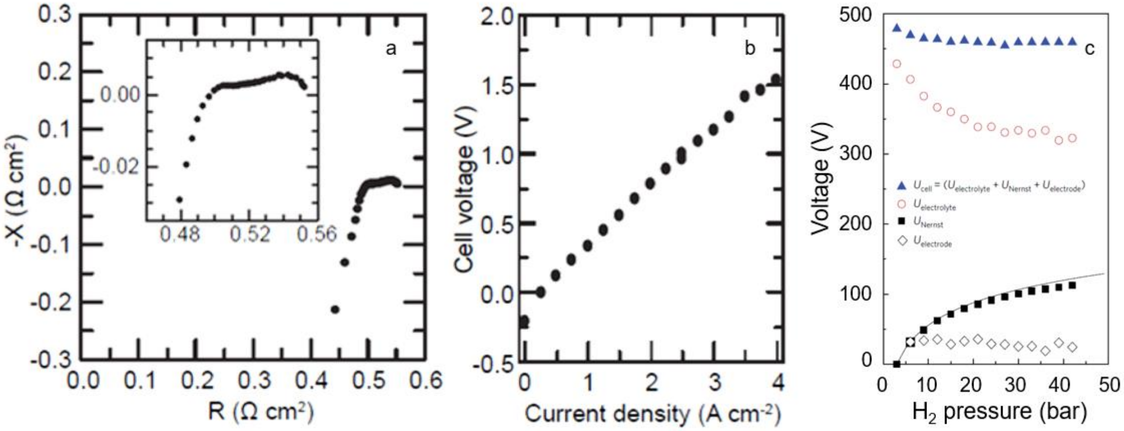

Figure 9.8. Experimental results about the PMR at 800°C and S/C = 2.5 and reforming pressure of 10bar. (a) Nyquist plot of the impedance spectroscopy in the frequency range of 0.04 – 8000 Hz and with a bias of 0.6 A·cm^{-2}; (b) Discharge curve; (c) Voltage contributions depending the hydrogen pressure considering a current density of 0.5 A·cm^{-2} and keeping the steam concentration in the hydrogen chamber at 4%. [20]

A PMR long-term test (800 h) showed stable operation in terms of catalytic activity, hydrogen production and area specific resistance, although coarsening of Ni particles is detected after 1,800 h in operation (see Figure 9.9).

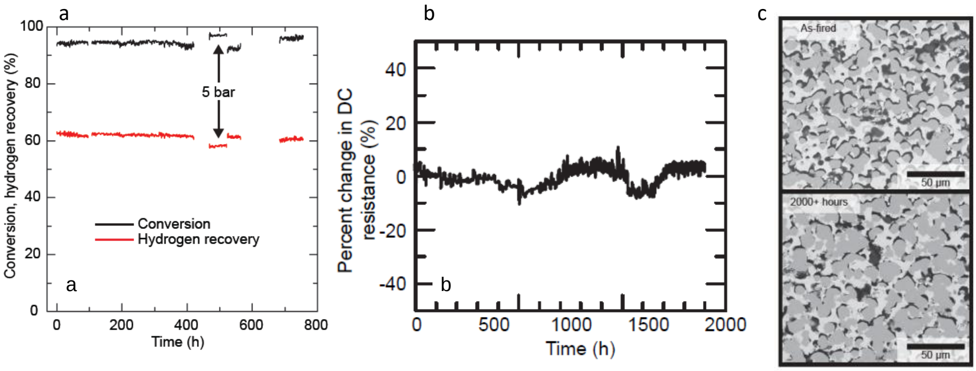

Figure 9.9. Stability experimental results at 800°C, S/C = 2.5 and reforming pressure of 10bar (unless the indicated points). (a) methane conversion and hydrogen extraction; (b) deviation of the overall electrochemical resistance; (c) SEM micrograph of polished cross-section of the Ni-BZCY cell support as-fired and after 2000+ hours of operation. [20]

9.4.2. Validation of the finite element model

9.4.2.1. *Refining of the mesh*

The first task of the study was the search of the suitable mesh for the geometry and phenomena with this process hold. Finite elements analysis presents higher precision with increasing number of nodes. However, an unreasonably high number of nodes leads to high times of convergence and, consequently, even overcoming the computer resources, the method does not reach a solution. To develop the work is important to find an optimal mesh to allow obtaining suitable results in reasonable times and computer resources. Additionally, it is important to focus the refining on the place of the geometry where the phenomena take place.

Figure 9.10 shows how the results changes when the mesh is gradually upgraded. Figure 9.10b-e show views of the initial and final meshes. Considering these results, temperatures distributions show differences lower than 10 °C between the initial mesh and the final mesh, and very low difference for the kinetics results. The final mesh presents a high number of nodes in the porous domain and its surroundings. In summary, the results show a stabilization below 10^6 degrees of freedom.

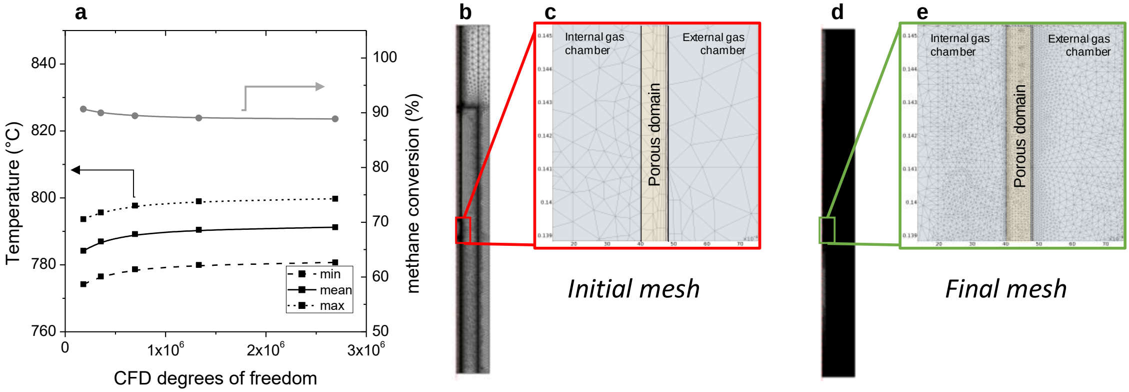

Figure 9.10. Refining of the mesh. (a) Results of the minimum, mean and maximum temperatures in the tube cell and methane conversion; (b) initial mesh; (c) zoom of the initial mesh; (d) final mesh; (e) zoom of the final mesh. Inlet gas flow and composition as reference conditions, inlet at 765°C, hydrogen chamber pressure 10 bar and current density at 0.36 A/cm^2.

9.4.2.2. Results in isothermal conditions

The experimental results reported by Malerød et. al. [20] comes from an isothermal setup at 800 °C. The built model was checked in isothermal conditions to compare with the experimental results.

Figure 9.11 depicts the first results regarding the overall kinetics when hydrogen extraction was gradually increased. The model shows how the system reaches the equilibrium for each hydrogen extraction situation in line with the experimental results (Figure 9.11a). Figure 9.11b shows the current density applied depending on the hydrogen recovery for different total inlet flows, i.e. methane inlet flow. Figure 9.11c shows the maximum hydrogen situation reached when the total inlet flow is increased. For all cases, the hydrogen recovery is higher than 99%, therefore, there is no hydrogen diffusion limitation for this process (at least with this range of inlet flows). Considering the CO_2 yield for the maximum hydrogen recovery, for methane flows higher 25 – 30 *NmL/min*, the CO_2 yield starts to decline. The reason is because the current applied has to be decreased. It means less hydrogen is extracted regarding the maximum theoretical and, consequently, the shifting of the WGS reaction decreases. The decrease of the current density when the total inlet flow is because the conventional forces sweep the reactive gases and, due to the geometry of the setup, these gases have higher difficulty to spread until the internal catalytic electrode.

Methane, CO, H_2 and H_2O are the reactive species. For all cases, the maximum hydrogen extraction and methane conversion overcomes 99%, consequently there is not hydrogen and methane diffusion limitations. *S/C* ratio is 2.58, then there is a steam excess, while the stoichiometric point is 2. Therefore, in these points the activity of steam remains high. However, the CO activity tends to zero and, consequently, for the CO is more difficult to reach the internal electrode than for the other species. Furthermore, although this decrease of the CO_2 yield (from around 98% to 96%) during the scale up of the setup is low, this effect must be taken into account to avoid the CO diffusion that could limit the process. For the maximum hydrogen recovery situation, the current applied was increased as higher as possible, but, this last current was not fitted until the last decimal. Therefore, Figure 9.11c shows the range of currents, considering the last point reached and the step-change used.

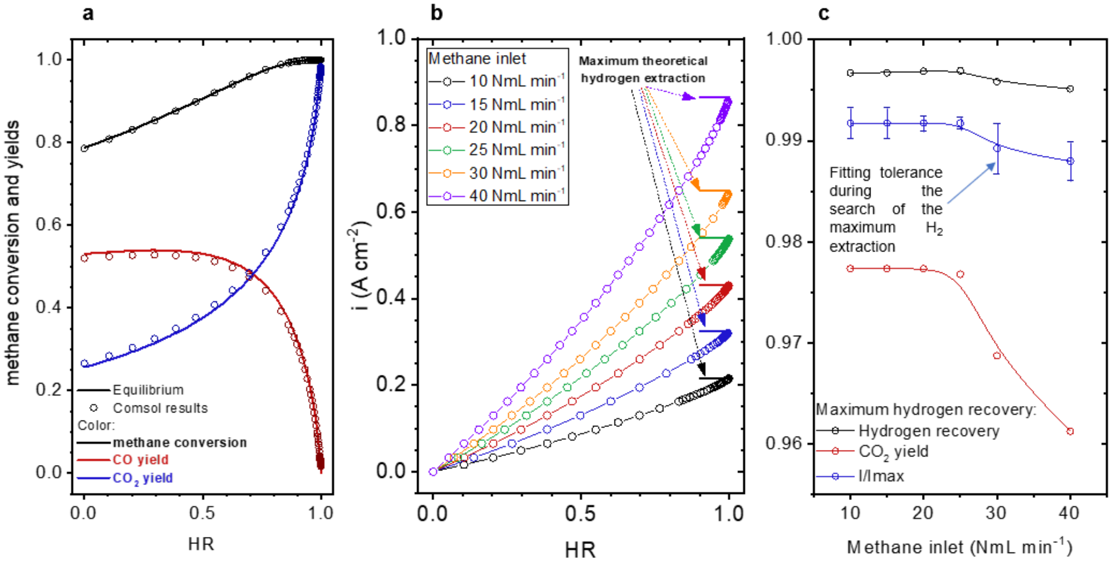

Figure 9.11. Isothermal results of the Comsol model at 800°C. (a) Kinetic results when the hydrogen extraction increases; (b) Current density applied depending on the hydrogen extraction reached; (c) Comparison of the maximum hydrogen extractions when the total inlet flow is increased. Reference conditions (less the total inlets flow).

Different profiles for methane conversion and CO_2 yield are depicted in Figure 9.12 for different hydrogen recoveries. Methane conversion profiles show how methane reacts quickly in the first centimeters of the tube reaching the equilibrium for non-hydrogen extraction. Additionally, methane conversion profiles show how the hydrogen extraction shifts effectively the reaction from the initial equilibrium status for non-hydrogen extraction (at the beginning of the tube cell) from total methane conversion. The WGS reaction presents low advances for the equilibrium in these conditions, CO_2 yield show a low value which is reached also in the first centimeters of the tube for non-hydrogen recoveries. In the same way that for SMR reaction, the profile of CO_2 yield shows how the hydrogen extraction shifts effectively the WGS reaction until almost 100% of CO_2 yield. These profiles show that there are not significant radial contributions for methane and CO_2 yields or concentrations, consequently, it can be affirmed the gas diffusion does not limit this process. That is not so surprising considering the radial distance between the center of the internal chamber and the porous domains, i.e. ~ 4 *mm* (which plays as catalyst and electrode) and the high temperature of this process 800°C which potentiate the diffusion of the gases.

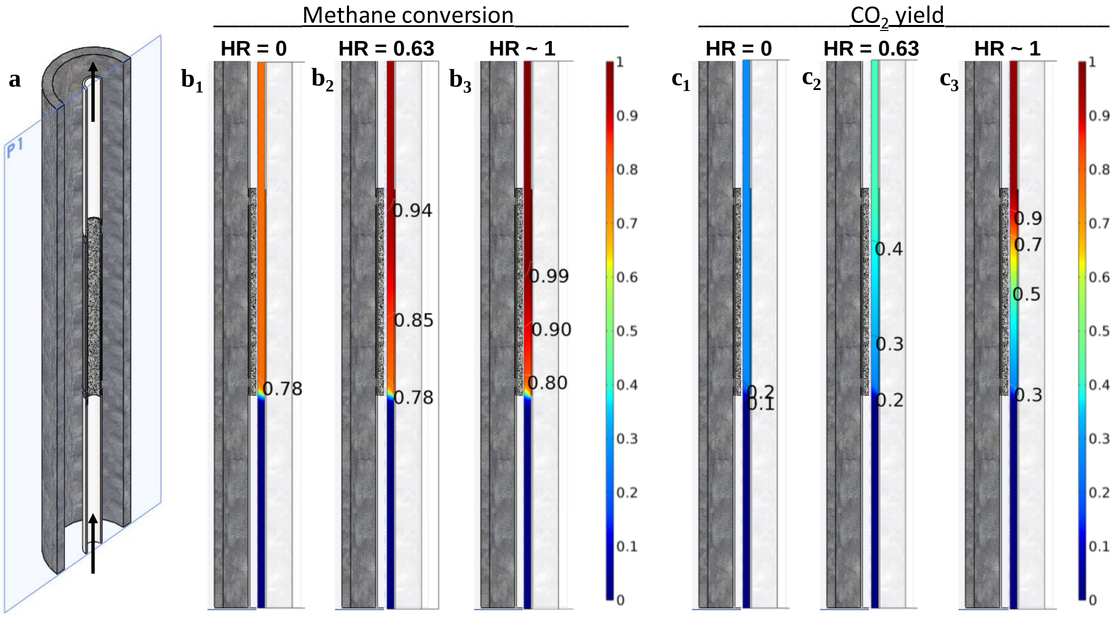

Figure 9.12. Results of the kinetics in isothermal conditions at 800°C. (a) View of the cross section plane on the geometry; methane conversion profiles for non hydrogen extraction (b_1) HR = 0.63 (b_2) and HR ~ 1 (b_3); CO_2 yield profiles for non hydrogen extraction (c_1) HR = 0.63 (c_2) and HR ~ 1 (c_3). Reference conditions.

Finally, the speed profile was analyzed for the maximum hydrogen recovery for the reference conditions at 800°C. Full conversion to CO_2 causes an increase of moles ($CH_4 + 2\,H_2O \rightarrow CO_2 + 4\,H_2$), leading to an increase of the speed in the chamber. However, when the hydrogen extraction increases, it causes a decrease of the 80% of the formed moles ($CH_4 + 2\,H_2O \rightarrow CO_2 + 4\,H_2 \rightarrow CO_2$) and, therefore, the speed decreases. Thus, considering the speed profile, the volumetric flow increases in the first centimeters of the tube cell where the hydrogen extraction has not significantly decrease of hydrogen percentage in the chamber, and at the end of the tube, the speed decreases substantially because the hydrogen extraction (Figure 9.13b). Additionally, the speed profiles also show a poor penetration of the gas flow in the porous domain (Figure 9.13c). It is mainly due to the gas flow is not oriented to the porous domain, but it goes tangentially. Finally, SMR (Figure 9.13d) and WGS (Figure 9.13e) reaction rates shows how the reactions take place in the first micrometers of the porous domain (considering the radial direction) because the poor penetration of the gas into the porous domain. Considering its final application, improvements in the reactor are suggested, as example: static mixers, lower internal radius for the tube, etc. because low penetration of the flow indicates the porous domains is being underused considering only its application as catalyst.

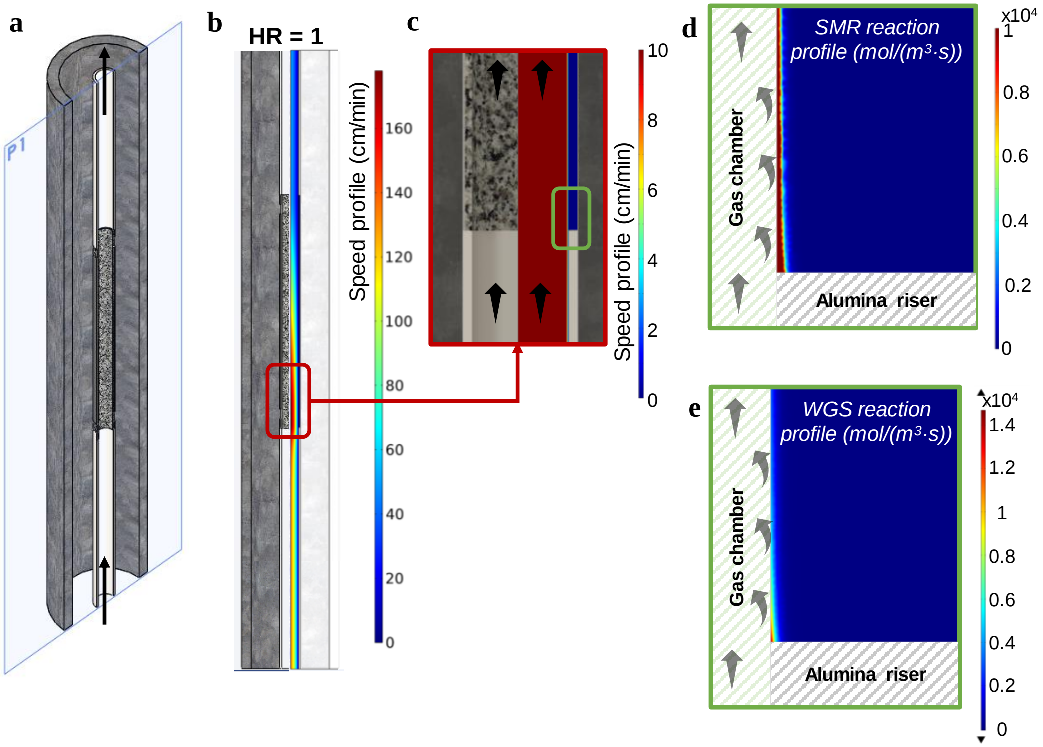
a
P1
b
HR = 1
Speed profile (cm/min)
160
140
120
100
80
60
40
20
0
c
Speed profile (cm/min)
10
8
6
4
2
0
d
SMR reaction profile (mol/(m³·s))
Gas chamber
Alumina riser
x10⁴
1
0.8
0.6
0.4
0.2
0
e
WGS reaction profile (mol/(m³·s))
Gas chamber
Alumina riser
x10⁴
1.4
1.2
1
0.8
0.6
0.4
0.2
0

Figure 9.13. Results in isothermal conditions at 800°C for maximum hydrogen extraction with the reference conditions. (a) general view of the assembly with the crossection plane; (b) speed profile for the maximum hydrogen recovery; (c) zoom of the speed profile; (d) SMR reaction rate profile; (e) WGS reaction rate profile.

Study of the porous domain in isothermal conditions

Experimental cells presented coarsening of the nickel particles of the internal electrode. After 2000 hours of operation the particles size of this electrode increases its size from the initial 10 μm up to around 20 μm (see Figure 9.9c). Experimental results show high stabilities regarding the kinetics and electrochemistry. However, these experimental tests were developed at HR = 60% and not for the maximum hydrogen extraction. This study aims at evaluating the effect of the porous domain on the maximum hydrogen extraction that could be reached.

Figure 9.14 shows the evaluation of the parameters of the porous domain in the maximum hydrogen extraction with the reference conditions at 800°*C*. A decrease of the porosity leads to a decrease in the maximum current that can be applied. If the porosity value for the internal electrode keeps above 0.15, then the maximum current density is higher than 0.99 (theoretical maximum). Figure 9.14b shows the hydrogen removed and the CO_2 yield for the maximum hydrogen extractions for each couple of porosity and particle size. Changes in these parameters do not causes significant decreases of the hydrogen which can be extracted because the hydrogen diffuses very fast in these conditions. Additionally, as a consequence of the decreasing of the maximum current when the porosity decreases, the yield of CO_2 decreases because the shifting of the WGS reaction is reduced.

Finally, it can be concluded that the changes in the porous domain does affect significantly to the maximum hydrogen which can be extracted from the reforming chamber.

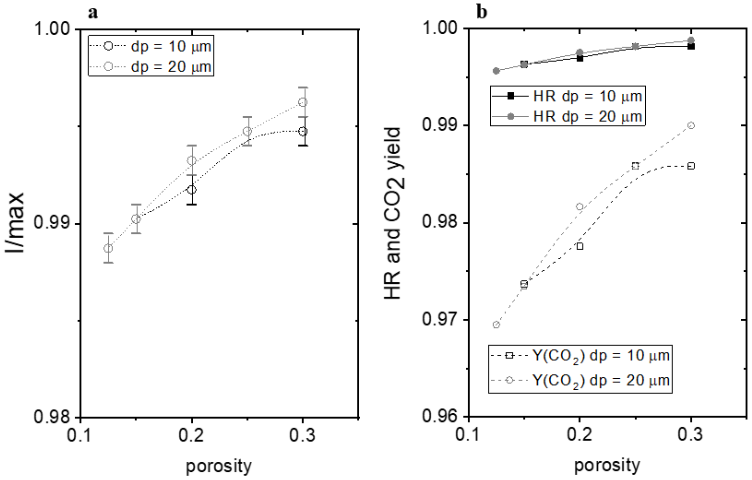

Figure 9.14. Isothermal study of the porous domain depending on the porosity and the particle size. (a) Ratio between maximum current applied and the maximum theoretical current; (b) hydrogen recovery and CO_2 yield.

Study of the SMR kinetics in isothermal conditions

The effect of kinetics in the steam methane reforming reaction was evaluated ($CH_4 + H_2O \rightarrow CO + 3\ H_2$), it should be considered that the kinetics of this reaction are taken from bibliography. The results do not show effects on the maximum current which can be applied to collect hydrogen from the reforming chamber (Figure 9.15). However, methane conversion profiles show that if the reaction kinetics worsen its value around 2 and 4 orders of magnitude, methane needs more length to react. It is necessary to remind two points: (i) although this reaction is controlled by the equilibrium, the equilibrium at this conditions is highly shifted to products, CO in this case, (conversion ~ 0.8 for non-hydrogen extractions), therefore, kinetics have to be extremely low to limit significantly this reaction; (ii) considering the conclusions of the analyzes regarding the speed and reaction rates profiles, the internal porous domain as catalyst is being underused. In summary, the cell should have enough catalyst charge to overcome the worsening of the kinetics of the SMR reaction (at least on the range tested).

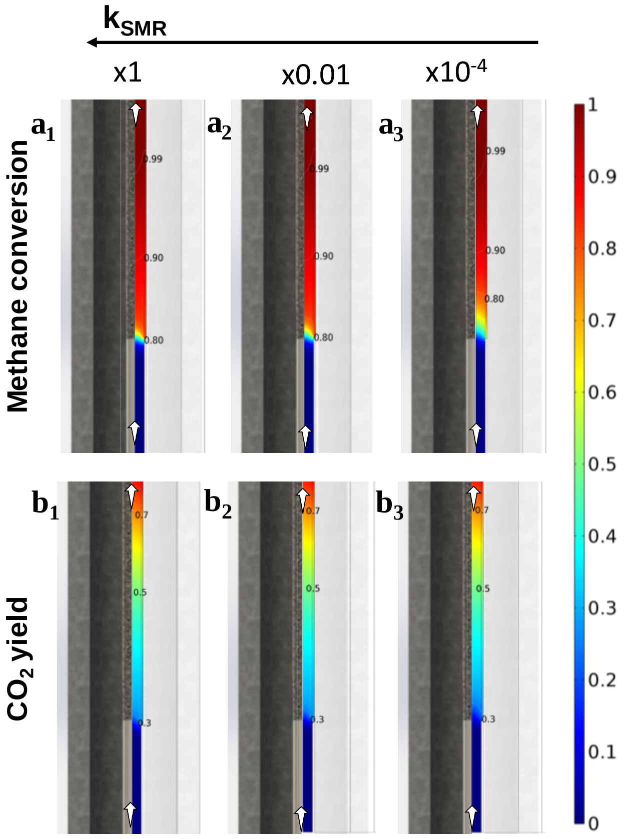

Figure 9.15. Isothermal study at 800°C with the reference conditions of the kinetic coefficient of the SMR reaction. Methane conversion profiles for $a_{SMR} = 1$ *(a*$_1$*),* $a_{SMR} = 0.01$ *(a*$_2$*),* $a_{SMR} = 10^{-4}$ *(a*$_3$*); CO*$_2$ *yield profiles for* $a_{SMR} = 1$ *(b*$_1$*),* $a_{SMR} = 0.01$ *(b*$_2$*),* $a_{SMR} = 10^{-4}$ *(b*$_3$*).* $k_{SMR} = a_{SMR} \cdot k_{0,SMR} \cdot exp\left(-\frac{Ea_{SMR}}{RT}\right)$

Study of the WGS kinetics in isothermal conditions

Similar to the SMR kinetics study, kinetics of the WGS reaction were evaluated to see its effect on the maximum hydrogen extraction reached. Figure 9.16 shows the results of this study for the reference conditions for the maximum hydrogen extraction reached when the WGS kinetics were varied. At the operation conditions, 800°C, this reaction is highly shifted to CO. Therefore, the worsening of the WGS kinetics could be critical for producing hydrogen (at least the hydrogen which can be collected from this reaction which is the 25% of the total theoretical hydrogen for 100% of CO_2 yield).

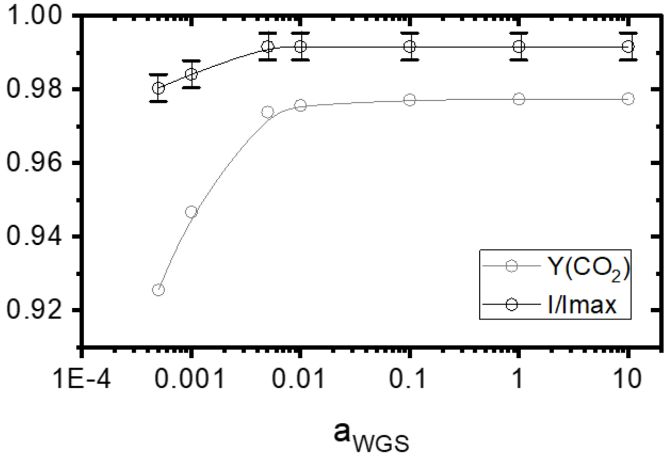

Figure 9.16. Isothermal study at 800°C with reference conditions of kinetics of the WGS reaction. CO_2 yield and ratio current/[maximum theoretical current] for the maximum hydrogen recovery reached depending of the WGS kinetic coefficient. $k_{WGS} = a_{WGS} \cdot k_{0,WGS} \cdot exp\left(-\frac{Ea_{WGS}}{RT}\right)$

The CO_2 yield profiles allow visualizing the decrease of the water gas shift reaction advance when the kinetic coefficient decreases (Figure 9.17).

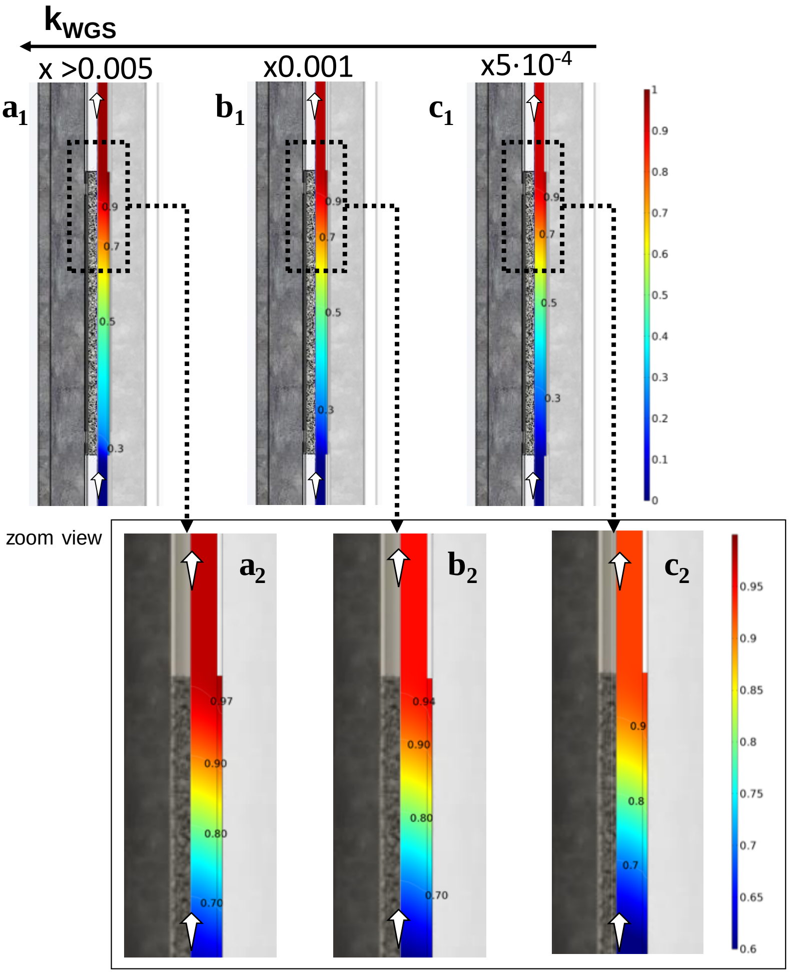

Figure 9.17. Isothermal study at 800°C with the reference conditions of the kinetics of the WGS reaction. CO_2 yield profiles for $a_{WGS} > 0.005$ (a_1 and a_2), $a_{WGS} = 0.001$ (b_1 and b_2), $a_{WGS} = 0.0005$ (c_1 and c_2). a_2, b_2 and c_2 are the respective zoom view of the images a_1, b_1 and c_1, respectively. $k_{WGS} = a_{WGS} \cdot k_{0,WGS} \cdot exp\left(-\frac{Ea_{WGS}}{RT}\right)$

9.4.3. Analysis of the PMR in adiabatic conditions

PMR can work independently as the heat balance is achieved. In this case additional heat is not required to keep the temperature in the reactor. Furthermore, it is necessary to guarantee the temperature inside the reactor keeps approximately constant (here it was accepted 800±30°C), e.g. it does not shoot up locally as a consequence of concentrated heats and insufficient heat exchange. Comsol model was evaluated in adiabatic conditions at maximum hydrogen extraction where the inlet temperature was adjusted to achieve the thermal microintegration at 800 °C in the place of the tube. Furthermore, the radiation heat transference in the setup was evaluated.

Adiabatic study neglecting radiation

Figure 9.18 shows different results profiles for adiabatic studies working with the reference conditions for the maximum hydrogen extraction ($428\,mA\cdot cm^{-2}$). Temperature profile shows that the temperature in the assembly keeps around 800 °C where the temperature gradients are not important. Therefore, it can be affirmed that the thermal microintegration of the process heats is achieved for these conditions. Comparing the temperature profile (Figure 9.18a) with methane conversion profiles (Figure 9.18b) and CO_2 yield (Figure 9.18c), allows the identification of three zones in the tube:

1- First centimeters of the tube: most of the methane (around 80%) is converted mainly to CO as WGS reaction barely takes place. Considering heats of the process, in this zone appears the main part of the heat demand of SMR reaction. There are low heat contributions from WGS (because the low advance of this reaction) and electrocompression (mainly due to the hydrogen partial pressure in the internal chamber for this zone is high). On the other hand, Joule effect is high due to the decrease of temperature and higher ASR. In summary, SMR reaction dominates this zone decreasing locally the temperature.

2- Center zone of the tube cell: methane is completely consumed and the WGS is gradually shifted to CO_2. Therefore, the rest of the heat demand appears, the heat of the WGS appears as this reaction is shifted due to the hydrogen extraction. The Joule effect is going down because the overall specific resistance decreases with the increase of the temperature according the Arrhenius expression. Finally, as H_2 is extracted, the H_2 partial pressure is going down and, consequently, the electrocompression heat increases gradually.

3- Final zone of the tube cell: the WGS is completely shifted to CO_2 and the rest of the H_2 is extracted. Therefore, the rest of heat from WGS appears. Considering the low H_2 partial pressure the heat from the electrocompression is high but, due to the increase of the temperature the ASR decreases and, consequently, the heat from Joule effect decreases. Therefore, in this place the heat sources are gathering what causes a local increase of the temperature. This increase of the temperature is mitigated when the system achieves proper heat exchange.

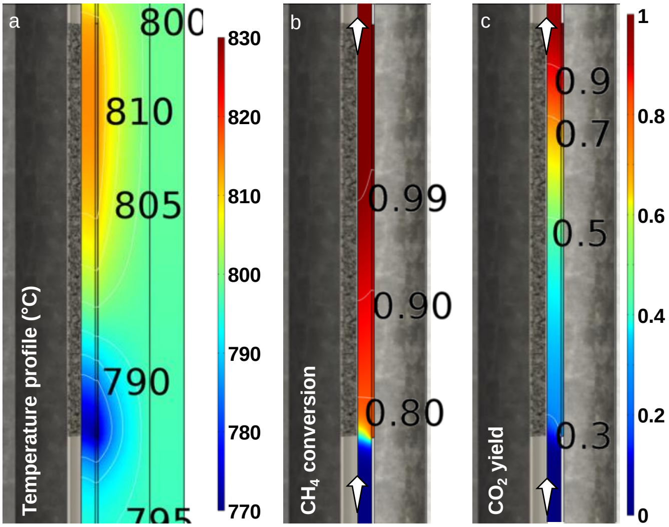

Figure 9.18. Results in adiabatic conditions for the reference conditions for the maximum hydrogen extraction. Inlet temperature 730°C and current density 428 mA·cm^{-2}. (a) Temperature around cell; (b) methane conversion; (c) CO_2 yield.

Figure 9.19 shows temperature profiles of the adiabatic studies working with reference conditions unless the specified total inlet flows (expressed with methane inlet flow) and the pressure of the hydrogen chamber. All these studies were developed working in the maximum hydrogen extraction. These hydrogen extractions were achieved working with 213*mA·cm*$^{-2}$, 317*mA·cm*$^{-2}$ and 428*mA·cm*$^{-2}$ as current density for the total inlet flows of 10 *NmL·min*$^{-1}$, 15 *NmL·min*$^{-1}$ and 20 *NmL·min*$^{-1}$ of methane, respectively. Results shows how when the pressure in the hydrogen chamber increases, temperature profiles shows higher peak temperatures (especially in the final zone of the tube cell). This is because there is more heat from electrocompression heat source. This effect is specially noted in the profiles of 10 *NmL·min*$^{-1}$ methane. At 10 *bar* in the H_2

chamber with this inlet the system does not have enough heat to overcome the SMR reaction heat demands and, consequently, the temperature decreases. However, this decrease of temperature causes an increase of the ASR and, consequently, the heat from the Joule effect increases, softening the decrease of temperature. Additionally, it is observed that the temperature is slightly higher when the total inlet flow increases. Therefore, for all these cases, the thermal microintegration can be achieved.

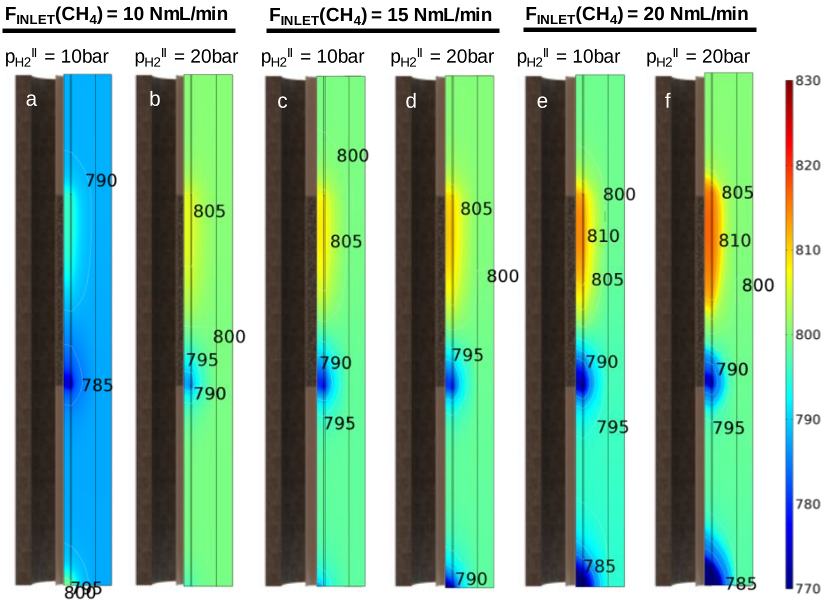

Figure 9.19. Temperature profiles. Inlet flow of 10 NmL/min of methane and a pressure in the H_2 chamber of 10 bar (a) and 20 bar (b); Inlet flow of 15 NmL/min of methane and a pressure in the H_2 chamber of 10 bar (c) and 20 bar (d); Inlet flow of 20 NmL/min of methane and a pressure in the H_2 chamber of 10 bar (e) and 20 bar (f)

In these previous adiabatic studies, the temperature of the inlet gas was fitted to achieve the tube cell works around 800 °C. Figure 9.20 shows the inlet temperatures depending on the pressure of the hydrogen chamber for the different inlet flow tested, and the temperature gradients in the tube cell depending the total inlet flow. Temperature gradients were estimated by the difference among the maximum temperature and minimum temperature on the tube cell domains. As the pressure in the H_2 chamber increases, the ratio of compression increases and, consequently, heat from electrocompression rises according to the logarithmic dependence with the ratio of compression. Therefore, with increasing pressures, the gas could be introduced at lower temperatures. With increasing inlet flows, the gas could be introduced at lower temperatures. The reason comes from the joule effect, because it is, in global terms, $R_{cell} \cdot I_{tot}^2$ and, consequently, while reactions and electrocompression heats are proportional to the total inlet, the Joule effect is proportional to the square of the inlet. Additionally, as the inlet flow is higher, the gradients on the cell increase (Figure 9.20b). The reason is the increase heats of this process presents higher magnitude as the inlet flow increases while the total area is fixed.

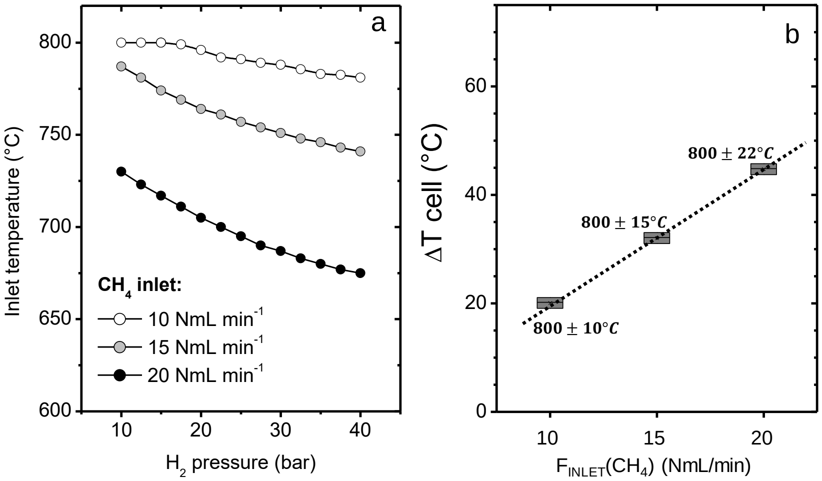

Figure 9.20. Results in adiabatic conditions. (a) Inlet temperature to obtain setup temperatures around 800°C depending on the pressure of the hydrogen chamber for different total inlet flows (expressed with methane inlet flow). (b) Temperature gradients depending on the total inlet flow (expressed considering the methane inlet flow). The current densities where 213, 317 and 428 mA·cm^{-2} for the inlet flows of 10, 15 and 20 NmL/min of methane, respectively.

The Joule heat comes from the energy dissipated per charge passing through resistor or, in this case, through the electrochemical cell. Simplifying the complexity of this phenomenon, an expression of this heat depending on the cell area can be obtained:

$$Heat_{joule} = \frac{ASR}{Area} \cdot I_{tot}^{2} = ASR \cdot i_{tot} \cdot I_{tot} \qquad (73)$$

Therefore, the parabolic increment of the joule effect with the total inlet flow (F_{inlet}) can be mitigated increasing the total area of the cell (*Area*).

Adiabatic study considering radiation

The radiation heat transference was evaluated in the study and compared with the respective test neglecting it. Figure 9.21 shows temperature profiles of the adiabatic studies considering and neglecting the radiation contribution working with reference conditions unless the pressure of the hydrogen chamber for the maximum hydrogen extraction. Figure 9.21 shows the temperature distribution along the reactor in the internal radius position. As can be observed, the temperature gradients are lower when radiation heat transference is considered and, consequently the setup is at more uniform temperature. Considering the heat sources are the same (WGS reaction, electrocompression and Joule effect), that implies a mitigation of the heats of the process. Moreover, considering the heat SMR supposes a heat demand this cannot be mitigated while this reaction takes place. Additionally, the coldest zone (dominated for the SMR reaction as previously was mention) are at temperatures slightly higher because the radiation improves the heat transport.

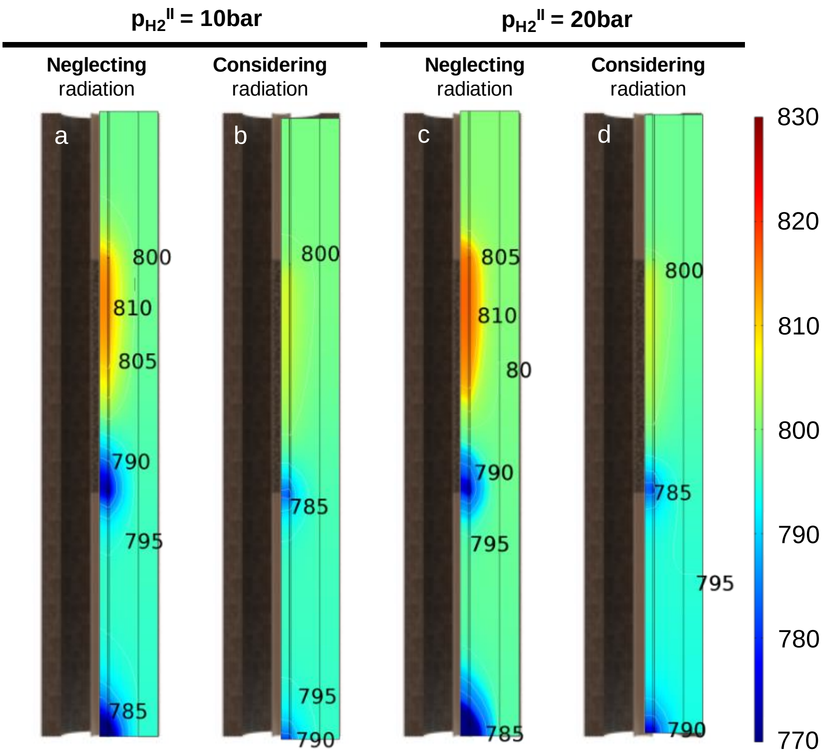

Figure 9.21. Temperature profiles when the radiation contribution is neglected and the hydrogen chamber pressure is 10 bar (a) and 20 bar (c). Temperature profiles when the radiation contribution is considered when the hydrogen chamber pressure is 10 bar (b) and 20 bar (d).

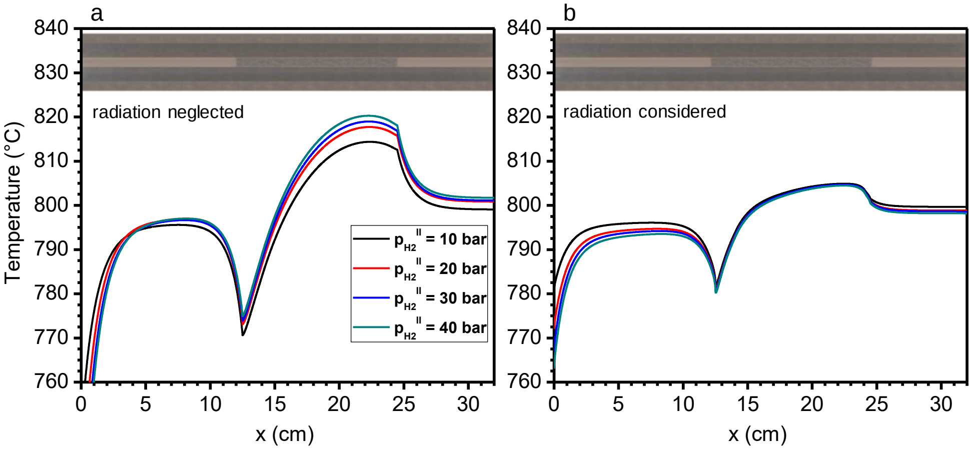

Figure 9.22. Evaluation of adiabatic results neglecting (a) and considering radiation (b) over the temperature distributions along the tube.

The heat transference of this process was studied until now considering conditions of the process. However, additional studies were made to evaluate the effect of different parameters on the heat transference as the isothermal study (study of the porous domain and kinetics). Finally, the Joule effect is the critical phenomenon to close the thermal balance and, consequently, the effect of the overall specific resistance of the electrochemical cell was evaluated.

The following studies were performed using the reference conditions at maximum hydrogen extraction. Maximum hydrogen extractions were evaluated in the respective isothermal study, apart from the overall specific resistance where the study was made comparing with the initial overall specific resistance considered (0.5 $\Omega \cdot cm^2$ at 800°*C* and an activation energy of 50.4 *kJ/mol*).

9.4.3.1. Results of the study of the porous domain on adiabatic conditions

The isothermal study of the porous parameters revealed the low impact of these parameters over the maximum hydrogen extraction. For the respective study in adiabatic conditions, all conditions were kept constant considering the initial case (i.e. porosity 0.25 and particle size 10 μm), and the electric current was varied considering the results obtained in the isothermal study when the porosity and the particle size were varied.

This study pretends to evaluate possible effects of the coarsening of the nickel particles in the heat transference. Figure 9.23 shows results of temperature profiles for different particle sizes and porosities for the internal porous electrode. The reference conditions were kept for all these studies. As the respective isothermal study did not show important changes for this study, the adiabatic study does not show changes in the temperature distribution. Additionally, the possible changes due to the minor decrease of the maximum applied current when the porosity is decreased below of 0.15 are mitigated by the effect of the radiation.

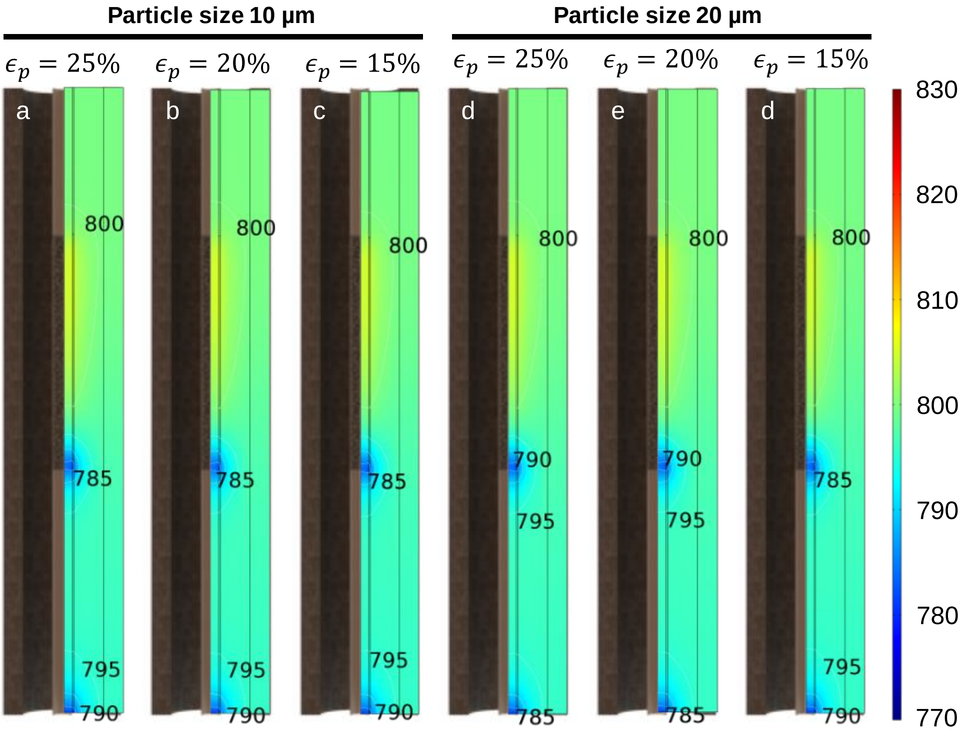

Figure 9.23. Evaluation of the coarsening on the heat transference. Temperature profiles considering a particle size for the internal porous domain of 10 μm and porosities of 0.25 (a), 0.2 (b) and 0.15 (c). Temperature profiles considering a particle size for the internal porous domain of 20 μm and porosities of 0.25 (d), 0.2 (e) and 0.15 (f).

In summary, the coarsening causes a low decrease of the maximum hydrogen which can be extracted if the porosity falls dramatically. In this case, in the real setup, the current would have to be adjusted to the new maximum hydrogen that can be extracted. However, these minor changes will not cause a significant impact in the heat balance of the process.

9.4.3.2. Results of the study of the SMR kinetics in adiabatic conditions

Isothermal study of the kinetics of the SMR reaction did not show significant influence on the maximum hydrogen extractions (in the tested range). However, methane is consumed more gradually along the tube as slower are the kinetics of this reaction. Figure 9.24 shows temperature profiles when the SMR kinetics were gradually worsened. These temperature profiles show how that the cooling down of the temperature at the beginning of the tube cell disappears gradually when the kinetics fall down dramatically. This is a consequence of the heat demand of this reaction distributing more uniformly along the cell for slow kinetics of the SMR reaction.

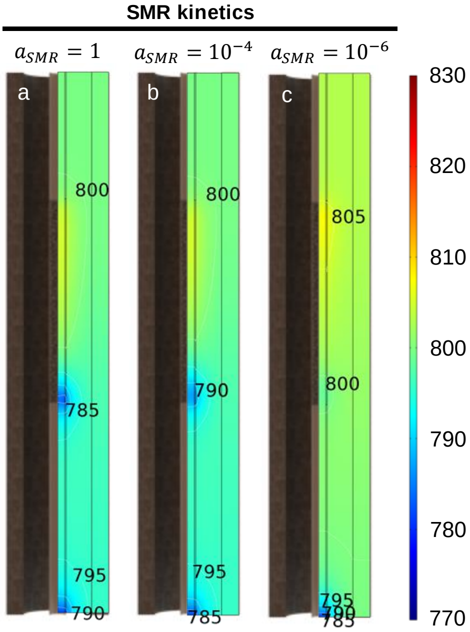

Figure 9.24. Evaluation of the effects of the kinetics of the SMR reaction on the temperature distribution. (a) Bibliography kinetics; (b and c) worsening the bibliography kinetics more than 4 orders of magnitude. $k_{MSR} = a_{MSR} \cdot k_{MSR}$

9.4.3.3. Results of the study of the WGS kinetics in adiabatic conditions

Repeating the methodology of the SMR reaction kinetics, the WGS reaction kinetics were analyzed. Isothermal study of the kinetics of the WGS reaction showed low decreases of the maximum hydrogen extractions. Figure 9.25 shows the temperature profiles when the WGS kinetics were gradually worsened for the maximum hydrogen situations reached in each case for the reference conditions. These temperature profiles show slightly lower temperatures when the kinetics of the WGS reaction falls around three orders of magnitude considering the initial kinetics. This can be explained as an effect of the applied current that had to be decreased in this point regarding the initial kinetics considered. Therefore, the heats related of the hydrogen extraction or to the respective current density applied (electrocompression and Joule effect) decreases, and the heat from the WGS reaction decrease proportionally to the lower of reaction shift.

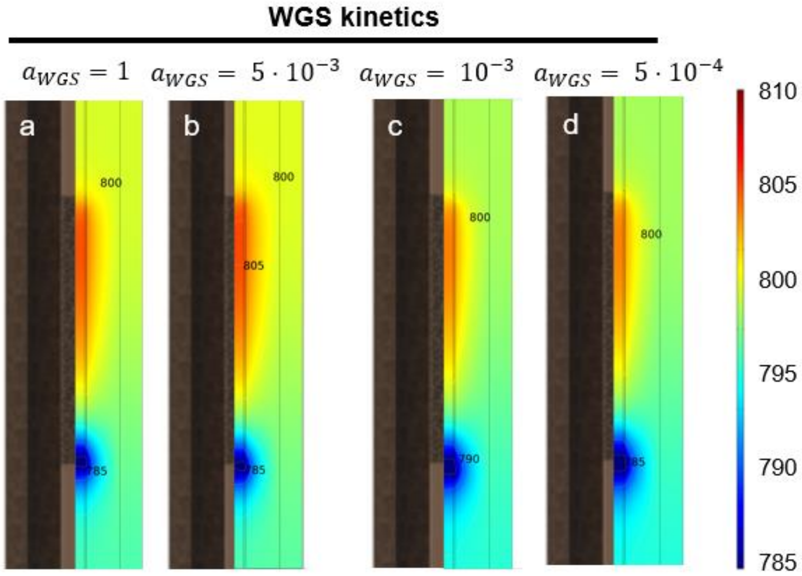

Figure 9.25. Evaluation of the effects of the kinetics of the WGS reaction on the temperature profiles. (a) bibliography kinetics; (b-d) worsening the bibliography kinetics. $k_{WGS} = a_{WGS} \cdot k_{WGS}$

9.4.3.4. Results of the study of the specific resistance in adiabatic conditions

Finally, the effect of the overall specific resistance of the electrochemical cell in adiabatic conditions was evaluated. Figure 9.26 shows the temperature profiles when the overall specific resistance of the cell is gradually decreased to the maximum hydrogen extractions at reference conditions. If the cell presents lower overall specific resistances, the heat of the Joule effect decreases and, keeping all the conditions and inlet constant, the temperature drops dramatically. To counteract this decrease of temperature, the total inlet flow of the reforming chamber can be increased. As previously was explained, the increase of Joule effect is higher than the increase of the rest of heats of the process. Therefore, the total inlet flow of the reforming chamber could be adjusted to reach the suitable temperature correction and to optimize the cell operation.

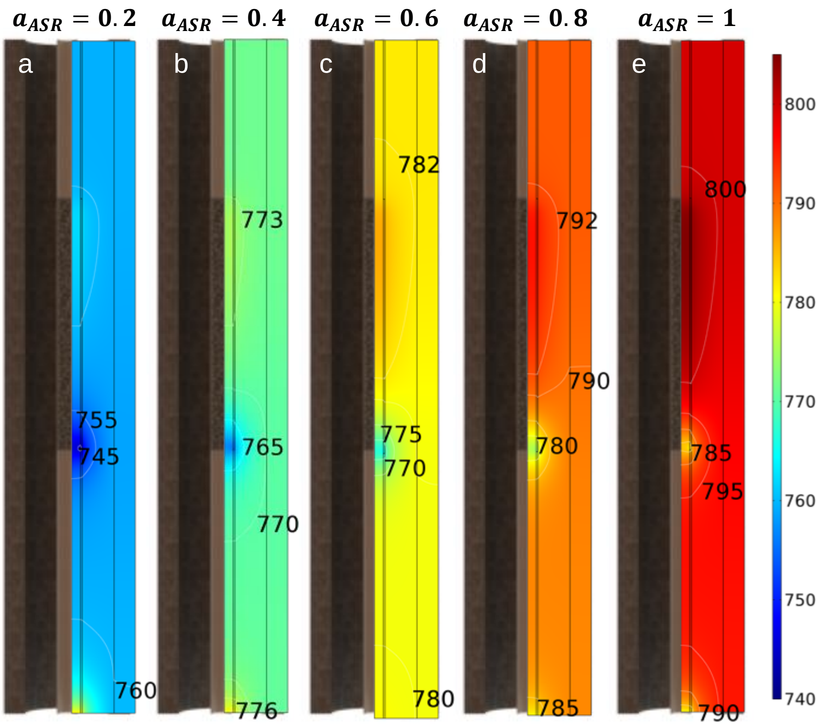

Figure 9.26. Evaluation of the overall specific resistance of the electrochemical cell on the heat transference. (a) $a_{ASR} = 0.2$, *(b)* $a_{ASR} = 0.4$, *(c)* $a_{ASR} = 0.6$, *(d)* $a_{ASR} = 0.8$, *(e)* $a_{ASR} = 1$. $ASR = a_{ASR} \cdot ASR_{800°C} \cdot exp\left(-\frac{Ea}{R} \cdot \left(\frac{1}{T} - \frac{1}{1073K}\right)\right)$

Figure 9.27 shows the temperature profiles when the overall specific resistance of the electrochemical is gradually increased for the maximum hydrogen extractions at reference conditions. If the cell presents higher overall specific resistances, the heat of the Joule effect increases and, keeping all the conditions and inlets constant, the temperature increases. Considering that radiation partially mitigates the heats sources of the process, the increase of temperature due to the increase of resistance are alleviated as the radiation heat transference has higher impacts under the overall heat transport. Finally, to adjust temperature along the tube cell around 800 °C, the inlet temperature of the reforming chamber and/or the total inlet flow of the reforming chamber can be decreased.

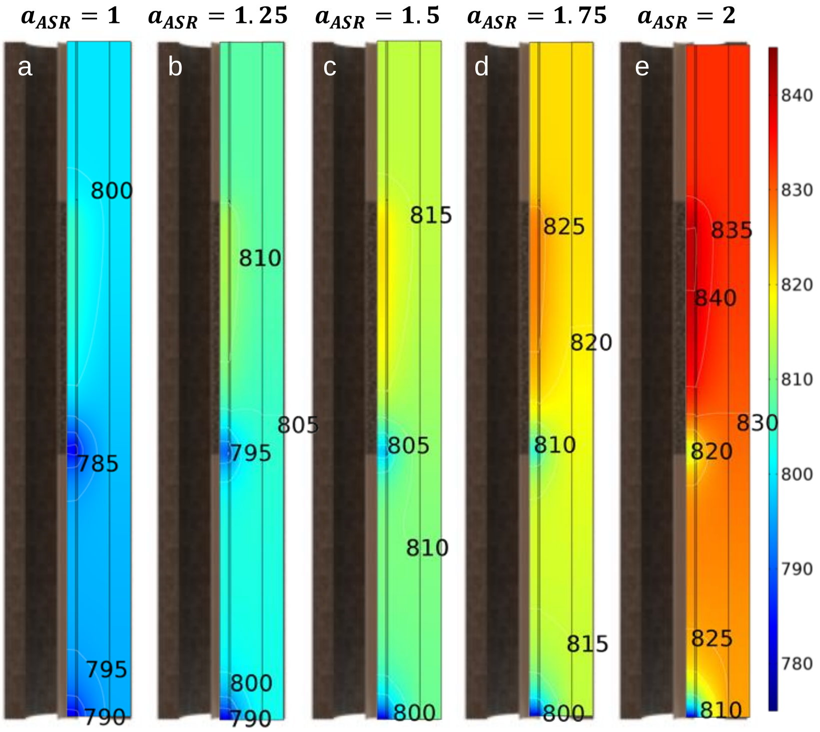

Figure 9.27. Evaluation of the overall specific resistance of the electrochemical cell on the heat transference. (a) $a_{ASR} = 1$, (b) $a_{ASR}1.25$, (c) $a_{ASR} == 1.5$, (d) $a_{ASR} = 1.75$, (e) $a_{ASR} = 2$. $ASR = a_{ASR} \cdot ASR_{800°C} \cdot exp\left(-\frac{Ea}{R} \cdot \left(\frac{1}{T} - \frac{1}{1073K}\right)\right)$

9.5. Summary

This work has built a finite element model to evaluate the integration of a current assisted membrane reaction based on protonic conducting materials in a methane steam reforming process. Additionally, this process allows the pressurization of the hydrogen obtained from the electrochemical cell. The model contains the gas flow, transport of species, reactions, electrochemistry and heat transport. Heat sources considered were reaction heats, Joule effect and heat of the pressurization of the hydrogen obtained. The conclusions of this work can be summarized as:

- The hydrogen pressurization phenomenon using an electrochemical cell takes place isothermally and it causes a releasing of the theoretical work as heat. Additionally, this heat needs to be balanced to avoid the increase of the process temperature. Otherwise, as the theoretical work is proportional to the temperature, this heat could cause over-control temperature situations.
- Isothermal analysis of the model shows there is no diffusion limitations in the hydrogen extractions in the conditions and flows considered at 800 °C. However, keeping the electrochemical area, the increase of the inlet flow could give diffusion limitations because the low CO content in the last zone of the cell.
- Isothermal analysis shows that, considering typical kinetics for these reactions, the process presents enough kinetic activity to reach the equilibrium.
- Isothermal analysis shows how the porous matrix of the internal electrode could only limit the hydrogen extraction if the porosity reaches very low values.
- The study shows how the microthermal integration at 800 °C for this process is achieved adjusting the temperature of the

inlet stream. In this microintegration three different regions can be identified: (i) first zone controlled by the SMR reaction with a local temperature decrease; (ii) the second zone where there is a mild increase of the temperature because the heats sources are slightly higher than the heat demands; (iii) the last area controlled by the electrocompression due to the low H_2 partial pressure substantially increasing the compression ratio in this zone.

- Radiation heat transference help to mitigate the heat sources and it help to homogenize the temperature in the setup.
- The most critical factor for the thermal balance is the specific resistance of the electrochemical cell. Experimental results show how this resistance is dominated by the electrolyte contribution. Moreover, porosity or kinetics do not present important effects in the adiabatic process unless very closed porous matrix and/or very slow kinetics.

List of factors

Factor	**Description**	***Factor***	**Description**
D_i^m	Average diffusion coefficient for the i compound	*F(i)*	molar flow for the i compound
Mn	average of the molecular weight	x_i	molar fraction of the i compound
k_{diff}	coefficient for the binary gas coefficient	v_i	molecular volume for the i compound
n_i	coefficient of the electrochemical reaction	M_i	molecular weight of the i compound
$\sigma_{(i)}$	conductivity (i=I ionic; i=S electric)	η	overpotential
R	Constant of the ideal gases	p_i	partial pressure of the i compound
$Q_{(i)}$	current density source term (i=I ionic; i=S electric)	d_p	particle diameter for the catalytic bed

Factor	**Description**	*Factor*	**Description**
ρ	density	κ	permeability of the catalytic bed
μ	dynamic viscosity	ϵ_p	porosity
$\mu_{g,i}$	dynamic viscosity of the pure i compound	p	pressure
i_S	electric current density	Kp_{ri}	Pressure equilibrium coefficient for the ri reaction
R_{cell}	electrical resistance of the assembly	r_i	reaction rate for the i compound
k_{eq}	equivalent thermal conductivity in the porous domain	E_{eq}	reversible potential
z	exchanged electrons	E_{eq}^0	reversible potential in standard conditions
F	Faraday constant	$\Delta H_{(ri)}$	ri reaction enthalpy
ΔG_{ri}	Gibbs energy for the i reaction	S_i	selectivity of the i compound
ΔG_{ri0}	Gibbs energy for the i reaction in standard conditions	θp	solid porous fraction
Cp	heat capacity	Q_{br}	source term
$Cp_{g,i}$	heat capacity of the pure i gas compound	$Temp$	Temperature
γ	heat capacity ratio	k	thermal conductivity
$\gamma_{g,i}$	heat capacity ratio for the pure i gas compound	$k_{g,i}$	thermal conductivity of the pure i gas compound
$Heat_{comp}$	Heat from hydrogen compression	kp	thermal conductivity of the solid of the porous domain
$Heat_{joule}$	Heat from the joule effect	$Itot$	total electrical current
$Heat_{(ri)}$	heat source of the ri reaction	$p^{(i)}$	total pressure of the i chamber
Q_{term}	heat source term	$Area$	transversal area of the electrochemical assembly
I	Identity matrix	u	velocity
Δn_i	increment of mols for the i reaction	N_i	weight flow for the i compound
i_I	ionic current density	j_i	weight flux for the i compound
β_F	isothermal compressibility coefficient	w_i	weight fraction of the i compound

Factor	**Description**	***Factor***	**Description**
k_{ri}	kinetic coefficient for the i reaction	$\phi_{i,j}$	wilke dimensionless number between i and j compounds
$D_{i,k}$	Maxwell-Stefan diffusivity	*F(i)*	molar flow for the i compound
$X(CH_4)$	methane conversion	x_i	molar fraction of the i compound
SMR	Steam methane reforming	*WGS*	Water gas shift

9.6. References

1. Kırtay, E., Energy Conversion and Management, 2011. **52**(4): p. 1778-89.
2. Dufour, J., et al., Energy & Fuels, 2011. **25**(5): p. 2194-202.
3. P L, S., *Life cycle assessment of hydrogen production via natural gas steam reforming*. 2017.
4. Gahleitner, G., International Journal of Hydrogen Energy, 2013. **38**(5): p. 2039-61.
5. BAN, M., et al., Journal of Modern Power Systems and Clean Energy, 2017. **5**(3): p. 337-49.
6. Götz, M., et al., Renewable Energy, 2016. **85**: p. 1371-90.
7. Schiebahn, S., et al., International Journal of Hydrogen Energy, 2015. **40**(12): p. 4285-94.
8. Guandalini, G., et al., Applied Energy, 2015. **147**(Supplement C): p. 117-30.
9. Qadrdan, M., et al., International Journal of Hydrogen Energy, 2015. **40**(17): p. 5763-75.
10. Varone, A. and M. Ferrari, Renewable and Sustainable Energy Reviews, 2015. **45**(Supplement C): p. 207-18.
11. Zhang, X., et al., Applied Energy, 2017. **190**(Supplement C): p. 326-38.

12. Iulianelli, A., et al., Renewable and Sustainable Energy Reviews, 2014. **29**(Supplement C): p. 355-68.
13. Iulianelli, A., et al., Catalysis Reviews, 2016. **58**(1): p. 1-35.
14. Oyama, S.T., et al., International Journal of Hydrogen Energy, 2012. **37**(13): p. 10444-50.
15. Chang, H.-F., et al., International Journal of Hydrogen Energy, 2010. **35**(23): p. 12986-92.
16. Morejudo, S.H., et al., Science, 2016. **353**(6299): p. 563-6.
17. Vasileiou, E., et al., Solid State Ionics, 2015. **275**: p. 110-6.
18. Skodra, A. and M. Stoukides, Solid State Ionics, 2009. **180**(23): p. 1332-6.
19. Kyriakou, V., et al., Applied Catalysis B: Environmental, 2016. **186**: p. 1-9.
20. Malerød-Fjeld, H., et al., Nature Energy, 2017.
21. Arzamendi, G., et al., Catalysis Today, 2009. **143**(1): p. 25-31.
22. Zhai, X., et al., International Journal of Hydrogen Energy, 2010. **35**(11): p. 5383-92.
23. Deshmukh, S.R. and D.G. Vlachos, Industrial & Engineering Chemistry Research, 2005. **44**(14): p. 4982-92.
24. Fazeli, A. and M. Behnam, *CFD Modeling of Methane Autothermal Reforming in a Catalytic Microreactor*, in *International Journal of Chemical Reactor Engineering*. 2007.
25. Cheng, C.-H., et al., Energy, 2014. **70**(Supplement C): p. 355-65.
26. Nijemeisland, M., et al., Chemical Engineering Science, 2004. **59**(22): p. 5185-91.
27. Dixon, A.G., et al., Chemical Engineering Science, 2007. **62**(18): p. 4963-6.
28. Kuroki, M., et al., JOURNAL OF CHEMICAL ENGINEERING OF JAPAN, 2009. **42**(Supplement.): p. s73-s8.

29. Wehinger, G.D., et al., Chemie Ingenieur Technik, 2015. **87**(6): p. 734-45.
30. Xuan, J., et al., International Journal of Hydrogen Energy, 2009. **34**(22): p. 9076-86.
31. Roses, L., et al., International Journal of Hydrogen Energy, 2010. **35**(22): p. 12668-79.
32. Bruce E. Poling, J.M.P., John O' Connell, *The properties of gases and liquids. 5th edition.* 2000, New York, Chicago, San Francisco, Athens, London, Madrid, Mexico City, Milan, New Delhi, Singapore, Sydney, Toronto: McGraw-Hill Education.
33. Donald A. Nield, A.B., *Convection in Porous Media. Third Edition*. 2006, United States of America: Springer.
34. Matyka, M., et al., Physical Review E, 2008. **78**(2): p. 026306.
35. Pisani, L., Transport in Porous Media, 2011. **88**(2): p. 193-203.
36. Xu, J. and G.F. Froment, AIChE Journal, 1989. **35**(1): p. 88-96.
37. Murthy, S. and A.G. Fedorov, Journal of Power Sources, 2003. **124**(2): p. 453-8.
38. Mahcene, H., et al., Energy Procedia, 2014. **50**(Supplement C): p. 229-36.
39. Zeng, M., et al., Journal of Power Sources, 2012. **206**(Supplement C): p. 185-96.
40. Calise, F., et al., International Journal of Hydrogen Energy, 2007. **32**(17): p. 4575-90.
41. Daun, K.J., et al., 2005(47349): p. 183-91.
42. Daun, K.J., et al., Journal of Power Sources, 2006. **157**(1): p. 302-10.
43. Mejri, I., et al., Internatiomal Journal of Heat and Technology, 2016. **34**(3): p. 351-6.
44. DiGiuseppe, G., Journal of Fuel Cell Science and Technology, 2012. **9**(6): p. 061007--9.

45. Pianko-Oprych, P., et al., *Quantification of the Radiative and Convective Heat Transfer Processes and their Effect on mSOFC by CFD Modelling*, in *Polish Journal of Chemical Technology*. 2014. p. 51.

46. Ong, K.M., et al., 2012(44823): p. 273-80.

47. Hajimolana, S., et al., Fuel Cells, 2012. **12**(5): p. 761-72.

48. VanderSteen, J. and J. Pharoah. *The effect of radiation heat transfer in solid oxide fuel cell modeling*. in *Combustion Institute/Canadian Section, Spring Technical Meeting*. 2004.

49. Lienhard, J.H., *A heat transfer textbook*. 2013: Courier Corporation.

50. de Wasch, A.P. and G.F. Froment, Chemical Engineering Science, 1972. **27**(3): p. 567-76.

51. Elnashaie, S.S., *Modelling, simulation and optimization of industrial fixed bed catalytic reactors*. Vol. 7. 1994: CRC Press.

52. Roses, L., et al., *Computational fluid dynamics (CFD) analysis of membrane reactors: Simulation of a palladium-based membrane reactor in fuel cell micro-cogenerator system*. Vol. 1. 2013. 496-531.

53. Wakatsuki, K., et al., *Determination of Planck Mean Absorption Coefficients for Hydrocarbon Fuels*. Vol. 180. 2008. 616-30.

54. Barlow, R.S., et al., Combustion and Flame, 2001. **127**(3): p. 2102-18.

55. Grosshandler, W., *RADCAL: a narrow-band model for radiation calculations in a combustion environment NIST Tech*. 1993, Note 1402.

56. Mossi, A., et al., Journal of the Brazilian Society of Mechanical Sciences and Engineering, 2012. **34**: p. 112-9.

57. Rohland, B., et al., Electrochimica Acta, 1998. **43**(24): p. 3841-6.

58. Kreuer, K.D., Solid State Ionics, 1999. **125**(1): p. 285-302.

59. Kochetova, N., et al., RSC Advances, 2016. **6**(77): p. 73222-68.

60. Yamazaki, Y., et al., Nature Materials, 2013. **12**: p. 647.

61. Kjølseth, C., et al., Solid State Ionics, 2010. **181**(5): p. 268-75.

10. FLUID DYNAMIC EVALUATION OF THE HYDROGEN EXTRACTION IN METHANE DEHYDROAROMATIZATION REACTOR

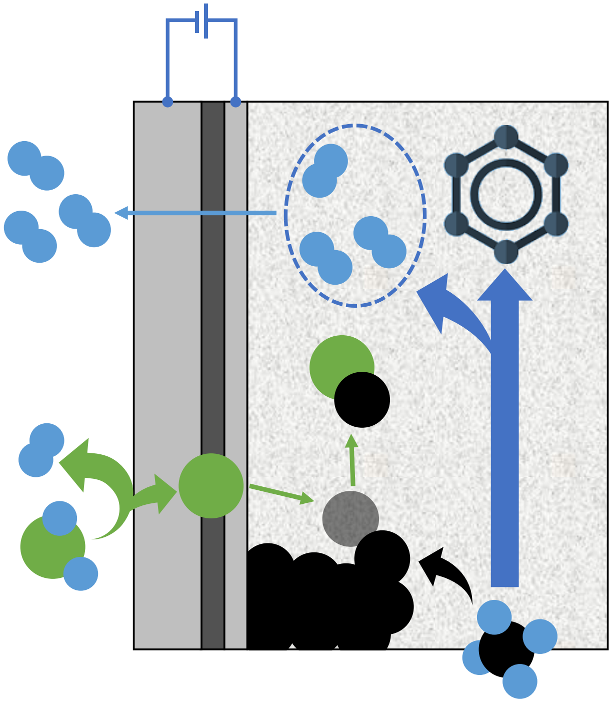

10.1. Introduction

Nowadays, the growing interest to find alternatives to synthetize liquid petroleum fractions have caused the developing of several processes using different sources such as biomass [1-3] or natural gas [4-7]. The main step of this kind of processes is the transformation of light fractions (C_1–C_2) into heavier fractions. Methane dehydroaromatization (MDA) allows methane to be converted into benzene in one-step [8-10]. However, it is an equilibrium-limited reaction with (methane conversion around 12% at 700ºC) prone to catalyst deactivation due to coke formation during the process. Previous works have attempted to improve this process using hydrogen selective membranes to shift the equilibrium, such as palladium-based membranes [11-16] or hydrogen ceramic membranes [12, 17, 18]. However, the hydrogen extraction does not solve the problem of catalyst deactivation due to coke formation [19]. The oxygen injection either directly in the feed or through oxygen selective membranes suppress coke formation what improves the catalyst stability [19-21]. Co-feed with steam improves the catalytic stability due to coke suppression but steam content above 2.5% can cause a fall in the catalytic activity after several hours as the steam reacts with the catalyst, in particular, with molybdenum carbides clusters – active catalyst sites [22-24].

According to Thermodynamics, temperatures above 650 ºC are necessary to achieve significant transformation of methane into ethylene what increases more coke formation, which is already significant at lower temperatures (Figure 10.1a). A thermodynamic analysis of the MDA reactions without considering coke formation indicates that to reach high methane conversion is necessary to extract a high hydrogen fraction (Figure 10.1b). However, as methane tends to be converted into complex aromatics, hydrogen extraction needs to be limited to achieve significant methane conversion and simultaneously orienting the process to benzene production. Bijani et al. [25] showed that low hydrogen co-feeding could improve benzene selectivity as it limits high aromatic formation. Their results also show that steam co-feeding with steam-to-methane ratios above 0.07 cause that the reforming reactions control the process.

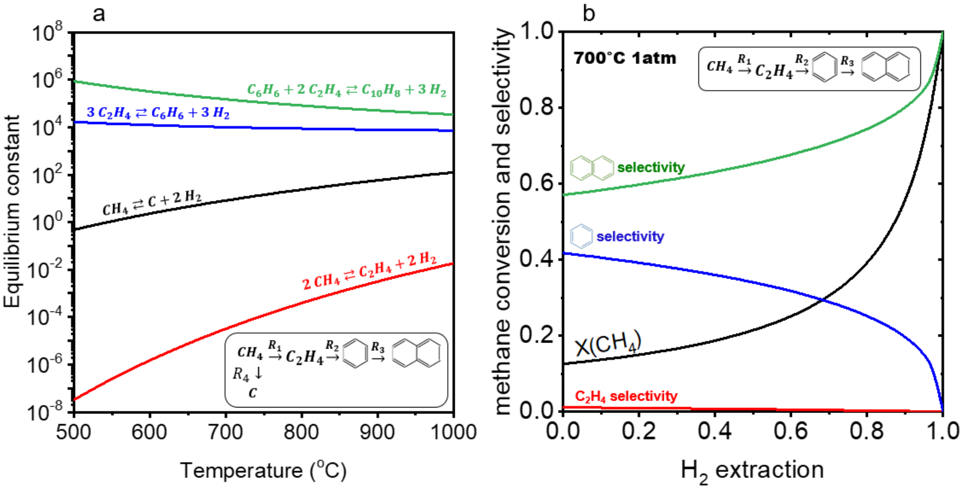

Figure 10.1. Thermodynamics of the MDA process. (a) Dependence of reaction equilibrium constants on temperature; (b) Methane conversion and selectivity at equilibrium as a function of hydrogen extraction (coke formation not taken into account).

Previous works have fitted the kinetics of MDA on experimental data obtained from reactors either assuming lumped or plug-flow models [26-28]. Corredor et al [29] built a plug-flow model for a reactor with a membrane for hydrogen removal. The reaction model did not include coke formation. Their results showed that removal of hydrogen shifts the conversion of methane to benzene and naphthalene. Kee et al [30] studied also a packed bed reactor with hydrogen selective membranes and observed relevant effects of the space velocity, for example, relatively high space velocities can minimize the impact of coke formation.

Recent research of our group has developed a membrane reactor using co-ionic conducting ceramic membranes that improves significantly the stability of the MDA reaction achieving very high benzene selectivities [31]. A scheme of the experimental set-up is shown in Figure 10.2a. In this reactor, an electrical potential is applied through the electrochemical membrane cell to simultaneously extract hydrogen and inject oxide ions thanks to the co-ionic conductivity of the membrane (Figure 10.2b). In the electrode of the bed chamber, steam is generated by the electrochemical reaction between the transferred oxide ions and the hydrogen present. In this way, the oxygen injected to the catalytic bed forms steam that reacts selectively with the coke particles enhancing the stability of the catalyst.

The aim of this chapter is to achieve a better understanding of the physical behavior of the experimental setup and to analyze the effect of process and geometric variables on the reactor performance, thus orienting the design of experiments in the laboratory but also the industrial development of the process. To do that, a model to simulate the experimental setup was implemented in a software for finite element analysis. Next, the model kinetic parameters were fitted to experimental information. Afterwards, several parametric studies were carried out to extrapolate the reactor performance at conditions different from those experimentally studied. The main responses studied were the benzene yield, hydrogen generation and extraction, and coke suppression.

10.2. Methods

10.2.1. Experimental setup and reference conditions

The catalytic membrane reactor setup consists of a catalytic bed contained in a quartz tube with a tubular co-ionic conducting membrane placed in the axis. The height of the catalytic bed is 4 *cm*, the tubular membrane has an outer diameter of 9.8 *mm* and the quartz tube has an inner diameter of 16.5 *mm*. The tubular electrochemical membrane is composed of a thin external layer, a dense electrolyte film (BCZY72) and an internal porous layer. The external layer acts as the anode (Cu-based) and the internal layer (a porous BCZY72-Ni support) acts as the cathode. The catalyst used is the 6Mo/MCM-22. The average particle size of the catalyst bed size is 300 *µm* and the porosity is 0.5.

The feed composition was a mixture of CH_4 and N_2 (95/5) injected at a space velocity of 1500 $NmL \cdot h^{-1} \cdot g_{cat}^{-1}$. The inner chamber was fed with a moist sweep gas. The reactor operated at isothermal conditions (700 ºC). Further details of the experiment are described in the referred work [31]. For this study, the reference conditions are those used in the experimental runs.

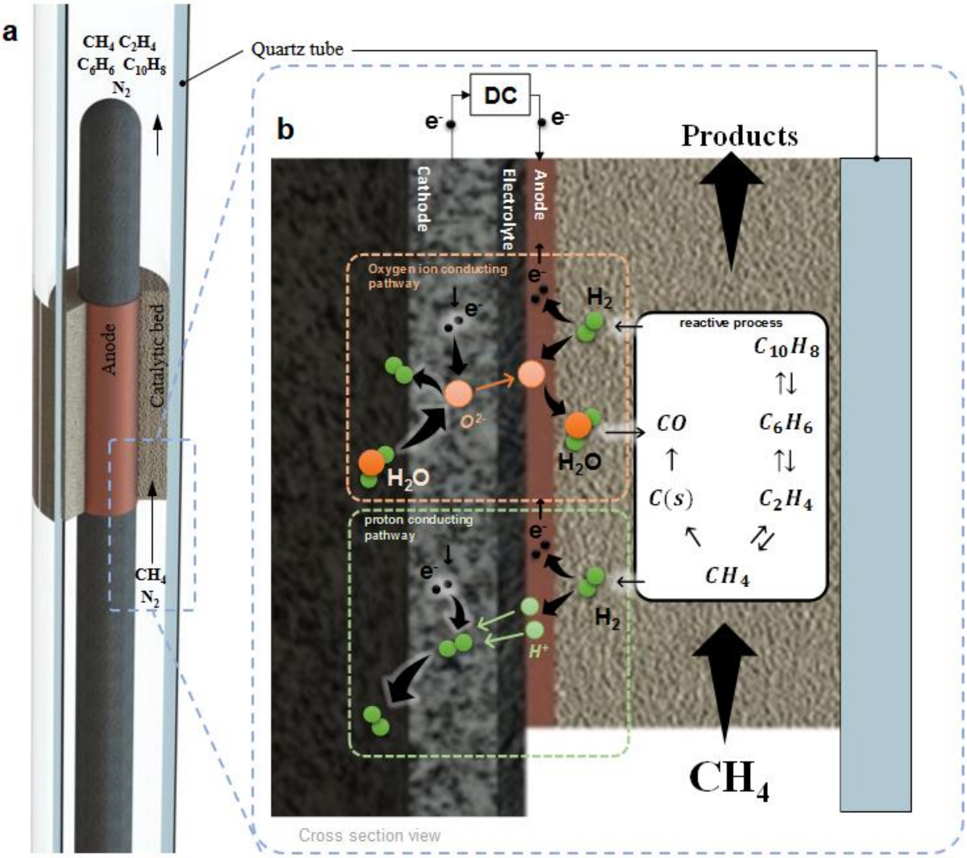
a
CH_4 C_2H_4
C_6H_6 $C_{10}H_8$
N_2
Quartz tube
Anode
Catalytic bed
CH_4
N_2
b
DC
e⁻
e⁻
Products
Cathode
Electrolyte
Anode
Oxygen ion conducting pathway
e⁻
e⁻
H_2
O^{2-}
H_2O
H_2O
reactive process
$C_{10}H_8$
C_6H_6
C_2H_4
CO
$C(s)$
CH_4
proton conducting pathway
e⁻
e⁻
H_2
H^+
CH_4
Cross section view

Figure 10.2. Description of the membrane reactor setup: (a) scheme of setup; (b) reactions in the catalyst bed and transport of species through the co-ionic membrane

10.2.2. Model implementation

The stationary model of the reactor was implemented in a finite element software (Comsol Multiphysics 4.4).

Compartment model and governing equations

As the reactor geometry is 2D axis-symmetric substantial computational simplification was achieved respect to a 3D model.

Three domains of annular section were considered, a feed chamber, the catalyst bed and the outlet chamber (Figure 10.3a).

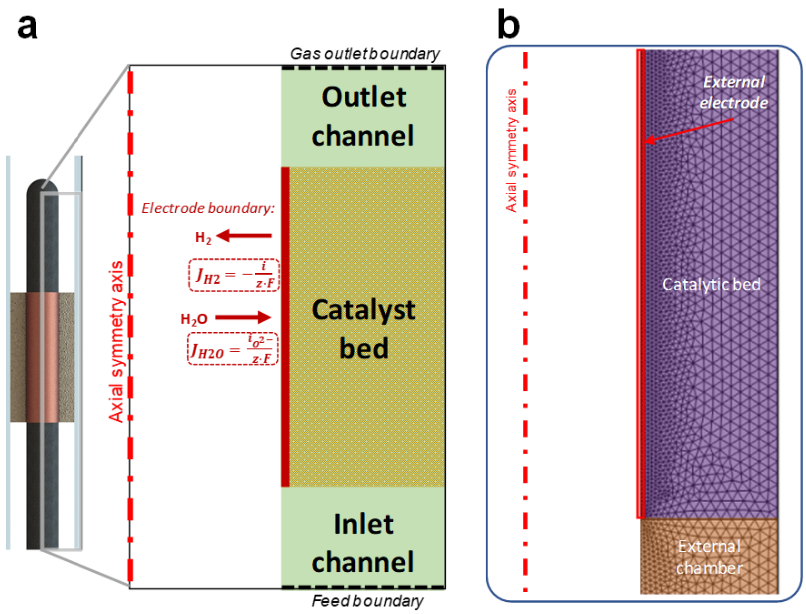
a
Gas outlet boundary
Outlet channel
Electrode boundary:
H_2
$J_{H2} = -\frac{i}{z \cdot F}$
H_2O
$J_{H2O} = \frac{i_{O^{2-}}}{z \cdot F}$
Axial symmetry axis
Catalyst bed
Inlet channel
Feed boundary
b
Axial symmetry axis
External electrode
Catalytic bed
External chamber

Figure 10.3. Model implementation of the membrane reactor setup: (a) 2D axisymmetric domains and boundaries description (b) meshes used.

The process involves several coupled reaction and transport phenomena. For this study, the following physics were taken into account: gas flow, reactions, hydrogen extraction and species diffusion in isothermal conditions (Table 10.1). Heat transfer and electrochemistry effects were not taken account to focus the analysis on the interactions between the fluid dynamics, diffusion and reactions phenomena. The composition only took into account the major species existing in the catalytic bed: methane, ethylene, benzene, naphthalene, hydrogen, water and nitrogen.

Table 10.1. Governing equations for the CFD model.

Governing equation	id	Properties equation	id
Navier-Stokes			
$\rho(u\cdot\nabla)u = \nabla\cdot\left[-pI + \mu(\nabla u + (\nabla u)') - \frac{2}{3}\mu(\nabla\cdot u)I\right]$	(1)	$\rho = \frac{p}{Rg\cdot T}\cdot M_n$	(8)
$\nabla\cdot(\rho u) = 0$	(2)	$\mu = \sum_i \frac{\mu_{g,i}}{1 + \frac{1}{x_i}\cdot\sum_{j,j\neq i} x_j\cdot\phi_{i,j}}$	(9)
$\frac{\rho}{\epsilon_p}\left((u\cdot\nabla)\frac{u}{\epsilon_p}\right) = \nabla\cdot\left[-pI + \frac{\mu}{\epsilon_p}(\nabla u + (\nabla u)') - \frac{2\mu}{3\epsilon_p}(\nabla\cdot u)I\right] - \left(\mu\kappa^{-1} + \beta_F\lvert u\rvert + \frac{Q_{br}}{\epsilon_p^2}\right)u$	(3)	$\phi_{i,j} = \frac{\left(1+\left(\frac{\mu_{g,i}}{\mu_{g,j}}\right)^{1/2}\cdot\left(\frac{M_j}{M_i}\right)^{1/4}\right)^2}{4/\sqrt{2}\cdot\left(\frac{M_i}{M_j}\right)^{1/2}}$	(10)
$\nabla\cdot(\rho u) = Q_{br}$	(4)	$\kappa = \frac{d_p^2\cdot\epsilon_p^3}{150\cdot\left(1-\epsilon_p\right)^2}$	(11)
Averaged-mixture model for transport of species			
$\nabla\cdot j_i + \rho(u\cdot\nabla)w_i = r_i\cdot\rho_{cat}\cdot M_i$	(5)	$D_i^m = \frac{1-w_i}{\sum_{k\neq i}\frac{x_k}{D_{i,k}}}$	(12)
$N_i = j_i + \rho u w_i$	(6)	$M_n = \left(\sum_i \frac{w_i}{M_i}\right)^{-1}$	(13)
$j_i = -\left(\rho D_i^m\nabla w_i + \rho w_i D_i^m\frac{\nabla M_n}{M_n}\right)$	(7)	$D_{i,j} = kd\cdot\frac{T^{1.75}\cdot\left(\frac{1}{M_i}+\frac{1}{M_j}\right)^{1/2}}{p\cdot\left(v_i^{1/3}+v_j^{1/3}\right)^2}$	(14)
		$Deff_{i,j} = \frac{\epsilon_p}{\tau_p}\cdot D_{i,j}$	(15)

The gas flow in the inlet and outlet chambers was modeled using the Navier-Stokes equations for laminar flow (Eq. 1, 2). In the catalytic bed, Navier-Stokes were coupled with Brinkman equations for porous media including coke deposition as source term (Eq. 3, 4). The averaged-mixture model (Eq. 5-7) was used to describe the transport of the different species. The properties of the pure gases were obtained from [32]. Density of the gas mixture was estimated assuming a mixture of ideal gases (Eq. 8) and viscosity was calculated using the Wilke mixing rule (Eq. 9, 10). The binary gas diffusion coefficient was obtained with an empirical correlation (Eq. 14) based on the Fuller kinetic gas theory.

The porous region was assumed to be a packed bed of randomly distributed spherical particles. Its permeability was calculated using the Carman-Kozeny model (Eq. 11) taken into account the average size and porosity [33]. Tortuosity of the bed was evaluated as the inverse of the square root of the porosity [34, 35]. The binary gas diffusion coefficient (Eq. 14) was calculated with an empirical equation based on the Fuller kinetic gas theory [36] and it was corrected with the ratio of porosity to tortuosity (Eq. 15).

Methane dehydroaromatization is a reactive process limited by equilibrium. The reaction model includes the following dehydrogenation reactions: conversion from methane to ethylene (R1), ethylene to benzene (R2), benzene to naphthalene (R3) and coke formation (R4). Although previous works have reported, coke formation can originate from different pathways, it was assumed that it is produced from methane exclusively. It was also assumed that coke suppression (R5) was achieved by selective reaction of steam with coke depositions.

Coke formation implies losses of mass from the gas flow. As steam could also react with each hydrocarbon species and to degrade the catalyst, water partial pressure in the bed was checked to evaluate if the reforming reactions or catalyst degradation take place. To simplify the model, the naphthalene concentration used in the calculations represents the sum of naphthalene and toluene concentrations measured in the experimental runs.

The kinetic model for the five main reactions considered (Eq. 15-20 of Table 10.2) was adapted from previous works [28, 37].

Table 10.2. Reactions and kinetics equations.

Reaction	id	Equation	id
$2\,CH_4 \rightleftarrows C_2H_4 + 2\,H_2$	r1	$r_1 = \dfrac{k_1 \cdot p_{CH4}^2 \cdot \left(1 - \dfrac{p_{C2H4} \cdot p_{H2}^2}{p_{CH4}^2 \cdot Kp_{R1}}\right)}{\psi(p_{CH4}, p_{C2H4}, p_{C6H6}, p_{C10H8})^2}$	(16)
$3\,C_{2H4} \rightleftarrows C_6H_6 + 3\,H_2$	r2	$r_2 = \dfrac{k_2 \cdot p_{C2H4}^3 \cdot \left(1 - \dfrac{p_{C6H6} \cdot p_{H2}^3}{p_{C2H4}^3 \cdot Kp_{R2}}\right)}{\psi(p_{CH4}, p_{C2H4}, p_{C6H6}, p_{C10H8})^3}$	(17)
$C_6H_6 + 2\,C_2H_4 \rightleftarrows C_{10}H_8 + 3\,H_2$	r3	$r_3 = \dfrac{k_3 \cdot p_{C6H6} \cdot p_{C2H4}^2 \cdot \left(1 - \dfrac{p_{C10H8} \cdot p_{H2}^3}{p_{C6H6} \cdot p_{C2H4}^2 \cdot Kp_{R3}}\right)}{\psi(p_{CH4}, p_{C2H4}, p_{C6H6}, p_{C10H8})^3}$	(18)
$CH_4 \rightleftarrows C + 2\,H_2$	r4	$r_4 = \dfrac{k_4 \cdot p_{CH4} \cdot \left(1 - \dfrac{p_{H2}^2}{p_{CH4} \cdot Kp_{R4}}\right)}{\psi(p_{CH4}, p_{C2H4}, p_{C6H6}, p_{C10H8})}$	(19)
$C + H_2O \rightleftarrows CO + H_2$	r5	$r_5 = \begin{cases} k_5 \cdot p_{H2O} & if\ \ k_5 \cdot p_{H2O} < r_4 \\ r_4 & if\ \ k_5 \cdot p_{H2O} > r_4 \end{cases}$	(20)

$$\psi = 1 + K_{CH4} \cdot p_{CH4} + K_{C2H4} \cdot p_{C2H4} + K_{C6H6} \cdot p_{C6H6} + K_{C10H8} \cdot p_{C10H8} + K_{H2} \cdot p_{H2}$$

Boundary conditions

Figure 10.3b shows the different boundary conditions used in the coupled domains. The mass flow and composition of the feed were specified in the lower boundary of the feed chamber. For the gas outlet, the boundary condition for flow was a pressure specification and convective drag was assumed for component transport.

In the electrode boundary, the extraction of hydrogen takes place as protons and the injection oxygen ions thanks to the electrochemical process. In the electrochemical reactions, that takes place in the side of the bed chamber, the hydrogen reacts with the oxygen ions to form water and additionally hydrogen is oxidized to protons. The net result is a positive flux of O atom as steam entering through the boundary and a negative flux of hydrogen is extracted from the bed chamber according to Faraday’s law (Figure 10.3a). The ratio of the oxygen ions to protons was fixed to 0.2 based on experimental results. It was assumed that the current applied is distributed uniformly along the electrode.

Meshing and solver

The meshes performed for each domain were based on triangular elements (Figure 10.3b). Their element size was calibrated for fluid dynamics. The studies of the effect of the dimensions have their respective meshes (Figures 10.4 and 10.5). The average mesh quality used was 0.9194. The areas next to the electrode boundary were refined to have a finer mesh.

The calculations were carried out using the Parallel Direct Solver (PARDISO) in steady state mode with parameter continuation to facilitate convergence. The relative tolerance of the method was 0.001. Consistent stabilization criterion was chosen for all phenomena using streamline diffusion and crosswind diffusion.

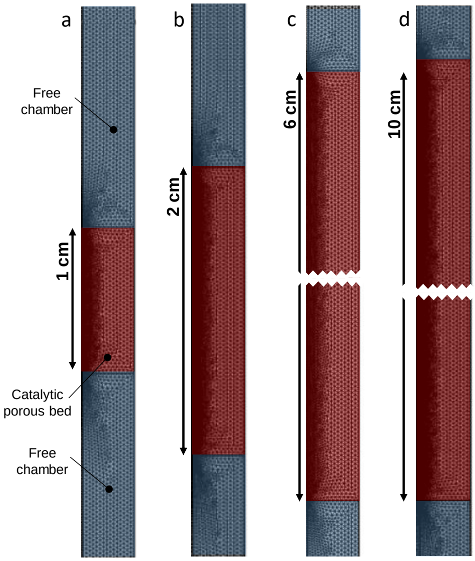
a
b
c
d
Free chamber
Catalytic porous bed
Free chamber
1 cm
2 cm
6 cm
10 cm

Figure 10.4. meshes of the geometries used for the study of the influence of the length of the catalytic bed and external electrode. (a) length of 1mm; (b) length of 2mm; (c) length of 6mm; length of 10mm

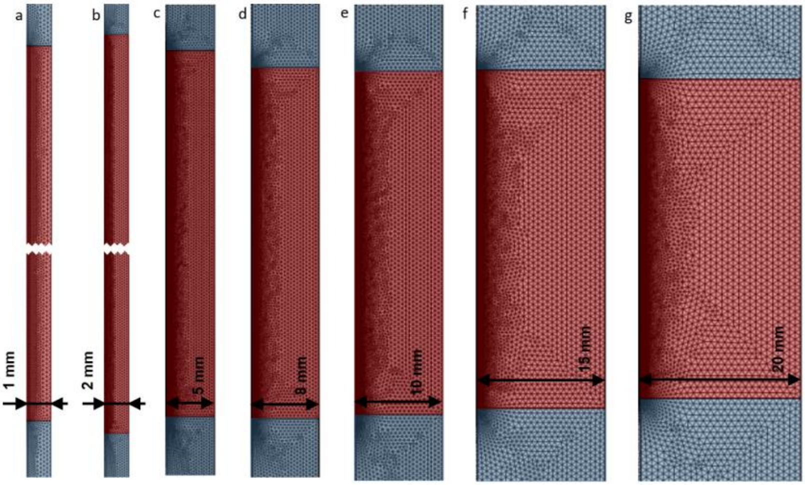
a
b
c
d
e
f
g
1 mm
2 mm
5 mm
8 mm
10 mm
15 mm
20 mm

Figure 10.5. meshes of the geometries used for the study of the influence of the length of the catalytic bed and external electrode. (a) catalytic width of 1mm; (b) 21mm; (c) 5 mm; (d) 8 mm; (e) 10mm; (f) 15mm; (g) 20mm.

10.2.3. Fitting of the kinetic model to experimental data

Prior to the parametric studies, the kinetic coefficients of the reaction system were fitted to experimental results obtained for the input reference conditions and different applied currents. The error function based on the difference of conversion and selectivity between the Comsol model and the experimental results was minimized.

10.2.4. Studies performed

Once the kinetic parameters were fitted, the model was used to obtain the composition and reaction rate profiles in the catalyst bed to improve the understanding of the process. The profiles were obtained for the experimental conditions corresponding to a case with a 25% of hydrogen extraction. This parameter is defined as the ratio of the hydrogen extracted –by the electrochemical cell– to the hydrogen generated by the process catalytic reactions (Eq. 25 of Table 10.3).

Afterwards, different parametric studies were carried out to evaluate how the operation parameters and set-up dimensions influence the performance of the process. For all studies, space velocity was studied in the range from 500 to 2000 $NmL/(h \cdot g_{cat})$ at the current for which maximum hydrogen extraction. To determine this maximum hydrogen extraction, the electrical current was gradually increased until zero hydrogen weight fraction was reached on the membrane boundary. The reference conditions different from the variables evaluated in each study were maintained to value of the experimental setup.

The studies performed were:

1. *Effect of hydrogen extraction*

The electrical current was increased for each space velocity to evaluate the percentage of hydrogen extracted and the impact on the catalytic performance.

2. *Influence of gas inlet velocity*

The total gas inlet flow was varied in the range of 10 – 250 *NmL/min* and the catalyst charge was recalculated for each space velocity studied.

3. *Influence of reactor geometry*

To study the influence of geometry on the hydrogen polarization, the length and width of the reactor were independently varied at constant catalyst charge for the reference feed. The reactor length (bed and membrane length) was varied from 1 to 10 *mm*. The bed width was varied from 1 to 20 *mm* keeping constant the outer radius of the electrochemical cell.

4. *Influence of catalyst bed porosity*

The effect of the porosity of the catalytic bed was studied to study their effect on hydrogen diffusion and process performance. The porosity was varied from 0.30 to 0.55.

5. *Influence of the kinetics of the ethylene formation reaction*

MDA is a complex reaction network process limited by the equilibrium but also by kinetics. After having identified the reaction kinetics limiting the process, a sensitivity study was performed by varying the magnitude of the specific kinetics parameter of this reaction.

10.3. Results

In this section, we show the results obtained in the simulation of the reference case and the several parametric studies performed. The main variables analyzed were methane conversion, benzene yield, hydrogen extraction ratio, and coke suppression. Additionally, an equilibrium ratio was defined to evaluate the degree of approach to equilibrium of the different reactions. Table 10.3 shows the equations used to calculate the mentioned variables.

Table 10.3. Variables used for result analysis

Parameters	Equation	id
Methane conversion	$X_{CH4} = \frac{F_{CH4,f} - F_{CH4,out}}{F_{CH4,f}}$	(21)
Yield	$Y_{C(n)} = \frac{F_{C(n),out} \cdot n}{F_{CH4,f}}$	(22)
Coke yield	$Y_{coke} = \frac{\int r_4 \, dV - F_{CO,out}}{F_{CH4,f}}$	(23)
H_2 extraction	$H_2\ extraction = \frac{\frac{I_{tot}}{z \cdot \mathrm{F}}}{\frac{I_{tot}}{z \cdot \mathrm{F}} + F_{H2,out}}$	(24)
Equilibrium ratio	$\beta_i = \frac{\prod_j p_j^{n_j}}{Kp_{rj}}$	(25)
Coke Suppression	$CS = \frac{\int r_5 \, dV}{\int r_4 \, dV}$	(26)

The results are mainly discussed on the basis of the maximum hydrogen extraction ratio attained for each situation. For the parametric studies performed, the supplementary figures (S3 to S6) relate the hydrogen extraction ratio with the current density applied and indicate the maximum hydrogen ratio.

10.3.1. Fitting the kinetics to the experimental data

The first step was to fit the model developed in Comsol. Kinetic coefficients were searched in ranges based in previous experimental results [31] of the catalytic membrane reactor under different current applied. The kinetic coefficients obtained are shown in Table 10.4. Figure 10.6 compares experimental and model results at reference conditions. The benzene yield is plotted against the hydrogen extraction obtained. It is also shown methane conversion and the components selectivity for a situation without hydrogen extraction and a situation with hydrogen extraction. It can be seen that obtained with the fitted model show good agreement with the experimental results (error < 15%, especially at lower hydrogen extraction).

Table 10.4. Fitting results of the kinetic model

Kinetic constant	**value**	**units**	**Adsorption coefficient**	**Value**	**units**
k_{r1}	5.69	$mol/(h\cdot kg_{cat}\cdot bar^2)$	K_{CH4}	0.3	$1/bar$
k_{r2}	$1.52\cdot 10^5$	$mol/(s\cdot g_{cat}\cdot bar^3)$	K_{C2H4}	0.17	$1/bar$
k_{r3}	2.5	$mol/(s\cdot g_{cat}\cdot bar^3)$	K_{C6H6}	$2.41\cdot 10^{-6}$	$1/bar$
k_{r4}	1.3	$mol/(h\cdot kg_{cat}\cdot bar)$	K_{C10H8}	$2.51\cdot 10^{-6}$	$1/bar$
k_{r5}	90	$mol/(h\cdot kg_{cat}\cdot bar)$	K_{H2}	5.06	$1/bar$

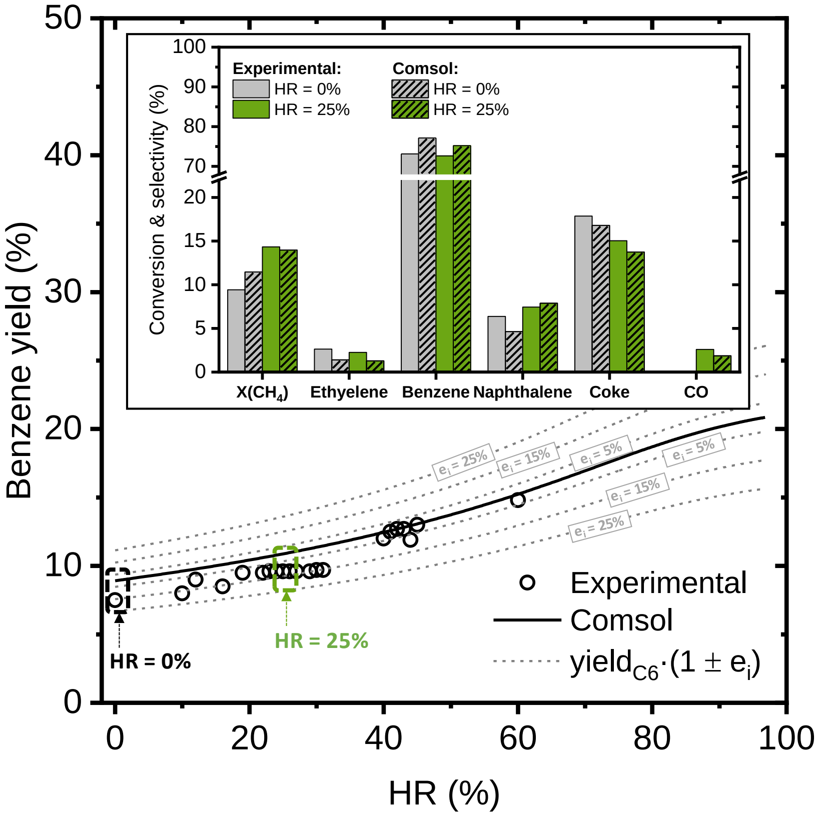

Figure 10.6. Comparison between the fitted model predictions and experimental results.

10.3.2. Spatial distribution of the reaction rates

Figure 10.7 shows the profiles of the reaction rates in carbon basis, equilibrium ratios, coke suppression ratio, and water and hydrogen fractions calculated by the model at reference experimental conditions. It can be seen that the ethylene (R1) and benzene formation reactions (R2) have very similar profile (Figure 10.7a). Both reaction rates decrease along the catalytic bed with insignificant radial gradients. The naphthalene formation (R3) barely advances in the catalytic bed what agrees the experimental results. The rate of the coke formation reaction (R4) is much lower than that of ethylene formation and show uniform values in the catalyst bed. To evaluate the degree in which each reaction is near to equilibrium, the profiles of the equilibrium ratio for reactions 1 to 3 were obtained (Figures 10.7b). It can be said that the ethylene formation reaction (R1) advances gradually until getting close to equilibrium at the end of the catalytic bed. This situation causes the decrease of the reaction rate profile. On the other hand, the benzene formation (R2) gets close to equilibrium in the first portion of the catalytic bed. This explains the similarity of the reaction rates of ethylene and benzene formation.

Figure 10.7c shows that the coke suppression ratio increases along the bed. The steam generated in the external electrode is dragged by the convective flow, thus determining the appearance of the water profile. As coke suppression is directly related with steam concentration has similar distribution. The coke suppression is lower in the bed entrance, especially in the more distant areas to the external electrode. This fact is critical because in these areas, the activity of the reactions from methane to benzene is high and, consequently, an inefficient suppression of coke depositions can deactivate these zones. Although the methane can react in other zones of the bed, these first zones, where the coke could be gathered, could orientate the methane to coke or third reactions. Therefore, when this process has to be scaled for final applications, the design has to be carefully designed to reduce the impact of dead-zones.

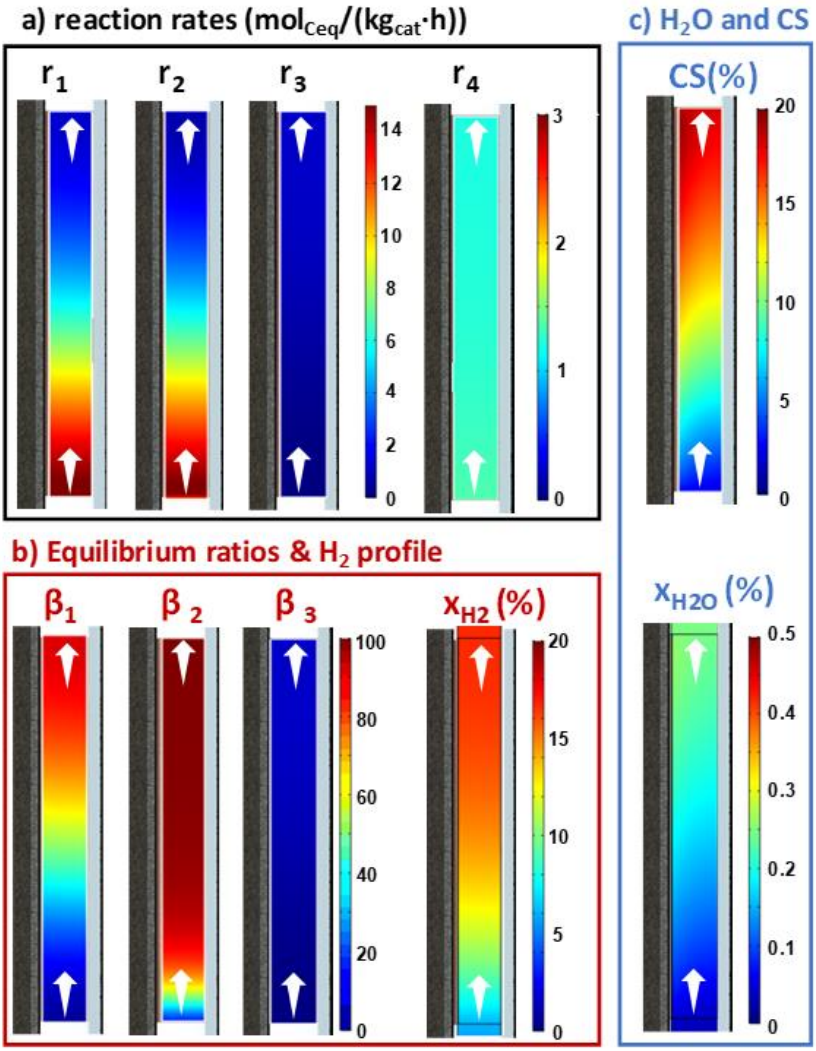

Figure 10.7. Profiles obtained at reference experimental conditions: (a) reaction rates; (b) equilibrium ratios and hydrogen molar fraction; (c) coke suppression and steam molar fraction

10.3.3. Hydrogen extraction analysis

Figure 10.8 shows the flows of hydrogen generated and extracted from the reaction chamber and the associated hydrogen extraction ratio. The maximum extraction of hydrogen from the reaction chamber is found at the point in which the hydrogen extracted (faradaic hydrogen) is close the hydrogen generated by all reactions (Figure 10.8a). For the same current density applied, the lower the space velocity, the higher the amount of hydrogen generated and consequently the lower the hydrogen extraction ratio. For all space velocities, there are not diffusional limitations, as it is possible to obtain high hydrogen extraction ratios (greater than 95%) independently of the amount of generated hydrogen (Figure 10.8b).

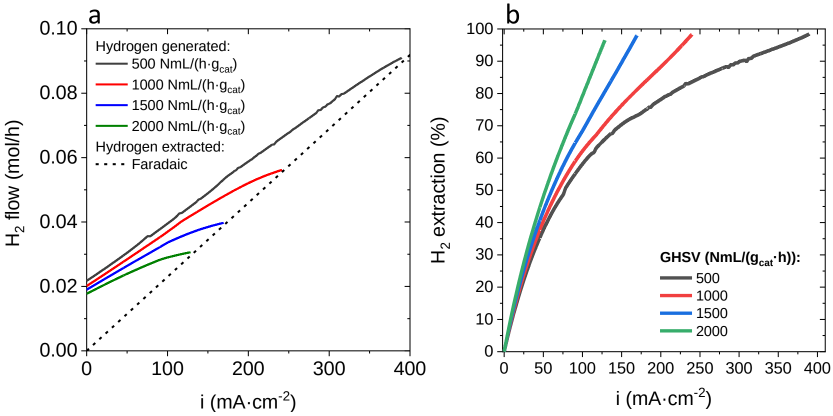

Figure 10.8. Effect of the applied current on the extraction and generation of H_2 for different space velocities: (a) total H_2 flow formed via MDA reactions and H_2 extraction flow; (b) H_2 extraction ratio

Figure 10.9 shows the effect of hydrogen extraction on component yields at different space velocities. As can be seen, hydrogen extraction has a significant effect on methane conversion, which is higher as the space velocity is lower.

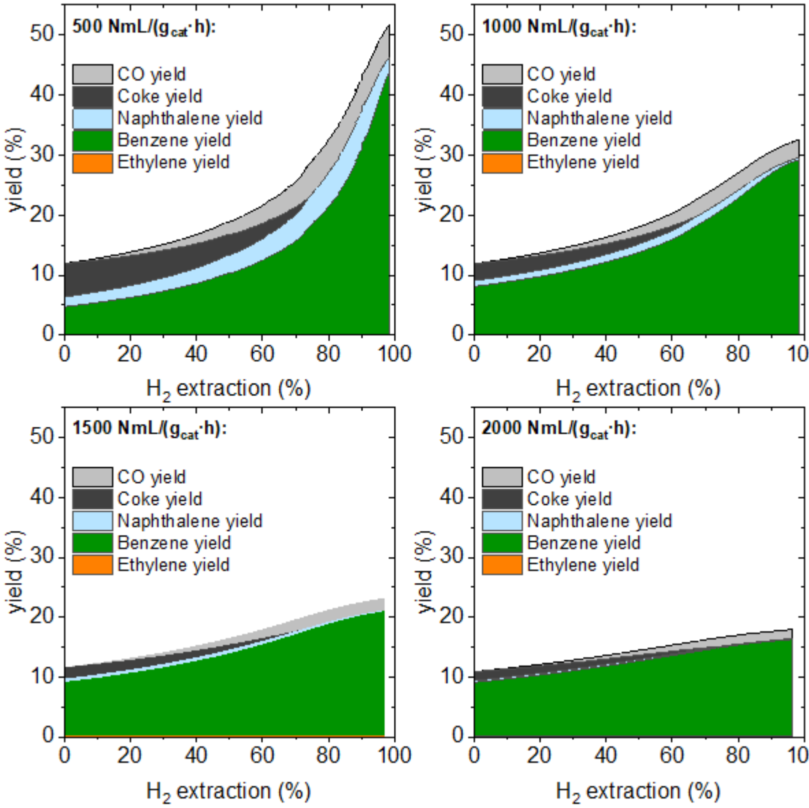

Figure 10.9. Effect of hydrogen extraction on the cumulative yield of the components at inlet reference conditions for different space velocities

The benzene yield represents the most important fraction of the total conversion and always increases with hydrogen extraction. For example, at the lowest space velocity, total conversion increases from 12% (no current density applied) to 52% (maximum current density) while benzene yield changes from 9% to 45%. For all space velocities, the ethylene yield was negligible. The naphthalene yield always remains approximately at a low value because it is limited by the low kinetics of its formation reaction. As can be observed, the higher the hydrogen extraction, the higher the CO yield and the lower the coke yield but the sum of both yields is slightly affected by the hydrogen extraction. The reason is that the increase of the hydrogen extraction implies an increase of the oxygen injection and consequently the steam generated causes the coke to become gradually in CO.

Although the hydrogen extraction shifts the reactions to the production of aromatics, methane conversion was only around 50% for the lowest space velocity studied at the maximum hydrogen extraction ratio. Consequently, the equilibrium is not limiting process under these conditions and, thus, the hydrogen generation is limited by the kinetics of the process. The low ethylene yield indicates that the rate dominant step of the process is the ethylene formation as the kinetics of the benzene formation is comparatively much faster. Figure 10.10 show the equilibrium ratios of reactions R1 and R2 for a situation of high hydrogen generation at 500 $NmL/(h \cdot g_{cat})$ and maximum hydrogen extraction. The equilibrium ratio of the reaction 1 shows the low advance of this reaction because the low kinetic activity. Otherwise, the equilibrium ratio profile of the reaction 2 (benzene formation), shows how the profile is corrected as the hydrogen is extracted. The hydrogen molar fraction profile shows how there is not important radial gradients. Steam molar fraction shows how the steam reaches values above 10% in the last points of the catalytic bed. Therefore, in this case this steam could cause the degradation of the catalyst or reforming reactions in this last zone where the activity of the steam is higher. Finally, the coke suppression profile shows how the coke is suppressed practically in all the catalytic bed.

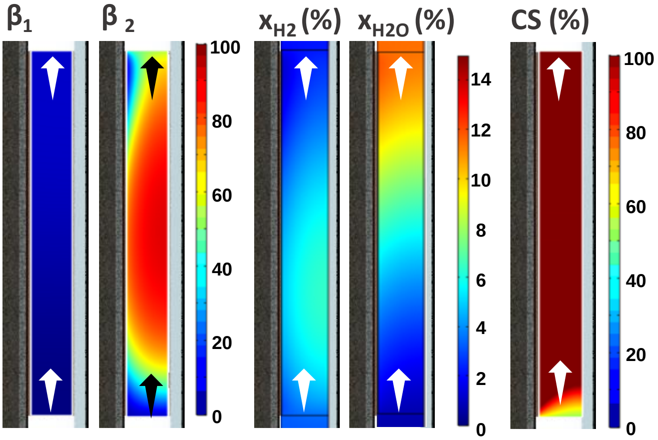

Figure 10.10. Profiles at maximum hydrogen extraction at a space velocity of 500 NmL·h^{-1}·g$_{cat}$$^{-1}$. (a) Equilibrium ratio of the reaction R1; (b) equilibrium ratio of the reaction R2; (c) hydrogen molar fraction; (c) steam molar fraction; (d) Coke suppression.

10.3.4. Influence of gas inlet velocity

Figure 10.11 shows the results for the hydrogen extraction, benzene yield, and coke suppression reached at the maximum hydrogen extraction for different spaces velocities when the feed inlet gas velocity is increased. Figure 10.11a shows that for inlet feed velocities ≤ 1.5 *cm/s*, a high hydrogen extraction ratio can be obtained, with its value being rather independent on the space velocity. Above this value, the hydrogen extraction ratio decreases as the input velocity increases because the convective drag of hydrogen overcomes the diffusion forces for hydrogen transport towards the electrode. The decrease on the hydrogen extraction ratio is less accused at low space velocity.

Lower space velocities have higher hydrogen generation but lower output gas volume because of the higher conversion. The increase on the average hydrogen concentration in the output is compensated by the volume reduction and consequently the changes on the convective drag of hydrogen are less important than the increase on hydrogen generation (Figures 12b and c). Therefore, greater values of maximum hydrogen extraction ratios are obtained at lower space velocities (see Figure 10.12a). Figure 10.11b shows how the benzene yield depends on feed velocity for the different space velocities and different constant catalytic loading. It can be seen that the decrease caused by the increase of velocity is more accused at low catalyst loading. As the space velocity is lower, the hydrogen extraction shifts more effectively the equilibrium and high benzene yields are obtained. The decrease of hydrogen extraction ratio due to the increase of inlet velocity causes a sharper decrease in the benzene yield at low space velocities. Similarly, Figure 10.11c shows how the coke suppression decreases with inlet feed velocity. This decrease is due to the generated steam is swept more effectively and, therefore, the steam concentration in the areas of the bed close to the inlet is highly reduced.

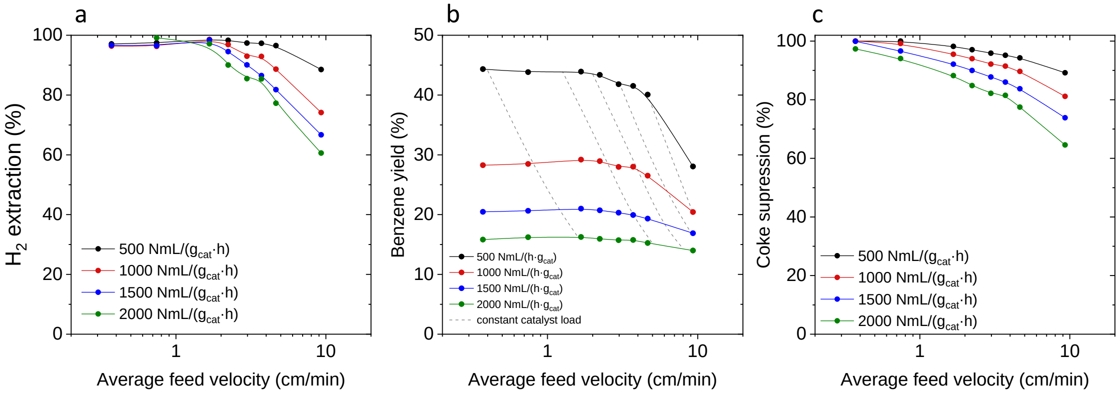

Figure 10.11. Effect of the average feed velocity at maximum hydrogen extraction for the geometry of reference: (a) fraction of hydrogen removed, (b) benzene yield, (c) and coke suppression for different space velocities

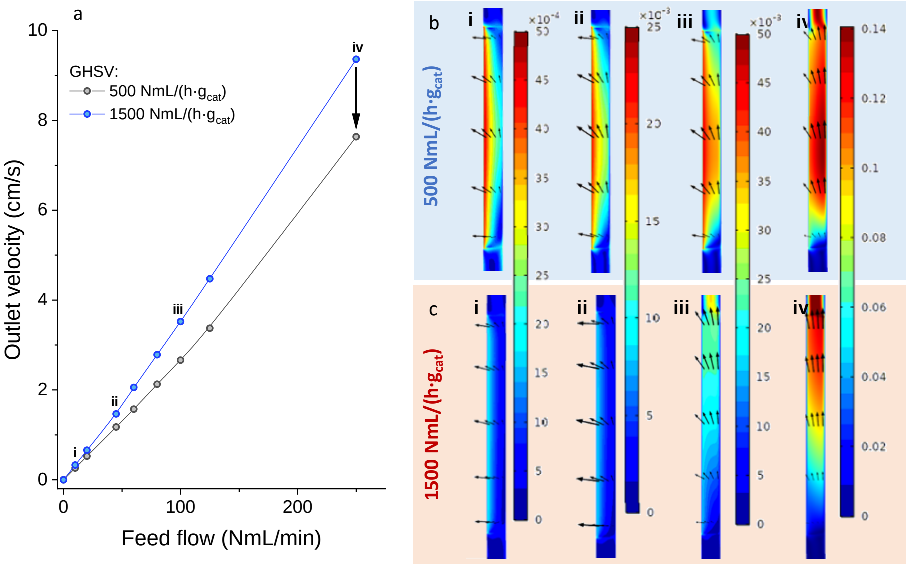

Figure 10.12. Effect of the inlet feed velocity at the maximum hydrogen extractions for several space velocities. Outlet velocity of the gas in the reaction chamber depending on the feed flow (a); H_2 molar flow profiles at space velocities of 500 NmL/(g$_{cat}$·h) (b); H_2 molar flow profiles at space velocities of 1500 NmL/(g$_{cat}$·h) (b);

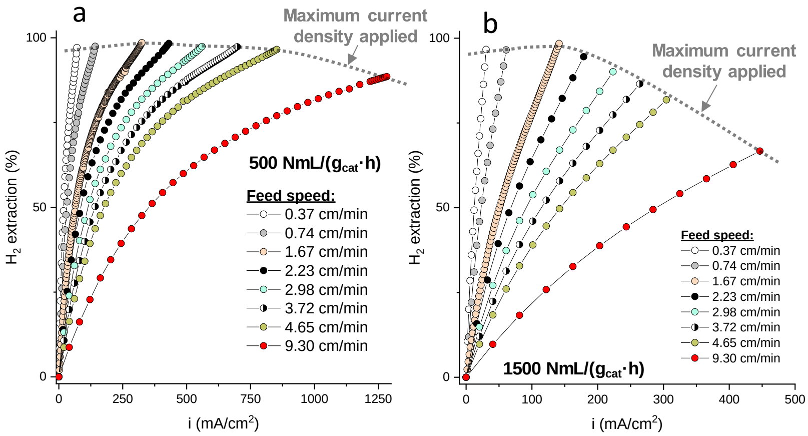

Figure 10.13. Effect of the inlet feed velocity. Hydrogen extraction ratio depending on current densities applied at 500 mL/(h·gcat) of space velocity (a) and at 1500 mL/(h·gcat) of space velocity (b).

10.3.5. Influence of reactor geometry

Given the feed flow, the changes on the reactor dimensions affected the local velocities. Besides, as length of the external electrode coincides with the bed length, the decrease of the length implied higher diffusion limitations for the hydrogen to reach the electrode.

Figure 10.14 shows the benzene yield and the maximum hydrogen extraction ratio as a function of the reactor length for different space velocities. As can be seen in Figure 10.14a, the effect of the reactor length on the benzene yield was only significant for the lowest space velocity where the effect of hydrogen extraction on this response was greater. The hydrogen extraction ratio keeps approximately constant for reactor length values greater than 4 *cm*. If the reactor length is decreased under this value, the hydrogen extraction ratio starts to decrease (Figure 10.14b). To understand this effect, the hydrogen molar fraction profiles were analyzed (Figure 10.14c). For the shortest reactor, the hydrogen molar fraction profile is highly polarized along all the reactor length because a significant fraction of the generated hydrogen is not able to reach the electrode. While for larger reactors, hydrogen polarization is gradually mitigated and the radial distribution of hydrogen near the output becomes more homogenous (Figure 10.14c).

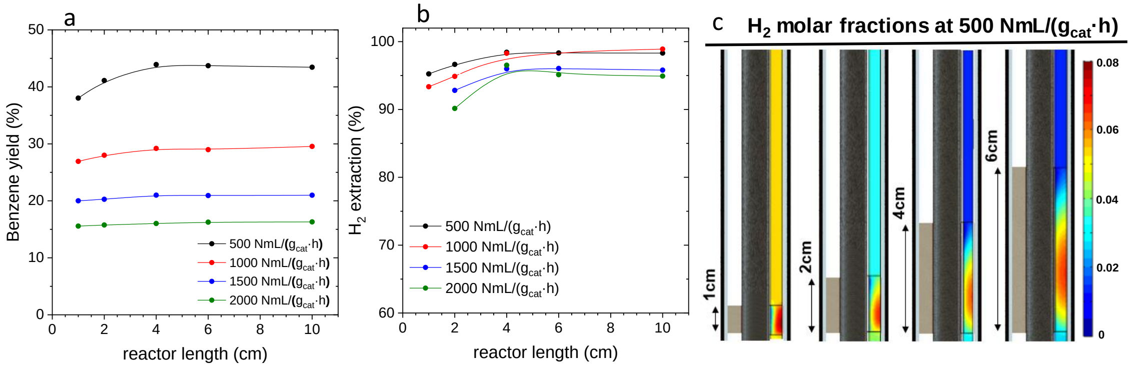

Figure 10.14. Effect of the reactor length at maximum hydrogen extraction ratio for different space velocities: (a) benzene yield (b)maximum hydrogen extraction ratio (c) profiles of hydrogen molar fraction at a space velocity of 500 NmL/(h·g_{cat}) for different reactor lengths

Figure 10.15 shows the analysis of the variation of the catalytic width. As the width of the bed is increased, there is a gradual decrease of the maximum hydrogen extraction ratio (Figure 10.15a). However, it only causes significant effects on the benzene yield at the lowest space velocity. Figure 10.15c shows the hydrogen molar fraction profiles for different catalytic bed widths at maximum hydrogen extraction ratio for the space velocity of 500 *NmL/(h·g_{cat})*. It can be seen an increase on hydrogen polarization due to the increase of the distance which the hydrogen has to cover to reach the electrode.

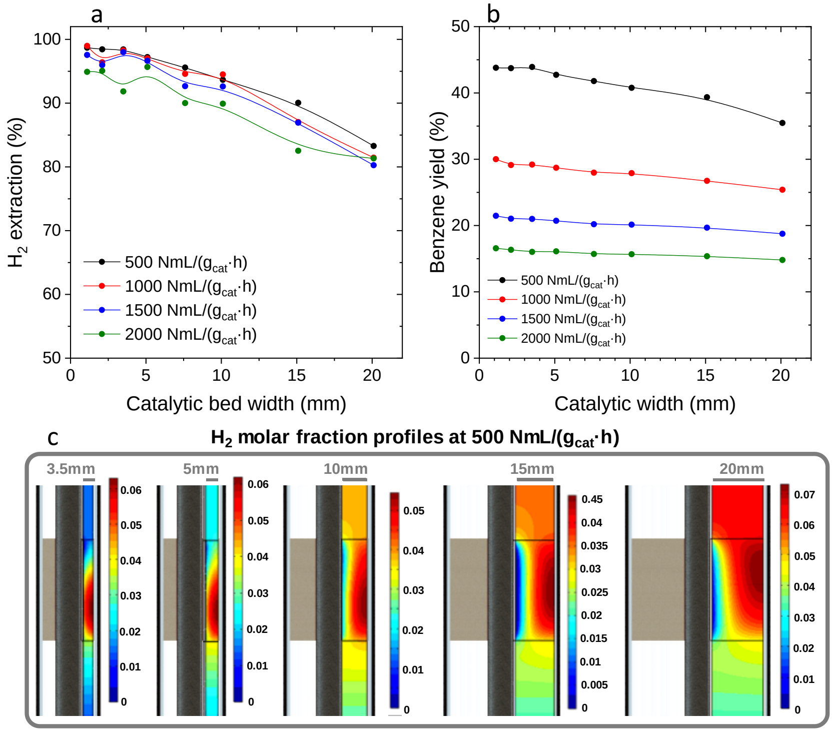

Figure 10.15 Effect of the width of the catalytic bed at maximum hydrogen extraction for different space velocities: (a) hydrogen extraction, (b) benzene yield, (c) profiles of hydrogen molar fraction at a space velocities of 500 NmL/(h·g_{cat}) and for different widths

Figure 10.16 and Figure 10.17 were used to select the maximum hydrogen extraction values for each case. They show the effect of the electric current density on the hydrogen extraction ratio for different lengths and widths and two space velocities (500 and 1500 *NmL/(h·g_{cat})*).

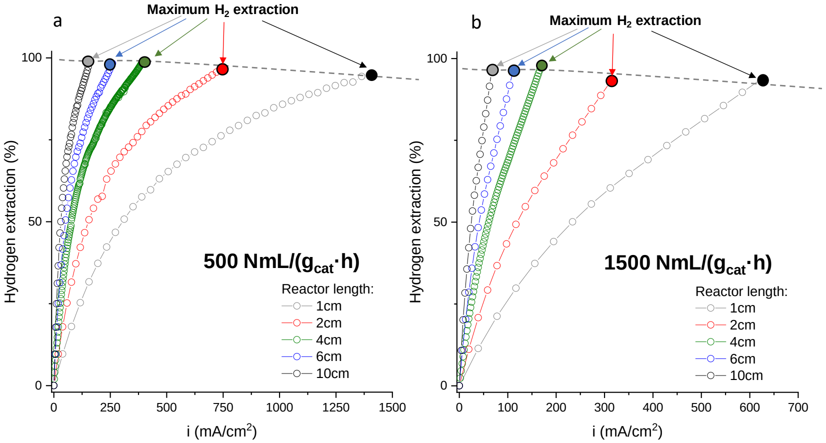

Figure 10.16. Hydrogen extraction ratio depending on the current density applied for different the reactor lengths at 500 NmL/(h·g$_{cat}$) of space velocity (a); and at 1500 NmL/(h·g$_{cat}$) of space velocity (b). Last points for each case represent the maximum hydrogen extraction.

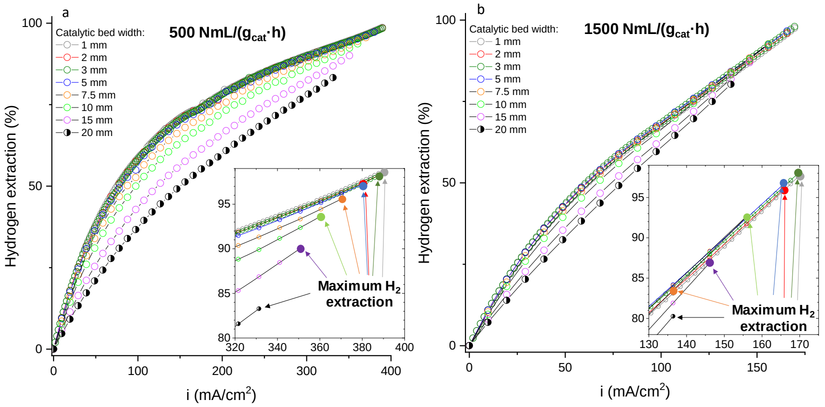

Figure 10.17. Hydrogen extraction ratio depending on the current density applied for different catalytic widths at 500 NmL/(h·g$_{cat}$) of space velocity (a); and at 1500 NmL/(h·g$_{cat}$) of space velocity (b). Last points for each case represent the maximum hydrogen extraction

10.3.6. Influence of catalyst bed porosity

The decrease of the bed porosity increases the gas velocity and decreases the effective coefficient diffusion. According to this, a decrease on the maximum hydrogen ratio and consequently on benzene yield is expected. Figure 10.18 shows the effect of the bed porosity on these variables for different space velocities. As can be observed, only a small decrease on the maximum hydrogen extraction ratio is observed if porosity is lower than 0.4 (Figure 10.18a). The observed decreased is not high enough to modify significantly to the benzene yield (Figure 10.18b). Figure 10.19 shows the current density applied to increase the hydrogen removed from the reaction chamber at different space velocities.

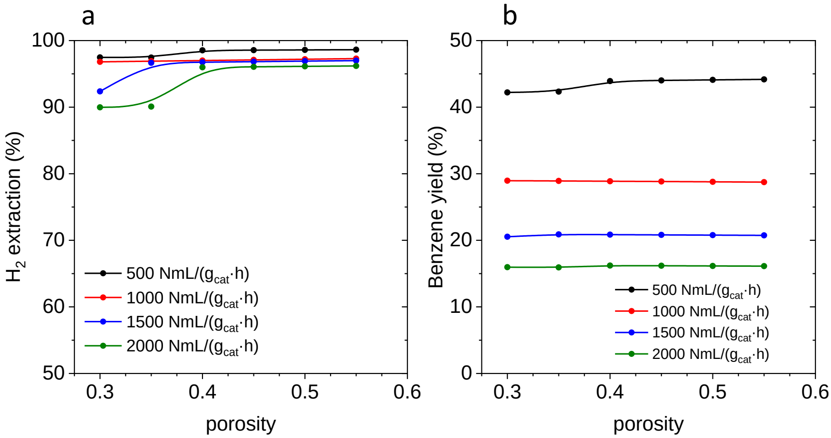

Figure 10.18. Effect of the catalytic bed porosity at maximum hydrogen extraction for different space velocities: (a) hydrogen extraction ratio (b) benzene yield.

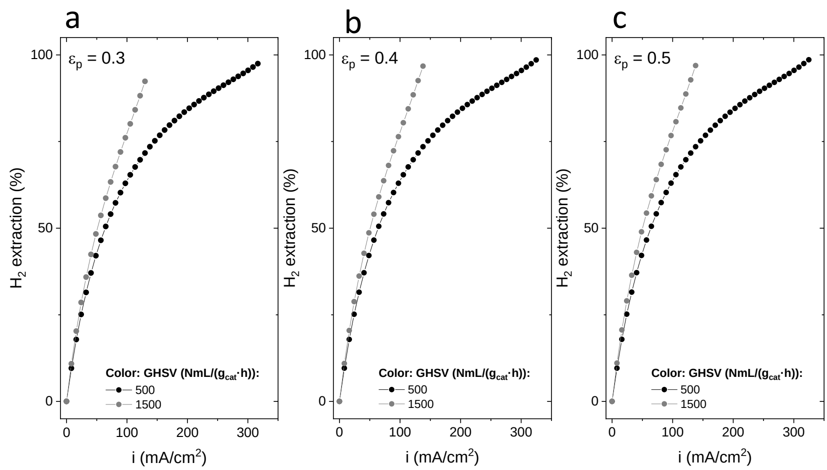

Figure 10.19. Effect of the influence of the porous matrix: hydrogen removed depending on current density applied for different space velocities for porosities of 0.3 (a), 0.4 (b) and 0.5 (c).

10.3.7. Influence of the ethylene formation kinetics

As previously was determined, the kinetics of the ethylene formation reaction is the rate dominant step of the process kinetics. Therefore, potential catalyst developments could enhance the kinetics of this reaction and improve the process conversion. Figure 10.20 shows a sensitivity study in which the fitted value of the kinetic parameter is multiplied by an enhancement factor. The results show that the kinetics enhancement causes a remarkable equilibrium shifting and increase of methane conversion, especially at higher hydrogen extraction. Above an enhancement factor of 5, methane conversion overcomes 50% (Figure 10.20a) and benzene yield is improved correspondingly (Figure 10.20b).

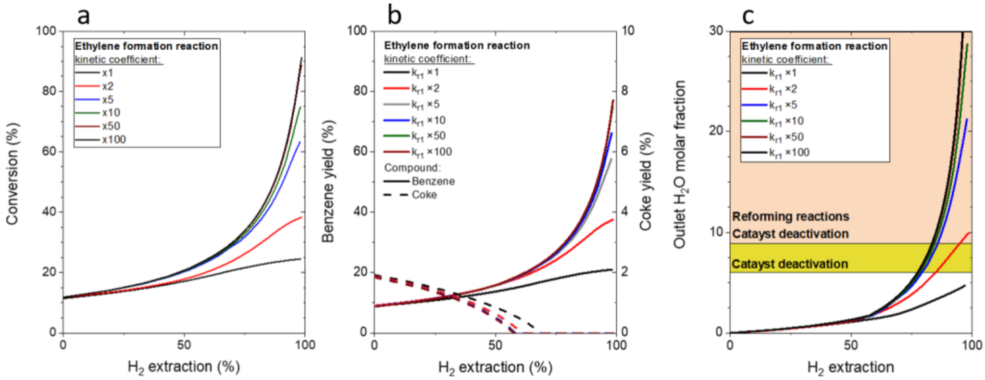

Figure 10.20. Effect of enhancing the kinetics of the ethylene formation reaction (r1) at space velocity of 1500 NmL/(h·g$_{cat}$): (a) methane conversion depending on the hydrogen extraction; (b) benzene and coke selectivity depending the hydrogen extraction; (c) average steam molar fraction in the outlet

Figure 10.21 shows the fraction of hydrogen extracted as a function of the current density for different enhancements factors of the kinetic parameter.

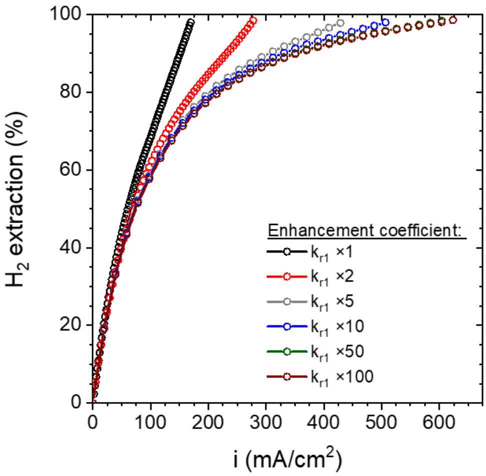

Figure 10.21. Effect of enhancing the kinetics of the ethylene formation reaction at space velocity of 1500 NmL/(h·g$_{cat}$): H_2 extraction depending on the current density.

Reaching higher methane conversion implies an increase of the hydrogen generated and therefore, higher amounts of oxygen are injected because of the hydrogen extraction for the co-ionic conducting membranes. For the fitted value of the kinetic parameter, the full coke suppression is achieved around 70% of hydrogen extraction, while for an enhancement factor of 5, full coke suppression is achieved around 60% of hydrogen extraction. However, it should be taken into account possible negative effects caused by the steam generated that accumulates along in the reaction chamber. Figure 10.19c shows the average steam molar fraction in the outlet as a function of the hydrogen extraction. The results show how high hydrogen extraction ratio causes significant steam concentration in the catalyst bed. Thus, considering the works of the steam influence on this kind of catalyst [22-24], this steam will cause catalyst deactivation or, even if this degradation would not take place, the reforming reactions will cause significant degradation not only for methane, but also for the rest of the hydrocarbon compounds [25]. Therefore, in order to avoid high steam concentrations in the reaction chamber, the oxygen injection through the electrolyte must be carefully controlled (Figure 10.2b).

10.4. Summary

A Multiphysics model was built to study the performance of a novel membrane catalyst reactor for the catalytic dehydroaromatization of methane. Once the kinetic parameters were fitted by using experimental results, the model enabled to describe accurately the catalytic behavior of the reactor setup.

A reference case using experimental conditions tested in the laboratory setup was used as a starting point for the different parametric studies. The analysis of the spatial distribution of the reactions for the reference case determined that the ethylene formation reaction gradually advances in the first zone of the reactor and it further does not significantly progresses. Benzene formation reaction showed similar profile except for the zones very close to the inlet. Further studies confirmed that the ethylene formation is the rate determining step of the process for all operation conditions studied. Naphthalene formation from benzene was not significant. Coke evolution (coke formation and coke suppression reactions) was not affected by the hydrogen removal as it is not an equilibrium-controlled reaction.

Hydrogen extraction was the most relevant factor to improve methane conversion and consequently benzene yield. In general, the diffusional limitations were not important and high extracted-to-produced ratios of hydrogen could be obtained. Lower space velocities gave rise to higher extraction ratios of hydrogen and consequently higher values of benzene yield.

The parametric studies determined the conditions leading to important polarization of hydrogen transport. Above a critical inlet feed velocity or below a critical reactor length, the maximum hydrogen extraction ratio starts to decrease for all space velocities. If the catalytic bed width is increased, the decrease of the ratio is gradual. For typical porosity ranges there was not observed significant effects. For all parametric studies, benzene yield was more sensible to hydrogen extraction.

Coke suppression is directly related to hydrogen extraction because of the steam formation thanks to the injection of oxygen ions through the co-ionic conducting membrane. The simulation results are useful to detect areas where steam concentration is not high enough to reach suitable coke suppression or concentrations that could deactivate the catalyst or promote reforming reactions. The mapping of coke suppression showed low activity in areas near to the reactor entrance that could be avoided with additional steam co-feeding. Besides, benzene yield could be significantly improved by the development of new catalysts that enhance the kinetics of the ethylene formation reaction. However, the higher hydrogen extraction implies higher steam concentration that could cause catalyst degradation or reforming reactions.

Therefore, the simulation model performed could be used to test geometries and conditions to obtain suitable steam distribution in the bed and to maximize hydrogen extraction. In order to use this model to optimize an industrial scale reactor future development like the inclusion of temperature gradients and implement of the detailed electrochemical model of the cell**.**

List of symbols

Factor	Description	Factor	Description
BZCY72	$BaZr_{0.7}Ce_{0.2}Y_{0.1}O_3$	***NmL***	Normal gas volume expressed in *mL*
CS	Coke suppression (*%*)	***p***	pressure (*Pa*)
DC	Direct electric current	p_i	partial pressure of the i compound (*Pa*)
$Deff_{i,j}$	Corrected diffusivity in the porous domain (m^2/s)	Q_{br}	source term for the mass balance ($kg/m^3/s$)
$D_{i,k}$	Maxwell-Stefan diffusivity (m^2/s)	***Rg***	Constant of the ideal gases (8.314 *J/mol/K*)
D_i^m	Average diffusion coefficient for the i compound (m^2/s)	r_i	reaction rate i (*mol/kg/s*)

Factor	Description	Factor	Description
d_p	average of particle size in the porous domain (m)	T	Temperature (*K*)
e_i	error (%)	u	gas velocity (*m/s*)
F	Faraday constant (96485 *C/mol*)	v_i	molecular volume for the i compound
$F_{i,b}$	Molar flow of the i compound in the b boundary (*mol/s*)	w_i	weight fraction for the i compound
GHSV	Gas hourly space velocity ($NmL/(h \cdot g_{cat})$)	XCH_4	methane conversion *(%)*
HR	Hydrogen removed (%)	x_i	molar fraction of the i specie
i	current density (A/m^2)	Y_i	Yield of the i compound *(%)*
i_{O2-}	current density of the oxygen ions (A/m^2)	z	electron exchanged
Itot	Total electric current applied (*A*)	β_F	isothermal compressiility coefficient
J_i	Boundary flux of the i specie ($kg/s/m^2$)	β_i	equilibrium ration of the i specie (%)
j_i	weight flux for i ($kg/m^2/s$).	ϵ_p	porosity (%)
kd	diffusion coefficient ($m^2 \cdot Pa/s$)	κ	permeability of the porous domain (m^2)
K_i	Adsorption constant for the i compound (*Pa*)	μ	viscosity (*kg/m/s*)
Kp_i	Pressure equilibrium constant for the reaction Ri (units depending on the reaction)	$\mu_{g,i}$	gas viscosity of the component i (*kg/m/s*)
k_{ri}	kinetic coefficient of the reaction r_i (units depending on the reaction)	ρ	gas density (kg/m^3)
MDA	Methane DehydroAromatization	ρ_{cat}	catalyst concentration in the porous domain (kg/m^3)
M_i	Molecular weight of the i compound (*g/mol*)	τ_p	tortousity of the porous domain
M_n	Mean of the molecular weight of the gas mixture (*g/mol*)	$\varphi_{i,j}$	wilke number for the couple of i and j components
nC_i	Carbon number of the i compound	ψ	Correction of the kinetics for the adsorption phenomena
N_i	weight flow for i ($kg/m^2/s$).	τ_p	Tortuosity

10.5. References

1. Menon, V. and M. Rao, Progress in Energy and Combustion Science, 2012. **38**(4): p. 522-50.
2. Zhang, L., et al., Energy Conversion and Management, 2010. **51**(5): p. 969-82.
3. Anex, R.P., et al., Fuel, 2010. **89**(Supplement 1): p. S29-S35.

4. Majhi, S., et al., Journal of Energy Chemistry, 2013. **22**(4): p. 543-54.

5. Karakaya, C. and R.J. Kee, Progress in Energy and Combustion Science, 2016. **55**: p. 60-97.

6. Spivey, J.J. and G. Hutchings, Chemical Society Reviews, 2014. **43**(3): p. 792-803.

7. Schwach, P., et al., Chemical Reviews, 2017. **117**(13): p. 8497-520.

8. Ismagilov, Z.R., et al., Energy & Environmental Science, 2008. **1**(5): p. 526-41.

9. Ma, S., et al., Journal of Energy Chemistry, 2013. **22**(1): p. 1-20.

10. Karakaya, C., et al., Industrial & Engineering Chemistry Research, 2016. **55**(37): p. 9895-906.

11. Natesakhawat, S., et al., Catalysis Science & Technology, 2015. **5**(11): p. 5023-36.

12. Xue, J., et al., ACS Catalysis, 2016. **6**(4): p. 2448-51.

13. Kinage, A.K., et al., Catalysis Letters, 2003. **88**(3): p. 199-202.

14. Rival, O., et al., Industrial & Engineering Chemistry Research, 2001. **40**(10): p. 2212-9.

15. Larachi, F., et al., Catalysis Letters, 2002. **84**(3): p. 183-92.

16. Iliuta, M.C., et al., Industrial & Engineering Chemistry Research, 2003. **42**(2): p. 323-30.

17. Liu, Z., et al., Catalysis Letters, 2002. **82**(3): p. 175-80.

18. Sakbodin, M., et al., Angewandte Chemie International Edition, 2016. **55**(52): p. 16149-52.

19. Caro, J., Chemie Ingenieur Technik, 2014. **86**(11): p. 1901-5.

20. Cao, Z.W., et al., Angew. Chem.-Int. Edit., 2013. **52**(51): p. 13794-7.

21. Kosinov, N., et al., Angewandte Chemie International Edition, 2016. **55**(48): p. 15086-90.

22. Liu, S., et al., Journal of Catalysis, 2003. **220**(1): p. 57-65.

23. Ma, H., et al., Catalysis Letters, 2005. **104**(1): p. 63-6.
24. Skutil, K. and M. Taniewski, Fuel Processing Technology, 2006. **87**(6): p. 511-21.
25. Bijani, P.M., et al., Chem. Eng. Technol., 2012. **35**(10): p. 1825-32.
26. Karakaya, C., et al., Chemical Engineering Science, 2015. **123**: p. 474-86.
27. Zeppieri, M., et al., Applied Catalysis A: General, 2010. **387**(1): p. 147-54.
28. Gao, K., et al., Chem. Ing. Tech., 2016. **88**(1-2): p. 168 - 76.
29. Corredor, E.C., et al., Fuel, 2016. **179**: p. 202-9.
30. Kee, B., et al., Industrial & Engineering Chemistry Research, 2017. **56**(13): p. 3551-9.
31. Morejudo, S.H., et al., Science, 2016. **353**(6299): p. 563-6.
32. Bruce E. Poling, J.M.P., John O' Connell, *The properties of gases and liquids. 5th edition.* 2000, New York, Chicago, San Francisco, Athens, London, Madrid, Mexico City, Milan, New Delhi, Singapore, Sydney, Toronto: McGraw-Hill Education.
33. Donald A. Nield, A.B., *Convection in Porous Media. Third Edition*. 2006, United States of America: Springer.
34. Matyka, M., et al., Physical Review E, 2008. **78**(2): p. 026306.
35. Pisani, L., Transport in Porous Media, 2011. **88**(2): p. 193-203.
36. Krishna, J.A.W.a.R., *Mass Transfer in Multicomponent Mixer*. 2000, Delft University Press.
37. Yao, B.Z., et al., J. Nat. Gas Chem., 2008. **17**(1): p. 64-8.

11. GENERAL REMARKS AND CONCLUSION

11. General conclusions

This thesis presents results of two differentiated parts: (i) experimental work focus in the development of electrodes for tubular electrochemical cells based on copper and (ii) simulation work based on CFD models. Therefore, separated conclusions were presented considering the experimental conclusions (E) and the modelling conclusions (M).

The main conclusions of the development of layers based on copper for tubular electrochemical cells are:

- Dip-coating technique to deposit the electrode

E_1: Dip-coating methodology presents high reproducibility while the sintering temperature is identified as the most critical parameter of the process.

E_2: Copper based cermet electrodes deposited on tubular cells by dip-coating present suitable and stable polarization resistance under moist conditions when the sintering temperature was between 1000 and 1025°C.

- Sputtering technique to deposit the electrode

E_3: Sputtering of copper electrodes requires high temperatures during the depositions to achieve suitable attachments to the electrolyte. Otherwise the copper layer is delaminated after the deposition.

E_4: Copper sputtered layers deposited at high temperatures present excellent and stable polarization resistances (around 0.1 $\Omega \cdot cm^2$) in moist conditions at 700°C in H_2 based atmospheres.

The development of the CFD models have revealed the next main conclusions:

- Oxygen permeation in MIEC membranes

M$_1$: although the fitting of a model is complex using a 3D Multiphysics approach, it allows including the possible effects of the concentration polarization on the permeation model. This phenomenon is usually neglected for the conventional modelling of this process (using 0D and 1D models).

M$_2$: higher membrane thicknesses are necessary (> 1mm) for that the bulk contribution resistance would be comparable to the surface resistances. It leads to the oxygen permeation could improve more efficiently using more effective surface area than using thinner membranes (e.g. using porous domains)

M$_3$: concentration polarization causes significant differences between the oxygen partial pressures in the chamber and in the surface contact of the membrane. The polarization of the permeated oxygen could be avoided using high flow of the sweep gas and, specially, using heavier gas compositions. Using heavier gases improves the force of the gas flow to sweep the oxygen permeated.

- Electrolysis based on protonic ceramics at high temperature

M$_4$: the temperature of the electrolyser depends on the heat from the Joule effect. Therefore, the control of the heat management of a electrolysis setup is based on the cell potential.

M$_5$: Upscaling electrolyser based on protonic ceramics are strongly affected by the relation potential – temperature. The configuration of the setup has to be carefully selected to avoid heterogeneous electrical current distribution along the different cells (considering multicell setup). Neglecting this concept leads the process to gather current in the favored cells that implies higher cell potentials and, finally, higher temperatures. This is not only inefficient, but it could lead to problems in the setup if the local temperatures reach material melting point. Thermoneutral potential could help to control the temperature of the electrolyser in the desired value.

M_6: The hydrogen could be obtained at high pressure. The increase of the hydrogen pressures causes an increase of the potential which could be partially mitigated increasing the pressure in the steam chamber. Furthermore, the efficiency of the process is controlled by the faradaic efficiency, the overpotentials and the steam conversion. The experimental results show that the process is more efficient working at potentials equal or lower than the thermoneutral potential as, in this regime, the faradaic efficiency is high and the overpotentials are low. Finally, a high steam conversion prevents the waste of the evaporation energy.

- Protonic membrane reformer

M_7: There is no H_2 diffusion limitations. However, the diffusion of CO could limit the shifting of the WGS reaction if the gas flow is high.

M_8: Microthermal integration of the heats of the process could be achieved at 800°C since the operation regime (methane flow and applied current) is adjusted. This microthermal integration allows the process to work thermally balanced and autonomously. For this microthermal integration the most important parameters are the magnitude of the cell resistance while cell support porosity is less important.

M_9: the pressure of the separated H_2 could be increased while the process could absorb the released heat.

- Methane dehydroaromatization by catalytic membrane reactor based on co-ionic ceramics.

M_{10}: there is no hydrogen diffusion limitations in these conditions for this process. However, the reactor dimensions have to be suitably selected during the design to avoid the hydrogen extraction is not limited by gas diffusion. Furthermore, the feeding of the inlet gas could limit the hydrogen extraction as the gas velocity increases the sweep of the hydrogen, stopping its diffusion until the electrode.

M_{11}: the shifting of the equilibrium-controlled reactions by the H_2 extraction is limited by the kinetic activity of the ethylene formation reaction. The coke suppression is achieved (completely or partially) by the oxygen injection because the co-ionic conductivity of the electrochemical cell. However, this oxygen injection has to be carefully controlled (e.g. by the steam presence in the non-reactive chamber) to avoid undesired reforming reactions or catalyst deactivation.

12. Acronyms

Id	Description
AC	Alternating Current
AFC	Alkaline Fuel Cell
BZCY	BaZrxCeyY1-x-yO3
CFD	Computational Fluid Dynamics
COMSOL	Comsol Multiphysics software
DC	Direct current
DMFC	Direct Methanol Fuel Cell
e-	electron
EDS	Energy Dispersive X-ray spectroscopy
EDTA	Ethylenediaminetetraacetic acid
EG	Ethylene glycol
EIS	Electrochemical Impedance Spectroscopy
FESEM	Field emission scanning electron microscope
h·	hole in the lattice
ICP	Inductively Coupled Plasma Optical Emission Spectroscopy
MIEC	mixed ionic and electronic conductivity
OC-SOFC	Oxygen ion conducting SOFC
OH·o	proton localized on the oxygen ion
Oox	oxygen ion in the oxygen ion lattice site
OTM	Oxygen Transport Membranes
P2h	Power to hydrogen

Id	Description
PAFC	Phosphoric Acid Fuel Cell
PC-SOFC	Protonic SOFC
PEMFC	Polymer Electrolyte Membrane Fuel Cell
PSA	Pressure Swing Adsortion process
PVP	Polyvinylpyrrolidone
SEM	scanning electron microscope
SMR	Steam Methane Reforming
SOEC	Solid Oxide Electrolyser Cell
SOFC	Solid Oxide Fuel Cell
SSR	Solid State Reaction
TEC	Themal Expansion Coefficient
TPB	Triple Phase Boundary
VÖ	Oxygen vacancy
WGS	Water Gas Shift reaction
XRD	X-ray diffraction technique
YSZ	Ytrium-Stabilized Zircona

13. Figure list

Figure 1.1*: Worldwide energy outlook and perspectives. (a) primary energy consumption by fuel (toe: tonne of oil equivalent); (b) shares for equivalent energy. * Renewables includes wind, solar, geothermal, biomass and biofuels [1]*..........11

Figure 3.1*. Publications about membrane reactors [1].* 29

Figure 3.2*: membrane reactor principle. (a) Shifting the chemical equilibrium removing products of the reaction chamber; (b) Shifting the chemical equilibrium injecting reactive of the reaction chamber.* 30

Figure 3.3*. Summary of processes where oxygen- and hydrogen-permeable membranes for membrane reactors at high temperatures. Figure from [41].* 34

Figure 3.4*. Electrochemical cells: generical discharge electrochemical curve.*..........35

Figure 3.5*. Electrochemical cells: view of general assembly considering cationic conducting based cell or anionic conducting based cell.* 36

Figure 3.6*. Ilustration of the different defects in a plane of the crystal structure.* 39

Figure 3.7*. Examples of combination of defects to keep the electroneutrality. (a) Schottky disorder; (b) Frenkel disorder; (c) Anti-site disorder.*..........40

Figure 3.8*. Electric conductivity for different materials according their energy bands* 41

Figure 3.9*. Semiconductors type n (a-b) and type p (c-d). (a) Two-dimensional representation and (b) corresponding energy bands for n-doped Si with As. (c) Two-dimensional representation and (d) corresponding energy bands for p-doped Si with Ga. CB: conduction band; E_C: lower energy level of the conduction band; E_D: energy level of the donor atoms; E_V: upper*

energy level of the valence band; E_A: energy level of the acceptor atoms. Image extracted from [46]..........42
Figure 3.10. *Fluorite crystal structure, AB_2, where the orange balls are tetravalent cations while green balls are the anions (in this case, O^{2-}). Image extracted from [48]. 43*
Figure 3.11. *Perovskite crystal structure, ABO_3. Green ball is the A large cation centered in the crystal cell; grey balls represent the B cations and the red balls are the O^{2-}. Image extracted from [48]. 44*
Figure 3.12. *Oxygen ion conductivity as function of the reciprocal temperature. LAMOX: $La_2Mo_2O_9$. [40]..........45*
Figure 3.13. *Grotthus type proton mechanism. Traces of the oxygen atoms of two octahedra where the protonic motion generates the ring -like object around the oxygen atom in the center and it diffuses to another oxygen position. Image obtained from [60] and mechanism discussed in [61]..........46*
Figure 3.14. *Summary of the protonic conductivity of different materials [60]..........49*
Figure 3.15. *Mechanism of oxygen permeation through an MIEC membrane [66]..........51*
Figure 3.16. *Crystal structure of the oxygen permeation materials based on mixed ion and electronic materials. (a) pyrochlore ($A_2B_2O_7$)) (obtained from [48]); (b) brownmillerite ($A_2B_2O_5$) (obtained from [71]); (c) K_2NiF_4 (obtained from [48]); (d) Ruddlesden-popper (obtained from [48])..........52*
Figure 3.17. *Schematic picture of dual-phase membranes. Image extracted from [83] 53*
Figure 3.18. *Methodology to use finite elements. Image extracted from [149]. 64*
Figure 3.19: *Main results of CFD model of cyclohexane dehydrogenation in a hydrogen membrane reactor. [151]. 65*
Figure 4.1. *Sol-gel method for pure multicomponent formation..........80*
Figure 4.2. *Solid State Reaction procedure. 82*

Figure 4.3. *Co-precipitation methodology.*..83

Figure 4.4. *Dip-coating methodology.*..85

Figure 4.5. *Sputtering technique. (a) Setup view; (b) detailed view of the sputter deposition on flat supports.* 86

Figure 4.6. *Sputtering setup for tubular supports. (a) View of the rotating technique to deposit the layer by sputtering; (b) View of the resistance for the heating and the themocouple on the sputtering assembly to deposit copper on tubular supports.* 87

Figure 4.7. *Screen-printing technique methodology.*..................................88

Figure 4.8. *Schematic diagram of diffraction of X-rays by a crystal (Bragg condition). Image obtained from [12].*..89

Figure 4.9. *X-ray diffraction setup: from diffractometer until crystal structure.* 90

Figure 4.10. *SEM device description. Image from [13].* 93

Figure 4.11. *Impedance spectroscopy applied to an electrochemical setup. (a) Description of the general response of the system; (b) Nyquist plot of the impedance; (c) Bode plots for the real contribution of the impedance (Z') and the imaginary contribution of the impedance (Z'').* 99

Figure 4.12. *Connection of the Solartron modules with the sample.*..........100

Figure 4.13. *Diagram of the experimental setup to make electrochemical impedance spectroscopy tests.*..101

Figure 5.1. *XDR patterns of coprecipitated CuO at different temperatures.* 108

Figure 5.2. *(a) CuO from coprecipitation with NaOH solutions > 2 M; (b) CuO from coprecipitation with NaOH solutions 2 M*.................................109

Figure 5.3. *CuO sintered at 600 °C (a), 700 °C (b) and 800 °C (c).*..........109

Figure 5.4. *XDR patterns of BZCY72 single phase. Black: SSR sintering at 1550ºC 15h; gray: SSR sintering at 1600ºC 10h; black patterns: BCZY27 patterns.*...110

Figure 5.5. *XDR patterns of the different sintered phases. BZCY72: sintering at 1550 °C; CuO: sintering at 550 °C; BZCY-CuO: mixture before the sintering; BZCY-CuO final: sintering at 1000 °C 2 hours.* 111

Figure 5.6. *XDR patterns of the different sintered phases. BZCY72: sintering at 1550 °C; CuO: sintering at 550 °C; BZCY-CuO: mixture before the sintering; BZCY-CuO final: sintering at 1050 °C 5h. #: $BaCeO_3$ peaks.* 112

Figure 5.7. *Size particle distribution of the sintered phases (CuO and final sintering cermet) with the SEM images. Each size distribution is shown using boxplots. Images was acquired at 25 kV* 113

Figure 5.8. *FESEM micrograph of cermet CuO/Cu– BZCY27: (a) as sintered electrode at 1000 °C in air (Image acquired at 5.00 kV); (b) as-sintered electrode at 1000 °C in air (Image acquired at 20.00 kV); (c) as-sintered electrode at 1000 °C in air (Image acquired at 3.00 kV); (b) reduced electrode at 700 °C in H_2 (Image acquired at 3.00 kV).* 114

Figure 5.9. *Reduced cermet on tubes using different BZCY initial particle sizes. Sintering at 1000ºC 2h and reduced at 700ºC in H_2. BZCY initial particle sizes: (a) 250-400 nm; (b) 425-700nm; (c) 500-900 nm.* 115

Figure 5.10. *Sintering cermet on tubes sintering at 1000ºC with different times. (a) 1h; (b) 2h; (c) 4h.* 115

Figure 5.11. *Reduced cermet on asymmetric initially unreduced tubes. Tubes were dipped once on slurry with ethylcellulose, sintered 1 h and reduced at 700 °C in H_2. (a) cermet sintered at temperatures < 1000 °C; (b) cermet sintered at temperatures > 1000 °C. (c) zoom view cermet sintered at temperatures < 1000 °C; (d) zoom view of the cermet sintered at temperatures >1000 °C.* 116

Figure 5.12. *Copper oxide phase diagram [19]* 117

Figure 5.13: *(a) Cross-section SEM image of reduced cermet on asymmetric tube initially unreduced. Sintered at 1015 °C 1h. (b–d) EDS analysis (Ba represents the BZCY).* 119

Figure 5.14. *Polarization resistances at 700 °C under different conditions for copper-based cermets deposited on asymmetric initially unreduced tubes with copper electrodes sintered at temperatures < 1000 °C (a-b) and > 1000 °C (c-d). The polarization resistances distribution for each sample was plotted using boxplots.*..120

Figure 5.15. *Cross section SEM images for reduced cermets on asymmetric tubes initially unreduced. The sintering step was developed at 1000 – 1025 °C 1h. (a) tube dipped once on slurry with ethylcellulose; (b) tube dipped three times on free-ethylcellulose slurry.*..121

Figure 5.16. *Images of the tube in the different steps across the dip-coating methodology. (a) clean asymmetric initially unreduced tube; (b) dipped tube; (c) sintered tube; (d) reduced tube).*..122

Figure 5.17. *Impedance spectroscopy results at 700 °C under different atmospheres. Sample dipped three times on free-ethylcellulose slurry on an asymmetric initially unreduced tube. The electrode was sintered at 1015 °C 1h. (a and c) Ohmic contribution; (b and d) polarization resistances.* 123

Figure 5.18. *Impedance spectroscopy results at 700 °C under different conditions. Sample dipped three times on free-ethylcellulose slurry. The electrode was sintered at 1000 °C 1h. (a) Normalized Nyquist plot; (b) view of the sample; (c) Imaginary bode plot.* 124

Figure 5.19. *Impedance spectroscopy results at 700 °C under different conditions. Sample dipped three times on free-ethylcellulose slurry. The electrode was sintered at 1000 °C 1h. (a) Dry H_2-Ar mixtures at 700 °C. (b) Wet H_2-CH_4 mixtures at 700 °C.* 125

Figure 5.20. *Impedance spectroscopy results at 700 °C under hydrogen in dry conditions. Sample dipped three times on free-ethylcellulose slurry. The electrode was sintered at 1000 °C 1h. (a) Normalized Nyquist plot (b) Bode plot.*..126

Figure 5.21. *Impedance spectroscopy results at 700 °C under different conditions. The electrodes were deposited on asymmetric initially unreduced* *tubes and sintered at 1000°C 1h. (a) Polarization resistances for dry hydrogen at 700 °C; (b) Polarization resistances for wet hydrogen at 700 °C.* 127

***Figure 5.22**. Cross section SEM images for the reduced cermet on asymmetric tube initially unreduced. The tube was dipped twice on slurry with ethylcellusose and sintered at 1000 – 1025 °C 1h. (a) Before the accelerating aging test; (d) zoom view of the sample before the aging test; (b) after the accelerating aging test at 750 °C (e) zoom view of the sample after the aging test at 750 °C; (c) after the accelerating aging test at 800 °C, (f) zoom view of the sample after the aging test at 800 °C.*..............................128

***Figure 5.23**. Tube dipped twice on slurry with ethylcellusose and sintered at 1000 °C 1h. (a) Cross-section SEM image of reduced cermet on asymmetric tube initially reduced; (b–d) EDS analysis; (e) Cross section SEM image of the reduced cermet on asymmetric tube initially reduced in the internal electrode – electrolyte interphase; (f – h) EDS analysis of the internal electrode.*...129

***Figure 5.24**. (a) Cross-section SEM image of symmetric Cu-BZCY screen-printed on BZCY disc. (b–c) EDS analysis (Ba represents BZCY). (d) Zoom view of the crack; (e-f) EDS analysis (Ba represents BZCY). Both electrodes were deposited on the disc pellets using screen printing technique. The electrode was sintered at 1000 °C 2h and reduced at 700 °C 2h with* H_2*.*..130

***Figure 6.1**. FESEM images of the copper sputtered electrode at room temperature. (a-b) View of the interphase electrode-tube (image adquisition at 2.00 kV); (c) frontal view of the copper layer (image adquisition at 3.00kV)* 139

***Figure 6.2**. Polarization resistance and electrolyte resistance for impedance spectroscopy test developed on* H_2 *atmospheres at 700 °C.*........................140

***Figure 6.3**. FESEM images of the copper electrode sputtered on tubes at high temperature. (a) View of cross section of the tube; (b-c) Zoom view of the copper electrode. Images adquired at 2.00kV.* 142

Figure 6.4. *EDS analysis of the copper sputtered on a tubular support at high temperature. (a) View of the cross section of external electrode - electrolyte - internal electrode; EDS results about copper (b), Ba (c) and Ni (d). Ba denotes all BCZY phase.*...*142*

Figure 6.5. *Polarization resistance and electrolyte resistance for impedance spectroscopy test developed in* H_2 *atmospheres at 700 °C.*.........................*143*

Figure 6.6. *Stability of the specific resistance contributions of the impedance spectroscopy test developed in* H_2 *atmospheres at 700 °C.*.........................*144*

Figure 6.7. *Impedance spectroscopy test with hydrogen atmospheres at 700 °C. (a-c) Nyquist plots*...*145*

Figure 6.8. *Impedance spectroscopy test with hydrogen atmospheres at 700 °C. (a) Bode plot of the imaginary contribution; (b) zoom of the Bode plot of the imaginary contribution.*..*146*

Figure 6.9. *Images of the tube: (a) after sputtering of Cu at high temperature; (b) after impedance spectroscopy test at 700 °C.* *147*

Figure 7.1. *Experimental set-up. (a) View of the general set-up; (b) adaptation of the geometry to 2D axial symmetry*......................................*158*

Figure 7.2. *Scheme of the oxygen chemical potential gradient for the oxygen permeation process through the MIEC membrane*.....................................*159*

Figure 7.3. *Mesh of the geometry* *164*

Figure 7.4. *Overall fitting procedure of the model parameters*.................*166*

Figure 7.5. *Fitting results (a) diffusion coefficient of oxygen vacancies (b) Pre-exponential factors for surface resistances.* *172*

Figure 7.6. *Comparison of experimental results (points) and model simulations using the fitted parameters (full lines) for oxygen flux at different temperatures (a) Effect of the oxygen partial pressure of the feed inlet; (b) Effect of the oxygen partial pressure of the sweep gas inlet (feed inlet conditions: air, 300* mL_{STP}*/min; sweep inlet conditions: argon, 300*mL_{STP}*/min, membrane thickness: 1mm).* *173*

Figure 7.7. *Effect of thickness on the average oxygen flux (Feed inlet conditions: air, 300mL$_{STP}$/min; sweep inlet conditions: argon ($2\cdot10^{-5}$ bar O_2), 300mL$_{STP}$/min).* *174*

Figure 7.8. *Contribution of the different resistances to the total resistance to oxygen permeation (a) 700 °C, (b) 850 °C, (c) 1000 °C. Feed inlet flow 300mL$_{STP}$/min, feed inlet: air, sweep inlet flow 300mL$_{STP}$/min, sweep inlet: Ar ($2\cdot10^{-5}$ bar O_2)* *175*

Figure 7.9. *Effect of the feed inlet flow on the average oxygen flux for different temperatures. (Feed conditions: air , Sweep inlet conditions : Ar ($2\cdot10^{-5}$ bar O_2) 300 ml$_{STP}$/min, membrane thickness: 0.8mm)*...................... *177*

Figure 7.10. *Effect of the sweep flow on the average oxygen flux, partial pressure over the membrane surface and shear rate. Feed inlet flow: 300mL$_{STP}$/min; feed inlet: air, sweep inlet: Ar ($2\cdot10^{-5}$ bar O_2), membrane thickness: 0.8mm.* *179*

Figure 7.11. *Oxygen partial pressure profile at different sweep inlet flows and 1000 °C. Feed inlet flow: 300mL$_{STP}$/min; feed inlet: air, sweep inlet: Ar ($2\cdot10^{-5}$ bar O_2), membrane thickness: 0.8 mm.* *180*

Figure 7.12. *Oxygen flux. Thickness: 0.8mm, feed inlet: air, sweep inlet: Ar ($2\cdot10^{-5}$ bar O_2). R = Reference case, LP = case with low polarization, HP = case with high polarization* *181*

Figure 7.13. *Apparent activation energies at LT (low temperature, <800 °C) and at HT (high temperature, >800 °C). Feed inlet: air, sweep inlet: Ar ($2\cdot10^{-5}$ bar O_2).* *182*

Figure 7.14. *Apparent driving force. Thickness: 0.8mm; feed inlet flow: 50 – 500 mL$_{STP}$/min; feed inlet: air; sweep inlet flow: 50 – 500 mL$_{STP}$/min; sweep inlet: Ar ($2\cdot10^{-5}$ bar)* *183*

Figure 7.15. *Oxygen pressure profile for the high polarization case (a) and the low polarization case (b) at 1000ºC. Streamlines: speed pathways.* *184*

Figure 7.16. *(a) Oxygen flux for different sweep gases (reference case) (b) shear rate in the sweep – membrane surface using different sweep gases (different sweep gas flow at reference conditions)* 186

Figure 7.17*. Activation energy at LT (low temperature, T < 800 °C) and at HT (high temperature, T > 800 °C)*...186

Figure 7.18*. Evaluation of the fluid dynamic effect in the oxygen permeation using correlations of Sherwood, Reynolds and Schmidt dimensionless numbers.*...188

Figure 7.19*. Vacuum results. (a) Oxygen flux results; (b) oxygen partial pressure in the sweep compartment. Feed inlet flow: 300mL$_{STP}$/min; feed inlet: air; thickness: 0.8mm*..190

Figure 7.20. *contour plots. (a) oxygen partial pressure profile (left bar: pressure profile in the vacuum compartment; middle bar: oxygen partial pressure in the feed compartment; right bar: oxygen equivalent pressure in the membrane; streamlines: speed pathways); (b) speed profile (left bar: oxygen flow profile in the membrane; middle bar: speed profile in the feed compartment; right bar: speed profile in the vacuum compartment; streamlines: speed pathways). Feed inlet flow: 500 mL$_{STP}$/min; feed inlet: air; vacuum pressure: 50 mbar; 1000 °C*..190

Figure 8.1*. Different geometries for this study: (a) expterimental setup (2.9cm electrode length); (b) geometry with 5 segments with 2.9cm electrode length per segment than expeimental setup; (c) geometry with 10 segments with 2.9cm electrode length per segment than expeimental setup; (d) geometry using a external electrode with 29cm electrode length. Meshes (a$_2$, b$_2$, c$_2$, d$_2$); flow directions (a$_3$, b$_3$, c$_3$, d$_3$).* 219

Figure 8.2. *Diagram of the overall electrolysis process for the study of the effect of the pressure of the hydrogen chamber.*...223

Figure 8.3*. Effect of increasing the mesh complexity on specific modelling results (T, V). gl: degrees of freedom of the computational study*...............227

Figure 8.4. *Results of the isothermal model. (a) Molar fractions of the steam (external chamber) and* H_2 *(internal chamber) regarding the current density applied; (b) Cell potential regarding the current density applied at different temperatures...228*

Figure 8.5. *Results of the model in isothermal conditions at 600°C. (a) Gas speed profile in both chambers when the current density is 99* $mA\cdot cm^{-2}$*; (b) zoom of the gas speed profile; (c) Molar fraction profiles of* H_2O *and* H_2 *when the current density is 99* $mA\cdot cm^{-2}$*; (d) Molar fraction profiles of* H_2O *and* H_2 *when the current density is 197* $mA\cdot cm^{-2}$*..229*

Figure 8.6. *Profiles of the current density distribution at 600°C when the cell works isothermally with 99* $mA\cdot cm^{-2}$*...230*

Figure 8.7. *Results of the isothermal model: potential profile when the cell works isothermally at 600°C and 99* $mA\cdot cm^{-2}$*. 231*

Figure 8.8. *Results of the CFD model for the electrolysis working at the thermoneutral voltage. (a) General view of the setup, (b) cross section view of the setup; (c) Temperature profile of the electrolyzer working at the thermoneutral voltage; (d) Molar fractions profile for the steam (external chamber) and hydrogen (internal chamber)..232*

Figure 8.9. *Evaluation of the radiation effect in the temperature distributions for an electrolyser working close to the thermoneutral point. (a) Temperature profile neglecting the radiation heat transference; (b) Temperature profile considering radiation; (c) Temperature distributions along the tube of the electrolysis setup working in the exothermic zone......................................234*

Figure 8.10. *Evaluation of the effect of the different radiation phenomena in the electrolysis temperature distribution...235*

Figure 8.11. *Final comparison of the CFD model. (a) Electrochemical results and average temperature for the CFD model (grey zone: endothermic mode operation, red zone: exothermic mode operation). Temperature profiles of the CFD model neglecting radiation for the endothermic mode (b), thermoneutral (c) and exothermic (d). Temperature profiles for the CFD* *model considering the radiation for the endothermic mode (e), thermoneutral (f) and exothermic zone (g)..237*

***Figure 8.12**. Results of the scaling study increasing the area of the cell working close the thermoneutral point. (a) Geometry of 29 cm of length; (b) Experimental setup (2.9cm); (c) Geometry of 5 segments of 2.9cm per segment; (d) Geometry of 10 segments of 2.9cm per segment....................239*

***Figure 8.13**. View of the different types of electric connection when the total area is switched in several segments; (a) segments connected in series; (b) segments connected in parallel. 240*

***Figure 8.14**. Results of the scaling study about tubular electrolyser. 1 segment: potentials depending the current density (a); ASR and temperature depending current density (d); 5 segments/tube: potentials depending the current density (b); ASR and temperature depending current density (e); 10 segments/tube: potentials depending the current density (c); ASR and temperature depending current density (f). 241*

***Figure 8.15**. Results of the average temperature of the study of the overall electrical resistance with the CFD model considering the radiative heat transference...243*

***Figure 8.16**. Cell potential results depending of the current density applied. Study of the overall electric resistance in the CFD model considering the radiation contribution. 244*

***Figure 8.17.** Thermoneutral and reversible voltages for water electrolysis at 400 – 800 °C with different pressures for the hydrogen chamber and steam chamber. (a) Results at atmospheric pressure for the steam chamber; (b) Results at 10 bar for the steam chamber; (c) Results at 30 bar for the steam chamber...246*

***Figure 8.18**. Electrolysis curves for different hydrogen pressures at 600°C. (a) Considering a fixed overall specific resistance; (b) simulating the improve of the conductivity when the steam partial pressure increases......247*

Figure 8.19. *Effect of the hydrogen pressure on the electrochemical results when the cell works at the thermoneutral voltage at 600°C.........................248*

Figure 8.20. *Effect of the hydrogen pressure in the energy contributions of the electrolysis process and in the steam conversion when the steam conversion is 90% at 1 bar of hydrogen...249*

Figure 8.21. *Efficiency in the stored energy in the hydrogen depending on steam conversion when the cell works at the thermoneutral voltage at 600°C. 251*

Figure 8.22. *Summary of the experimental results at several temperatures. (a) Cell potential regarding the current density applied; (b) Faradic efficiency regarding the current density applied...252*

Figure 8.23. *Results of the energy efficiency of the electrolysis. (a) results at 500°C; (b) results at 600°C; (c) results at 700°C. 253*

Figure 8.24. *Energy efficiency for different temperatures..........................254*

Figure 9.1. *(a) Schematic of the protonic membrane reformer; (b) heat balance achieved with the different phenomena of this process. [20].........266*

Figure 9.2. *View of the PMR setup 269*

Figure 9.3. *description of the process. (a) View of the setup (i: SMR reaction; ii: H_2 pumping; iii: WGS reaction; iv: electrocompression); (b) zoom view of the electrochemical cell; (c) 2D axial symmetry. 271*

Figure 9.4. *Hydrogen transport across the protonic conducting material. 275*

Figure 9.5. *Definition of the boundary conditions in the geometry. 281*

Figure 9.6. *Methodology of the model. Grey lines: isothermal study; Black lines: adiabatic study. HR test: hydrogen recovery test. 800°C test: fitting the temperature distribution along the tube cell around 800°C........................283*

Figure 9.7. *Experimental PMR results at 800°C and S/C = 2.5 and reforming pressure of 10bar. (a) hydrogen production rate depending on the current density; (b) methane conversion and yields depending on the hydrogen extraction (points: experimental results; lines: equilibrium); (c) purity of the hydrogen extracted. [20] 291*

Figure 9.8. *Experimental results about the PMR at 800°C and S/C = 2.5 and reforming pressure of 10bar. (a) Nyquist plot of the impedance spectroscopy in the frequency range of 0.04 – 8000 Hz and with a bias of 0.6 A·cm^{-2}; (b) Discharge curve; (c) Voltage contributions depending the hydrogen pressure considering a current density of 0.5 A·cm^{-2} and keeping the steam concentration in the hydrogen chamber at 4%. [20]..................................293*

Figure 9.9. *Stability experimental results at 800°C, S/C = 2.5 and reforming pressure of 10bar (unless the indicated points). (a) methane conversion and hydrogen extraction; (b) deviation of the overall electrochemical resistance; (c) SEM micrograph of polished cross-section of the Ni-BZCY cell support as-fired and after 2000+ hours of operation. [20].....................................294*

Figure 9.10. *Refining of the mesh. (a) Results of the minimum, mean and maximum temperatures in the tube cell and methane conversion; (b) initial mesh; (c) zoom of the initial mesh; (d) final mesh; (e) zoom of the final mesh. Inlet gas flow and composition as reference conditions, inlet at 765°C, hydrogen chamber pressure 10 bar and current density at 0.36 A/cm^2. .....295*

Figure 9.11. *Isothermal results of the Comsol model at 800°C. (a) Kinetic results when the hydrogen extraction increases; (b) Current density applied depending on the hydrogen extraction reached; (c) Comparison of the maximum hydrogen extractions when the total inlet flow is increased. Reference conditions (less the total inlets flow). 297*

Figure 9.12. *Results of the kinetics in isothermal conditions at 800°C. (a) View of the cross section plane on the geometry; methane conversion profiles for non hydrogen extraction (b$_1$) HR = 0.63 (b$_2$) and HR ~ 1 (b$_3$); CO$_2$ yield profiles for non hydrogen extraction (c$_1$) HR = 0.63 (c$_2$) and HR ~ 1 (c$_3$). Reference conditions. 299*

Figure 9.13. *Results in isothermal conditions at 800°C for maximum hydrogen extraction with the reference conditions. (a) general view of the assembly with the crossection plane; (b) speed profile for the maximum* *hydrogen recovery; (c) zoom of the speed profile; (d) SMR reaction rate profile; (e) WGS reaction rate profile.* *301*

***Figure 9.14**. Isothermal study of the porous domain depending on the porosity and the particle size. (a) Ratio between maximum current applied and the maximum theoretical current; (b) hydrogen recovery and* CO_2 *yield.* *303*

***Figure 9.15**. Isothermal study at 800°C with the reference conditions of the kinetic coefficient of the SMR reaction. Methane conversion profiles for* $a_{SMR} = 1$ *(*a_1*),* $a_{SMR} = 0.01$ *(*a_2*),* $a_{SMR} = 10^{-4}$ *(*a_3*);* CO_2 *yield profiles for* $a_{SMR} = 1$ *(*b_1*),* $a_{SMR} = 0.01$ *(*b_2*),* $a_{SMR} = 10^{-4}$ *(*b_3*).* $kSMR = aSMR \cdot k0, SMR \cdot exp - EaSMRRT$ *304*

***Figure 9.16**. Isothermal study at 800°C with reference conditions of kinetics of the WGS reaction.* CO_2 *yield and ratio current/[maximum theoretical current] for the maximum hydrogen recovery reached depending of the WGS kinetic coefficient.* $kWGS = aWGS \cdot k0, WGS \cdot exp - EaWGSRT$ *305*

***Figure 9.17**. Isothermal study at 800°C with the reference conditions of the kinetics of the WGS reaction.* CO_2 *yield profiles for* $a_{WGS} > 0.005$ *(*a_1 *and* a_2*),* $a_{WGS} = 0.001$ *(*b_1 *and* b_2*),* $a_{WGS} = 0.0005$ *(*c_1 *and* c_2*).* a_2*,* b_2 *and* c_2 *are the respective zoom view of the images* a_1*,* b_1 *and* c_1*, respectively.* $kWGS = aWGS \cdot k0, WGS \cdot exp - EaWGSRT$ *306*

***Figure 9.18**. Results in adiabatic conditions for the reference conditions for the maximum hydrogen extraction. Inlet temperature 730°C and current density 428* $mA \cdot cm^{-2}$*. (a) Temperature around cell; (b) methane conversion; (c)* CO_2 *yield.* *309*

***Figure 9.19**. Temperature profiles. Inlet flow of 10 NmL/min of methane and a pressure in the* H_2 *chamber of 10 bar (a) and 20 bar (b); Inlet flow of 15 NmL/min of methane and a pressure in the* H_2 *chamber of 10 bar (c) and 20 bar (d); Inlet flow of 20 NmL/min of methane and a pressure in the* H_2 *chamber of 10 bar (e) and 20 bar (f)* *310*

Figure 9.20*. Results in adiabatic conditions. (a) Inlet temperature to obtain setup temperatures around 800°C depending on the pressure of the hydrogen chamber for different total inlet flows (expressed with methane inlet flow). (b) Temperature gradients depending on the total inlet flow (expressed considering the methane inlet flow). The current densities where 213, 317 and 428* $mA\cdot cm^{-2}$ *for the inlet flows of 10, 15 and 20 NmL/min of methane, respectively.*..312

Figure 9.21*. Temperature profiles when the radiation contribution is neglected and the hydrogen chamber pressure is 10 bar (a) and 20 bar (c). Temperature profiles when the radiation contribution is considered when the hydrogen chamber pressure is 10 bar (b) and 20 bar (d).* 314

Figure 9.22*. Evaluation of adiabatic results neglecting (a) and considering radiation (b) over the temperature distributions along the tube.* 315

Figure 9.23*. Evaluation of the coarsening on the heat transference. Temperature profiles considering a particle size for the internal porous domain of 10 µm and porosities of 0.25 (a), 0.2 (b) and 0.15 (c). Temperature profiles considering a particle size for the internal porous domain of 20 µm and porosities of 0.25 (d), 0.2 (e) and 0.15 (f).*..317

Figure 9.24*. Evaluation of the effects of the kinetics of the SMR reaction on the temperature distribution. (a) Bibliography kinetics; (b and c) worsening the bibliography kinetics more than 4 orders of magnitude.* $kMSR = aMSR \cdot kMSR$ 319

Figure 9.25*. Evaluation of the effects of the kinetics of the WGS reaction on the temperature profiles. (a) bibliography kinetics; (b-d) worsening the bibliography kinetics.* $kWGS = aWGS \cdot kWGS$ 320

Figure 9.26*. Evaluation of the overall specific resistance of the electrochemical cell on the heat transference. (a)* $aASR = 0.2$, *(b)* $aASR = 0.4$, *(c)* $aASR = 0.6$, *(d)* $aASR = 0.8$, *(e)* $aASR = 1$. $ASR = aASR \cdot ASR800°C \cdot exp - EaR \cdot 1T - 11073K$..322

Figure 9.27. *Evaluation of the overall specific resistance of the electrochemical cell on the heat transference. (a)* $aASR = 1$*, (b)* $aASR1.25$*, (c)* $aASR == 1.5$*, (d)* $aASR = 1.75$*, (e)* $aASR = 2$*.* $ASR = aASR \cdot ASR800°C \cdot exp - EaR \cdot 1T - 11073K$*..323*

Figure 10.1. *Thermodynamics of the MDA process. (a) Dependence of reaction equilibrium constants on temperature; (b) Methane conversion and selectivity at equilibrium as a function of hydrogen extraction (coke formation not taken into account). 336*

Figure 10.2. *Description of the membrane reactor setup: (a) scheme of setup; (b) reactions in the catalyst bed and transport of species through the co-ionic membrane..339*

Figure 10.3. *Model implementation of the membrane reactor setup: (a) 2D axisymmetric domains and boundaries description (b) meshes used..........340*

Figure 10.4. *meshes of the geometries used for the study of the influence of the length of the catalytic bed and external electrode. (a) length of 1mm; (b) length of 2mm; (c) length of 6mm; length of 10mm....................................345*

Figure 10.5. *meshes of the geometries used for the study of the influence of the length of the catalytic bed and external electrode. (a) catalytic width of 1mm; (b) 21mm; (c) 5 mm; (d) 8 mm; (e) 10mm; (f) 15mm; (g) 20mm.......345*

Figure 10.6. *Comparison between the fitted model predictions and experimental results. 350*

Figure 10.7. *Profiles obtained at reference experimental conditions: (a) reaction rates; (b) equilibrium ratios and hydrogen molar fraction; (c) coke suppression and steam molar fraction..352*

Figure 10.8. *Effect of the applied current on the extraction and generation of* H_2 *for different space velocities: (a) total* H_2 *flow formed via MDA reactions and* H_2 *extraction flow; (b)* H_2 *extraction ratio..353*

Figure 10.9. *Effect of hydrogen extraction on the cumulative yield of the components at inlet reference conditions for different space velocities......354*

Figure 10.10. *Profiles at maximum hydrogen extraction at a space velocity of 500 NmL·h-1·gcat-1. (a) Equilibrium ratio of the reaction R1; (b) equilibrium ratio of the reaction R2; (c) hydrogen molar fraction; (c) steam molar fraction; (d) Coke suppression…………………………………………......356*

Figure 10.11. *Effect of the average feed velocity at maximum hydrogen extraction for the geometry of reference: (a) fraction of hydrogen removed, (b) benzene yield, (c) and coke suppression for different space velocities..358*

Figure 10.12. *Effect of the inlet feed velocity at the maximum hydrogen extractions for several space velocities. Outlet velocity of the gas in the reaction chamber depending on the feed flow (a); H_2 molar flow profiles at space velocities of 500 NmL/(g_{cat}·h) (b); H_2 molar flow profiles at space velocities of 1500 NmL/(g_{cat}·h) (b); 358*

Figure 10.13. *Effect of the inlet feed velocity. Hydrogen extraction ratio depending on current densities applied at 500 mL/(h·gcat) of space velocity (a) and at 1500 mL/(h·gcat) of space velocity (b).......................................359*

Figure 10.14. *Effect of the reactor length at maximum hydrogen extraction ratio for different space velocities: (a) benzene yield (b)maximum hydrogen extraction ratio (c) profiles of hydrogen molar fraction at a space velocity of 500 NmL/(h·g_{cat}) for different reactor lengths 360*

Figure 10.15 *Effect of the width of the catalytic bed at maximum hydrogen extraction for different space velocities: (a) hydrogen extraction, (b) benzene yield, (c) profiles of hydrogen molar fraction at a space velocities of 500 NmL/(h·g_{cat}) and for different widths...361*

Figure 10.16. *Hydrogen extraction ratio depending on the current density applied for different the reactor lengths at 500 NmL/(h·g_{cat}) of space velocity (a); and at 1500 NmL/(h·g_{cat}) of space velocity (b). Last points for each case represent the maximum hydrogen extraction. 362*

Figure 10.17. *Hydrogen extraction ratio depending on the current density applied for different catalytic widths at 500 NmL/(h·g_{cat}) of space velocity* *(a); and at 1500 NmL/(h·g_{cat}) of space velocity (b). Last points for each case represent the maximum hydrogen extraction 362*

Figure 10.18. *Effect of the catalytic bed porosity at maximum hydrogen extraction for different space velocities: (a) hydrogen extraction ratio (b) benzene yield. 363*

Figure 10.19. *Effect of the influence of the porous matrix: hydrogen removed depending on current density applied for different space velocities for porosities of 0.3 (a), 0.4 (b) and 0.5 (c)...364*

Figure 10.20. *Effect of enhancing the kinetics of the ethylene formation reaction (r1) at space velocity of 1500 NmL/(h·g_{cat}): (a) methane conversion depending on the hydrogen extraction; (b) benzene and coke selectivity depending the hydrogen extraction; (c) average steam molar fraction in the outlet...365*

Figure 10.21. *Effect of enhancing the kinetics of the ethylene formation reaction at space velocity of 1500 NmL/(h·g_{cat}): hydrogen extraction ratio depending on the current density applied...365*

14. Table list

***Table 3.1**: Classification of membrane reactor considering the membrane material [11] 31*

***Table 3.2**. Summary of the fuel cell technologies [42-44]. [a]: oxygen ion conducting ceramics; [b]: proton ion conducting ceramics. 38*

***Table 3.3**: Comparison of target properties of the proton-conducting electrolytes. [55] 48*

***Table 3.4**. Reactions for electrochemical synthesis of ammonia using oxygen ion conducting and protonic conducting materials. 62*

***Table 4.1**. Composition and thicknesses of the tubular half-cell electrochemical support. 84*

***Table 4.2**. Slurry compositions. 84*

***Table 4.3**. The fourteen Bravais lattices. From [12]. 91*

***Table 4.4**. Advantages and limitations for the EIS [14]. 98*

***Table 7.1**. Model equations 160*

***Table 7.2**. Equations used for the unidimensional model. 162*

***Table 7.3**. Values of the factors for the oxygen transport model. 162*

***Table 7.4**. Conditions for the reference case. STP: Standard Temperature and Pressure 167*

***Table 7.5**. Parameter fitting as a function of the temperature $fT = A \cdot exp - EaRT$ 171*

***Table 7.6.** Conditions for the activation energies study 180*

***Table 7.7**. Comparison of the values for the fluid dynamic correlation ($Sh=a \cdot Re^b \cdot Sc^c$). 187*

***Table 8.1**. Governing equations for the CFD model. 212*

***Table 8.2**. Total inlet flow in each chamber for each geometry considered. 221*

***Table 9.1**. Governing equations of the Finite element model. 272*

Table 9.2. *Boundary conditions of the model. * number of the domain is referred to the Figure 9.5 ....280*

Table 9.3. *Theoretical maximum current according regarding the inlet flow. 284*

Table 9.4. *Coefficient for the Planck mean absorption coefficient for the reforming gases. 289*

Table 10.1. *Governing equations for the CFD model. 341*

Table 10.2. *Reactions and kinetics equations. 343*

Table 10.3. *Variables used for result analysis 348*

Table 10.4. *Fitting results of the kinetic model 349*

15. Scientific contribution

Publications

1. H. Malerød-Fjeld, D. Clark, I. Yuste-Tirados, R. Zanón, **D. Catalán-Martinez**, D. Beeaff, S.H. Morejudo, P.K. Vestre, T. Norby, R. Haugsrud, J.M. Serra, C. Kjølseth, Thermo-electrochemical production of compressed hydrogen from methane with near-zero energy loss, Nature Energy 2(12) (2017) 923-931.
2. **D. Catalán-Martínez**, M.E. Domine, J.M. Serra, Liquid fuels from biomass: An energy self-sustained process integrating H2 recovery and liquid refining, Fuel 212(Supplement C) (2018) 353-363.
3. Vøllestad, E., R. Strandbakke, M. Tarach, **D. Catalán-Martínez**, M. L Fontaine, D. Beeaff, D. R. Clark, J. M. Serra, T. Norby. Mixed Proton and Electron Conducting Double Perovskite Anodes for Stable and Efficient Tubular Proton Ceramic Electrolysers."Nature Materials 18 (7) 2019 752-759.

Congress participation

Poster contributions

2015

- CFD modelling of the oxygen permeation in BSCF membranes. EN Inorganic Membrane Summer School. Ionic and protonic conducting ceramic membranes for green energy applications. Valencia, Spain.

- Dual Phase composite materials as O2 suppliers under harsh CO2 and SO2-containing environments. EN 20th Int Conf on Solid State Ionics. Keystone, Colorado, USA

2016

- Freeze - Casting for the fabrication of highly ordered and porous microstructured reactor and its implementation as catalyst support for CO2 methanation catalytic reaction. EN 5th Int Conf on Structured Catalysts and Reactors. Donostia-San Sebastian, Spain.
- Liquid fuels from biomass: conversion and refinement in a selfsustainable process based on an integrated H2-membrane reactor. EN 5th Int Conf on Structured Catalysts and Reactors. Donostia-San Sebastian, Spain.

2017

- High temperature electrolyser with proton conducting ceramic tubular cells. EN Int Conf on Electrolysis. Copenhagen, Denmark.

2018

- High efficient H2 production in a multitubular electrolyser using protonic ceramic conductors. EN European Hydrogen Energy Conf. Málaga, Spain.

- Direct conversion of CH4 to aromatics in a catalytic membrane reactor; 15th Int Conf on Inorganic Membranes, Dresden, Germany

Oral contributions

2017

- TFD study of the H2 extraction in MDA process using a coionic membrane reactor. EN 21st Int Conf on Solid State Ionics. Padua, Italy.
- A TFD study of the H2 extraction in a steam-reforming protonic-membrane reactor. EN 21st Int Conf on Solid State Ionics. Padua, Italy.
- Sputtered thin film protective layers for the operation of OTMs in oxyfuel-like environments. EN 15th Conf of the European Ceramic Society. Budapest, Hungary.
- Development of steam electrodes in water splitting reaction for high temperature proton electrolysers. EN 15th Conf of the European Ceramic Society. Budapest, Hungary.

2018

- Intensified conversion of natural gas using proton-conducting ceramics to produce pressurized H2. EN European Hydrogen Energy Conf. Málaga, Spain.
- Direct conversion of CH4 to aromatics in a catalytic co-ionic membrane reactor. EN European Hydrogen Energy Conf. Málaga, Spain.

- Modelling of natural gas reforming using proton-conducting membrane reactors to produce pressurized H2; 15th Int Conf on Inorganic Membranes, Dresden, Germany

Agradecimientos

Bueno, finalmente este momento ha llegado. Creo que no soy capaz de poner con palabras mi agradecimiento al incontable número de personas que me han ayudado durante estos años. En fin, como tengo que intentarlo para terminar este jaleo, allá voy…

En primer lugar, me gustaría dar las gracias a mi familia. Siempre han estado ahí sin pedirme nada. No hubiera llegado hasta aquí sin ellos. Gracias a mis padres, a Pedro, a María, a Pablo y a Manolo. Gracias. También a Celia, y a los peques Vera, Celeste y Martín (y los que vengan).

La verdad es que no sabes que te depara el camino cuando lo empiezas: las cosas buenas, los momentos complicados, ... En ese sentido, me gustaría dar las gracias a Jose. Por la oportunidad de trabajar aquí, por la paciencia y la confianza que ha tenido conmigo a lo largo de los años. Ha sido un lujo poder trabajar en este centro.

Ahora me toca hablar del grupo. Si hubiera acabado hace un par de años no tendría que acordarme de tanta gente, pero ahora somos tantos… Para meterle mano empezaré por la gente que estaba aquí cuando yo llegué. A Vicente, Cecilia, Cyril y Raquel, que ya no están en el grupo y que se les echa mucho de menos. A María F., Sonia E. y Laura N., ya que los cafés mañaneros son siempre el mejor momento del día (si, Marwan, luego te nombro). Perdonar las abreviaturas en los apellidos, pero la tesis es suficientemente larga. A María B. y Julio, siempre son capaces de alegrarme el día con alguna broma. Luego llegaron Fidel, Nuria, Sara, Mateusz y Juan B. Más adelante Juan Escribano, Jorge, Marwan y sus ideacas, Maria V., Sonia R., Laura A., Alfonso, Álvaro, Nahum y Nora. Gracias por tantas veces *que me habéis echado una mano estos años. No habría terminado sin vosotros. Gracias por tantas anécdotas y tantos momentos. Las visitas cortas no las voy a comentar (hay que cortar en algún punto). Menos la de Art, pero eso es harina de otro costal. Gracias también a taller, gases e informáticos, sobre todo informáticos que son los que más me han sufrido. Mucho del trabajo de la tesis no hubiera salido delante de no ser por ellos.*

También querría acordarme de los mis antiguos profesores del departamento: Jose Marcial Gozálvez y Asunción Santafé. Por la paciencia y la ayuda a la hora de redactar esta tesis.

I would like to thank to the people of Oslo. The Coorstek Membrane Science group: Per, Harald, Christian, Dan, Michael, Selene and Irene; and the SINTEF group: Marie Laure, Truls and Einar.

Ahora quiero acordarme de Cristian y Maria Siurana, porque de momento la vida no ha conseguido separarnos, que así siga. Por ser siempre amigos dispuestos a estar a mi lado.

A mis amigos el máster, Raquel, Marta, Santi, Esther, Patricia y Ruben. Por esas cervezas que me han rescatado tantas veces. Por estar siempre ahí cuando más falta me hacía. Por todo.

A mis amigos de la Parroquia y a mi comunidad. En especial a Miguel y Ana, por preocuparse siempre por mí. También a Juan.

Gracias porqué, además de que nunca hubiera conseguido llegar hasta aquí sin ellos, mi vida es una pasada por teneros a mi lado.

- *Then the prophecies of the old songs have turned out to be true, after a fashion! – said Bilbo*

- *Of course! – said Gandalf – And why should not they prove true? Surely you don't disbelieve the prophecies, because you had a hand in bringing them about yourself? You don't really suppose, do you, that all your adventures and escapes were managed by mere luck, just for your sole benefit? You are a very fine person, Mr. Baggins, and I am very fond of you; but you are only quite a little fellow in a wide world afterall!*

- *Thank goodness! - said Bilbo*

Extracted from The Hobbit. J.R.R. Tolkien